Liquid Crystal Devices for Laser and Optical Beam-steering Applications

Doctor of Philosophy



Guanxiong Zhang

Somerville College

Department of Engineering Science

University of Oxford

Supervised by Prof. Stephen M. Morris and Prof. Steve J. Elston

October 2024

Abstract

LIQUID CRYSTAL DEVICES FOR LASER AND OPTICAL BEAM-STEERING APPLICATIONS

by GUANXIONG ZHANG

This thesis explores the properties and applications of liquid crystal (LC) lasers, with a focus on their integration into optical beam-steering systems and the establishment of a free-space optical communication link using LC-based beam-steering. LC lasers, known for their unique optoelectronic properties, offer several advantages, including compactness, flexibility, and tunability, making them promising candidates for next-generation light sources in applications such as display technologies, biomedical imaging, and optical communications. Despite considerable progress, there remains a limited understanding of the polarisation states and coherence characteristics of LC lasers. This research addresses this gap by systematically studying the polarisation state and temporal coherence of band-edge LC lasers, using techniques such as Stokes parameter measurements and Michelson interferometry.

Challenges like pulse-to-pulse variations and wavelength mismatches between LC lasers and measurement systems were successfully overcome. The key findings reveal that band-edge LC lasers are nearly circularly polarised, with the same handedness as the LC helical structure. Several factors, including excitation fluence, LC layer thickness, and alignment quality, were identified as influencing the circularity and degree of polarisation of these LC lasers. Regarding temporal coherence, the longest coherence length of 275.32 µm was observed at a layer thickness of 10.91 µm. Thinner or thicker LC layers resulted in broader spectral linewidths and reduced temporal coherence, although the excitation fluence of the pump laser had little effect on the coherence length.

The insights gained on polarisation properties provide a basis for the development of a two-dimensional optical beam-steering system for LC lasers, employing polarisation gratings and tunable LC waveplates. This system preserves the laser wavelength and characteristics with minimal impact on intensity. The far-field beam-steering pattern was validated using a Jones matrix simulation, which explained the appearance of additional diffraction orders beside the primary beam.

The same beam-steering method was applied to both the transmitter and receiver in a free-space optical communication link, leading to substantial improvements in the field of view and link margin of the system. This approach is low-cost, lightweight, and requires only simple voltage controls. To demonstrate its viability, the thesis presents a link capable of transmitting 50 Mbps pseudo-random binary sequence signals over a distance of 1 metre with a bit error rate below 10^{-3} in a point-to-point scenario. The beam-steering system, with a steering bandwidth of 58.82°/sec, can be adapted for different transmission rates and wavelengths, offering significant flexibility for applications such as indoor mobile terminals.

"You got a dream... You gotta protect it. People can't do somethin' themselves, they wanna tell you you can't do it. If you want somethin', go get it. Period."

— **Christopher Gardner**, *The Pursuit of Happyness*

To Mom, Dad, and everyone who offered invaluable help throughout my academic journey...

Acknowledgements

It would have been impossible for me to reach this stage of my academic journey without the invaluable support of my exceptional supervisors, Professor Stephen M. Morris and Professor Steve J. Elston. They not only gave me the opportunity to study and conduct research at the University of Oxford, but also guided me in exploring the fascinating world of soft matter photonics. Words fall short of expressing my deep gratitude and admiration for them, and I often reflect on how fortunate I have been to experience these past four years at Oxford.

First and foremost, I want to thank Steve M. for your unwavering support since the very beginning of my D.Phil. Your guidance has been invaluable, and I am especially grateful for recommending me to Professor Dominic O'Brien, which helped me with the opportunity for a post-doctoral research associate position in his group. I still recall the moment when I sent you my First Year Transfer Report and received 654 detailed comments for the 56-page report, from correcting prepositions to improving paragraphs. I was deeply moved by your extraordinary attention to detail and your genuine care for my development as a research student. I have carried forward this sense of responsibility to my own students, not just at Oxford but worldwide, across all ages. I would also like to express my heartfelt thanks to Steve E. for your endless patience and thoughtful advice whenever I faced challenges in my research. Your sense of humor and wisdom created a happy and welcoming atmosphere within the group. Among the students, we affectionately call you 'Grandpa Steve' because you always make us feel cared for with kindness, warmth, and love.

A special mention goes to Andy, whose immense contribution to my beam-steering communication link project was invaluable. From discussing research approaches to helping me to address the most challenging reviewer comments on my manuscript, I have truly cherished our collaboration and co-authorship. When I drafted this thesis, I revisited the program codes you wrote and was once again impressed by how meticulously organised and detailed everything was. Thank you, Andy, for this extra tutorial on the 'best' way to code and organise data, and for all the guidance you gave me during my time at Oxford.

To the members of the Soft Matter Photonics group and collaborators from the Optical Communications group, especially Chao, James, Atchutananda, and Xiuze, who I had the privilege of working with and publishing manuscripts alongside. Thank you for your generous support and remarkable contributions to our research. To my friends at Oxford, Zipei, Xuke, Bohan, Mengmeng, Yihan, Peng, and Linpei, I am beyond grateful to have shared this journey with you and to have so many beautiful memories in this lovely city.

Last but not least, to my Mom and Dad, whose pride in me and constant support, both financial and emotional, have made this journey possible. Being the first in my family to pursue a D.Phil. is an honour I could not have achieved without the support from my beloved parents. Education has always been a top priority in our family, and I will never forget my Mom driving me between classes when I was young, or my Dad searching for the best educational opportunities around the world. Their sacrifices have been my greatest source of strength. I love you, Mom and Dad.

Publications

Peer-reviewed Journal Publications

Zhang, G.; Schreier, A.; Wang, X.; Matthews, W.; Farmer, J.; Faulkner, G.; Elston, S. J.; Morris, S. M.; O'Brien, D. Free-Space Optical Communication Link with Liquid Crystal Beam-Steering. *IEEE Photonics Technology Letters* **2023**, 1–1. https://doi.org/10.1109/LPT.2023.3308774.

Zhang, G.; Elston, S. J.; Schreier, A.; Faulkner, G.; Surampudi, A.; O'Brien, D.; Morris, S. M. Non-Mechanical Optical Beam-Steering of a Liquid Crystal Laser. *Opt Laser Technol* **2023**, 157. https://doi.org/10.1016/j.optlastec.2022.108623.

Surampudi, A.; **Zhang, G.**; Singh, R.; Faulkner, G.; O'Brien, D. C.; Booth, M. J.; Morris, S. M. Liquid Crystals for Luminescent Concentrators: A Review. *Crystals* **2023**, 13 (12), 1615. https://doi.org/10.3390/cryst13121615.

Zhang, G., He, C., Elston, S. J., Morris, S. M. Stokes Parameters and Polarisation States of Band-edge Liquid Crystal Lasers. [In submission]

Zhang, G., Elston, S. J., Morris, S. M. Coherence Characterisation of Band-edge Liquid Crystal Lasers. [In preparation]

Conference Proceedings

Zhang, G.; Schreier, A.; He, C.; Surampudi, A.; Faulkner, G.; Elston, S. J.; O'Brien, D.; Morris, S. M. Optical Beam-Steering and Polarization Property of a Liquid Crystal Laser. In *Liquid Crystals XXVII*; SPIE, 2023; p 17. https://doi.org/10.1117/12.2676363.

Surampudi, A.; Singh, R.; **Zhang, G.**; Faulkner, G.; Booth, M. J.; Elston, S. J.; O'Brien, D.; Morris, S. M. A Polarization Sensitive Thin Film Optical Wireless Concentrator. In *2022 IEEE Photonics Conference*; IEEE, 2022; pp 1–2. https://doi.org/10.1109/IPC53466.2022.9975470.

Presentations

British Liquid Crystal Society Annual Meeting, Oxford, April 2024 (Poster), "Stokes Parameters and Polarisation Properties of Band-edge Liquid Crystal Lasers"

Oxford Photonics Day, Oxford, October 2023 (Poster), "Free-Space Optical Communication Link with Liquid Crystal Beam-Steering"

SPIE Optics + Photonics, San Diego, August 2023 (Oral), "Optical Beam-steering and Polarization Property of a Liquid Crystal Laser"

Oxford Photonics Day, Oxford, October 2022 (Poster), "Non-Mechanical Optical Beam-Steering of a Liquid Crystal Laser"

Patents

Wang, X.; **Zhang, G.**; Morris, S. M.; Elston, S. J.; O'Brien, D.; Faulkner G.; Schreier, A. "Beam steering system for wireless optical communications" [In application]

Contents

List of Figures **xii**

List of Tables **xvii**

List of Abbreviations **xviii**

1 Introduction **1**
1.1 Motivation and Context . . . 1
1.2 Structure of the Thesis . . . 2

2 Background **8**
2.1 Liquid Crystals . . . 8
2.1.1 Nematic Phase . . . 10
2.1.2 Chiral Nematic Phase . . . 17
2.2 LC Lasers . . . 24
2.2.1 Band-edge LC Lasers . . . 26
2.2.2 Defect-mode LC Lasers . . . 29
2.3 Characteristics and Functionalities of Band-edge LC Lasers . . . 30
2.3.1 Excitation Threshold and Slope Efficiency . . . 30
2.3.2 Wavelength and Direction Tunability . . . 32
2.4 Mathematical Descriptions of Polarisation . . . 33
2.4.1 Stokes Parameters and Mueller Matrix . . . 34
2.4.2 Jones Vector and Jones Matrix . . . 37
2.5 Summary . . . 39

3 Experimental Procedures **41**
3.1 Mixture Preparation . . . 41
3.1.1 PVA Solution . . . 41
3.1.2 LC Mixtures . . . 43
3.2 LC Glass Cells . . . 45
3.3 Optical Characterisation Techniques . . . 50
3.3.1 Polarising Optical Microscopy . . . 50
3.3.2 Optical Fluorescence Microscopy . . . 51
3.3.3 Ultraviolet-visible Spectrophotometry . . . 51
3.3.4 USB Spectrometer . . . 54
3.4 Nd:YAG Pump Laser . . . 56
3.4.1 Laser Beam Profile . . . 56
3.4.2 Knife-edge Measurement Method . . . 58
3.5 Band-edge LC Lasers . . . 60
3.5.1 Fundamentals . . . 60
3.5.2 Material Preparation . . . 61

3.5.3 Chiral Nematic LC Hosts . . . 62
3.5.4 Dye-doped Nematic LCs . . . 63
3.5.5 Fluorescence Emission from Dye-doped Chiral Nematic LCs . . . 70
3.5.6 Laser Emission from Dye-doped Chiral Nematic LCs . . . 72
3.6 Summary . . . 75

4 Stokes Parameters Characterisation of Liquid Crystal Lasers 78
4.1 Introduction and Aims . . . 78
4.2 Stokes Parameters Measurements and Calibration . . . 80
4.2.1 Calibration . . . 80
4.2.2 Stokes Imaging Polarimeter . . . 83
4.3 Stokes Parameters of a Continuous-wave Laser . . . 85
4.4 Stokes Parameters of a Pulsed Laser . . . 90
4.5 Stokes Parameters of LC Lasers . . . 93
4.5.1 Excitation Energy . . . 96
4.5.2 LC Layer Thickness . . . 100
4.5.3 Alignment Quality . . . 103
4.6 Summary . . . 105

5 Optical Beam-steering of a Liquid Crystal Laser 107
5.1 Chapter Introduction and Aims . . . 107
5.2 Polarisation Gratings . . . 110
5.3 Nematic LC Waveplates . . . 113
5.4 Beam-steering Characterisation and Simulation . . . 114
5.4.1 Characterisation of PGs . . . 116
5.4.2 LC Laser Beam-steering . . . 121
5.5 System Configuration and Experimental Results . . . 124
5.6 Reconstructing the Jones Vector . . . 131
5.7 Summary . . . 133

6 Liquid Crystal Beam-steering for Optical Communications 135
6.1 Introduction and Aims . . . 135
6.2 Optical Characterisation of Diffusers . . . 138
6.3 Free-space Optical Communications Link . . . 144
6.3.1 Communications Link without Diffuser . . . 147
6.3.2 Communications Link with a Diffuser . . . 149
6.4 Signal-to-noise Ratio Optimisation . . . 150
6.4.1 Fibre-coupled Laser Diode . . . 151
6.4.2 Amplified Differential PIN Photodiode . . . 156
6.5 Optimised Free-space Optical Communications Link . . . 159
6.6 Summary . . . 163

7 Coherence Measurements of Liquid Crystal Lasers **168**
7.1 Chapter Introduction and Aims 168
7.2 Temporal Coherence Measurements 170
7.2.1 Michelson Interferometer 170
7.2.2 Coherence Length of a Pulsed laser 171
7.2.3 Coherence Length of LC lasers 174
7.3 Summary 180

8 Conclusions and Future Work **182**
8.1 Conclusion to Thesis 182
8.2 Stokes Parameters Measurements of Left-handed Band-edge LC Lasers 184
8.3 Spatial Coherence Study of LC Lasers 187
8.4 Polarisation States and Coherence of Polymerised Blue Phase LC Lasers 188
8.5 Bidirectional Optical Communication Link Using LC Beam-steering 192
8.6 Advanced LC Laser Device Architectures 193

References **194**

List of Figures

1.1 An overview of the structure of this thesis. . . . 3

2.1 The chemical structure of a nematic LC and the molecular structure of nematic LCs. . . . 10
2.2 A demonstration of homogeneous and homeotropic alignment of nematic LCs, as well as the pseudo-homeotropic alignment which can be achieved in experiments. 12
2.3 An illustration of the optical path when observing a nematic LC cell on a polarising optical microscope. . . . 14
2.4 Optical textures of a nematic LC cell observed on a polarising optical microscope with different applied voltages and LC director orientations. . . . 16
2.5 The molecular structure of chiral nematic LCs and an illustration of the pitch length. . . . 17
2.6 A demonstration of the Grandjean texture, fingerprint or uniform lying helix, and focal conic texture. . . . 18
2.7 A demonstration of the selective reflection in ideal chiral nematic LCs solved using the eigenmode solutions to Maxwell's wave equation. . . . 23
2.8 An illustration of the PBG of a chiral nematic LC simulated based on the Berreman 4×4 matrix method. . . . 24
2.9 A simplified schematic diagram for lasers. . . . 25
2.10 Geometrical illustrations of the Poincaré sphere and the corresponding polarisation ellipse. . . . 37

3.1 The preparation procedures of the PVA solution. . . . 42
3.2 The preparation procedures of LC mixtures. . . . 44
3.3 An illustration of the structure of the Instec cells. . . . 46
3.4 The fabrication process of an empty glass cell with homogeneous alignment. . . . 48
3.5 The fabrication process of capillary filling an empty glass cell with an LC mixture. 49
3.6 A simplified schematic diagram a polarising optical microscope. . . . 50
3.7 A simplified schematic of an optical fluorescence microscope. . . . 52
3.8 A simplified schematic of the UV-Vis spectrometer. . . . 53
3.9 The transmission spectrum of an empty LC cell and an illustration of measuring the cell thickness from the spectrum. . . . 55
3.10 A simplified schematic of the USB spectrometer. . . . 56
3.11 A demonstration of the Gaussian beam generated from the Nd:YAG laser. . . . 57
3.12 The system configuration for measuring the diameter of the Nd:YAG laser beam waist using the knife-edge method. . . . 59
3.13 The measurement results of the diameter of the Nd:YAG laser beam waist. . . . 59
3.14 The configuration of a band-edge LC laser cell filled with dye-doped chiral nematic LCs. . . . 61
3.15 The transmittance spectra of four different chiral nematic LC mixtures measured by the UV-Vis spectrometer. . . . 63

3.16 Demonstration of the guest-host effect in dye-doped nematic LCs in the homogeneous alignment and the pseudo-homeotropic alignment. 64
3.17 The relative permittivity measurement of a dye-doped nematic LC. 65
3.18 The absorption spectra of a dye-doped nematic LC with and without the application of an electric field. 66
3.19 Optical textures of a dye-doped nematic LC cell observed on an optical fluorescence microscope with and without the application of an electric field and a polariser. 68
3.20 The system configuration of the fluorescence spectrometer for characterising fluorescence emissions from LC samples. 69
3.21 The fluorescence spectrum and anisotropic emission properties of a dye-doped nematic LC. 69
3.22 Optical textures of dye-doped chiral nematic LC cells observed on a polarising optical microscope with different thicknesses and alignment quality. 71
3.23 The absorbance spectra of a dye-doped chiral nematic LC with and without the application of an electric field as well as its fluorescence spectrum. 71
3.24 The system configuration for generating LC lasers 73
3.25 The spectrum of single-mode laser emission from a dye-doped chiral nematic LC. 74
3.26 Excitation threshold measurements of a band-edge LC laser fabricated using a dye-doped chiral nematic LC. 75

4.1 System configurations for calibrating polarisers and waveplates. 81
4.2 An illustration of the Stokes imaging polarimeter used for the measurement of the polarisation. 83
4.3 The system configuration for measuring the Stokes parameters of the green He-Ne laser with and without a thin-film linear polariser, as well as the measurement results including normalised Stokes parameters, DOP, and polarisation ellipse diagrams. 87
4.4 The system configuration for measuring the Stokes parameters of a linearly polarised green He-Ne laser with its polarisation direction rotated, as well as the measurement results including normalised Stokes parameters, DOP, and polarisation ellipse diagrams. 88
4.5 The system configuration for measuring the Stokes parameters of a circularly polarised green He-Ne laser, as well as the measurement results including normalised Stokes parameters, DOP, and polarisation ellipse diagrams. 89
4.6 The system configuration for measuring the Stokes parameters of an Nd:YAG laser tuned to be either linearly polarised or circularly polarised, as well as the measurement results including normalised Stokes parameters, DOP, and polarisation ellipse diagrams. 92
4.7 An investigation on the impact of wavelength mismatch, between the design wavelength of the rotatable QWP in the Stokes imaging polarimeter and the wavelength of the laser, on the Stokes parameters measurements. 94
4.8 System configuration for measuring the Stokes parameters of LC lasers. 95

4.9 An investigation on the impact of averaging over a different number of pulses of the LC laser on the Stokes parameters measurements. 97
4.10 The output emission intensity of the LC laser as a function of the excitation fluence. 98
4.11 The polarisation states of an LC laser with various excitation fluences. 99
4.12 The structure of a wedge cell and The transmittance spectra for the LC cell at three selected thicknesses. 101
4.13 The polarisation states of a wedge LC laser with different LC layer thicknesses. . 102
4.14 The structure of a wedge cell and the optical textures of the cell observed on an optical polarising microscope at two thicknesses with good and poor alignment quality. 104
4.15 The polarisation states of a wedge LC laser with and without alignment defects. 105

5.1 An illustration of the structure of a polymerisable LC PG. 110
5.2 The optical texture of the PG observed on an optical polarising microscope. . . 111
5.3 Optical beam-steering of an LC laser using tuneable nematic LC waveplates and PGs. 115
5.4 Experimental demonstration of one-dimensional beam-steering of a He-Ne laser using a PG and the corresponding far-field patterns. 117
5.5 Experimental demonstration of two-dimensional beam-steering of a He-Ne laser using PGs and the corresponding far-field patterns. 118
5.6 Simulations and experimental results for the relative intensity of each spot in the far-field for both one and two-dimensional beam-steering of a He-Ne laser. . . . 121
5.7 Experimental demonstration of one-dimensional beam-steering of an LC laser using a PG and the corresponding far-field patterns. 123
5.8 Experimental demonstration of two-dimensional beam-steering of an LC laser using two PGs and the corresponding far-field patterns. 124
5.9 Simulations and experimental results for the relative intensity of each spot in the far-field for both one and two-dimensional beam-steering of an LC laser. 125
5.10 The system configuration used to demonstrate dynamic optical beam-steering of an LC laser. 126
5.11 Experimental results of the far-field pattern of a non-mechanical LC laser beam-steering. 128
5.12 The relative intensity spectra of the LC laser beam after been steered. 129
5.13 The response time measurement of the nematic LC phase shifters. 131
5.14 The Stokes parameters measurement results for the LC laser used for beam-steering. 133

6.1 The optical textures of the diffusers when viewed on an optical polarising microscope. 139
6.2 The system configuration and far-field diffraction patterns after introducing the diffuser on the PG beam-steering. 141
6.3 The system configuration for the transmitter of the optical communications link and the diffraction pattern of the steered diffused beam. 143

6.4 The structural representation of the 3D-printed rack for stacking the beam-steering components and the diffuser. . . . 144
6.5 The system configuration of a proposed prototype of the free-space optical communications link using LC beam-steering. . . . 145
6.6 The transmitted and received signals for a 35 cm communications link without the diffuser. . . . 148
6.7 The transmitted and received signals after taking an averaging of 4096 for a 15 cm communications link with the diffuser. . . . 150
6.8 The transmitted and received signals after taking an averaging of 8 for a 10 cm and a 20 cm communications link. . . . 153
6.9 The voltage-current-power curves measured for the fibre-coupled laser diode. . . . 154
6.10 The transmitted and received signals after taking an averaging of 1024 for a 40 cm and an 80 cm communications link. . . . 155
6.11 Displacement measurement results for the point-to-point and the point-to-two-point scenarios 156
6.12 Demonstration of 50 MHz, 1.4 Vpp PRBS data transmission and reception for a 60 cm communications link using a differential PIN PD. . . . 158
6.13 Schematic diagram of the free space optical communications link. . . . 160
6.14 The beam profile of all four beam-steered states at the output of the transmitter. 161
6.15 Displacement measurements with and without the beam-steering stack at 40 cm distance from the transmitter. . . . 161
6.16 The eye diagram for the transmitted 50 Mbps PRBS signal of the free-space optical communications link. . . . 163
6.17 The eye diagrams for the received signals of the 40∼80 cm free-space optical communications link. . . . 164
6.18 The eye diagrams for the received signals of the 100 cm free-space optical communications link. . . . 165
6.19 The BER measured as a function of the received power, the link distance, or the link geometrical loss. . . . 166

7.1 System configuration for measuring the coherence length of a commercial pulsed Nd:YAG laser using a Michelson interferometer. . . . 172
7.2 Measurement of the coherence length of the Nd:YAG laser. . . . 173
7.3 System configuration for measuring the coherence length of LC lasers using a Michelson interferometer. . . . 174
7.4 The structure of a wedge cell fabricated for the investigation of the coherence length of band-edge LC lasers of different thicknesses. . . . 175
7.5 Measurement of the coherence length of a band-edge LC laser with various thicknesses. . . . 176
7.6 The emission spectra of band-edge LC lasers with various thicknesses. . . . 179
7.7 Measurement of the coherence length of a band-edge LC laser under various excitation fluences. . . . 181

8.1 The transmittance spectra for three different left-handed chiral nematic LC mixtures with various concentrations of the chiral additive. 185
8.2 The optical textures of a left-handed LC cell on a polarising optical microscope. 186
8.3 The transmittance spectra for the left-handed LC cell altered over time with the photonic bandgap blue-shifting to longer wavelengths. 186
8.4 The optical textures of another left-handed LC cell on a polarising optical microscope. 187
8.5 A proposed system configuration for measuring the coherence area of LC lasers. 188
8.6 The textures of a BPLC cell on a polarising optical microscope during the formation of a BPLC. 190
8.7 The optical textures of a polymerisable BPLC cell on a polarising optical microscope during the formation and UV curing of BP. 191
8.8 A proposed system design for a bidirectional free-space optical communication link. 192

List of Tables

3.1 The LC mixtures prepared and studied in the subsequent experiments. 62

4.1 The circularity, linearity, and DOP of an LC laser with various excitation fluences. 99
4.2 The circularity, linearity, and DOP of a wedge LC laser with various LC layer thicknesses. 103
4.3 The circularity, linearity, and DOP of a wedge LC laser with and without alignment defects. 105

5.1 Voltage response of each spot of the beam-steering. 129
5.2 Relative intensities of each spot of the beam-steering. 130
5.3 The simulation and measurement results of the one-dimensional beam-steering diffraction intensities of the primary beam, zero-order, and the opposite order. . 133

7.1 The LC layer thickness, spectral width, and coherence length of a wedge LC laser. 178

List of Abbreviations

LC . . . . . **L**iquid **C**rystal.

POM . . . . . **P**olarising **O**ptical **M**icroscope.

PG . . . . . **P**olarisation **G**rating.

ITO . . . . . **I**ndium **T**in **O**xide.

CCD . . . . . **C**harge-**c**oupled **D**evice.

PBG . . . . . **P**hotonic **B**and-**g**ap.

DOS . . . . . **D**ensity **o**f **S**tates.

DFB . . . . . **D**istributed **F**eed**b**ack.

QD . . . . . **Q**uantum **D**ots.

DOP . . . . . **D**egree **o**f **P**olarisation.

UV-Vis . . . . . **U**ltra**v**iolet-**vis**ible.

SNR . . . . . **S**ignal-to-**n**oise **R**atio.

LCR . . . . . Inductance (**L**), Capacitance (**C**), and Resistance (**R**).

LED . . . . . **L**ight **E**mitting **D**iode.

QWP . . . . . **Q**uarter **W**ave**p**late.

OD . . . . . **O**ptical **D**ensity.

HWP . . . . . **H**alf **W**ave**p**late.

SLM . . . . . **S**pacial **L**ight **M**odulator.

FWP . . . . . **F**ull **W**ave**p**late

He-Ne . . . . . **He**lium-**Ne**on.

PD . . . . . **P**hoto**d**iode.

LiDAR . . . . . **L**ight **D**etection **a**nd **R**anging.

RF . . . . . **R**adio **F**requency.

VLC . . . . . **V**isible **L**ight **C**ommunications.

RGB . . . . . **R**ed, **G**reen, **B**lue.

FOV . . . . . **F**ield **o**f **V**iew.

BER . . . . . **B**it **E**rror **R**ate.

PRBS . . . . . **P**seudo-**r**andom **B**inary **S**equence.

FWHM . . . . . **F**ull **W**idth at **H**alf **M**aximum.

DSLR . . . . . **D**igital **S**ingle-**l**ens **R**eflex.

AWG . . . . . **A**rbitrary **W**aveform **G**enerator.

NEP . . . . . **N**oise **E**quivalent **P**ower.

BP . . . . . **B**lue **P**hase.

1 Introduction

Contents

1.1 Motivation and Context 1
1.2 Structure of the Thesis 2

1.1 Motivation and Context

The continual advancement of laser technologies over the past half-century has led to significant progress in improving emission quality, miniaturising device dimensions, introducing novel materials, and enhancing power efficiency. The diverse benefits and capabilities of lasers, such as their monochromaticity, low divergence, high coherence, and energy concentration, have made them indispensable across various industries and applications in recent years, including holography [1], spectroscopy [2], navigation [3], photolithography [4], and quantum communications [5].

Liquid crystals (LCs), which exhibit characteristics of both isotropic liquids and crystalline structures, are well-known for their optoelectronic properties that offer desirable tunability and flexibility, making them suitable for applications where conventional materials may face limitations. At the intersection of laser technologies and LCs, LC lasers have rapidly advanced in the field of soft matter photonics over the past few decades [6–8]. These lasers exhibit notable features, including ultra-thin dimensions, compatibility with flexible and conformable device structures, a large coherence area, and a wide range of wavelength tunability. These advantages stem from the intrinsic versatility and optical characteristics of LCs. Owing to this tunability, compatibility with flexible substrates, and the self-organisation of their periodic structures, LC

lasers hold great promise for next-generation technologies that require compact and adaptable light sources with unique emission properties not typically observed in conventional laser systems. Potential applications span various industries, from display technologies [9, 10] to biomedical imaging[11], thermal and chemical sensors [12, 13], and optical communication fields[14].

While a considerable body of literature has demonstrated the functional versatility of LC lasers, very few studies have explored their polarisation and coherence properties. As a result, the understanding of these characteristics in LC lasers remains relatively underdeveloped. The polarisation states and coherence properties of LC lasers appear to differ from those of conventional lasers, suggesting that detailed investigations into these aspects could provide valuable fundamental insights and spark new technological innovations.

This thesis aims to investigate the polarisation and coherence properties of LC lasers, along with relevant beam-steering applications that leverage these characteristics. Specifically, the polarisation state and temporal coherence were systematically studied, with the inherent near-circular polarisation emission leading to the development of a novel LC laser beam-steering system and an optical communications link featuring LC-based beam-steering. The challenges addressed in this work include managing pulse-to-pulse variations in LC lasers and identifying multiple factors that influence their emission performance. Focusing on LCs, this thesis seeks to enhance the understanding of the physical fundamentals of LC lasers and to advance the potential of non-mechanical beam-steering and free-space communication technologies.

1.2 Structure of the Thesis

Chapter 1 introduces the research motivation and outlines the structure of this thesis. The subsequent chapters, as shown in **Fig. 1.1**, form the main body of the thesis, combining background information, fundamental studies, and application studies. The research background and experimental procedures discussed in Chapter 2 and Chapter 3, respectively, provide the foundation for the entire research presented in this thesis. Studies on the properties of LC lasers, including their polarisation states and coherence, are covered in Section 4.5 and Chapter 7, respectively. The polarisation studies of LC lasers are then linked to the simulation and analysis of an LC laser optical beam-steering approach based that exploits the polarisation states of these lasers in Chapter 5. This beam-steering technique subsequently leads to a free-space optical

communications link in Chapter 6, showcasing another novel application of LC technologies. The thesis concludes with a summary of the findings and proposals for future work in Chapter 8. Here, A brief description of the content of each chapter is provided individually.

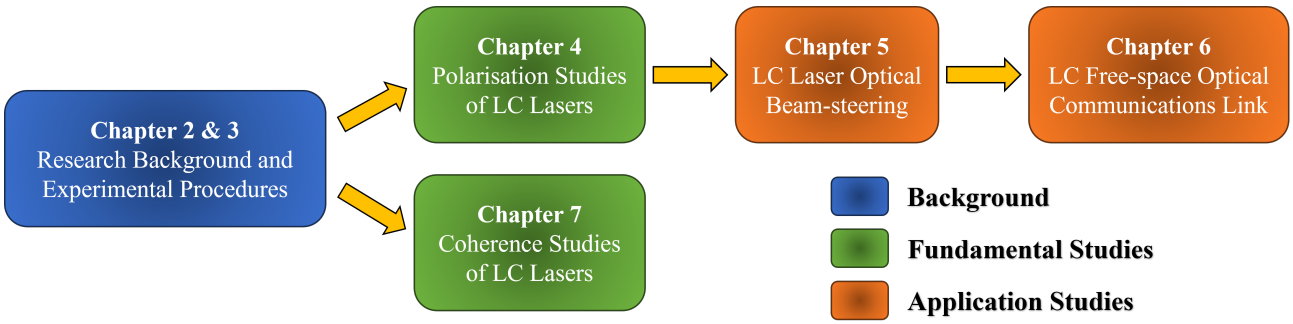

Figure 1.1: An overview of the structure of the thesis, containing background information related to the research, fundamental studies on LC lasers and the development of new LC optical communications systems.

Chapter 2 introduces a general background on LCs, LC lasers, and the mathematical descriptions of polarisation, providing a theoretical foundation for the research presented in subsequent chapters. Recent research published in the literature is also presented to summarise the current state-of-the-art. The chapter begins with an introduction to LCs, focusing on their electrical and optical properties, and covers two of their most common and widely studied mesophases: the nematic phase and the chiral nematic phase. Both mesophases are central to the experiments conducted throughout the thesis. LC lasers are the major focus of this thesis and are based on the essential concepts and physics provided in this section. Subsequently, an illustration of LC lasers is presented, including the working principle and research progress of band-edge LC lasers and defect-mode LC lasers. Band-edge LC lasers are a particular research focus in this thesis, thus their key characteristics and functionalities are specifically demonstrated, such as the excitation threshold, slope efficiency, wavelength tunability and beam-steering approaches reported thus far. These illustrations provide a reference for the performance of the LC lasers fabricated and experimented with in subsequent chapters. Finally, this chapter finishes with an introduction to the mathematical descriptions of the polarisation states of light. Two approaches illustrated in this section, the Stokes parameters combined with the Mueller matrix and the Jones vector integrated with the Jones matrix, were applied to analyse the polarisation states of band-edge LC lasers in Chapter 4 and to simulate the far-field diffraction from polarisation gratings introduced in Chapter 5, respectively.

Chapter 3 outlines the core experimental techniques and procedures employed in this thesis. The illustration begins with a description of the mixture preparation procedure including the PVA solution and the LC mixtures, as well as the structure of commercial LC glass cells, which are widely used in the experiments described in subsequent chapters. When commercial LC cells do not meet specific experimental requirements, custom LC glass cells were fabricated in a cleanroom; therefore, the fabrication process is presented accordingly in this chapter. Subsequently, a series of optical characterisation techniques, including polarised optical microscopy (POM), optical fluorescence microscopy, ultraviolet-visible spectrophotometry, and USB spectrometry, are described in detail along with their working principles and experimental procedures. These techniques are essential for characterising the alignment of LCs and the optical behaviour of LC cells throughout the thesis. Following this, the chapter introduces the beam profile of the Nd:YAG pump laser and the knife-edge method used to measure the beam waist, followed by detailed studies of chiral nematic LC hosts, dye-doped nematic LCs, focusing on their optical textures on a POM, absorption, and fluorescence properties. These descriptions, combined with the theoretical background introduced in Chapter 2, provide the foundation for fabricating band-edge LC lasers using a nanosecond pulsed Nd:YAG pump laser and a dye-doped chiral nematic LC cell. The chapter concludes by presenting the typical parameters of a single-mode LC laser, specifically E7 + 2.5 wt.% R5011 + 1 wt.% DCM, which will be used as the laser source for the beam-steering work described in Chapter 5.

Chapter 4 presents a study on the Stokes parameters and polarisation states of band-edge LC lasers. While these lasers are often considered inherently circularly polarised due to the helical structure of LCs, multiple reports published in the literature have provided evidence of observing imperfect circular polarisation. This chapter characterises the specific polarisation states of these lasers by measuring their Stokes parameters using a Stokes imaging polarimeter. It begins with a literature review and an introduction to the measurement method and the calibration of key components, including polarisers and waveplates. To validate the accuracy of the characterisation technique, a commercial continuous-wave He-Ne laser and a pulsed Nd:YAG laser were adjusted to various polarisation states (linear, circular, and elliptical) using combinations of polarisers and waveplates, with the corresponding Stokes parameters measurements presented thereafter, showing consistency with the theoretical analysis. This chapter then investigates the impact of wavelength mismatch between the laser and the designed

wavelength of waveplates, as well as the influence of the averaging number of pulses on the polarisation measurement results. These detailed calibration and investigations establish a solid foundation for the subsequent Stokes parameter measurements of band-edge LC lasers. Finally, this chapter demonstrates the Stokes parameters of LC lasers under multiple excitation fluences of the pump laser, varying LC layer thicknesses, and different LC alignment qualities. Compared to other LC laser polarisation studies in the literature, this approach provides polarisation information at each pixel across the laser wavefront and considers factors that could affect the polarisation states of LC lasers. The results could be of significant benefit to understanding the polarisation states and applications involving polarisation control of band-edge LC lasers. *This work has been prepared for submission to a peer-reviewed journal.*

Chapter 5 presents non-mechanical optical beam-steering of an LC laser, which is achieved by adjusting the polarisation state of the LC laser using voltage-tuneable nematic LC cells and then steering the beam according to its polarisation state by diffraction when incident upon a polarisation grating (PG). The chapter begins with a literature review covering both mechanical and non-mechanical beam-steering technologies and the techniques used to specifically steer the beam of an LC laser. It then introduces the working principles of two core components for the beam-steering approach, the PGs and nematic LC waveplates, along with their Jones matrices to describe the light propagation through these devices. Prior to demonstrating the LC laser beam-steering, this chapter characterises the PGs using a commercial He-Ne laser and a MATLAB-based Jones matrix simulation method to analyse imperfections in the PGs and derive the far-field diffraction patterns. Similar calibration procedures were conducted for the beam-steering of an LC laser, and its simulation and experimental results are presented subsequently. Finally, the chapter presents the beam-steering of an LC laser to four distinct locations in two-dimensional space, highlighting advantages such as maintaining the laser wavelength, minimising the impact on laser intensity, and establishing a system configuration entirely based on LC and polymer thin films. This work also provides further evidence of the imperfect circular polarisation of band-edge LC lasers, and when the Jones vector of the LC laser used for beam-steering is reconstructed from the Stokes parameters measured using the technique in Chapter 4, the simulation results show consistency with experimental measurements of the far-field diffraction pattern intensities. *This work has been published in a peer-reviewed journal, Optics & Laser Technology, Volume 157, January 2023, 108623. A part of the work in this chapter was presented*

as an oral presentation at the SPIE Organic Photonics + Electronics 2023 and published in the conference proceedings, Liquid Crystals XXVII, September 2023, PC1265805.

Chapter 6 presents a free-space optical communications link using LC beam-steering technologies, incorporating PGs, tuneable LC waveplates, and diffusers, based on part of the work demonstrated in Chapter 5. This chapter begins with a literature review on visible light communications and the state-of-the-art beam-steering technologies employed in communications links. The subsequent section introduces the optical characterisation of the diffusers, including their optical textures when viewed on a POM, birefringence, and optimal positioning within the transmitter. The establishment of the communications link is illustrated initially without a diffuser to demonstrate the beam-steering concept, followed by a demonstration with a diffuser to achieve the entire space coverage of the transmitted light. The transmitter and receiver components were stacked in a 3D-printed rack to minimise the geometrical loss of the link. This chapter then introduces two implementations, the addition of a fibre-coupled laser diode and an amplified differential photodiode, both of which significantly enhance the signal-to-noise ratio, leading to an optimised free-space optical communications link. Additionally, employing a beam-steering stack for the receiver improves the field of view and intensities received by the photodetector. This chapter concludes with experimental results including eye diagrams and bit error rates of links with various distances and application scenarios. Compared to other techniques published in the literature, this approach of LC beam-steering in a communications link is lightweight, low-cost and not limited to any operational wavelength or bandwidth. *This work has been published in a peer-reviewed journal, IEEE Photonics Technology Letters, Volume 35, Issue 22, November 2023.*

Chapter 7 presents a study on the temporal coherence of band-edge LC lasers. Despite the importance of understanding and manipulating the coherence of light in various applications and the multitude of publications on band-edge LC lasers so far, there have been no reports specifically focusing on directly measuring the coherence properties of these lasers or detailed investigations on the factors that could affect the coherence of LC laser emissions. This chapter characterises the temporal coherence of these lasers by measuring their coherence length using a Michelson interferometer built in-house. It begins with a literature review and an explanation of how the interferometer system is employed to measure the coherence length of a commercial pulsed Nd:YAG laser to validate the accuracy of the characterisation technique, where the results

agree with those published in the literature. This chapter then measures the coherence length of band-edge LC lasers, including demonstrations of two essential factors, the LC layer thickness and excitation fluence, on the coherence length of the emission. The measurement results are compared with an estimated value from the corresponding centre wavelength and spectral width, showing good consistency with the spectral measurements. These results could provide significant insights into the temporal coherence and applications involving coherence control of band-edge LC lasers. *This work is being prepared for submission to a peer-reviewed journal.*

Chapter 8 summarises the key findings of the research presented in this thesis, which generally focused on the fundamental physical properties of band-edge LC lasers, including their polarisation states and temporal coherence, along with related beam-steering technologies and applications. This chapter also highlights potential future work that could extend the research, such as investigating the Stokes parameters of left-handed LC lasers and exploring the spatial coherence of LC lasers, further advancing the studies outlined in Section 4.5 and Chapter 7. Additionally, the development of a bidirectional communication link, based on the optical system described in Chapter 6, offers a promising direction for continued exploration. Furthermore, research into the polarisation states and coherence properties of blue phase LC lasers, alongside the development of LC lasers with advanced architectures, could provide deeper insights and contribute to the ongoing development of LC laser technologies.

2
Background

Contents

2.1 Liquid Crystals 8
2.1.1 Nematic Phase 10
2.1.2 Chiral Nematic Phase 17
2.2 LC Lasers 24
2.2.1 Band-edge LC Lasers 26
2.2.2 Defect-mode LC Lasers 29
2.3 Characteristics and Functionalities of Band-edge LC Lasers 30
2.3.1 Excitation Threshold and Slope Efficiency 30
2.3.2 Wavelength and Direction Tunability 32
2.4 Mathematical Descriptions of Polarisation 33
2.4.1 Stokes Parameters and Mueller Matrix 34
2.4.2 Jones Vector and Jones Matrix 37
2.5 Summary 39

2.1 Liquid Crystals

Two of the common phases for condensed matter are solids and liquids, which can be generally distinguished by their physical form or the microscopic molecular order. The molecules in isotropic liquids are arranged randomly with no order, while in crystalline solids they have both orientational order and positional order. Liquid crystals (LCs), on the contrary, are a class of material that exhibits characteristics associated with both isotropic liquids and crystalline solids, behaving as intermediate materials that possess some degree of the order of crystalline solids but the physical form of isotropic liquids. First discovered in 1888 by botanist F. Reinitzer [15], the unique behaviour of LCs has, since the mid-1970s, played a revolutionary role in display

technologies and various other optoelectronic techniques [16].

Specifically, orientational order is possible when the symmetry axes of molecules are preferentially aligned along a particular direction, which in the case of LCs is represented by a unit vector, known as the director $\hat{\mathbf{n}}$. Positional order implies that the molecules are constrained to occupy specific sites forming a microscopic periodic lattice structure. A scalar order parameter, S, is introduced to specify the degree of orientational order of the LC molecules, which can be written by finding the average of the second Legendre polynomial [17]:

$$S = \frac{1}{2}\langle 3\cos^2\theta - 1\rangle \tag{2.1}$$

where θ is the angle between a certain molecule and the director $\hat{\mathbf{n}}$, as shown in **Fig. 2.1**(b) and $\langle\theta\rangle$ is the average of such angle over all the molecules.

In crystalline solids, θ for all molecules is uniformly equal to zero since they are perfectly oriented to one direction and S equals one in this case. Conversely, if the molecules are completely disordered and randomly oriented, for example as in a liquid, S can be calculated by the following double integral equation where a result of $S = 0$ can be found.

$$S = \frac{\int_0^{\pi} \frac{1}{2}\langle 3\cos^2\theta - 1\rangle \sin\theta d\theta \int_0^{2\pi} d\phi}{\int_0^{\pi} \sin\theta d\theta \int_0^{2\pi} d\phi} = \frac{\int_{-1}^{1} \frac{1}{2}\langle 3\cos^2\theta - 1\rangle d\cos\theta}{\int_{-1}^{1} d\cos\theta} = 0 \tag{2.2}$$

LCs can be divided into various mesophases based on their molecular orientational and positional orders, such as nematic, smectic, and hexatic. Depending on the conditions for the transition of LC mesophases, they are often categorised into two main groups, named the thermotropic and lyotropic LCs [18]. Thermotropic LCs exhibit mesophases within a certain range of temperatures, with the ordering of the LC molecules strongly dependent on the temperature. As the temperature increases, the mesophase becomes more symmetric and less ordered. Above a threshold temperature, thermotropic LCs behave as isotropic liquids. On the other hand, lyotropics form LC phases when mixed with certain solvents, with phase transitions determined by both temperature and the concentration of LC molecules in the solvents. For the interest of the research work presented in this thesis, only thermotropic LCs are considered and two of their specific mesophases, nematic and chiral nematic, are briefly introduced in the subsequent paragraphs.

2.1.1 Nematic Phase

Among all the mesophases, the nematic phase is the most common and the least ordered, exhibiting only long-range orientational order but no positional order. Therefore, the orientational order parameter satisfies $0 < S < 1$ in this case. Fig. 2.1(a) shows the typical chemical structure of a well-known nematic LC, 5CB, with its rod-like molecular shape. Molecules with this long and thin shape are also known as calamitic LCs, whereas those with flat and rounded disc shapes are referred to as discotic LCs [19].

For the research presented in this thesis, all the LCs are calamitic even without specific declarations. Calamitic LC molecules are polar in nature, and the polar ordering can be induced for some nematic LC materials under applications of external electric fields or mechanical distortions, leading to a phenomenon referred to as the flexoelectric effect [20, 21]. If the flexoelectric effect is not considered; for instance, there are as many electric dipoles in $\hat{\mathbf{n}}$ as in $-\hat{\mathbf{n}}$, nematic LC molecules become indistinguishable from one rotated by 180° (within the plane) in the bulk material. In the nematic mesophase, the long axes of the molecules point, on average, along a preferred direction $\hat{\mathbf{n}}$ as shown in Fig. 2.1(b). The macroscopic optical axis aligns with the director, making nematic LCs optically uniaxial and anisotropic.

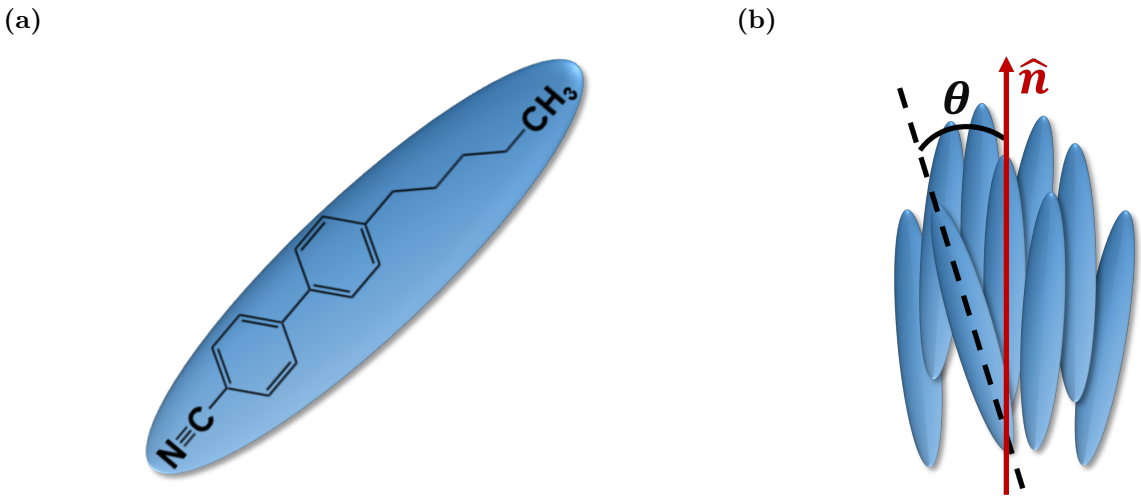

Figure 2.1: (a) The chemical structure of a calamitic nematic LC, 5CB, whose molecules have rod-like shapes and are symmetrical about their long axes. (b) The molecular structure of nematic LCs where the average direction of the LC molecules can be represented by the $\hat{\mathbf{n}}$ with the angle between a particular molecule and the director given by θ.

The capacitance of a capacitor will increase by a certain factor when a dielectric material is placed between the plates. This factor, represented as ϵ, is called the dielectric permittivity of

the material. Although the permittivity is constant for most materials, it varies along different directions for LCs due to their uniaxially symmetrical molecular structure. In the nematic phase, the permittivity can be represented by two orthogonal components, one parallel to the director, $\epsilon_{\parallel}$, and another component perpendicular to the director, $\epsilon_{\perp}$. The difference between $\epsilon_{\parallel}$ and $\epsilon_{\perp}$ is defined as the dielectric anisotropy, such that

$$\Delta\epsilon = \epsilon_{\parallel} - \epsilon_{\perp} \tag{2.3}$$

Due to the liquid physical appearance of LCs around room temperature, they are usually housed in glass cells for experiments, although independent films of polymerised LC gels have been reported for various LC mesophases [22–24]. If a nematic LC sample is filled into a cell made of two parallel glass substrates, the LC configuration can be categorised into two alignment conditions. The homogeneous (planar) alignment is obtained when the director $\hat{\mathbf{n}}$ lies uniformly in a certain direction parallel to the glass plates, and the homeotropic alignment is obtained when the director $\hat{\mathbf{n}}$ is uniformly aligned perpendicular to the substrates. The ideal homogeneous and homeotropic alignment of nematic LCs is shown in **Fig. 2.2**(a) and (b), respectively.

In experimental practices, nematic LC cells are prepared by coating transparent electrically conducting metallic films, for example, indium tin oxide (ITO) films, or attaching them with electrodes on the glass substrates to react with external electrical stimuli as shown in Fig. 2.2(c). To achieve the homogeneous alignment of nematic LCs, one possible routine is to generate a template of parallel microgrooves on the cell substrates so as to align the LC molecules, as suggested by the homogeneous alignment layers on both glass substrates shown in Fig. 2.2(c). This can be accomplished by implementing mechanical rubbing or photo-alignment techniques [25, 26]. These homogeneous cells can be directly purchased from commercial suppliers or manually fabricated following the experimental procedures introduced in Chapter 3.

If a nematic LC with positive dielectric anisotropy ($\epsilon_{\parallel} > \epsilon_{\perp}$) is filled into a cell with homogeneous alignment layers, the director will be tilted from the horizontal under an electric field perpendicular to the substrates due to higher permittivity along the director. Specifically, the molecules gradually rotate from a horizontal to a vertically aligned (homeotropic) state when the electric field increases, and eventually, as shown in Fig. 2.2(d), the nematic LCs can reach homeotropic alignment above an appropriate applied voltage, except for those molecules close to the substrates that are anchored by the alignment layers. Although negative dielectric

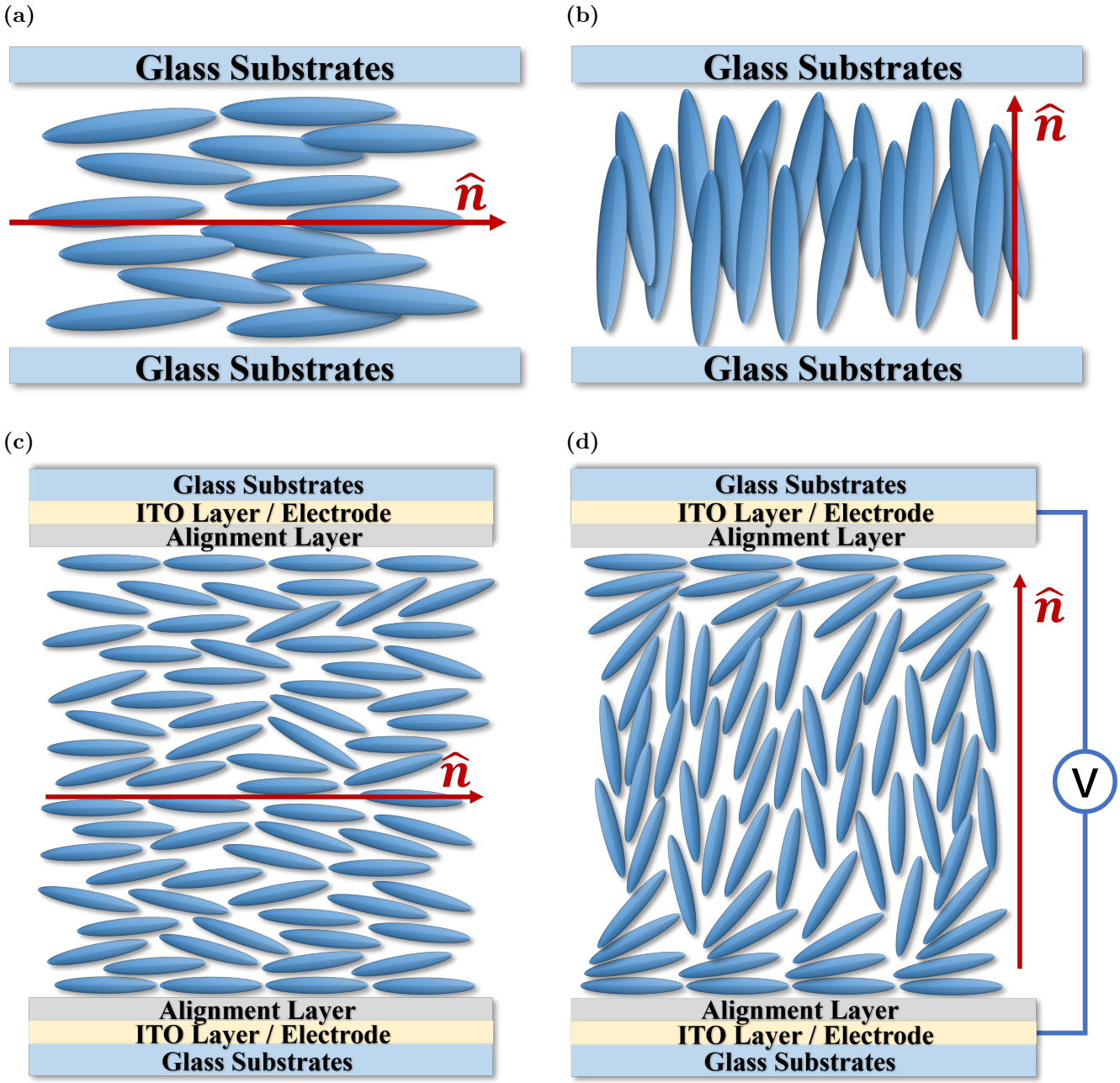

Figure 2.2: Demonstrations of the alignment of nematic LCs between glass substrates. The rod-like LC molecules are represented by the blue ellipses. Ideally, a nematic LC can form (a) a homogeneous alignment when the director is parallel to the substrates or (b) a homeotropic alignment when the director is aligned perpendicular to the substrates. For a nematic LC with positive dielectric anisotropy filled into a glass cell with ITO and alignment layers, (c) a homogeneous alignment naturally or (d) a pseudo-homeotropic alignment under an electric field across the cell with the appropriate applied voltage. The orientations of the molecules alongside the substrates are always anchored by the alignment layers.

anisotropy LCs have shown advantages in display technologies [27, 28] and fringe-field switching [29, 30], LCs with positive dielectric anisotropy have received significantly more attention and are of interest for the work presented in this thesis.

The Optical properties of LCs are another fundamental aspect that requires some consideration. According to Maxwell's electromagnetic wave equation, the velocity of light in a uniform isotropic dielectric medium in which there are no space charges or currents can be given by

$$v = c(\epsilon\mu)^{-\frac{1}{2}} \tag{2.4}$$

where c is the speed of light in vacuum, ϵ and μ are the dielectric permittivity and magnetic permeability of the medium, respectively. Given that LCs used in this thesis are non-magnetic materials such that $\mu = 1$, the refractive index can be calculated by

$$n = \frac{c}{v} = \sqrt{\epsilon} \tag{2.5}$$

As calamitic nematic LCs are uniaxially symmetrical, the refractive indices parallel and perpendicular to the director are different and equal to the square root of the corresponding permittivity [31]. This optical property of LCs is referred to as birefringence. When an electromagnetic wave propagates through the optical medium, the direction of its electric field, i.e., the polarisation direction, determines which refractive index is seen. As for uniformly aligned nematic LCs, the refractive index of light with polarisation perpendicular to the director is also called the ordinary refractive index $n_o = n_\perp$, while that parallel to the director is the extraordinary refractive index $n_e = n_\parallel$.

$$\begin{cases} n_o = n_\perp = \sqrt{\epsilon_\perp} \\ n_e = n_\parallel = \sqrt{\epsilon_\parallel} \end{cases} \tag{2.6}$$

The birefringence, Δn, is therefore defined as the difference between the extraordinary and ordinary refractive indices, and the phase difference between two electric field components parallel and perpendicular to the director introduced by the optical medium, also known as retardance, can be given by the product of the angular wave vector and the optical path length, that is

$$\Delta n = n_e - n_o \tag{2.7}$$

$$\Delta\phi = \frac{2\pi}{\lambda}\Delta n d \tag{2.8}$$

where λ and d are the wavelength of the incident light and the thickness of the optical medium, respectively.

By combining the properties of dielectric anisotropy and birefringence, nematic LCs can behave as tunable optoelectronic devices over a broad range of frequencies when filled into a glass cell with wires attached to the substrates. An electric field applied perpendicular to the substrates can be created by applying a voltage across the cell, causing the director to experience electrical torques that induce rotation. As the external voltage gradually increases, the director aligns more closely with the electric field direction, resulting in a decrease in both the birefringence and retardance, until the LC director reaches a homeotropic alignment with birefringence close to zero. For positive uniaxial LCs with $n_e > n_o$, the LC director can be regarded as the direction of the slow axis for the LC variable waveplate. The LC device can function as a variable waveplate with continuously adjustable retardance when the incident light has components parallel and perpendicular to the director. Additionally, it can be utilised as an intensity modulator when placed between crossed polarisers.

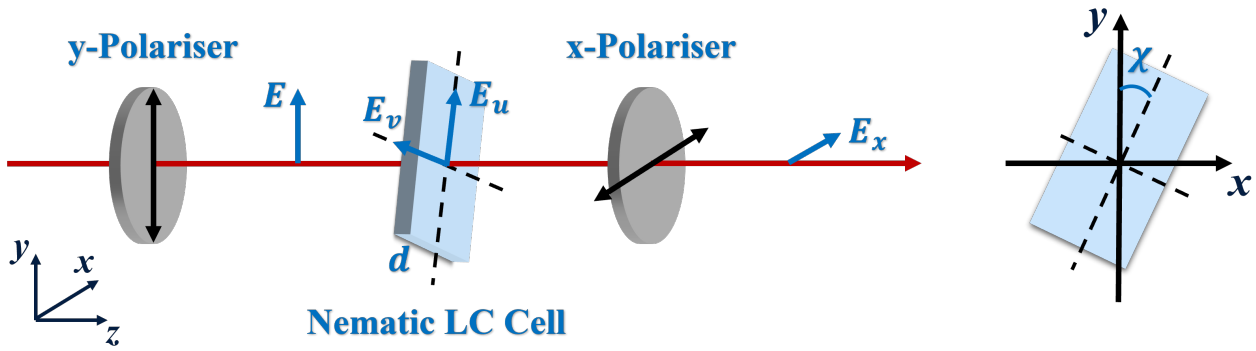

Figure 2.3: An illustration of the optical path when a nematic LC cell is placed on an polarising optical microscope. The polarisation directions of the crossed polarisers are sequentially parallel to the y- and x-axes and the light propagates along the z-axis. The fast axis of the nematic LC cell is placed at an angle of χ with respect to the y-axis, as illustrated by a separate diagram next to the optical path.

An effective way to observe the alignment of a nematic LC is to fill it in a glass cell and observe it on a polarising optical microscope. The optical path can be illustrated by the configuration demonstrated in **Fig. 2.3** consisting of a y-polariser, an anisotropic material with thickness d and birefringence Δn, and a x-polariser. Suppose χ is the orientation angle between the y-polariser and the fast axis of the LC cell, the propagated electric field along the

fast and slow axes of the nematic LC cell can be respectively given by:

$$\begin{cases} E_u = E\cos\chi \\ E_v = E\sin\chi e^{i\Delta\phi} \end{cases} \tag{2.9}$$

where E is the electric field after the y-polariser. Subsequently, only the component parallel to the x-direction can propagate through the x-polariser, such that the final electric field, E_x, and the intensity of light, I, can be given by

$$E_x = E_u\cos(\frac{\pi}{2}-\chi) - E_v\sin(\frac{\pi}{2}-\chi) = E[\cos\chi\cos(\frac{\pi}{2}-\chi) - \sin\chi\sin(\frac{\pi}{2}-\chi)e^{i\Delta\phi}] \tag{2.10}$$

$$\begin{aligned} I = E_xE_x^* &= E^2[\cos\chi\cos(\frac{\pi}{2}-\chi) - \sin\chi\sin(\frac{\pi}{2}-\chi)\cos\Delta\phi]^2 + E^2[\sin\chi\sin(\frac{\pi}{2}-\chi)\sin\Delta\phi]^2 \\ &= E^2\sin^2 2\chi\sin^2\frac{\pi\Delta nd}{\lambda} \end{aligned} \tag{2.11}$$

Let us assume that the incident light is unpolarised such that half of its intensity can be transmitted through the first polariser of the system. Consequently, the transmittance through the crossed polariser pair and the nematic LC cell can then be calculated as:

$$T = \frac{1}{2}\sin^2 2\chi\sin^2\frac{\pi\Delta nd}{\lambda} \tag{2.12}$$

A nematic LC, BL006, was capillary filled into a commercial anti-parallel rubbed cell with a thickness of 5 µm (Instec2-5.0, Instec) and observed on a polarising optical microscope (BX51, Olympus) equipped with a charge-coupled device (CCD) camera (puA2500-14ucMIC, Basler). The typical birefringence of BL006 was reported as $\Delta n = 0.2853$ at 20°C for an incident wavelength of 589.3 nm [32]. When no electric field was applied to the cell, the LC maintained a homogeneous alignment, resulting in the cell reaching its dark state with $T = 0$ at $\chi = 0°$ or 90° and a maximum bright state at $\chi = 45°$, as shown in **Fig. 2.4**(a) and (b), respectively. The colour in Fig. 2.4(b) is due to varied transmittance for different wavelengths, with green wavelengths having higher transmittance for this particular LC cell. When the LC cell was subjected to a series of 1 kHz alternating current square waves with voltages ranging from 2 to 15 Vpp provided by a waveform generator, the observed colour under the microscope switched and gradually darkened, following the Michel-Levy birefringence chart [33], as demonstrated in Fig. 2.4(c) to (h). Note that χ was maintained at 45° for optimal observation. Eventually, Fig. 2.4(i) shows that a dark state reappeared when the voltage reached 20 Vpp. At this point, the LC director approached a homeotropic alignment, except at the alignment layers, causing Δn and T to become almost zero.

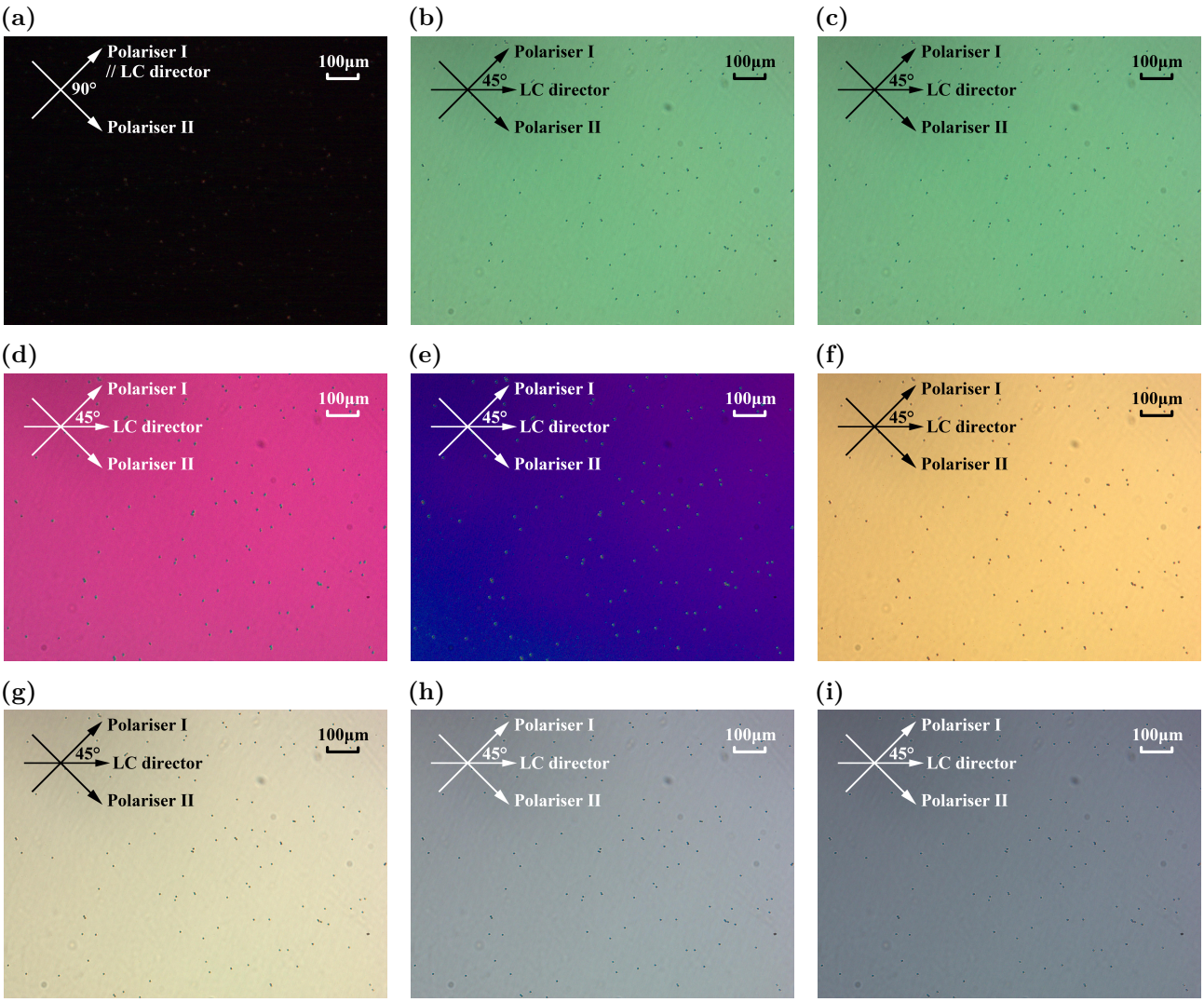

Figure 2.4: A BL006 nematic LC cell with different applied voltages was observed on a polarising optical microscope and a CCD camera. The observation of Michel-Levy colours illustrates how the LC cell interacts with various external voltages. The thickness of the cell was 5 µm and the observation was conducted at a room temperature of 20°C. (a) The dark state with no electric field where the director is aligned with one of the polarisers on the microscope. (b) The maximum bright state with no electric field where the director is aligned to be at the centre of the two crossed-polarisers on the microscope ($\chi = 45°$). The optical textures of the LC cell with applied voltages of (c) 2 Vpp, (d) 4 Vpp, (e) 6 Vpp, (f) 8 Vpp, (g) 10 Vpp, (h) 15 Vpp, and (i) 20 Vpp are then demonstrated with the orientation of the LC cell maintained at $\chi = 45°$.

2.1.2 Chiral Nematic Phase

The chiral nematic phase, historically referred to as the cholesteric phase due to its initial discovery in cholesteryl benzoate [15], is a variant of the nematic phase. Many natural substances derived from cholesterol exhibit this phase, characterised by an asymmetrical and chiral molecular structure that cannot be superimposed on its mirror image. **Fig. 2.5**(a) illustrates the molecular configuration of chiral nematic LCs, where molecules are generally aligned parallel to the director $\hat{\mathbf{n}}$, but also arrange themselves into a macroscopic helical structure. In this structure, the director continuously rotates along the helical axis, which is perpendicular to the plane of the local director. It is important to note that chiral nematic LCs do not possess a layered structure; the grey slices in Fig. 2.5(a) are depicted only to clarify the spiral configuration of the chiral nematic LCs.

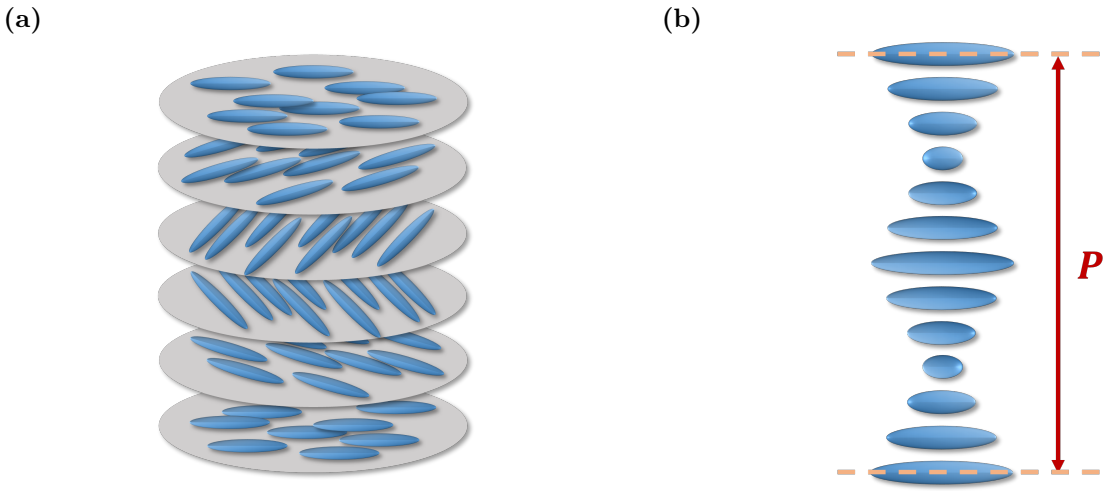

Figure 2.5: Configurations of the molecular structure of a chiral nematic LC. (a) A demonstration of the spatial structure of a chiral nematic LC. The chiral nematic phase does not exhibit a layered structure while the grey shades are only to suggest the continuous rotation of the LC director. (b) The helical structure where the pitch is defined as the length for a 2π rotation of the LC director in space.

In an ideal chiral nematic mesophase, the uniaxial helical structure can be described using Cartesian coordinates $\{\mathbf{x}, \mathbf{y}, \mathbf{z}\}$ as follows:

$$\hat{\mathbf{n}} = -\sin(qz)\mathbf{x} + \cos(qz)\mathbf{y} \tag{2.13}$$

where the helical axis aligns with the $\mathbf{z}$ direction.

A crucial parameter in this helical structure is the pitch, P, as shown in Fig. 2.5(b). The pitch is defined as the spatial distance over which the director $\hat{\mathbf{n}}$ completes a full 2π rotation. The pitch can be either positive or negative, corresponding to right-handed or left-handed

systems, respectively, and can be modulated by temperature or an external electric field [34]. The periodicity of the chiral nematic phase is half of the pitch because the properties along $\hat{\mathbf{n}}$ and $-\hat{\mathbf{n}}$ are identical. This phase can occur due to molecules that are inherently chiral or through the addition of chiral dopants to a nematic LC. Examples of such chiral dopants include R5011, R811, S811, and BDH1281, where 'R' indicates right-handed and 'S' indicates left-handed chiral dopants.

The chiral nematic phase can also be identified through its optical texture when viewed under a polarising optical microscope. Depending on the anchoring at the substrates of the cell, chiral nematic LCs can exhibit various configurations, including Grandjean texture, fingerprint texture or uniform lying helix, and no alignment (focal conic), as illustrated in **Fig. 2.6**.

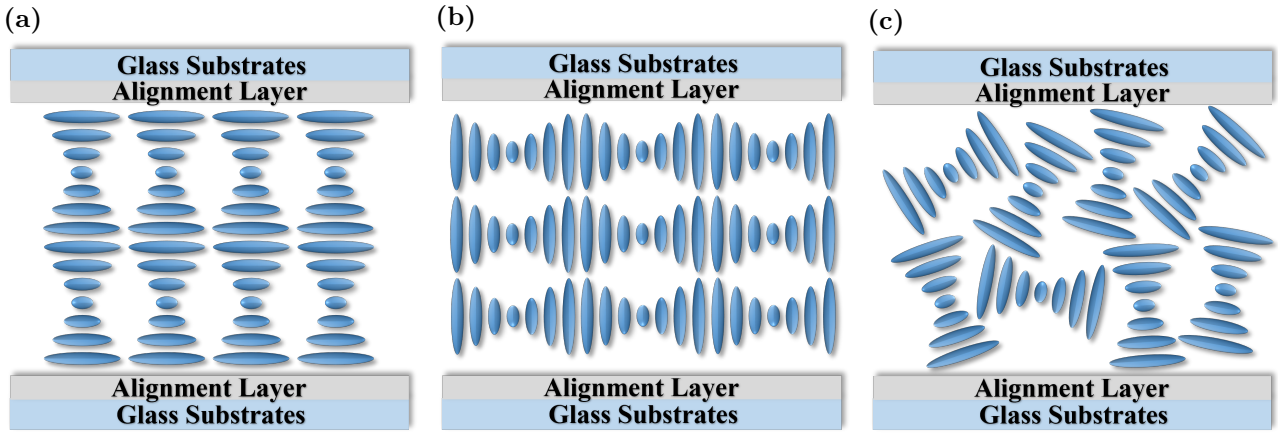

Figure 2.6: Diagram of different alignments of chiral nematic LCs. Typical alignments in an LC cell are (a) the Grandjean texture which is usually achieved by applying two planar alignment layers in between the substrates, (b) the uniform lying helix, which is more difficult to achieve in experiments (fingerprint texture can be obtained with homeotropic alignment layers and long pitch chiral nematics), and (c) focal conic where the helices are randomly aligned.

In the case of planar (homogeneous) alignment layers, the helical axis is oriented perpendicular to the substrates. This results in the cell exhibiting a planar (Grandjean) texture, characterised by a uniform colour that remains unchanged regardless of the polarisation angle of the microscope [35]. This uniformity is a distinct feature of the planar alignment. In terms of a homeotropic alignment, the cell displays a fingerprint-like texture, where the helical axes lie within the plane of the substrates and the rotation of the director is directly visualised. This distinctive pattern can be observed between surfaces that induce perpendicular orientation alignment layers, particularly in long-pitch chiral nematic LCs (where P is greater than a few micrometres). In the absence of alignment layers on the substrates, the helical axes are randomly distributed across

the cell, resulting in a chaotic focal conic texture. This texture is marked by its irregular and disordered appearance, reflecting the random orientation of the helices within the LC structure.

Planar-aligned chiral nematic LCs act as one-dimensional Bragg reflectors when the wavelength of the incident light is on the order of the pitch [36]. This Bragg reflection arises due to the anisotropic nature of the LC molecules and the continuous rotation of the director throughout the sample. In this scenario, the sample reflects incident circularly polarised light that has the same handedness to the helix, while it transmits light with the opposite handedness. This selective transmission property for light propagating parallel to the helical axis has been investigated in detail by Mauguin [37], Oseen [38], and de Vries [39], who provided analytic solutions to Maxwell's equations for ideal chiral nematic structures.

The wave equation in a Cartesian coordinate laboratory frame $\{\mathbf{x}, \mathbf{y}, \mathbf{z}\}$ for light propagating through such a chiral nematic LC structure is given by

$$\frac{\partial^2}{\partial z^2}\begin{bmatrix} E_x \\ E_y \end{bmatrix} = \mu_0 \frac{\partial^2}{\partial t^2}\begin{bmatrix} D_x \\ D_y \end{bmatrix} \tag{2.14}$$

where E_x and E_y are the electric field vector components, D_x and D_y are the electric displacement field vector components, t is the time, and μ_0 is the free space permeability. This wave equation can be transformed to a Cartesian coordinate local frame, $\{\xi, \eta, \mathbf{z}\}$, which co-rotates with the helical structure, such that

$$\begin{bmatrix} \frac{\partial^2}{\partial z^2} - q^2 & -2q\frac{\partial}{\partial z} \\ 2q\frac{\partial}{\partial z} & \frac{\partial^2}{\partial z^2} - q^2 \end{bmatrix}\begin{bmatrix} E_\xi \\ E_\eta \end{bmatrix} = \frac{1}{c^2}\frac{\partial^2}{\partial t^2}\begin{bmatrix} \epsilon_\perp E_\xi \\ \epsilon_\parallel E_\eta \end{bmatrix} \tag{2.15}$$

Suppose the angular frequency is ω, the wave vector is $k = 2\pi/\lambda$, and the ellipticity is f, then the eigenmodes, m, of the wave equation take the form of

$$\mathbf{E}^{\mathbf{eigen}} = \begin{bmatrix} E_\xi \\ E_\eta \end{bmatrix} = \frac{1}{\sqrt{1+|f|^2}}\begin{bmatrix} 1 \\ if \end{bmatrix}\exp\left[i(\omega t - mkz)\right] \tag{2.16}$$

then Eq. (2.15) can be simplified as a system of two independent equations:

$$\begin{cases} \epsilon_\perp k^2 - m^2k^2 - q^2 = 2mkqf \\ f(\epsilon_\parallel k^2 - m^2k^2 - q^2) = 2mkq \end{cases} \tag{2.17}$$

A few quantities, ϵ', α', m', and λ', can be further defined to simplify the equations, which are indicated in Eq. (2.18):

$$\epsilon' = \frac{\epsilon_\parallel + \epsilon_\perp}{2}, \quad \alpha' = \frac{\epsilon_\parallel - \epsilon_\perp}{\epsilon_\parallel + \epsilon_\perp}, \quad m' = \frac{m}{\sqrt{\epsilon'}}, \quad \lambda' = \frac{\lambda}{P\sqrt{\epsilon'}} \tag{2.18}$$

Upon substituting Eq. (2.18) into Eq. (2.17) and eliminating the ellipticity f, the eigenmodes should then satisfy

$$m'^4 - 2(1+\lambda'^2)m'^2 + (1-\alpha'-\lambda'^2)(1+\alpha'-\lambda'^2) = 0 \tag{2.19}$$

Eq. (2.19) can be regarded as a quadratic function of m'^2 so that its solutions are

$$\begin{cases} {m'_1}^2 = 1+\lambda'^2 - \sqrt{4\lambda'^2+\alpha'^2} \\ {m'_2}^2 = 1+\lambda'^2 + \sqrt{4\lambda'^2+\alpha'^2} \end{cases} \tag{2.20}$$

with the corresponding ellipticities denoted as

$$f_{1,2} = \frac{1-\alpha'-{m'_{1,2}}^2-\lambda'^2}{2m'_{1,2}\lambda'} \tag{2.21}$$

It can be seen from Eq. (2.20) that the four solutions to m' correspond to four propagation eigenmodes of the wave equation. Among these, two modes are forward-traveling when $m' > 0$, and two are backward-traveling when $m' < 0$. An exception occurs in the regime where $|\lambda'| > \sqrt{1+\alpha'}$, in which the negative root of ${m'_1}^2$ is required for forward-traveling waves. The determination of these eigenmodes specifically depends on the light wavelength, the pitch of the helical structure, and the dielectric permittivities of the LC. Besides, Eq. (2.20) suggests that ${m'_1}^2$ can be negative, leading to an imaginary m'_1. In this case, the first eigenmode becomes evanescent, as given by

$$-\alpha' < 1-\lambda'^2 < \alpha' \tag{2.22}$$

or, in terms of the LC refractive indices and the pitch of a right-handed helical structure ($P > 0$), this condition implies that the wavelength falls within the range of

$$n_o P < \lambda < n_e P \tag{2.23}$$

This wavelength range is also known as the photonic bandgap (PBG) of chiral nematic LCs, which selectively reflects incident light with specific polarisation states. The PBG can be quantitatively analysed by examining the propagation of light in ideal chiral nematic LC layers using Maxwell's equations. The relationship between the electric field vector, $\mathbf{E}$, and the magnetic field vector, $\mathbf{H}$, of light in the laboratory frame $\{\mathbf{x}, \mathbf{y}, \mathbf{z}\}$ can be given by

$$\mu_0 \frac{\partial}{\partial t}\begin{bmatrix} H_x \\ H_y \end{bmatrix} = \frac{\partial}{\partial z}\begin{bmatrix} E_y \\ -E_x \end{bmatrix} \tag{2.24}$$

which can be transformed in the rotating frame $\{\xi, \eta, \mathbf{z}\}$ in chiral nematic LCs as

$$\mu_0 c \begin{bmatrix} H_\xi \\ H_\eta \end{bmatrix} = \sqrt{\epsilon'} \begin{bmatrix} -E_\eta/\beta' \\ \beta' E_\xi \end{bmatrix} \tag{2.25}$$

where β' is a quantity defined as

$$\beta' = \lambda' f + m' \tag{2.26}$$

Thus, given the electric field vectors for the eigenmodes described in Eq. (2.16), the corresponding magnetic field vectors are

$$\mathbf{H^{eigen}} = \begin{bmatrix} H_\xi \\ H_\eta \end{bmatrix} = \frac{\sqrt{\epsilon'}}{\mu_0 c} \begin{bmatrix} -E_\eta/\beta' \\ \beta' E_\xi \end{bmatrix} = \frac{1}{\sqrt{1+|f|^2}} \begin{bmatrix} -if/\beta' \\ \beta' \end{bmatrix} \exp\left[i(\omega t - mkz)\right] \tag{2.27}$$

Suppose light is incident from an isotropic medium with a refractive index n_0 onto an ideal chiral nematic LC layer. In that case, different polarisation states of the light can excite different eigenmodes, resulting in varying propagation behaviours through the LC. The incident electric field and magnetic field vectors, $\mathbf{E^{in}}$ and $\mathbf{H^{in}}$, respectively, and reflected electric field and magnetic field vectors, $\mathbf{E^{ref}}$ and $\mathbf{H^{ref}}$, respectively, in the lab frame can be represented as follows:

$$\begin{cases} \mathbf{E^{in}} = \begin{bmatrix} E_x^{in} \\ E_y^{in} \end{bmatrix} = \begin{bmatrix} E_{0x}^{in} \\ iE_{0y}^{in} \end{bmatrix} \exp\left[i(\omega t - n_0 kz)\right] \\ \mathbf{H^{in}} = \begin{bmatrix} H_x^{in} \\ H_y^{in} \end{bmatrix} = \dfrac{n_0}{\mu_0 c} \begin{bmatrix} -E_y^{in} \\ E_x^{in} \end{bmatrix} = \begin{bmatrix} -iE_{0y}^{in} \\ E_{0x}^{in} \end{bmatrix} \exp\left[i(\omega t - n_0 kz)\right] \end{cases} \tag{2.28}$$

$$\begin{cases} \mathbf{E^{ref}} = \begin{bmatrix} E_x^{ref} \\ E_y^{ref} \end{bmatrix} = \begin{bmatrix} E_{0x}^{ref} \\ iE_{0y}^{ref} \end{bmatrix} \exp\left[i(\omega t + n_0 kz)\right] \\ \mathbf{H^{ref}} = \begin{bmatrix} H_x^{ref} \\ H_y^{ref} \end{bmatrix} = \dfrac{n_0}{\mu_0 c} \begin{bmatrix} E_y^{ref} \\ -E_x^{ref} \end{bmatrix} = \begin{bmatrix} iE_{0y}^{ref} \\ -E_{0x}^{ref} \end{bmatrix} \exp\left[i(\omega t + n_0 kz)\right] \end{cases} \tag{2.29}$$

The rotating frame coincides with the lab frame at the boundary of $z = 0$. Additionally, the electric field vector and the magnetic field vector of the incident light should also be continuous at the boundary. Therefore, the boundary conditions for the propagation of light are

$$\begin{cases} \mathbf{E^{in}} + \mathbf{E^{ref}} = \mathbf{E^{eigen}}, \quad z = 0 \\ \mathbf{H^{in}} + \mathbf{H^{ref}} = \mathbf{H^{eigen}}, \quad z = 0 \end{cases} \tag{2.30}$$

The chiral nematic LCs are usually housed in between glass substrates where the refractive index for the glass material is close to the ordinary and extraordinary refractive indices for the LCs. Thus, by substituting Eq. (2.28), Eq. (2.29), Eq. (2.16), and Eq. (2.27) into

Eq. (2.30) and taking an estimation of $n_0 = \sqrt{\epsilon'}$, the incident and reflected electric field components can be solved such that

$$\begin{aligned} E_{0x}^{in} &= \frac{1+\beta'}{2}\frac{1}{\sqrt{1+|f|^2}}, \quad E_{0y}^{in} = \frac{f}{\beta'}\frac{1+\beta'}{2}\frac{1}{\sqrt{1+|f|^2}}, \\ E_{0x}^{ref} &= \frac{1-\beta'}{2}\frac{1}{\sqrt{1+|f|^2}}, \quad E_{0y}^{in} = -\frac{f}{\beta'}\frac{1-\beta'}{2}\frac{1}{\sqrt{1+|f|^2}}. \end{aligned} \tag{2.31}$$

Therefore, the incident waves with E_i^{in} that can excite the corresponding eigenmode E_i^{eigen}, as well as the reflected electric field vector E_i^{ref} are

$$\mathbf{E_i^{in}} = \frac{1}{\sqrt{1+|f_i|^2}}\frac{1+\beta_i'}{2}\begin{bmatrix}1\\ if_i/\beta_i'\end{bmatrix}\exp\left[i(\omega t - n_0 kz)\right] \tag{2.32}$$

$$\mathbf{E_i^{ref}} = \frac{1}{\sqrt{1+|f_i|^2}}\frac{1-\beta_i'}{2}\begin{bmatrix}1\\ -if_i/\beta_i'\end{bmatrix}\exp\left[i(\omega t + n_0 kz)\right] \tag{2.33}$$

The reflectance can be given by the square of the magnitude of the reflection coefficient, which is the ratio of the reflected to incident electric field, $\mathbf{E_i^{ref}}/\mathbf{E_i^{in}}$:

$$R_i = \left|\frac{1-\beta'}{1+\beta'}\right|^2 \tag{2.34}$$

To visualise the solutions mentioned above, the reflectances of the two forward-travelling eigenmodes, R_1 and R_2, as well as their corresponding ellipticities, f_1/β' and f_2/β', are simulated in **Fig. 2.7** for a nematic LC, BL006. The refractive indices of BL006 were reported as $n_o = 1.5293$ and $n_e = 1.8146$ at 20°C and 589.3 nm [32], resulting in $\alpha' = 0.0853$. The chiral nematic LCs (right-handed, $P > 0$) in this simulation are assumed to have ideal homogeneous alignment and an infinite number of layers.

In the upper pane of Fig. 2.7, it can be seen that the incident electric field $\mathbf{E_1^{in}}$, which excites the first eigenmode, is entirely reflected within the PBG. The ellipticity of this wave is approximately one, as illustrated in the corresponding lower pane, suggesting that $\mathbf{E_1^{in}}$ is right-circularly polarised light. This behaviour remains consistent within the PBG, except at very low λ', which are outside the commonly considered experimental wavelength range. On the other hand, the second incident electric field $\mathbf{E_2^{in}}$ is approximately left-circularly polarised and exhibits no reflection from the chiral nematic LC layers. This means that $\mathbf{E_2^{in}}$ passes through the LC layers without being reflected, indicating that the chiral nematic structure does not affect left-circularly polarised light within the same wavelength range.

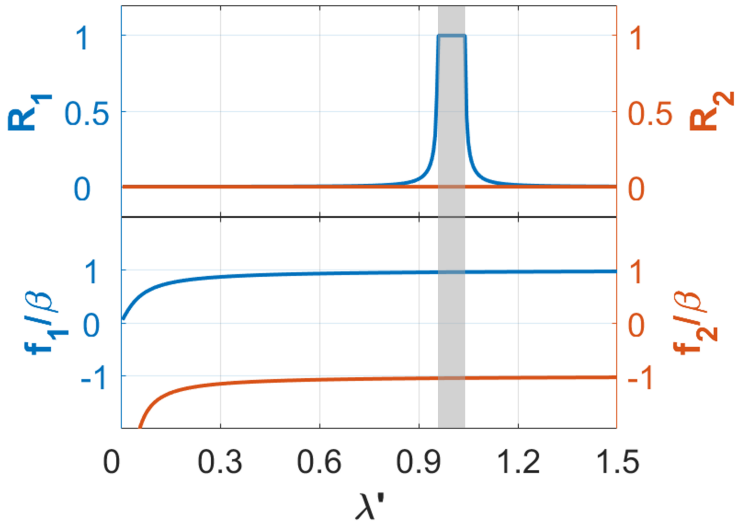

Figure 2.7: A demonstration for the selective reflection in ideal chiral nematic LCs solved using the eigenmode solutions to Maxwell's wave equation specified by the reflectances, R_i, and their ellipticities, f_i/β', as a function of the reduced wavelength, λ'. The chiral nematic LC is right-handed ($P > 0$). The parameter related to the dielectric anisotropy is set to $\alpha' = 0.0853$ for a nematic LC, BL006, and the PBG is highlighted by the grey shaded area. The incident waves could excite two forward-travelling eigenmodes, with their reflectances and ellipticities demonstrated in the upper pane and lower panes, respectively. The first wave, which excites the first eigenmode as illustrated by the blue curves in the figure, is approximately right-circularly polarised and experiences total reflection within the frequency bandgap, whereas the second wave, which excites the second eigenmode as illustrated by the orange curves in the figure, is approximately left-circularly polarised and exhibits no reflection.

This selective reflection property can also be demonstrated by introducing another simulation based on the Berreman 4×4 matrix method [40], in which the chiral nematic LCs are treated as multiple ideal layers with continuous rotation angles of the director that are sandwiched between two glass substrate layers. The transmittance of right-circularly polarised and left-circularly polarised light is simulated over the wavelength range from 400 nm to 800 nm, with the results demonstrated by the blue curve and the orange curve in **Fig. 2.8**, respectively. Here, the pitch was set to 380 nm with a right-handed helical rotation sense ($P > 0$) and the refractive indices of a nematic LC, BL006, were considered as a function of incident wavelengths, according to Cauchy's equation [41] and the fitting parameters at the temperature of 20°C as reported in the literature [32]. Note that these parameters are selected solely for a demonstration of the PBG, rather than simulating any particular LC cell. The transmittance spectra demonstrate an ideal PBG where the right-circularly polarised light is entirely reflected while the left-circularly

polarised light is completely transmitted, and the PBG occurs with the band-edges located at

$$\begin{cases} \lambda_S = n_o P \\ \lambda_L = n_e P \end{cases} \tag{2.35}$$

where λ_S and λ_L correspond respectively to the short and long wavelength band-edge and the width of the band-gap is defined as $\Delta\lambda = \Delta n P$.

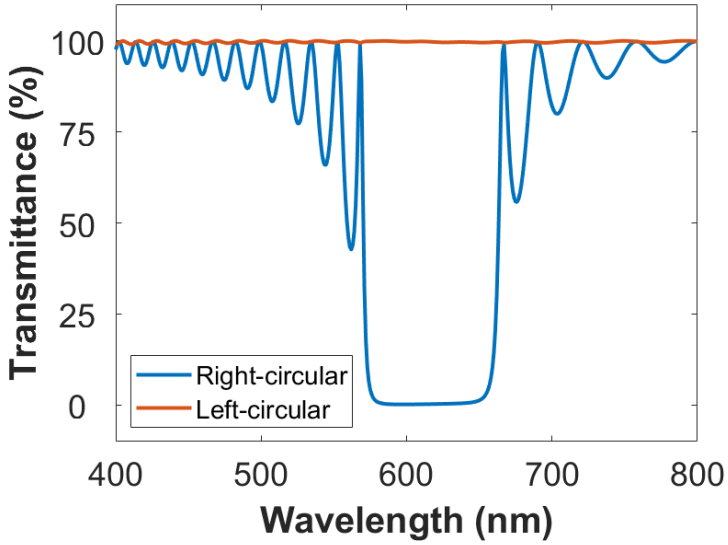

Figure 2.8: An illustration of the PBG of a chiral nematic LC with a right-handed helical structure which is specified by transmittance spectra as a function of incident wavelengths. The spectra are simulated based on the Berreman 4×4 matrix method with the pitch being set to 380 nm. The transmittance for right-circularly polarised incident light is approximately zero suggesting a photonic bandgap between two band-edge wavelengths.

2.2 LC Lasers

Lasers, shortened for light amplification by stimulated emission of radiation, were first demonstrated by T. Maiman of Hughes Laboratories in May 1960 [42]. Since then, numerous types of lasers have emerged and proliferated. The wide range of advantages and capabilities of lasers, including monochromaticity, low divergence, high coherence, and energy concentration, have enabled their use in numerous industries and applications such as holography [43], spectroscopy [44], navigation [45], photolithography [46], and quantum communications [47].

In general, three fundamental factors are of essential importance for laser emission. First, a pumping acting as the energy source must be present to achieve population inversion. Second, there must be some form of a gain medium that enables the absorption and stimulated emission

upon the pumping. The third factor is the resonator, which allows the laser beam to propagate back and forth through the gain medium before the final emission when it reaches the excitation threshold. The threshold is the minimum excitation level at which the stimulated emission dominates the spontaneous emission. **Fig. 2.9** illustrates the most basic laser structure, featuring one fully reflective plane mirror and another slightly transmissive plane mirror that allows a small proportion of light to be emitted as the laser output.

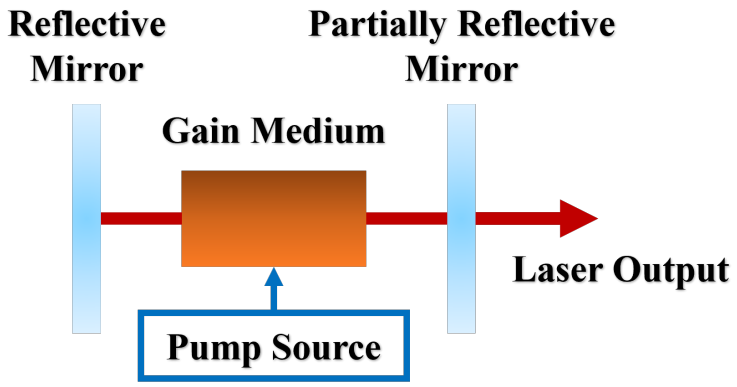

Figure 2.9: A simplified schematic diagram for a laser comprising a pump source providing energy and population inversion, a gain medium where the stimulated emission happens, and a resonator cavity consisting of a reflective mirror and a partially reflective mirror.

LC lasers are a type of dye laser generally fabricated by doping organic fluorescent laser dyes or inorganic molecules into LC mixtures. LC lasers inherit the wideband tunability and large coherence area of dye lasers, along with various remarkable beneficial properties of LCs, such as being ultrathin, lightweight, highly flexible and versatile, as well as having direction-tunable emission in some cases [6, 7]. Additionally, these lasers offer the advantages of vertical-cavity surface-emitting lasers without the need for sophisticated fabrication and the tunability of dye lasers without the use of toxic solvents.

There is tremendous potential for applications of LC lasers in numerous technologies and commercial products, given the advantages mentioned above. Researchers have demonstrated simultaneous red-green-blue lasing from a two-dimensional polychromatic laser array fabricated from dye-doped chiral nematic LCs housed in a cell with a pitch gradient [48]. Subsequent reports have introduced new approaches for 3D laser displays based on circularly polarised lasing from inkjet-printed cholesteric LC arrays [9, 49]. Additional techniques in random lasers involving molecular rearrangement with external electric fields provide opportunities for adjusting the polarisation and brightness, potentially leading to new implementations in

LC holographic displays [10, 14]. These technologies can achieve a high colour gamut and superior resolution without the need for colour filters or polarisers, thanks to their high spectral purity and compact dimensions of only a micrometre scale.

LC lasers also hold significant promise in the field of bio-sensing due to their broad range of tunable wavelengths on a single sample. Literature reports demonstrate real-time and quantitative detection of urea based on whispering gallery mode lasing, providing high sensitivity and accuracy [13]. LC laser-based sensors have also been introduced for detecting various biological molecules [50] and heavy-metal ions [51]. Techniques facilitating Förster energy transfer can combine visible and near-infrared lasing from LC devices, envisaging more applications including medical imaging, diagnostics, telecommunications, and optical signatures for security identifications [52].

Band-edge and defect-mode LC lasers are the most commonly studied LC lasers, but other laser configurations involving LCs have also been considered. These include random LC lasers [53–55], whispering gallery mode LC microlasers [56–58], plasmonic LC microlasers [59–61], and biological LC microlasers [62–64]. These approaches offer many advantages, including ultrahigh Q-factors (reaching up to 10^{10}), generation of coherent light beyond the diffraction limit (down to nanometre-scale), low threshold, and short response time.

The majority of the content in this thesis focuses on band-edge LC lasers fabricated by dye-doped chiral nematic LCs. Therefore, only a comprehensive introduction to band-edge LC lasers is presented, followed by recent progress on the development of defect-mode LC lasers as they relate strongly with band-edge LC lasers. This focus allows for a detailed exploration of the principles, fabrication techniques, and performance characteristics that define these specific types of LC lasers.

2.2.1 Band-edge LC Lasers

The concept of laser oscillations in cholesteric LCs was proposed and patented in 1973 [65], with the first experimental demonstration occurring 25 years later by Kopp et al. [66]. Since then, multiple studies have been reported on lasing in LC photonic structures [67, 68], particularly in the chiral nematic phase [69], smectic phases [70], and blue phases [71]. These LC mesophases possess periodic structures that give rise to a PBG. Theoretically, the emission is suppressed

within the PBG, whereas the photonic density of states (DOS) suddenly diverges and the gain factor is significantly enhanced at both the band-edges [72]. In the presence of a gain medium, this large DOS provides sufficient gain leading to laser emission when other sufficient and necessary conditions for laser generation are met. This type of LC laser, known as a band-edge LC laser, generates lasing at the band-edges which resembles distributed feedback (DFB) lasers first proposed in 1972 [73].

PBGs can spontaneously form in multiple LC mesophases as long as the material possesses periodic birefringent structures with a continually rotating LC director, indicating a spatial alternation of high and low refractive indices. However, the PBG only exists for circularly polarised incident light with the same handedness as the rotation sense of the helix. For example, right circularly polarised light (with right-handed rotation sense) will be theoretically reflected by a right-handed chiral nematic LC if its wavelength falls within the corresponding PBG. The most studied and reported PBG is formed in chiral nematic LCs, behaving as a one-dimensional Bragg reflector, a phenomenon also observed in the chiral smectic C phase. In comparison, blue phases I and II exhibit three-dimensional periodic structures, leading to PBGs in all three dimensions.

For a band-edge LC laser, band-edges on either side of the PBG can be treated as resonant modes. However, the two band-edges are not equivalent due to differences between the electric field vectors of propagation modes and the transition dipole moment of the dye [74]. The gain materials in band-edge LC lasers are typically laser dyes such as DCM, pyrromethene series, coumarin series, and rhodamine series, although ultraviolet lasing can be generated without the presence of a dye [69]. Various studies have evaluated the performance of different laser dyes in typical Nd:YAG pumped dye-laser systems [75–77], including detailed comparisons of their spectral properties, molar extinction coefficients, quantum efficiencies, fluorescence lifetimes, optimum laser wavelengths, and laser emission characteristics.

Band-edge LC lasers are primarily based on homogeneously aligned dye-doped chiral nematic LCs with the cell substrates placed perpendicular to the incident light. A step-by-step fabrication process and experimental records of these laser cells are introduced in Chapter 3. Laser emission occurs only if the emission spectrum of the dye overlaps the band-edges, which must be matched to achieve maximum coupling efficiency and the lowest excitation threshold. The helical structure suppresses the fluorescence frequency components within the PBG while enhancing them at the band-edges, due to the sudden increase in the photonic DOS, leading to a significant

increase in the gain factor at the band-edges [72]. This enhancement is also demonstrated experimentally in Chapter 3. Most studies so far indicate that the long-wavelength band-edge exhibits a lower excitation threshold [6], although some techniques have been reported to achieve low-threshold lasing at the shorter wavelength band-edge [78].

Laser emission is typically achieved using a solid-state picosecond or nanosecond pulsed Nd:YAG laser as the optical pump source, where shorter pulse durations are essential to prevent triplet state formation and to maintain the performance of the laser [79]. Additionally, laser diode pumping of LC lasers has also been demonstrated in recent years [79, 80]. In terms of conventional solid-state laser pumping, higher pulse widths could result in higher excitation thresholds [81]. Two aspects must be carefully considered for efficient and long-lasting LC laser emissions. Firstly, the pump laser beam should ideally be circularly polarised with the opposite handedness as the rotation sense of the LC helices to achieve maximum excitation efficiency due to the polarisation-selective nature of the PBG [78, 82]. Secondly, the repetition rate of the pump laser must be chosen carefully to avoid photo-bleaching of the laser dye, with a typical frequency of 10 Hz. Although higher repetition rates have been found to reduce the total emission energy of conventional band-edge LC lasers [83], researchers also published a method of overcoming repetition rate limitations by implementing a rapidly spinning stage which achieved 3.5 mW average output power at 10 kHz [11].

The emission from the dye-doped chiral nematic LCs is always along the helical axis, regardless of the optical pumping direction of the pump source. However, LC laser intensity strongly depends on the incident polarisation state when the incident angle exceeds 18° [84]. In practical experimental setups, the Nd:YAG laser is usually incident orthogonally onto the LC laser cell for straightforward optical axis alignment. Apart from the spontaneous PBG formed in specific LC mesophases discussed above, band-edge LC lasers have also been achieved using LCs without naturally formed periodic structures, such as holographic polymer-dispersed LCs combined with a photocuring technique to form desired polymer networks [85–87].

Despite all the advantages mentioned so far, laser dyes generally suffer from irreversible photo-bleaching, which limits the application of dye-based LC lasers, especially in scenarios requiring stable performance under high photo-excitations and long-term usage. Therefore, in recent years, researchers have explored and reported multiple alternatives for the gain material in LC lasers, with the most notable being quantum dots (QDs). Functional nanocrystals, such as

$CuInS_2 - ZnS$, have been dispersed in nematic LCs to achieve reduced thresholds and increased Q-factors [88], and doped in ferroelectric LCs to enhance electro-optic responses [89]. Other approaches, including $InP - ZnS$ and ZnO QDs [90–92], exhibit various performance benefits and enhancements in photo-luminescence intensities. Another well-known suitable inorganic gain material for LC lasers is perovskite QDs, which offer potential emission across the entire visible spectrum with high quantum efficiencies [93, 94] and high absorption coefficients [95]. Perovskite nanocrystals have been implemented in multiple configurations to create amplified spontaneous emission, as well as single and multi-mode laser emission [96–98], successfully operating as an advanced gain material for band-edge LC lasers and other optoelectronic devices [99–101].

2.2.2 Defect-mode LC Lasers

In addition to lasing at the band-edges, researchers have also studied lasing modes within the PBG. This type of laser, referred to as the defect-mode LC laser, generally operates by introducing a defect layer into the periodic LC structure. The entire cavity can be regarded as a combination of a classic Fabry–Perot resonator and DFB resonators, which consist of distributed Bragg reflectors on at least one end of the sandwiched defect layer, selectively reflecting the stimulated emission from the gain medium within the defect layer.

Early research focused on providing theoretical derivations [102–104] and experimental approaches based on a phase jump in the helical structure [105, 106] and isotropic LCs [107–109] for the defect layer. It was later reported for defect-mode LC lasers with architectures of sandwiching dye-doped nematic polymer layers between polymerised chiral nematic LC layers [110, 111], which also led to multi-mode lasing with thicker defect layers (around 100 µm) [112] and novel structures involving multiple PBGs [113, 114].

In recent years, reports have demonstrated other defect-mode architectures and lasing with 3D photonic structures [115] and colloidal photonic crystals [116, 117]. A spectrally discrete white-light laser device was proposed by Jui-Chieh Huang et al., composed of a layer of dye-doped chiral nematic LC sandwiched between two identical inorganic multi-layer photonic crystals, where the red, green, and blue colour lasing originated from two band-edges and one of the defect modes [118]. Laser emission can be electrically switched so that combinations of three resonant wavelengths are achieved under a sole optical pump.

These configurations published in the literature provide various means of increasing the DOS and altering the resonant modes within the cavity, resulting in lower excitation thresholds and wider on-demand tunability. However, their emission energy was found to be lower than band-edge LC lasers, which can be considered as a trade-off between the excitation threshold and emission energy [6].

2.3 Characteristics and Functionalities of Band-edge LC Lasers

General laser emission characteristics of a band-edge LC laser based on dye-doped chiral nematic LCs are presented in Chapter 3 in detail. Typically, band-edge LC lasers have been observed to exhibit a laser linewidth of the order of 0.1 nm, depending on the quality of the alignment of the chiral nematic LC. This corresponds to a Q-factor of 4600, calculated as the centre wavelength divided by the linewidth [6]. This laser is proposed to have a coherence length of 5 mm, where the coherence length equals the square of the centre wavelength divided by the linewidth.

2.3.1 Excitation Threshold and Slope Efficiency

Two important parameters to characterise the LC lasers are excitation threshold and slope efficiency. The excitation threshold is the lowest excitation pump power at which laser emission is observed. The output power increases slowly with the excitation below the excitation threshold, while the slope largely increases above the threshold. Only when the excitation is above the threshold is it called lasing. A previous report has assumed that the excitation threshold energy could be expressed in terms of the threshold gain in the form $E_{th} = A\gamma_{th}d$ [81], where A is a constant related to factors involving the pumping conditions and d is the thickness of the cell. By introducing the concept of the DOS, this report further considered the threshold gain of the dye-doped chiral nematic LC laser as:

$$E_{th} = A(\alpha + \frac{\beta}{DOS \cdot d})d \tag{2.36}$$

where α is the absorption coefficient and β represents a fitting constant. The authors in Reference [81] argued that the DOS could be expressed as $DOS = cd^2$, where c is another fitting constant

specific to the material. This implies that Eq. (2.36) can be written as:

$$E_{th} = A(\alpha + \frac{\beta}{cd^2 \cdot d})d = (A\alpha)d + (\frac{A\beta}{c})\frac{1}{d^2} \tag{2.37}$$

The relationship between cell thickness d and excitation threshold is shown in Eq. (2.37), which represents that there would be a specific cell thickness at which the threshold reaches its minimum. Research also indicates that the DOS increases as a function of the birefringence suggesting a relationship between excitation threshold energy and birefringence of the material [119].

The slope efficiency of a laser is the differential power conversion efficiency. Above the excitation threshold, the dependence of the output power as a function of the input power can be approximated as a straight line, and the slope of this line is defined as the slope efficiency of the laser. The slope efficiency is proportional to $1/E_{th}$, which could imply that

$$\eta_S \propto [d + \frac{\beta}{\alpha c}(d^{-2})]^{-1} \tag{2.38}$$

Research has shown that these two parameters are influenced by a wide range of factors relating to the physical properties of the LC and the external environment [120]. For example, as the diameter of the pump laser increases, the excitation threshold and the slope efficiency increase and decrease, respectively. Cell thickness is another relevant influencing factor. Experimental studies show that the excitation threshold and slope efficiency vary with cell thickness and that there is an optimum thickness at which the threshold is minimised and the slope efficiency is maximised [121, 122]. The exact value of the optimal thickness appears to vary depending on the LC material that is used as the host.

In addition, changing dyes for the gain medium also has an impact on the value of these two parameters. For instance, lasers doped with pyrromethene dyes such as PM597 exhibit lower threshold energies and higher slope efficiencies in comparison to the DCM-doped lasers [77]. Polymeric dyes were used to achieve better alignment between the LC director and the transition dipole moment, resulting in higher order parameter of the dye and lower excitation threshold energy value [123]. Oligofluorene dyes also exhibit high order parameters and quantum yields leading to higher lasing efficiencies [124]. Typical values reported of slope efficiency for conventional dye-doped chiral nematic LC lasers are above 30% with the appropriate laser dyes and device geometries [120], while subsequent research shows that this parameter can be optimised to be as high as 60% for reflective geometries resulting in a multiple pass of the pump

beam [125]. Typical values of threshold energy is $\sim 1000\mu J/cm^2/pulse$ for DCM laser (1 wt.%) and $\sim 600\mu J/cm^2/pulse$ for PM580 laser (1 wt.%) when they are both doped in a nematic LC, E49, and excited by a pulsed Nd:YAG laser (repetition rate 1 Hz, pulsed length 6 ns) [77].

2.3.2 Wavelength and Direction Tunability

Wavelength tuning and beam steering have been demonstrated using LC lasers. Wavelength tunability makes LC laser particularly attractive as a laser source, while beam steering is potentially important for a wide range of communications applications. Here research on these two functionalities is briefly illustrated and reviewed.

Electrically-induced wavelength tunability has been reported in numerous studies [126–130]. For band-edge LC lasers, the pitch and the dielectric anisotropy directly affect the wavelength of the laser. Alternatively, the pitch can be unwound and elongated using ferroelectric coupling for a dye-doped chiral smectic LC laser [126] or applying an in-plane electric field for a dye-doped chiral nematic LC laser with a tunability of up to 15 nm [127]. The pitch can also be contracted in the presence of an electric field in a negative dielectric anisotropy cell [128]. In terms of distributed feedback lasers, electrically tunable action has been demonstrated by holographic excitation in a dye-doped nematic LC waveguide consisting of a transient grating [129]. It has a total wavelength shift of 30 nm, and is feasible due to the changing of the effective refractive index of the nematic LC with the changing external electric field. A report also presents possible wavelength-voltage controllable lasing in a defect-mode laser, in which a homogeneously aligned nematic LC layer is sandwiched in between two layers of chiral nematic LCs [130].

Mechanical strain has been reported to tune the laser wavelength in free-standing chiral nematic LC elastomers. This observation is consistent with the strong coupling between the mechanical field and the pitch of the helical structure. When the sample is subjected to a biaxial distortion, the laser wavelength shifts, with a line width of 0.35 nm, over a range of 544 nm to 630 nm [131].

Temperature is another factor that has an impact on the laser wavelength. The literature suggests that a dye-doped chiral nematic LC laser shifts to a shorter wavelength as the temperature increases, whereas a temperature decrease results in longer laser wavelengths [132]. This thermally induced wavelength tunability corresponds to a shift of the band-gap

which is attributed to the pitch. It has also been reported that the shift of the lasing wavelength is discontinuous because pitch changes in a chiral nematic LC are discrete with the appearance or disappearance of every half period of the chiral nematic LC helix [133].

Alternative ways of wavelength tuning in LC lasers include spatial tuning, photochromic tuning, etc. [134–138]. Spatial wavelength tuning typically involves forming a pitch gradient and mechanically changing the position of the active region (the pump area) of the cell, resulting in a wide range of wavelength tunability. This can be achieved by doping multiple dyes into a chiral nematic LC sample [134] (with wavelength range from 370 nm to 680 nm), or utilising photopolymerisation in chiral nematic polymer films [135] (with wavelength range from 595 nm to 643 nm). Photochromic tuning, on the other hand, is achieved by dispersing photoactive components into the sample so that the periodicity of the chiral nematic helix can be elongated or contracted under UV illumination. Reports have shown that phototunability can be achieved by controlling the exposure time [136] or exposure energy of the UV light source [137]. Research has also demonstrated a phototunable chiral nematic LC using a new dithienylcyclopentene-based molecule, (S,S)-D4, as the chiral additive [138]. This chiral material has open and closed molecular forms and is switchable under ultraviolet (310 nm) or visible light (550 nm) introducing the possibility of light-induced, three-dimensional control of the in-plane rotation of the helical axis and the pitch.

2.4 Mathematical Descriptions of Polarisation

Light can be treated as a transverse electromagnetic wave consisting of an orthogonal pair of coupled oscillating electric and magnetic fields, both perpendicular to the direction of light propagation. The polarisation of light is defined by the geometrical orientation of the electric field oscillation. By convention, light can be divided into unpolarised, partially polarised, and polarised light. Polarised light can further be categorised as linearly, elliptically, and circularly polarised. In linear polarisation, the electric fields oscillate in a single direction, whereas in elliptical and circular polarisation, the field rotates in the plane perpendicular to the propagation direction, either in the right-handed or left-handed direction.

The handedness of circularly polarised light has been defined in opposite ways in literature [139, 140]. In this thesis, circularly polarised light is defined to be right-circularly polarised,

if the projection of its electric field vector in a fixed plane rotates clockwise with time, when an observer looks back along the propagation direction towards the light source. The tip of its electric field vector traces a right-handed helix in space, hence it is also known as right-handed circularly polarised light. Likewise, left-circularly polarised light, or left-handed circularly polarised light, refers to its electric field vector rotating anti-clockwise in a fixed plane with time following a left-handed rotation sense.

The exact form of the electric field oscillation, i.e., the polarisation state of light, can be specifically indicated by its wave function. It can also be characterised by two mathematical descriptions, known as the Stokes parameters and Jones vector. Both characterisation methods of the polarisation states of light were implemented in the experiments mentioned in this thesis. Their principles as well as particular application advantages and limitations will be illustrated in detail in the following paragraphs.

2.4.1 Stokes Parameters and Mueller Matrix

One of the representations for the polarisation of light was proposed by G. G. Stokes in 1852 [141], where he introduced four quantities, known as the Stokes parameters, which can describe the polarisation of natural, partially polarised, or fully polarised light. The four parameters, S_0, S_1, S_2, and S_3, are defined by the emergent irradiances upon four imaging optical filters, I_0, I_1, I_2, and I_3 measured by a detector insensitive to polarisation. Here, the first filter is isotropic to incident polarisation, and the second and third are linear polarisers with their transmission axis horizontal, and at +45°, respectively. The last filter is opaque to left-handed circularly polarised light. These optical filters can transmit half of the incident light under natural illumination and therefore, the operational definition of the Stokes parameters can be given by:

$$\begin{cases} S_0 = 2I_0 \\ S_1 = 2I_1 - 2I_0 \\ S_2 = 2I_2 - 2I_0 \\ S_3 = 2I_3 - 2I_0 \end{cases} \tag{2.39}$$

The first parameter, S_0, represents only the incident irradiance while the other three parameters, S_1, S_2, and S_3, indicate the incident polarisation state and the specific tendency of being horizontally ($S_1 > 0$) or vertically ($S_1 < 0$) linearly polarised, +45° ($S_2 > 0$) or -45°

($S_2 < 0$) linearly polarised, and right-handed ($S_3 > 0$) or left-handed ($S_3 < 0$) circularly polarised. The parameters can be related to the electromagnetic theory of light by considering the two electric field components of quasimonochromatic light that propagates along the z-direction with angular frequency ω and angular wave vector $k = (0, 0, k)$:

$$\begin{cases} \mathbf{E_x}(t) = \hat{\mathbf{i}} E_{0x} \cos[(kz - \omega t) + \phi_x] \\ \mathbf{E_y}(t) = \hat{\mathbf{j}} E_{0y} \cos[(kz - \omega t) + \phi_y] \end{cases} \tag{2.40}$$

where $\hat{\mathbf{i}}$ and $\hat{\mathbf{j}}$ are unit vectors, ϕ_x and ϕ_y the phase terms, E_{0x} and E_{0y} the amplitude terms, in the x- and y-directions, respectively. The electric field can be determined by $\mathbf{E}(t) = \mathbf{E}_x(t) + \mathbf{E}_y(t)$. Note that the irradiance measured by a detector in experiments would be the average (root mean square) over comparatively longer time intervals than the lightwave period, hence, the incident irradiance $I(t)$ and that being directly measured $\bar{I}$ by a detector are:

$$I(t) = \epsilon_0 c \langle \mathbf{E}^2(t) \rangle = \epsilon_0 c (\langle \mathbf{E_x}^2(t) \rangle + \langle \mathbf{E_y}^2(t) \rangle) \tag{2.41}$$

$$\bar{I} = \frac{1}{2} \epsilon_0 c (\langle E_{0x}^2 \rangle + \langle E_{0y}^2 \rangle) \tag{2.42}$$

Result in Eq. (2.42) is equivalent to S_0 or $2I_0$ in Eq. (2.39), that is, $S_0 = \frac{1}{2}\epsilon_0 c(\langle E_{0x}^2 \rangle + \langle E_{0y}^2 \rangle)$. In terms of the second Stokes parameter, S_1, the irradiance after a horizontal polariser is $\epsilon_0 c \langle E_{0x}^2 \rangle$ with $I_1 = \frac{1}{2}\epsilon_0 c \langle E_{0x}^2 \rangle$ being detected, therefore, $S_1 = 2I_1 - 2I_0 = \frac{1}{2}\epsilon_0 c(\langle E_{0x}^2 \rangle - \langle E_{0y}^2 \rangle)$. Similarly, the electric field component that can propagate through a $+45°$ polariser is $\frac{\sqrt{2}}{2}(\mathbf{E_x}(t) + \mathbf{E_y}(t))$, thus, the irradiance being detected can be given by substituting this transmitted electric field component to Eq. (2.41) then multiplied by a factor of a half, which results in $I_2 = \frac{1}{4}\epsilon_0 c(\langle E_{0x}^2 \rangle + \langle E_{0y}^2 \rangle + \langle 2E_{0x}E_{0y} \cos\delta \rangle)$ and $S_2 = 2I_2 - 2I_0 = \frac{1}{2}\epsilon_0 c \langle 2E_{0x}E_{0y} \cos\delta \rangle$. Here, δ is the relative phase defined as $\delta = \phi_y - \phi_x$. The last filter is a right-handed circular polariser, which can be regarded as a combination of a $+45°$ polariser followed by a quarter waveplate with its fast axis aligned with the y-direction. Consequently, the propagated electric field component and the derivation of the irradiance received by the detector is the same as that of the case for the $+45°$ polariser, with only the relative phase δ being replaced by $(\delta - \frac{1}{2}\pi)$. Accordingly, the fourth Stokes parameter can be given by $S_3 = \frac{1}{2}\epsilon_0 c \langle 2E_{0x}E_{0y} \cos(\delta - \frac{1}{2}\pi) \rangle = \frac{1}{2}\epsilon_0 c \langle 2E_{0x}E_{0y} \sin\delta \rangle$.

It has been generally accepted for the simplification to drop the common factor $\frac{1}{2}\epsilon_0 c$ [142], which finally leads to the definition of Stokes parameters explicitly based on the electric

field amplitudes and relative phase of light.

$$\begin{cases} S_0 = \langle E_{0x}^2 \rangle + \langle E_{0y}^2 \rangle \\ S_1 = \langle E_{0x}^2 \rangle - \langle E_{0y}^2 \rangle \\ S_2 = \langle 2E_{0x}E_{0y}\cos\delta \rangle \\ S_3 = \langle 2E_{0x}E_{0y}\sin\delta \rangle \end{cases} \tag{2.43}$$

Stokes parameters can also be related to the corresponding polarisation ellipses by introducing a Poincaré sphere. Upon neglecting the first Stokes parameter, the other three parameters consist of a three-dimensional vector of the Cartesian coordinates (S_1, S_2, S_3) constrained within the Poincaré sphere. As shown in **Fig. 2.10**(a), the Stokes parameters can be given geometrically by:

$$\begin{cases} S_0 = I \\ S_1 = Ip\cos 2\psi \cos 2\chi \\ S_2 = Ip\sin 2\psi \cos 2\chi \\ S_3 = Ip\sin 2\psi \end{cases} \tag{2.44}$$

where I is the total intensity of the beam, 2ψ and 2χ are the two spatial angles. The degree of polarisation (DOP) is indicated by the factor p, where $p = 1$, $0 < p < 1$, and $p = 0$ represent fully polarised, partially polarised, and unpolarised light, respectively. The Poincaré sphere has a radius of Ip such that the polarisation states of fully polarised sources can be represented by points on the Poincaré sphere, while partially polarised states are represented by points within the sphere. The spatial angles, ψ and χ, can also be applied to indicate the corresponding polarisation ellipse as shown in Fig. 2.10(b). The polarisation ellipse is indistinguishable from one rotated by 180° and the one with the semi-axis lengths swapped accompanied by a 90° rotation, which provides an explanation for the presence of the factor of two before ψ and χ in Eq. (2.44), respectively. In the study introduced in Chapter 4 where the Stokes parameters of various laser sources were measured, the laser intensity, DOP, and polarisation ellipse parameters were solved according to the following formula.

$$\begin{cases} I = S_0 \\ p = \dfrac{\sqrt{S_1^2 + S_2^2 + S_3^2}}{S_0} \\ \psi = \dfrac{1}{2}\arctan\dfrac{S_2}{S_1} \\ \chi = \dfrac{1}{2}\arctan\dfrac{S_3}{\sqrt{S_1^2 + S_2^2}} \end{cases} \tag{2.45}$$

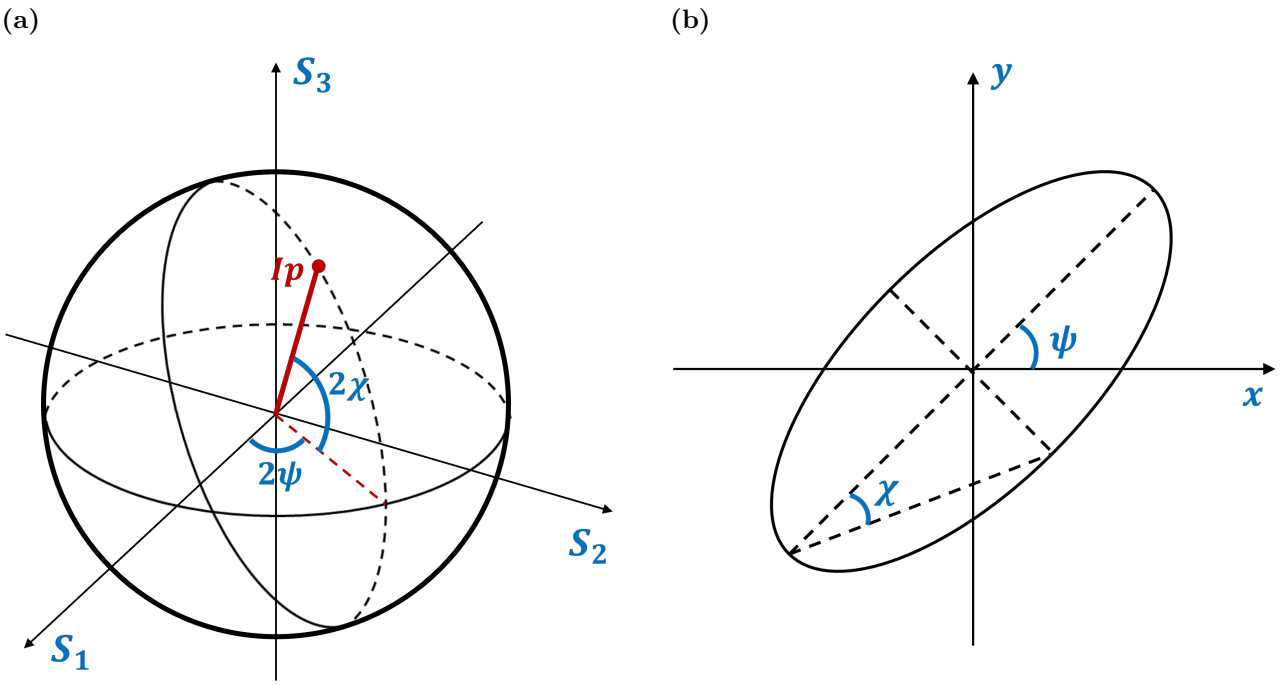

Figure 2.10: (a) A geometrical illustration of the Poincaré sphere with the three axes being S_1, S_2, and S_3. The Stokes parameters of any fully polarised or partially polarised states can be represented by the spatial coordinates of points constrained on or within the sphere, respectively. The essential geometrical parameters for indicating the Stokes parameters are labelled in the figure. (b) An illustration of the relationship between the spatial angles and the corresponding polarisation ellipse.

To mathematically describe the variation of the Stokes parameters when light propagates through optical media, H. Mueller proposed a transfer matrix method in 1943 [143] known as the Mueller matrix. Suppose light propagates through an optical element, and the Stokes parameters for the incident and emergent light are S_{in} and S_{out}, respectively, then the Mueller matrix for the optical element, M, can be expressed by satisfying:

$$S_{out} = M \cdot S_{in} \tag{2.46}$$

Consecutive matrix multiplication to the incident Stokes parameters is needed if the light propagates through a sequence of optical elements, such as polarisers and waveplates. These Mueller matrices have a common dimension of 4×4 and can indicate how the Stokes parameters alternate between optical elements.

2.4.2 Jones Vector and Jones Matrix

Another mathematical representation of polarisation is the Jones vector, which was invented by R. C. Jones in 1941. Although only applicable to fully polarised light, the Jones vector

has advantages over the Stokes parameters for directly describing the electric field components and concisely preserving the phase information which is essential for analysing coherent light. The complex electric field vector, $\mathbf{E}$, of quasimonochromatic light that propagates along the z-direction with angular frequency ω and angular wave vector $k = (0, 0, k)$ can be written as:

$$\mathbf{E} = \begin{bmatrix} E_x \\ E_y \end{bmatrix} = \begin{bmatrix} E_{0x} e^{i(kz-\omega t+\phi_x)} \\ E_{0y} e^{i(kz-\omega t+\phi_y)} \end{bmatrix} = e^{i(kz-\omega t)} \begin{bmatrix} E_{0x} e^{i\phi_x} \\ E_{0y} e^{i\phi_y} \end{bmatrix} \tag{2.47}$$

where E_x and E_y are two complex electric field components in the x- and y-direction, respectively, and i is the imaginary unit. The Jones vector is then defined with only the amplitude terms, E_{0x} and E_{0y}, and the phase terms, ϕ_x and ϕ_y:

$$\begin{bmatrix} E_{0x} e^{i\phi_x} \\ E_{0y} e^{i\phi_y} \end{bmatrix} \tag{2.48}$$

In some applications when $E_{0x} = E_{0y}$ and only the relative phase is of interest, the Jones vector can be further simplified by neglecting the amplitude terms and normalising the modulus of the vector to 1. For example, the simplified Jones vector for right-handed circularly polarised light, $\mathbf{E_R}$, can be expressed as:

$$\mathbf{E_R} = \begin{bmatrix} E_{0x} e^{i\phi_x} \\ E_{0x} e^{i(\phi_x - \frac{\pi}{2})} \end{bmatrix} = E_{0x} e^{i\phi_x} \begin{bmatrix} 1 \\ e^{-i\frac{\pi}{2}} \end{bmatrix} = E_{0x} e^{i\phi_x} \begin{bmatrix} 1 \\ -i \end{bmatrix} \rightarrow \frac{\sqrt{2}}{2} \begin{bmatrix} 1 \\ -i \end{bmatrix} \tag{2.49}$$

Similar to the Mueller matrices, Jones matrices represent the transformation of the Jones vectors of particular optical elements. Suppose the Jones vector for the incident and emergent light are E_{in} and E_{out}, respectively, then the 2 × 2 Jones matrix for the optical element, J, can be expressed by satisfying:

$$E_{out} = J \cdot E_{in} \tag{2.50}$$

Both mathematical descriptions of the polarisation states of light are implemented in the subsequent chapters. The selection of either method was considered for their characteristics and limitations. The Stokes parameters and Mueller matrices directly operate on intensities and their differences whereas they cannot be applied to optical scenarios where coherence needs to be considered, such as interference and diffraction. In comparison, the Jones vector and Jones matrices directly identify the electric field components retaining the phase information, however, they can only be applied to fully polarised light. Therefore, in the work presented in Chapter 4, the polarisation states of LC lasers were quantified using Stokes parameters and Mueller matrices

since these lasers were found to be partially polarised in some cases and their coherence was disregarded for the research interest. In terms of the research introduced in Chapter 5, the Jones vector and Jones matrices were implemented to describe the laser propagation through tunable LC waveplates and polarisation gratings (PGs), considering the specific electric field components and their phases are of significant importance for the far-field diffraction pattern simulations.

2.5 Summary

The study of LCs involves exploring various mesophases, which are defined by different degrees of molecular orientational and positional order. These mesophases can transition from one to another due to the introduction of internal dopants or by application of external stimuli. Among these mesophases, the nematic phase is one of the most prevalent, characterised by its long-range orientational order and no positional order. In this phase, nematic LC molecules exhibit anisotropy in their dielectric permittivity and refractive indices, meaning their optical properties vary depending on the orientation relative to the molecular director. By sandwiching nematic LCs between glass substrates with alignment layers and electrodes, and applying electric fields, the orientation of the director can be altered, allowing the LC to function as a voltage-controlled, continuously tunable waveplate.

The chiral nematic phase, a variant of the nematic phase, is created by introducing chiral additives into nematic LCs and aligning them between substrates. This dopant-induced twisting gives rise to a macroscopic helical structure within the LCs. The planar alignment of chiral nematic LCs acts as a one-dimensional Bragg reflector, resulting in a PBG that reflects circularly polarised light with the same handedness when the wavelength falls within the bandgap. The behaviour of chiral nematic LCs can be analysed by deriving the eigenmodes from Maxwell's equations or simulated using mathematical approaches such as the Berreman 4x4 matrix method.

Lasers, regardless of their specific types and working principles, generally consist of a pump source that establishes a population inversion, a gain medium that facilitates absorption and stimulated emission, and a resonant cavity that enhances optical feedback and enables advanced emission techniques such as Q-switching and mode-locking. LC lasers, a type of dye laser, offer advantages like wideband tunability, large coherence areas, ultrathin dimensions, lightweight, high flexibility, and versatility. The most studied LC lasers are band-edge LC lasers, which

typically combine the PBG in chiral nematic LCs and an organic laser dye. The sudden increase in the photonic DOS at the band-edges provides sufficient gain for lasing when pumped by picosecond or nanosecond pulsed solid-state lasers. Two essential parameters characterising LC lasers are the excitation threshold and slope efficiency. LC lasers find applications in various fields, particularly where wavelength and emission direction tunability are required.

The polarisation state is a crucial property of light considered in this thesis. Two mathematical descriptions of polarisation are employed with the first being Stokes parameters and Mueller matrices, and another being Jones vectors and Jones matrices. Stokes parameters directly operate on light intensities and can be applied to partially and unpolarised light, whereas Jones vectors identify the electric field components and retain phase information but are only valid for fully polarised light.

3

Experimental Procedures

Contents

3.1 Mixture Preparation 41
3.1.1 PVA Solution 41
3.1.2 LC Mixtures 43
3.2 LC Glass Cells 45
3.3 Optical Characterisation Techniques 50
3.3.1 Polarising Optical Microscopy 50
3.3.2 Optical Fluorescence Microscopy 51
3.3.3 Ultraviolet-visible Spectrophotometry 51
3.3.4 USB Spectrometer 54
3.4 Nd:YAG Pump Laser 56
3.4.1 Laser Beam Profile 56
3.4.2 Knife-edge Measurement Method 58
3.5 Band-edge LC Lasers 60
3.5.1 Fundamentals 60
3.5.2 Material Preparation 61
3.5.3 Chiral Nematic LC Hosts 62
3.5.4 Dye-doped Nematic LCs 63
3.5.5 Fluorescence Emission from Dye-doped Chiral Nematic LCs 70
3.5.6 Laser Emission from Dye-doped Chiral Nematic LCs 72
3.6 Summary 75

3.1 Mixture Preparation

3.1.1 PVA Solution

As illustrated in the previous chapter, some liquid crystal (LC) mesophases require alignment layers to establish the desired macroscopic structure. Compared to more recent photo-alignment

techniques, rubbed alignment methods have been widely implemented in displays as it results in a stable alignment. In this case, a thin film is established across the glass substrates and then mechanically rubbed to generate a preferential alignment direction on the film. In the experiments introduced in this thesis, for glass cells fabricated in-house, the alignment thin film was made from 1 wt.% PVA (polyvinyl alcohol) solution dissolved in distilled water with the preparation process illustrated in **Fig. 3.1**(i)∼(vi).

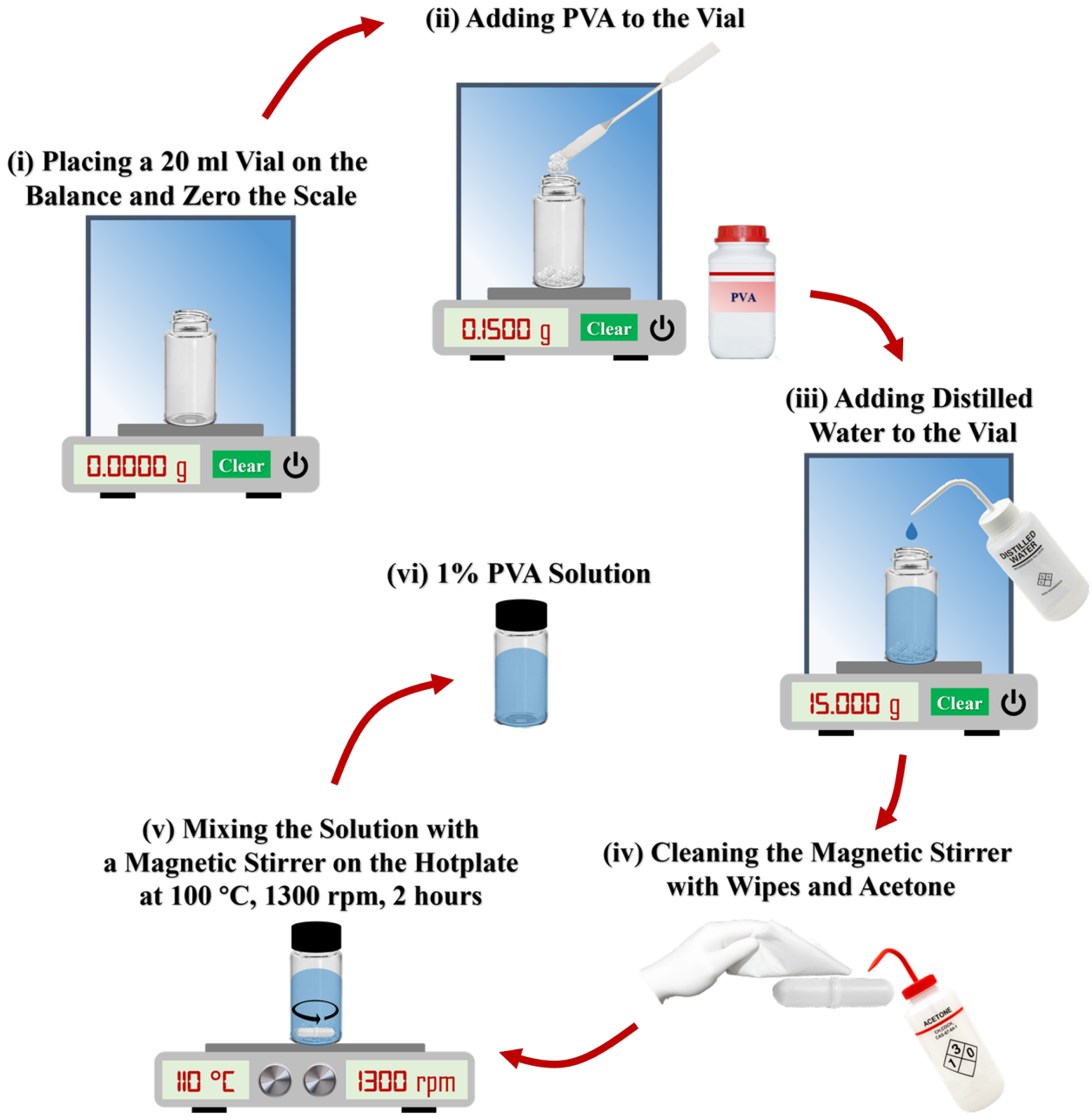

Figure 3.1: The preparation procedures of the 1 wt.% PVA solution. A typical mass of 15 grams was usually prepared, where the mixture consisted of 0.15 g PVA and 14.85 g distilled water. The solution was mixed with a magnetic stirrer on a hotplate and then stored at room temperature once fully dissolved.

The process begins with placing a 20 ml empty vial on a precision micro-balance with an accuracy of 0.1 mg (AB104-S, Mettler Toledo). A quantity of 0.15 grams of PVA powder was then measured and added to the vial, followed by distilled water until the total weight reached 15 grams. After adding the PVA and water, a magnetic stirrer was cleaned with acetone and placed into the vial. The vial was then removed from the balance, covered with a lid, and positioned on a hotplate. The magnetic stirrer rotated rapidly under the magnetic field of the hotplate, accelerating the dissolution process. A heating block was usually equipped to secure the vial on the hotplate, ensuring stability during the stirring process. Typically, the hotplate was set to 110°C, with the stirrer rotating at 1300 rpm. The solution will eventually become colourless and transparent after 1 to 2 hours of heating and mixing, resulting in 15 grams of 1 wt.% PVA solution.

3.1.2 LC Mixtures

Various LC mixtures investigated in the following chapters were prepared in the labs in the Department of Engineering Science. For example, the preparation process for a mixture of E7 + 4 wt.% BDH1281 is illustrated in **Fig. 3.2**(i)∼(v) where E7 is a nematic LC mixture comprised of compounds, including 51 wt.% 5CB, 25 wt.% of 7CB, 16 wt.% of 8OCB and 8 wt.% 5CT.

Similar to the preparation of the PVA solution, the process started by placing an empty vial on a precision balance, waiting for the reading to stabilise, and then resetting it to zero. For filling an LC cell, a mixture volume of around 5 to 20 µl was typically required, so the LC sample was usually prepared in a quantity of approximately 100 mg. A precise amount of 4 mg of BDH1281 powder was weighed and added to the vial, followed by the addition of E7 using a pipette to bring the total weight to 100 mg. Given the small mass of the required sample, it was crucial to wait for the balance reading to stabilise fully at each step before proceeding to the next procedure. Subsequently, the vial was removed from the balance, covered with a lid, and placed in an oven set to 70°C. The mixture was left to heat overnight, ensuring that the LC sample was fully mixed in the isotropic phase, resulting in 100 mg of the LC sample. Note that it was essential to reheat the LC sample in the oven for several hours before each use to guarantee that the sample remains fully mixed when filling the glass cell.

Similar steps were followed when preparing other LC mixtures. As shown in Fig. 3.2(ii), powder samples (e.g., chiral additives, organic dyes, etc.) were added to the vial first because they generally had a smaller proportion in the mixture. This approach allowed for minor

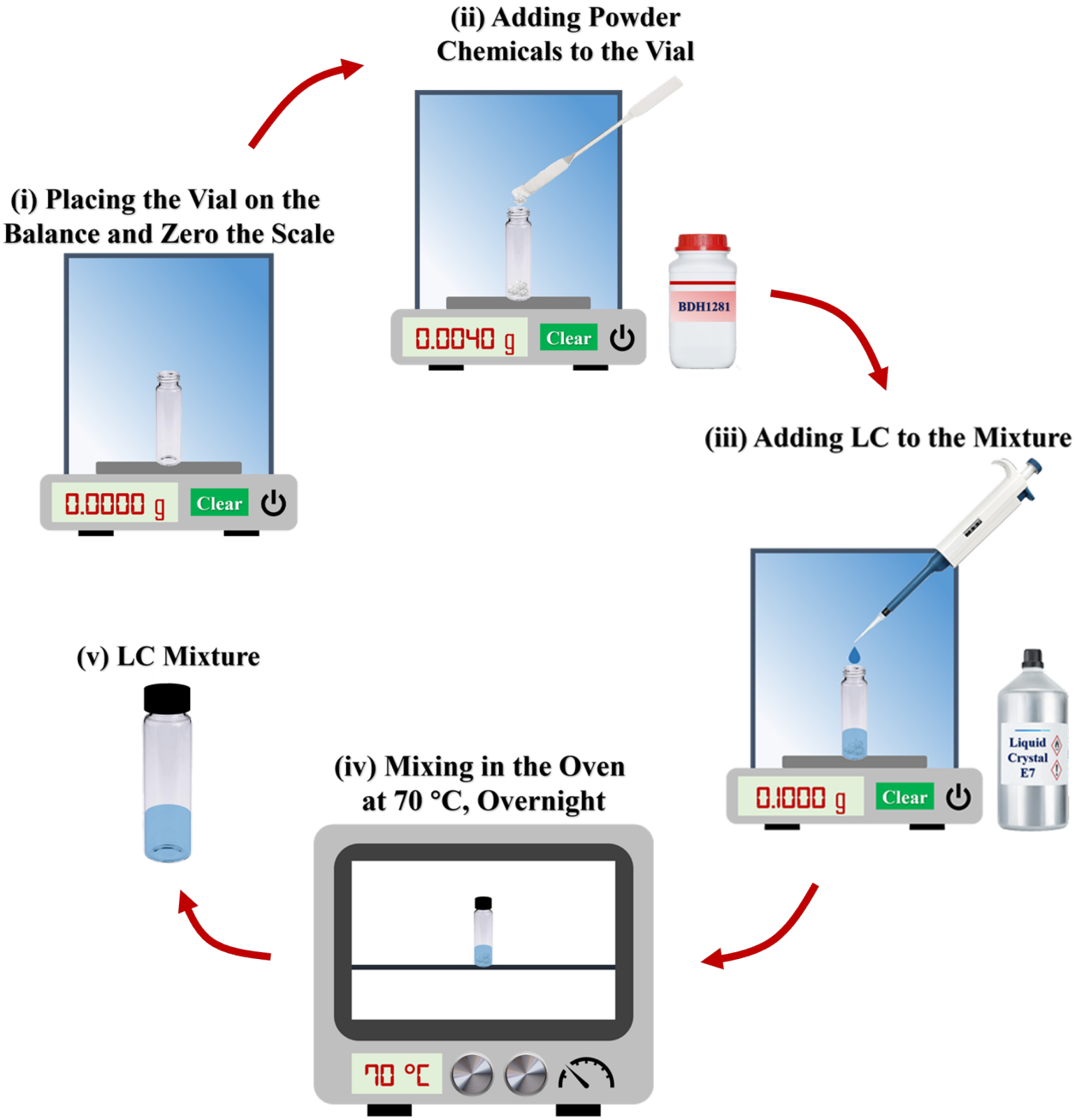

Figure 3.2: The preparation procedures of LC mixtures. Most LC mixtures consisted of chemicals in the form of powders and nematic LCs, thus their preparation procedures were similar. The figure illustrates an example of a chiral nematic LC mixture, specifically E7 (nematic LC host) with 4 wt.% BDH1281 (chiral dopant). A typical total mass of 0.1 grams was prepared, considering the volume of a small sample vial and the amount required to fill an empty cell. To create the mixture, 4 mg of BDH1281 and 96 mg of E7 were needed. The solution was mixed in an oven at 70°C overnight in the isotropic phase, then stored at room temperature once fully dissolved. Before filling an empty glass cell, the mixture was reheated in the oven for several hours to ensure optimal mixing.

deviations in the powder mass in practice, as the amount of LC to be added later could be adjusted accordingly to maintain the correct ratio, as demonstrated in Fig. 3.2(iii).

3.2 LC Glass Cells

LCs are typically sandwiched between glass substrates due to their fluid-like properties. These substrates are often combined with indium tin oxide (ITO) electrodes and alignment layers to ensure that the LCs align as required. LC glass cells can be sourced from commercial suppliers or fabricated in-house to meet specific needs of the study under investigation. Two critical factors for LC glass cells are the air gap, which defines the thickness of the LC layer between the glass substrates, and the alignment direction for the LCs.

Fig. 3.3 illustrates the structure of a commercial homogeneous cell from Instec, which has been used in several experiments mentioned in this thesis. This cell comprises two glass substrates, which may be made from soda-lime, BK7, or quartz, and are coated with ITO transparent electrodes and alignment layers. As shown in Fig. 3.3(a), the cell is equipped with two U-shaped spacers, complemented by spacer beads distributed across the cell to ensure uniform thickness. However, they can disrupt the alignment of the LC director, particularly in chiral nematic LCs, where uniform alignment is crucial for the desired optical properties. The spacers are sandwiched between and glued to the substrates, with openings left for capillary filling of the LC mixture into the cell.

The top and bottom substrates are horizontally displaced, as depicted in Fig. 3.3(b), creating two edge regions on both substrates that allow for the connection of wires that connect to signal generators. The geometry of the ITO electrodes on the two substrates differs slightly, as shown in Fig. 3.3(a) and (b), with only a square region at the centre of the cell being covered by both ITO electrodes. This configuration allows for the establishment of an electric field at the central area when a voltage is applied across the two substrates. The dimensions of the Instec cell are 15.25 x 17 x 1.4 mm, with a central area being 5 x 5 mm. The thickness of the air gap can range from 5.0 µm to 20 µm, depending upon the size of the spacers used, and the alignment direction of the Instec cells used in this thesis is anti-parallel.

Empty glass cells can also be manually fabricated in a clean room following the procedure shown in **Fig. 3.4**. Either microscope glass slides or ITO-coated glass were used as substrates,

(a)

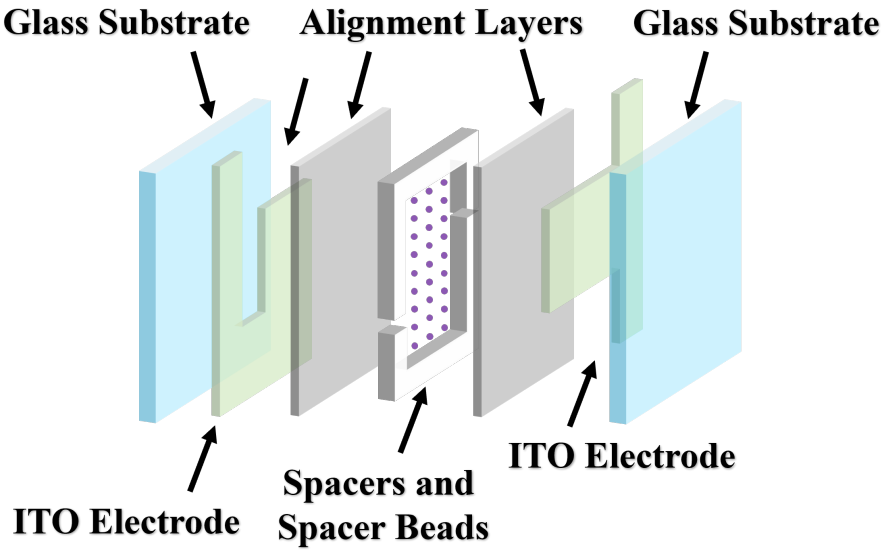

(b)

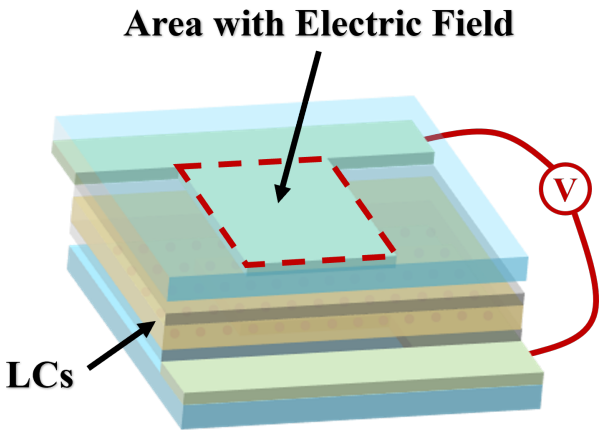

Figure 3.3: An illustration of the structure of the Instec cells. (a) The Instec cells are comprised of two glass substrates, each of which is coated with an ITO electrode and an alignment layer. The alignment layer of the Instec cells used in this thesis is anti-parallel. A pair of spacers, along with randomly distributed spacer beads, are sandwiched between the substrates to provide an air gap with uniform thickness across the cell. (b) The LCs can be capillary-filled into the air gap of the Instec cell. External voltages can be applied by attaching wires to the substrates with ITO coating. The central region of the cell is covered by both ITO electrodes, allowing an electric field to be established.

starting with a thorough cleaning using acetone and wipes to remove dust and residual particles. After cleaning, the substrate was transferred to a spin-coating machine, where a 1 wt.% PVA solution dissolved in distilled water was dispensed. The spin-coating machine holds the substrate using vacuum suction and rotates it at 1500 rpm for 30 seconds. This rotation, combined with the surface tension of the liquid, resulted in a uniform thin film of PVA on the substrate. Experiments have shown that repeating the coating process and controlling the acceleration of the rotation can lead to improvement of the final alignment quality. To remove any remaining solvent, the substrate was placed in an oven at 70°C for 2 minutes, with the PVA layer facing upward.

Next, the substrate was transferred to a rubbing machine, which consists of a rotating drum covered with velvet cloth and a translation stage with a vacuum suction pump to hold the substrate in place. The relative height of the drum was carefully adjusted to ensure effective one-directional mechanical rubbing of the PVA layer. Typically, the drum rotated at 2000 rpm in an anti-clockwise direction. The rubbing process can be repeated two to three times to optimise the final alignment quality of the cell, ensuring a consistent location of the substrate on the translation stage and the rubbing direction throughout the process. The rubbing direction was usually marked on the back of the substrate with a marker, as it is crucial for the subsequent assembly process to indicate the type of cell and the alignment of the LC.

The above processes, as illustrated in Fig. 3.4(i)∼(iv), were usually repeated to prepare two substrates with mechanically rubbed PVA alignment layers. After the alignment layers were prepared, spacers were attached to one of the substrates using tweezers. The selection of spacers and their positioning on the substrate depend on the specific requirements. One common choice was to use Kapton film, which is commercially available in various thicknesses such as 5, 10, 23, and 50 µm. For typical cells designed for planar-aligned LCs, two identical spacers were used, as shown in Fig. 3.4(v). On the other hand, wedge cells were fabricated using only one spacer, creating a gradient in the air gap between the substrates.

The second substrate was then placed on top of the spacers, with its alignment layer facing downward. In the case of anti-parallel rubbed cells, the rubbing directions of the alignment layers on the two substrates was opposite to achieve the desired alignment. The substrate stack was then secured using clips and/or magnets. Subsequently, UV glue was applied to the edges of the substrates using a glue dispenser (Performus V, Nordson) with a syringe (30GA Lavender, Nordson), as shown in Fig. 3.4(vi). The stack was then photo-polymerised under

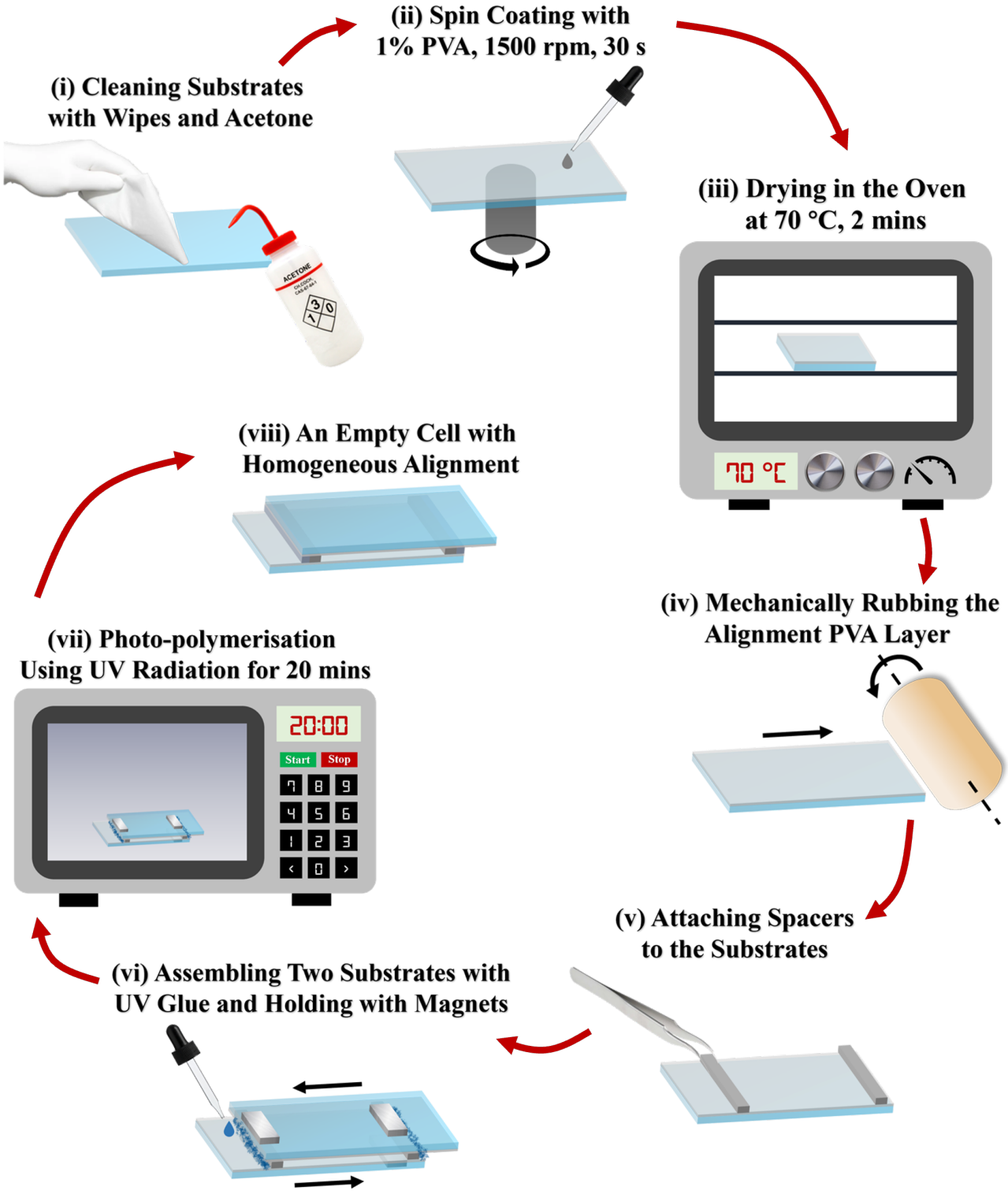

Figure 3.4: The fabrication process of an empty cell with homogeneous alignment. Other types of empty cells, such as wedge cells and homeotropic aligned cells can be manufactured using similar procedures. The glass substrates are cleaned and spin-coated with mechanically rubbed PVA layers, before being assembled and applied with the UV glue at the cell edges. The fabrication is completed by photo-polymerising the glue under UV curing.

UV radiation for 20 minutes, completing the fabrication of an anti-parallel rubbed cell with homogeneous alignment, as demonstrated in Fig. 3.4(vii) and (viii).

The empty cell manufactured above was then transferred onto a hotplate, where the prepared LC sample was capillary-filled into the cell through the edge gaps, as shown in **Fig. 3.5**(i)∼(iv). The temperature of the hotplate was typically set at 70°C, although higher temperatures may be used to reduce the viscosity of the LC and expedite the filling process across the entire cell. Once the LC mixture fully filled the cell gap, a wipe moistened with acetone was used to clean any residual LC mixture from the cell surfaces. Note that it was essential to avoid excessive acetone on the wipe, as it could flow into the cell gap and disrupt the LC. Experiments have shown that, for chiral nematic or dye-doped chiral nematic LC cells, gently rubbing the alignment layer with wafer tweezers along the alignment direction can improve the alignment quality. This step was performed on the hotplate and/or during the cooling process of the cell.

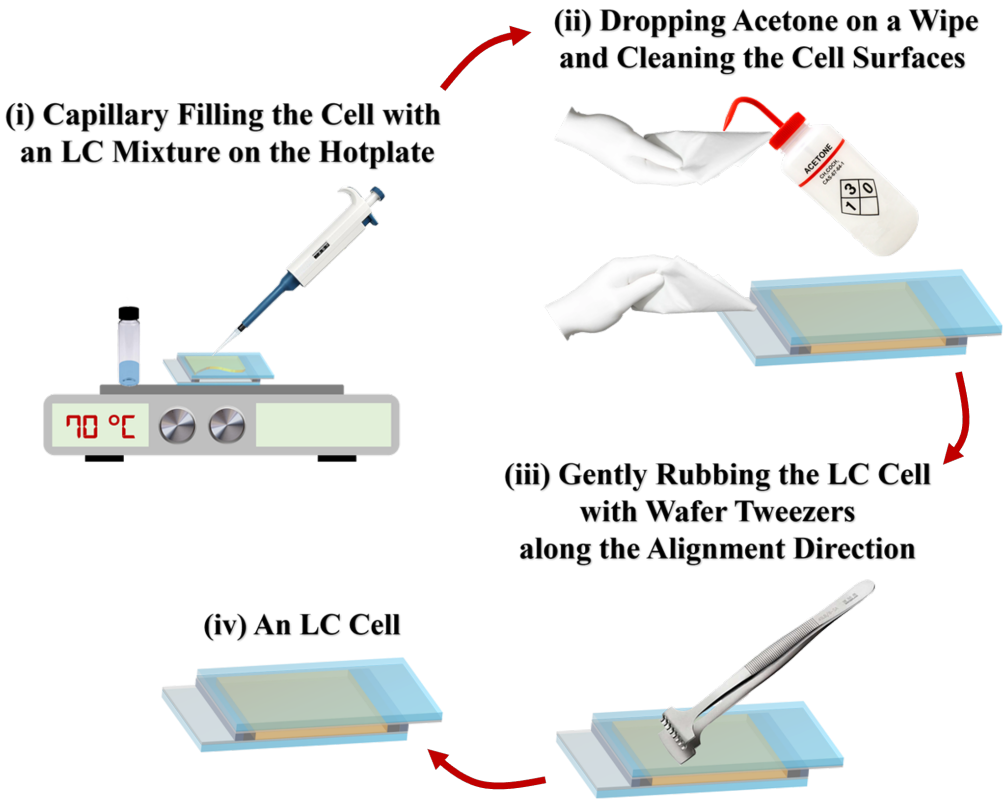

Figure 3.5: The fabrication process of capillary filling an empty cell with an LC mixture through one of the cell edges. The filling is conducted on a hotplate to speed up the process. The cell is subsequently cleaned with acetone and gently rubbed with tweezers along the rubbing direction to achieve better alignment.

3.3 Optical Characterisation Techniques

3.3.1 Polarising Optical Microscopy

Polarising optical microscopy was employed throughout this thesis to observe the optical texture of various samples and analyse the alignment and mesophase of different LC mixtures. **Fig. 3.6** presents a simplified configuration of a typical polarising optical microscope (BX51, Olympus) and illustrates its essential components along the optical path. The unpolarised illumination provided by the halogen bulb passes through a series of components, beginning with a field diaphragm that regulates the intensity of the incident light, followed by a condenser that focuses the light, and then a polariser before it reaches the sample. The sample is positioned on a mechanical stage that allows for two-dimensional horizontal translation as well as vertical adjustment controlled by coarse and fine focus knobs.

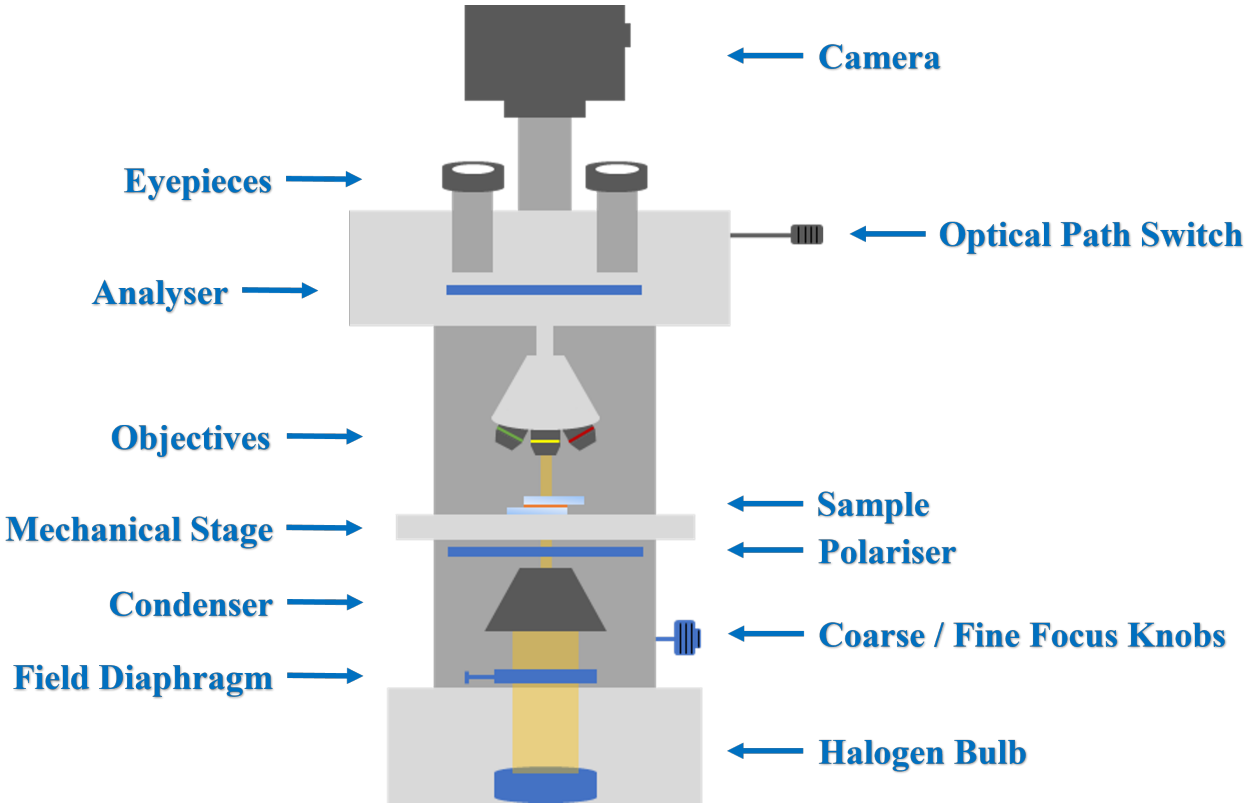

Figure 3.6: A simplified schematic diagram of a polarising optical microscope where the optical path for imaging is highlighted in orange. The sample is positioned between a polariser and an analyser, and its image can be captured by a camera mounted at the top of the microscope or observed through the eyepieces. Additional optical and mechanical components offer adjustments to the imaging path, allowing for various brightness and magnifications of the sample.

Objectives with varying magnifications were mounted on a rotating turret, allowing for easy

switching between objectives, with the one located on the optical axis collecting the transmitted light. This light then passed through an analyser, typically positioned with its polarisation direction perpendicular to that of the polariser beneath the mechanical stage. The image of the sample can be captured by a camera (Retiga R6, Teledyne Photometrics) mounted on the microscope, or observed through eyepieces, with the optical path mechanically switched by beam-splitters controlled by an optical path switch. Most components of the microscope can be removed or inserted based on the observation needs, and multiple filters can be applied to the halogen bulb (not shown in the figure) to adjust the illumination spectrum.

3.3.2 Optical Fluorescence Microscopy

Apart from polarising optical microscopy, optical fluorescence microscopy was also employed in the experiments discussed in this thesis, particularly for observing samples that emit fluorescence upon photo-excitation. **Fig. 3.7** provides a simplified configuration of a typical fluorescence microscope (Axioplan2, Zeiss) and illustrates its essential components along the optical path. Unlike in polarising optical microscopy, the illumination source in a fluorescence microscope comes from a lamphouse located at the back of the microscope, rather than a halogen bulb at the bottom. For clarity, Fig. 3.7 depicts the lamphouse on the left side to demonstrate the optical path. The excitation light generated by the lamphouse is reflected by a dichroic mirror and then passes through a filter and the objective lens before illuminating the sample. A rotating filter turret allows the selection of different filters to control the excitation wavelength. The fluorescence emitted by the sample after absorbing the excitation light is collected by the objective lens and can be captured by a camera (Retiga R6, Teledyne Photometrics) mounted on the microscope and/or observed through eyepieces, with the optical path mechanically switched by beam-splitters controlled by an optical path switch. When examining samples containing organic dye molecules, it is important to avoid prolonged exposure of the same area to the excitation light, as the high intensity can cause photo-bleaching of the dye molecules.

3.3.3 Ultraviolet-visible Spectrophotometry

Ultraviolet-visible (UV-Vis) spectrophotometry is a widely used quantitative analytical technique to measure how samples interact with wavelengths from the ultraviolet to beyond visible light, and the results are usually represented in terms of the absorbance spectra of the sample, measured

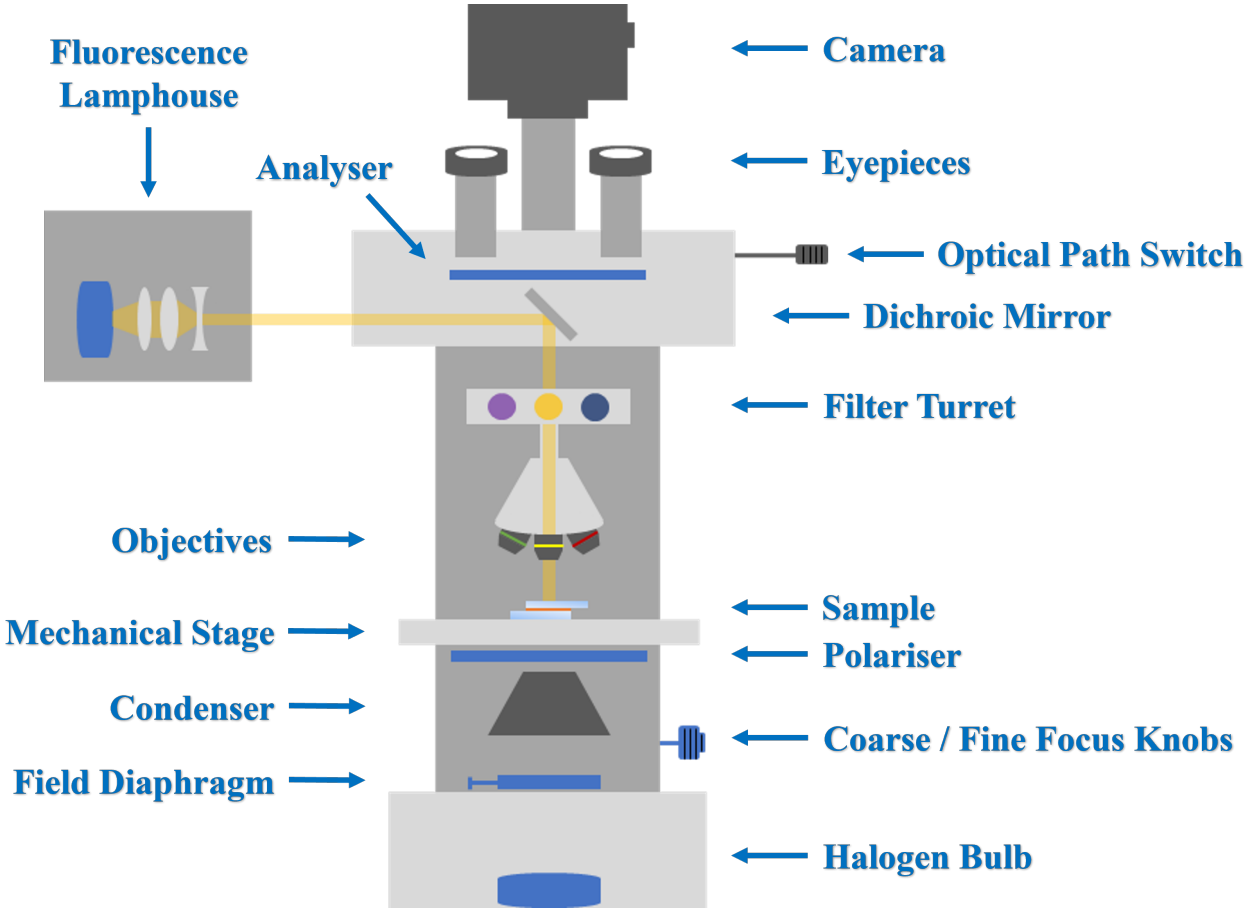

Figure 3.7: A simplified schematic of an optical fluorescence microscope where the optical path for imaging is highlighted in orange. The excitation irradiance is generated from the lamphouse and the filter before the illumination of the sample. The fluorescence image of the sample is further collected by a camera mounted at the top of the microscope or observed through the eyepieces. Additional optical and mechanical components offer adjustments to the imaging path, allowing for various excitation wavelengths and magnifications of the sample.

by comparing the intensity of light that passes through with that through a blank reference across all wavelengths. **Fig. 3.8** demonstrates the simplified configuration and the working principle of a UV-Vis spectrometer (Cary 8454, Agilent) being used in this thesis, where the illumination is provided by a combination of light sources including a tungsten-halogen lamp which generates visible to infrared light and a deuterium arc lamp that provides ultraviolet radiation.

The UV-Vis spectrometer was connected to an external PC and was operated by the corresponding software. Due to the characteristics of the light sources used, a warm-up period of approximately 20 minutes was required to achieve stable illumination, which was essential to ensure accurate measurements. The process begins with measuring the spectrum of the blank background without any sample for calibration, during which light passes through a series of lenses into the monochromator with the shutter open, which consists of a lens, a single

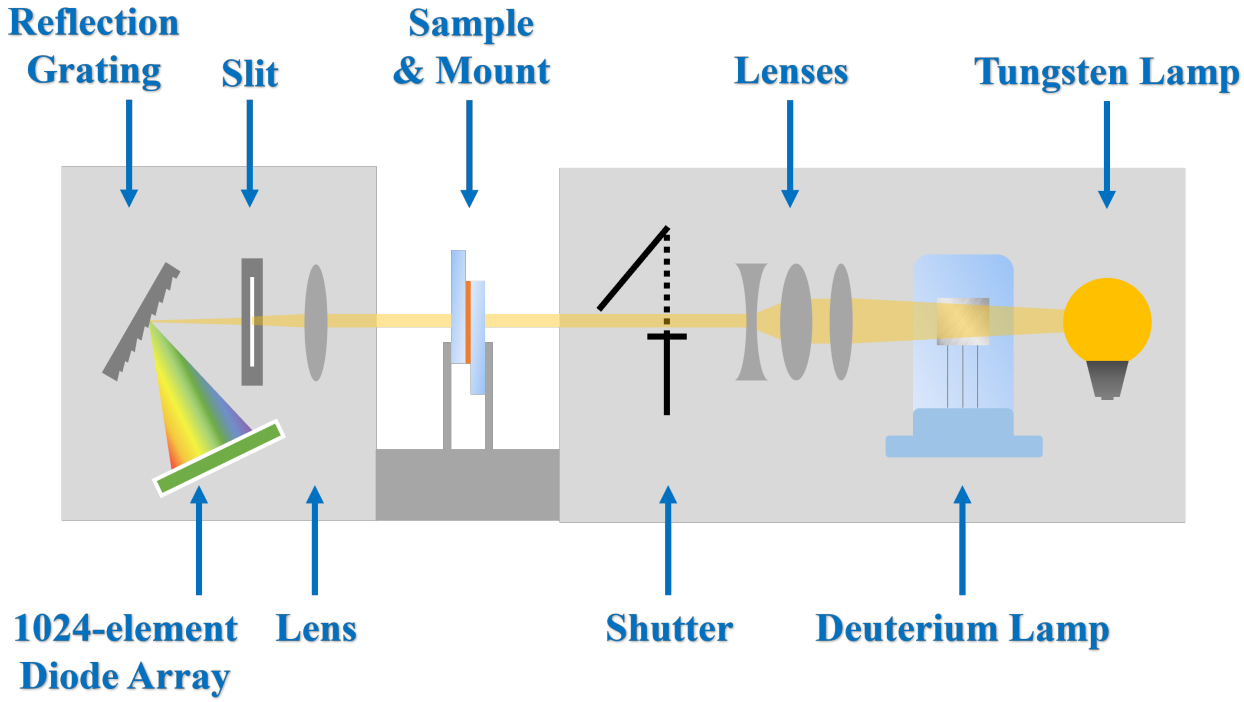

Figure 3.8: A simplified schematic of the UV-Vis spectrometer consisting of light sources, a monochromator, and a detector. The optical path is highlighted in orange. The sample absorbs some of the irradiance generated from the light sources and the transmitted light is dispersed by a reflection grating and detected by a diode array. This configuration allows for the measurement of the transmittance and absorbance spectra of the samples.

slit, and a reflection grating. The reflection grating disperses the incident light at various angles depending on the wavelength, directing it towards a diode array detector of 1024 pixels. Subsequently, the sample is placed within the system absorbing a proportion of the light leading to a change in the intensities received by the diode array. Suppose the intensities received for the blank background and the sample are $I_0(\lambda)$ and $I_s(\lambda)$, respectively, then the transmittance, $T(\lambda)$, and absorbance, $A(\lambda)$, of the sample can be given by

$$T(\lambda) = \frac{I_s(\lambda)}{I_0(\lambda)}, \quad A(\lambda) = -\log T(\lambda) \tag{3.1}$$

In addition to measuring the absorption and transmission spectra of LC samples, the UV-Vis spectrometer was also used to measure the air gap of empty glass cells based on the principle of the Fabry-Pérot interferometer. An empty glass cell can be treated as a Fabry-Pérot etalon, where the cell gap typically ranges from a few to several tens of microns. When light is incident normal to the substrate surface, it creates an interference fringe pattern, leading to wavelength-dependent variations in the transmission. In an ideal scenario, the transmittance, $T(\lambda)$, of an empty cell

with an air gap of d can be described as a function of the incident wavelength, λ, given by

$$T(\lambda) = \frac{I_s}{I_0} = \frac{1}{1 + F\sin^2(\frac{2\pi d}{\lambda})} \tag{3.2}$$

where I_s and I_0 are the transmitted and incident intensities, respectively. F is the coefficient of finesse, which is given by

$$F = \frac{4R}{(1-R)^2} \tag{3.3}$$

where R represents the reflectance of both substrates. From Eq. (3.2), it is evident that the transmittance reaches its maxima when $2\pi d/\lambda = m\pi$, where m is a positive integer. Thus, by plotting the linear relationship between m and $1/\lambda$ for the maxima in the transmittance spectrum, the slope of the resulting curve corresponds to $1/2d$, allowing for the calculation of the air gap.

To solve the relationship equation involving the two unknown variables, d and m, in practical experiments, the transmittance spectrum of an empty cell was first measured using the UV-Vis spectrometer, as shown in **Fig. 3.9**(a) for an empty anti-parallel rubbed cell sourced from LG Displays, which was used to fabricate LC lasers in the experiments discussed in this thesis. Then, consecutive maxima, $\lambda_1, \lambda_2, ..., \lambda_N$, were selected in an increasing sequence such that

$$\frac{1}{\lambda_1} - \frac{1}{\lambda_{m+1}} = (-\frac{1}{2d})m, \quad m \in 1, 2, ..., N-1 \tag{3.4}$$

Finally, a linear regression was applied to the points with coordinates $(m, \frac{1}{\lambda_1} - \frac{1}{\lambda_{m+1}})$ using a MATLAB code, as shown in Fig. 3.9(b). The gradient of the regression line corresponds to $-1/2d$, from which the air gap is calculated to be 8.06 µm.

3.3.4 USB Spectrometer

The UV-Vis spectrometer (Agilent) has a limitation in that it can only be applied to measure the transmittance or absorbance spectra of free-standing samples. In contrast, USB spectrometers offer advantages due to their lightweight and portable design, allowing them to be integrated into optical systems to measure the wavelength components of any incident light coupled through a fibre. **Fig. 3.10** illustrates the component structure of a typical USB spectrometer (USB2000, Ocean Optics). The incident light is coupled into a fibre connected to the fibre mount on the spectrometer, and then reflected by a mirror and dispersed by a reflection grating. The

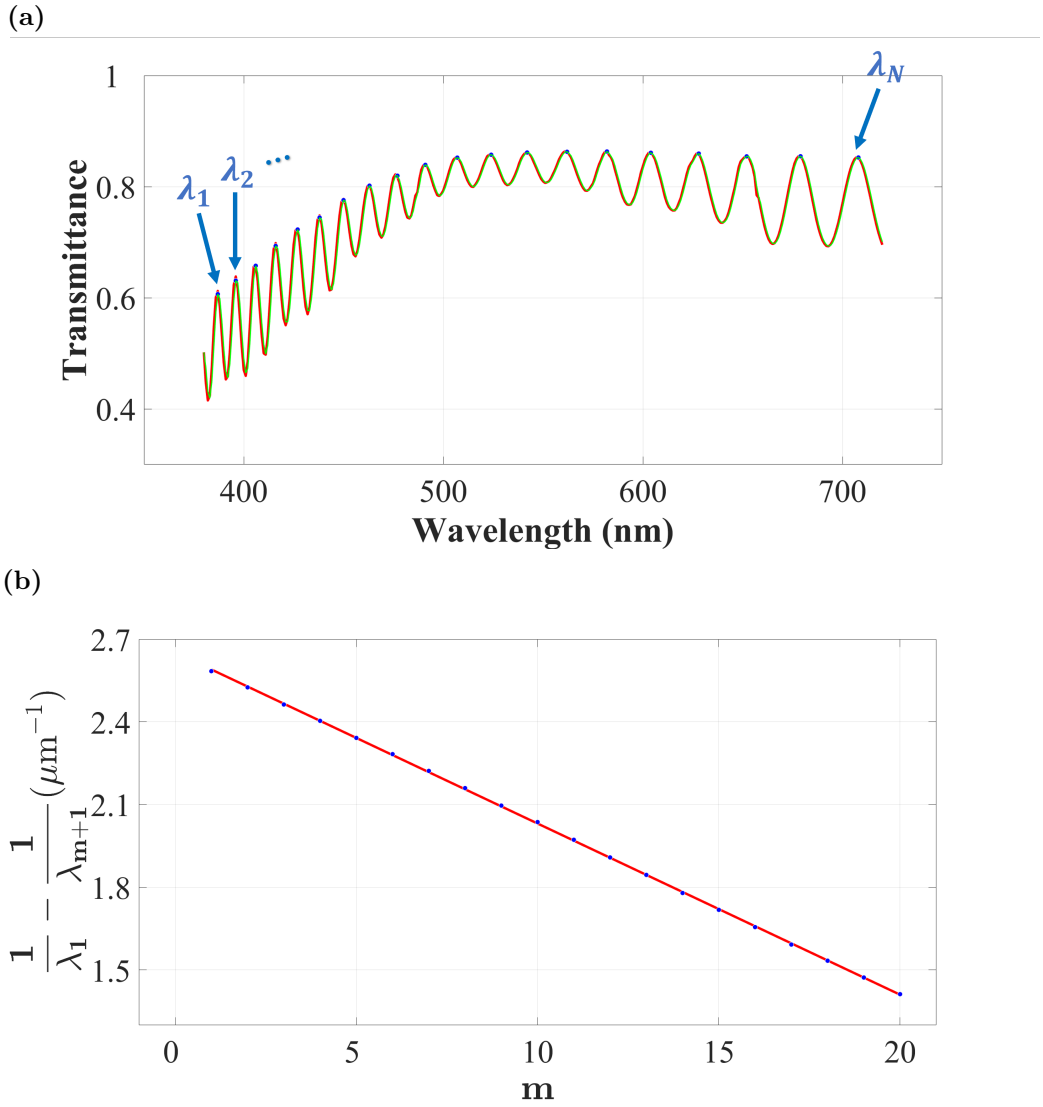

Figure 3.9: (a) The transmission spectrum of an empty anti-parallel rubbed LG cell measured by the UV-Vis spectrometer. The parallel substrates of the cell act as a Fabry-Pérot etalon, where the local maxima in the spectrum are labelled as λ_1 to λ_N. (b) The plot of $1/\lambda_1 - 1/\lambda_{m+1}$ against m where m is an integer between 1 to (N-1). The thickness of the empty cell is determined to be 8.06 µm, as calculated from the gradient of the regression line.

dispersed light is collected by another mirror and directed onto a diode array sensor, where the corresponding spectral data is processed and exported to an external PC through a USB cable.

Two types of USB spectrometers that were used in the experiments are the USB2000 and HR4000, both sourced from Ocean Optics. The USB2000 contains a 2048-element CCD array with an optical resolution of 0.3 nm, while the HR4000 is equipped with a 3648-element CCD array offering a finer optical resolution of 0.03 nm. However, the USB2000 spectrometer provides higher sensitivity, detecting up to 90 photons per count, with readout noise reported by the supplier at 3.5 counts, compared to 5 counts for the HR4000. It has been observed in experiments

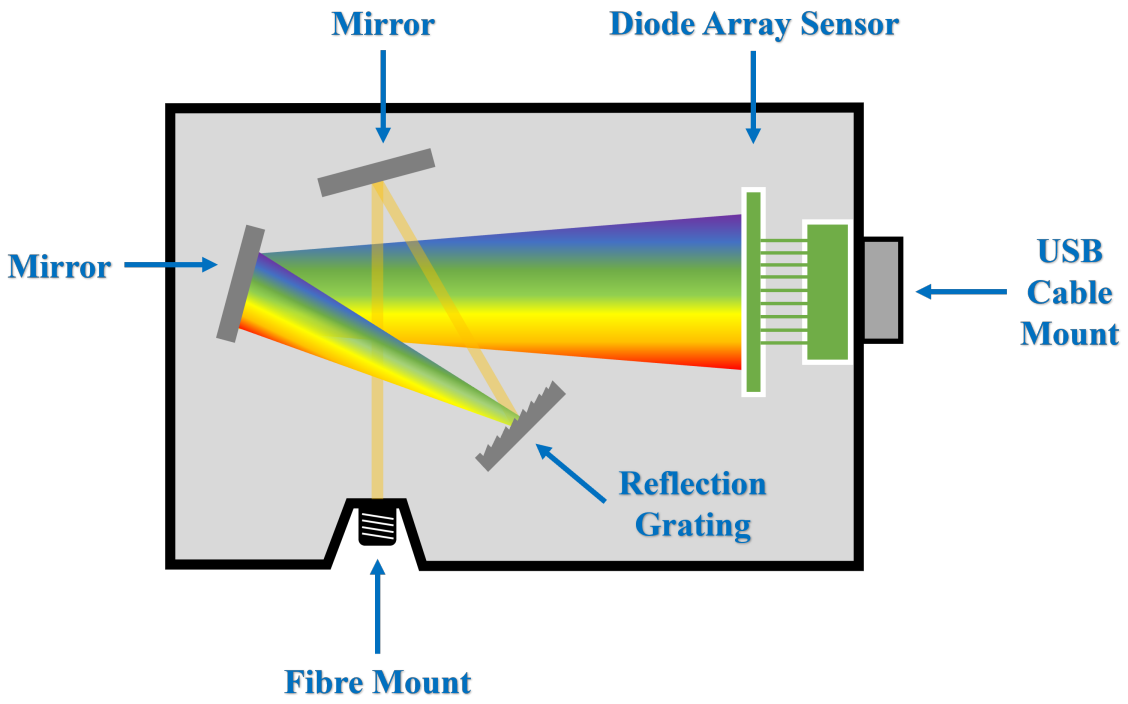

Figure 3.10: A simplified schematic of the USB spectrometer. The optical path is highlighted in orange. The incident light is coupled into a fibre and then dispersed within the spectrometer by a reflection grating. The dispersed light is detected by a diode array sensor. The spectrum of the incident light can be measured directly using the USB spectrometer and analysed on a connected PC.

that the enhanced resolution of HR4000 comes at the cost of higher noise levels and lower intensity counts, resulting in a reduced signal-to-noise ratio (SNR) compared to the same measurement taken with the USB2000. Considering the characteristics and trade-offs of the two USB spectrometers, the USB2000 was primarily utilised for measuring fluorescence emission that exhibits lower intensity and broader wavelength ranges. Its higher sensitivity makes it a desirable component for capturing weaker signals across a wide spectral range. In contrast, the HR4000 was predominantly used for measuring laser emission, which typically have significantly higher peak intensities and require higher resolution due to their narrow linewidth.

3.4 Nd:YAG Pump Laser

3.4.1 Laser Beam Profile

The LC lasers studied in this thesis were optically pumped using a nanosecond pulsed Nd:YAG laser (CryLas 6FTSS355-Q4-S) operating with doubled frequency. The pulse width of this laser is reported to be less than 1.4 ns, with an adjustable pulse repetition rate ranging from

1 Hz to 1 kHz. The pulse energy drift was typically within 5%, although higher fluctuations have been observed in experiments when the laser was working at higher temperatures. To avoid temperature surges and unstable output power, the repetition rate of the Nd:YAG laser was usually set between 10 Hz and 100 Hz. Besides, a lower repetition rate also prevents photo-bleaching of the organic dye in the LC laser cells.

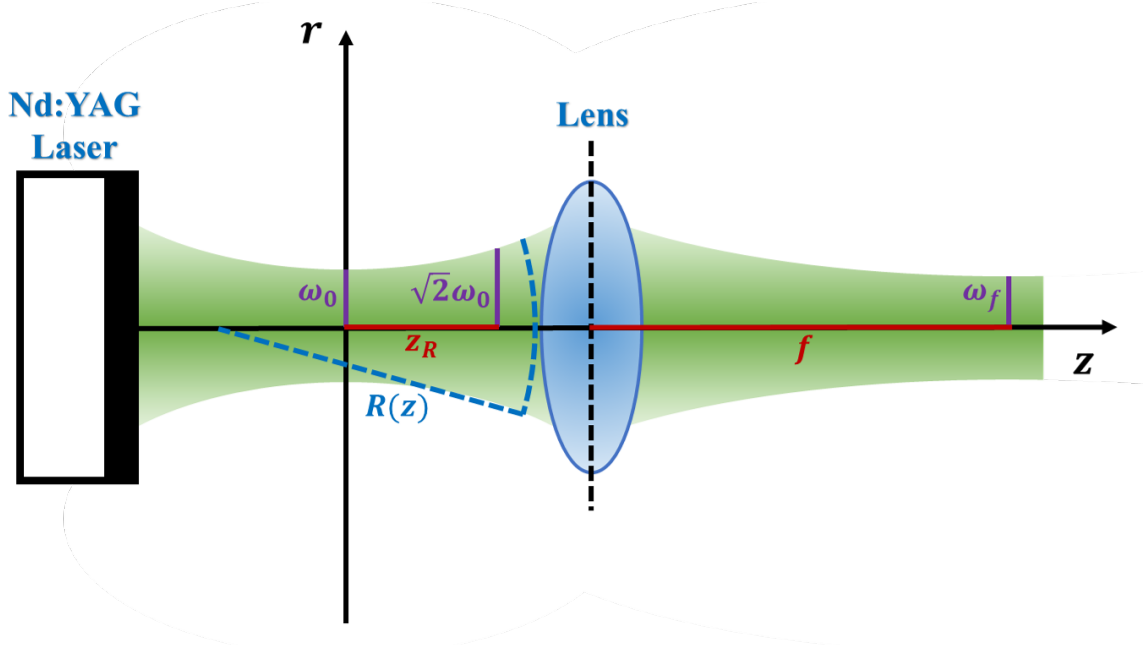

Figure 3.11: A demonstration of the Gaussian beam generated from the Nd:YAG laser. The beam propagates along the z-direction with continuously varied beam width. The radius of the beam waist, ω_0, the Rayleigh length, z_R, the focal length of the lens, f, and the beam radius at the focus are illustrated on the figure. Gaussian beams cannot be perfectly collimated, but an approximately parallel propagated beam can be generated using an appropriate lens.

The Nd:YAG laser can be regarded as an approximate Gaussian beam source where the irradiance follows a Gaussian distribution, resulting in a beam profile that is centrally symmetrical with the highest intensity at the beam centre, as shown in **Fig. 3.11**. Near the optical axis, the Gaussian beam can be approximately considered a non-uniform Gaussian spherical wave, exhibiting spherical equiphase surfaces with continuously varying centres and radii of curvature during propagation. As illustrated in Fig. 3.11, a Gaussian beam converges at the beam waist at $z = 0$ with a radius of ω_0 and subsequently diverges. The beam radius along the propagation direction, $\omega(z)$, and the corresponding radius of curvature of the wavefront, $R(z)$, can be expressed as

$$\begin{cases} \omega(z) = \omega_0 \sqrt{1 + (\frac{z}{z_R})^2} \\ R(z) = z[1 + (\frac{z_R}{z})^2] \end{cases} \tag{3.5}$$

where ω_0 is the radius of the beam waist and z_R is the Rayleigh length given by $\pi\omega_0^2/\lambda$, representing the distance from the beam waist to the point where the beam radius reaches $\sqrt{2}\omega_0$. Gaussian beams cannot be perfectly collimated, but it is possible to approximate one using lenses to minimise divergence. Within the range $-z_R < z < z_R$, the Gaussian beam can be approximately considered as propagating parallel, maintaining a relatively consistent beam radius. This quasi-collimated range of the Gaussian beam is also represented by the confocal parameter, which is equal to $2z_R$.

The intensity of the Nd:YAG laser in free space follows a Gaussian distribution across the wavefront, which can be expressed in the coordinate system $\{\mathbf{r}, \mathbf{z}\}$, illustrated in Fig. 3.11, as

$$I(r,z) = I_0(\frac{\omega_0}{\omega(z)})^2 \exp -\frac{2r^2}{w^2(z)} = \frac{2P_0}{\pi\omega^2(z)} \exp -\frac{2r^2}{w^2(z)} \tag{3.6}$$

where I_0 is the maximum intensity at the centre of the beam ($r = 0$), and P_0 is the total power of the laser beam. When a lens with a focal length of f is placed after the Nd:YAG laser, as shown in Fig. 3.11, the radius of the beam waist afterwards, ω_f, becomes

$$\omega_f = \frac{\lambda f}{\pi\omega_0} \tag{3.7}$$

3.4.2 Knife-edge Measurement Method

Due to the approximate Gaussian distribution of the Nd:YAG laser intensity in free space, a common method to identify its beam diameter is by defining the beam edge where the intensity falls to $1/e^2$, which corresponds to 13.5% of the maximum intensity, I_0. In practical experiments, a knife-edge method [144] was employed to measure the laser beam waist diameter, as illustrated in **Fig. 3.12**. The laser beam was focused by a lens with a focal length of 75 mm after passing through a variable neutral density filter and an iris diaphragm. A knife blade was mounted on a two-dimensional translation stage equipped with micrometres in both the x- and z-directions, allowing precise positioning of the blade at the beam waist. The blade edge was gradually displaced across the laser beam, progressively blocking a portion of the beam during the movement. The energy of the remaining beam was measured by a pyroelectric energy meter (PE9-ES-C, Ophir), and the results were plotted as a function of the x-position of the blade, as demonstrated in **Fig. 3.13**(a).

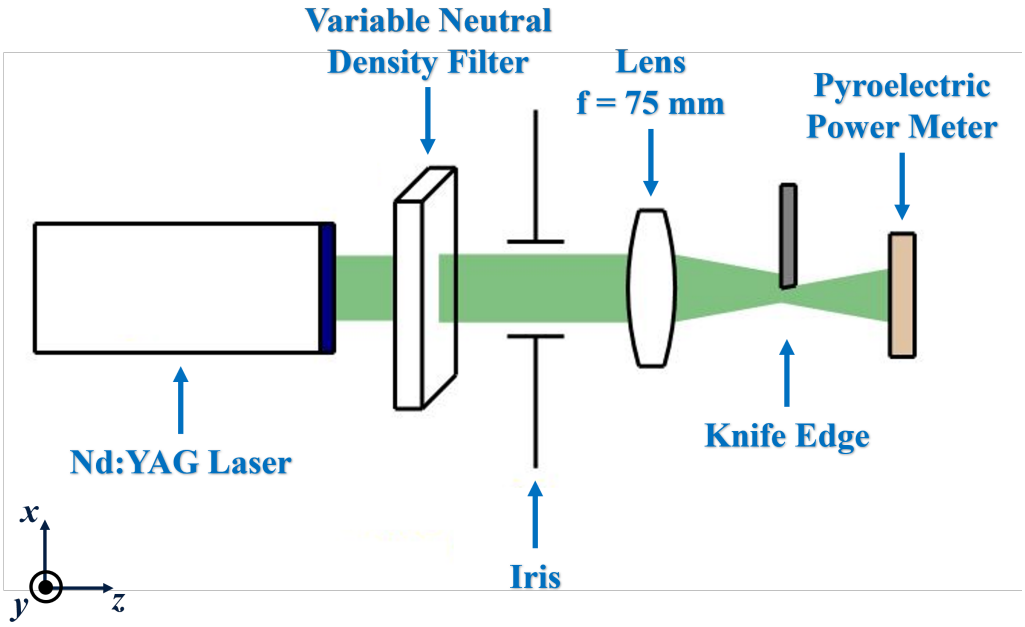

Figure 3.12: The system configuration for measuring the diameter of the Nd:YAG laser beam waist using the knife-edge method. The knife blade is mounted on a two-dimensional translation stage equipped with micrometres. The laser energy received by the pyroelectric power meter is recorded as a function of the x-position of the knife blade, leading to the calculation of the beam diameter.

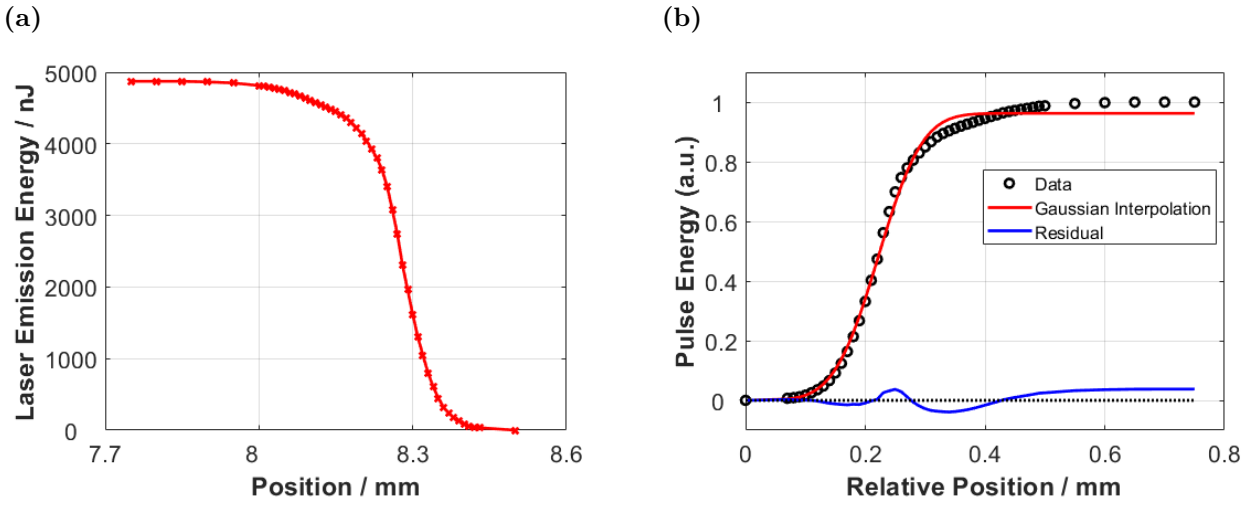

Figure 3.13: The measurement results of the diameter of the Nd:YAG laser beam waist (a) The laser energy received by the pyroelectric power meter is plotted as a function of the knife blade position during its displacement across the beam. (b) A Gaussian interpolation is subsequently applied to the energy-position curve. The beam diameter is then calculated to be 0.232 ± 0.052 mm by determining the distance between the 2.3% and 97.7% energy levels.

There are several variations of the knife-edge measurement method [145]. One such variation involves plotting and Gaussian interpolating the pulse powers received by the pyroelectric energy meter as a function of the x-position of the blade. Subsequently, the diameter of the beam waist can be determined by calculating the distance between the 2.3% and 97.7% energy levels. Fig. 3.13(b) demonstrates the Gaussian interpolation along with the corresponding residuals of the measured laser powers, where the diameter of the beam waist was determined to be 0.232 ± 0.052 mm. This method offers a precise determination of the beam waist diameter by analysing the gradual decrease in energy as the knife edge cuts through the beam, providing an accurate measurement of the Gaussian beam profile.

3.5 Band-edge LC Lasers

3.5.1 Fundamentals

As illustrated in the previous chapter, band-edge LC laser cells can be fabricated by doping chiral additives and organic dyes into LCs. Lasing occurs under appropriate optical pumping when the fluorescence spectrum overlaps with the photonic bandgap (PBG). One type of band-edge LC laser is the dye-doped chiral nematic LC laser. If right-handed chiral dopants, such as BDH1281, are added to the LC, the director rotates to form a right-handed helical structure, as depicted in **Fig. 3.14**.

According to the transmission eigenmode solution of Maxwell's equations, the incident Nd:YAG laser must be modulated to left circular polarisation to propagate through the cell effectively to avoid unwanted losses due to reflection from the chiral nematic LC PBG, providing optical pumping to achieve population inversion. The dye molecules, such as DCM, align with the rotation of the director due to the guest-host effect [146]. Theoretically, the LC laser emission is inherently right circularly polarised due to the right-handed helical structure. However, several researchers have reported observing imperfect circular polarisation in the emission [147–150]. A detailed discussion of the polarisation state of this type of LC laser will be introduced in Chapter 4.

The following sections illustrate the step-by-step preparation of band-edge LC lasers, including material preparation and characterisation. The subsequent demonstration includes the fluorescence and laser emission from dye-doped chiral nematic LCs.

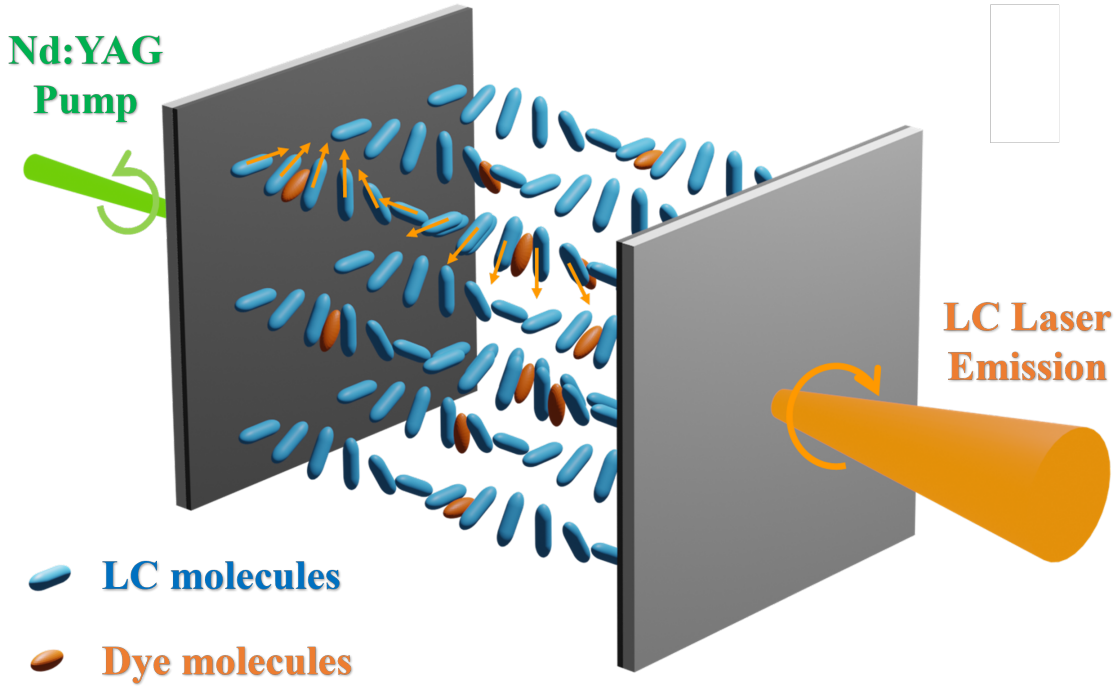

Figure 3.14: The configuration of a band-edge LC laser cell filled with dye-doped chiral nematic LCs. The director rotates to form a right-handed helical structure because of the addition of right-handed chiral additives. The dye molecules align with the orientation of the director according to the guest-host effect. The Nd:YAG pump source needs to be adjusted to be left-circularly polarised in this case so as to propagate through the cell and achieve population inversion. Ideally, the LC laser emission is right-circularly polarised due to the right-handed helical structure.

3.5.2 Material Preparation

For the fabrication of chiral nematic LCs, a few milligrams of chiral dopant was first added to an empty vial and weighed using a precision balance (AB104-S, Mettler Toledo), following the experimental procedures illustrated in Fig. 3.3. The amount of nematic LC required was then calculated based on the desired concentration and added to the vial using a pipette. In the experiments described in this chapter, the chiral dopants employed have a high twisting power, and approximately a few percent of the total weight for their concentration was required. The mixtures were then placed in an oven at 70°C for several hours, typically overnight, to ensure that the chiral dopant was fully dissolved and uniformly mixed with the nematic LC host, forming a chiral nematic LC phase.

The fabrication process for dye-doped nematic LCs followed a similar procedure. Based on the experiments reported by Mowatt et al. [77], the dye concentration was optimised and set at 1 percent of the total weight. Dye powder was first added to an empty vial, followed by

the corresponding proportion of nematic LC. The mixture was then placed in the oven under the same conditions (70°C, overnight). The process for making a dye-doped chiral nematic LC mixture was identical, except for an additional step of adding the chiral dopants to the vial before the nematic LCs. The materials and mixtures prepared and studied in this chapter are listed in **Table 3.1**, including four chiral nematic LC mixtures, one dye-doped nematic LC mixture, and one dye-doped chiral nematic LC mixture. The mixtures were capillary filled into Instec cells with thicknesses of 5 µm and 20 µm, depending on the experiment.

Table 3.1: The LC mixtures prepared and studied in the subsequent experiments.

Sample Category	Mixture Composition
Chiral Nematic LC Host	E7 + 4.2 wt.% BDH1281 E7 + 4.0 wt.% BDH1281 E7 + 3.6 wt.% BDH1281 E7 + 3.4 wt.% BDH1281
Dye-doped Nematic LC	E7 + 1 wt.% DCM
Dye-doped Chiral Nematic LC	E7 + 2.5 wt.% R5011 + 1 wt.% DCM

3.5.3 Chiral Nematic LC Hosts

As described in the previous chapter, chiral nematic LCs possess a macroscopic helical structure and exhibit a PBG when the pitch of the helix is of the same order as the wavelength of the incident light. This PBG prevents the propagation of certain frequencies with circular polarisation that matches the handedness of the helix. To achieve LC laser emission, the concentration of the chiral dopant in the nematic LCs must be carefully selected so that the PBG overlaps with the emission spectrum of the laser dye.

As Eq. (2.35) illustrates, the two band-edges blue shift (to shorter wavelengths) when the pitch is decreased, and the width of the PBG is also reduced due to $\Delta\lambda = \Delta n \cdot P$. To demonstrate how the concentration of the chiral dopant affects the frequency of the PBG and to identify the most suitable concentration for band-edge LC lasers, four mixtures with different concentrations of BDH1281 doped into a nematic LC, E7, were prepared: 4.2 wt%, 4.0 wt%, 3.6 wt%, and 3.4 wt%. All four mixtures were capillary filled into 5 µm anti-parallel rubbed Instec cells. Their transmittance spectra at room temperature were measured using the UV-Vis spectrometer (Cary 8454, Agilent), and the results are shown in **Fig. 3.15**.

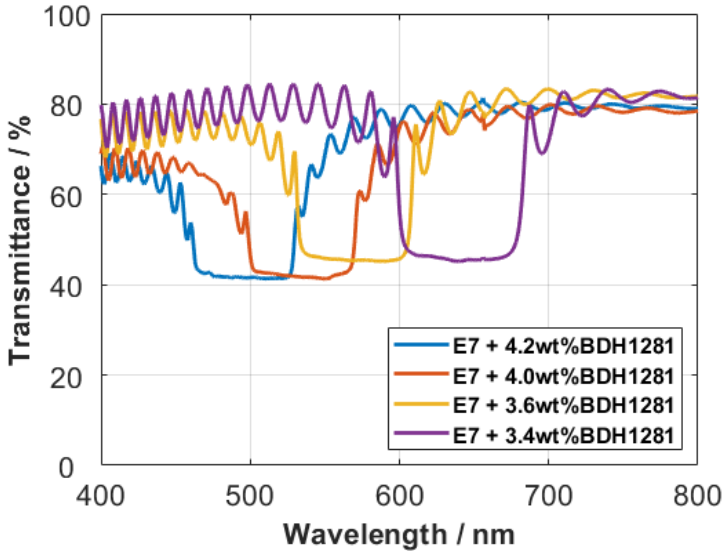

Figure 3.15: The transmittance spectra of four different chiral nematic LC mixtures measured by the UV-Vis spectrometer. Higher concentrations of the chiral additive result in shorter pitches and PBGs with shorter wavelengths. The LC layer thickness was 5 µm and measurements were conducted at a room temperature of 20°C.

The laser dye chosen for this study was DCM, which has a fluorescence emission peak around 590 nm. Consequently, a concentration of 3.6 wt% BDH1281 was identified as the optimal choice because its long-wavelength band-edge is closest to 590 nm, as indicated by the transmission spectra in Fig. 3.15. For further LC laser fabrication, a chiral nematic LC host comprising E7 + 3.6 wt% BDH1281 was utilised.

3.5.4 Dye-doped Nematic LCs

The optical properties of an organic laser dye, such as DCM, can be studied by doping it into a nematic LC host, E7. It has been verified that, in dye-doped nematic LCs, low concentrations by weight of a dye do not adversely affect the alignment of the LC [151], and more interestingly,the dye molecules tend to align with the LC director. For example, a homogeneous nematic LC alignment results in the homogeneous alignment of the dye. Dye molecules also rotate with the LC director when an electric field is applied. This phenomenon is called the dye guest-host effect [146] and is illustrated in **Fig. 3.16**.

An inductance-capacitance-resistance (LCR) meter (4284A, Agilent) was used to measure the capacitance of an empty 5 µm Instec cell, C_0, and another identical cell filled with E7 + 1 wt.% DCM. The capacitance measurement of a dye-doped nematic LC cell can also

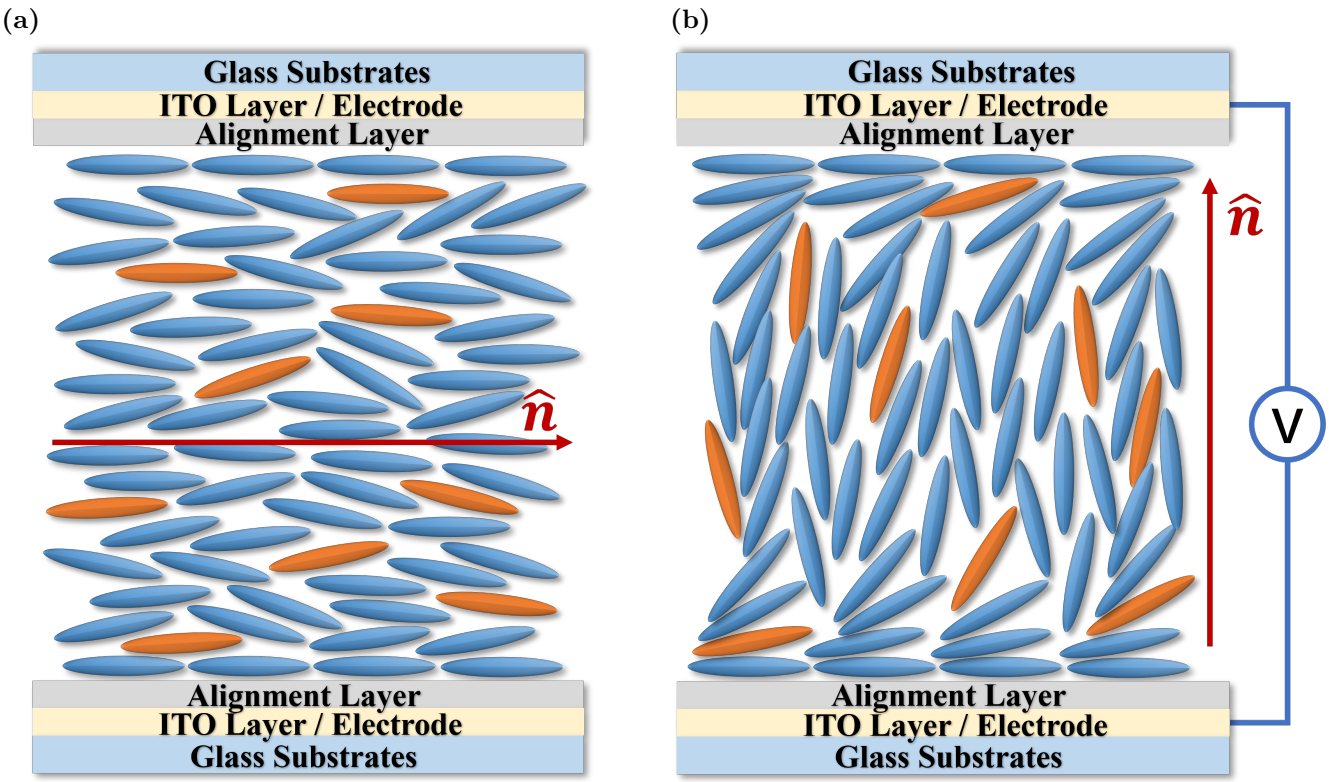

Figure 3.16: The guest-host effect in dye-doped nematic LCs where the dye molecules align with the orientation of the director. In experiments when a dye-doped nematic LC with a positive dielectric anisotropy is filled into a glass cell with ITO layers and alignment layers, it can adopt (a) a homogeneous alignment naturally or (b) a pseudo-homeotropic alignment under an electric field across the cell with appropriate applied voltage. The orientation of the molecules at the substrates are always anchored by the alignment layers.

demonstrate what the alignment is inside. The relationship between the capacitance of the dye-doped nematic LC cell, C_r, and the relative permittivity of the mixture filled between the substrates, ϵ_r, can be given by

$$C_r = \epsilon_0 \epsilon_r \frac{A}{d} \tag{3.8}$$

where ϵ_0 is the permittivity of free space, A is the surface area and d is the thickness of the cell. This equation indicates that the capacitance of the filled cell divided by that of the empty cell, $C_0 = \epsilon_0 A/d$, equals the relative permittivity of the filled mixture, ϵ_r.

The relative permittivity of the filled mixture was measured as a function of the applied voltage, with the results shown in **Fig. 3.17**. The relative permittivity increases with the applied voltage because the LC has a positive dielectric anisotropy ($\epsilon_{\parallel} > \epsilon_{\perp}$). Besides, the curve rises significantly slower when the voltage reaches 20 Vpp, indicating the dye-doped nematic LC was changed from a homogeneous alignment and approached a homeotropic alignment as the

applied voltage gradually increased. This observation is consistent with the optical textures of a nematic LC cell demonstrated in the previous chapter, where Fig. 2.4(i) shows that the cell appears almost dark on a polarising optical microscope. Note that birefringence is zero for ideal homeotropic alignment, therefore an electric field with an applied voltage of 20 Vpp is enough for this sample to be tending towards a homeotropic alignment.

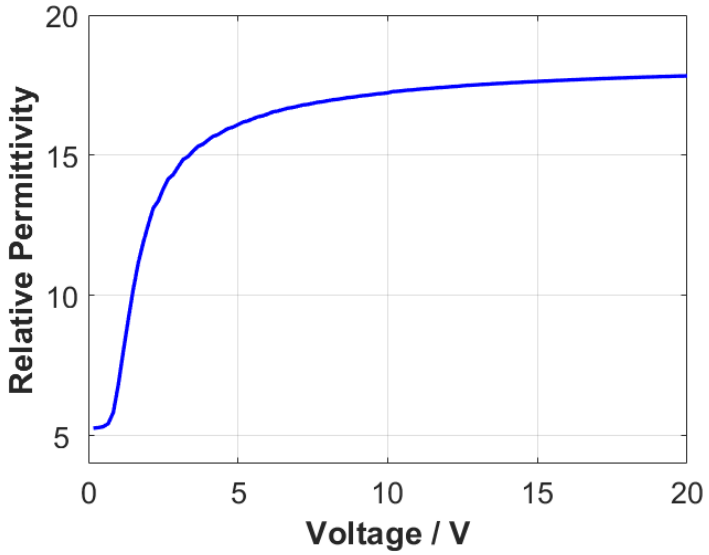

Figure 3.17: The relative permittivity measurement of a dye-doped nematic LC, E7 + 1 wt.% DCM, shows that the relative permittivity increases with the applied voltage. This suggests a continuous rotation of the director, transitioning from a homogeneous alignment to a pseudo-homeotropic alignment. The significant reduction in the gradient of the curve at 20 Vpp indicates that a pseudo-homeotropic alignment is achieved for this cell under an electric field with an applied voltage of 20 Vpp. The LC layer thickness was 5 µm and measurements were conducted at a room temperature of 20°C.

Since the dye absorption for incident polarisation perpendicular to the director is typically lower than that parallel to the director, the homogeneous alignment of a dye-doped nematic LC generally exhibits lower transmittance compared to a homeotropic alignment when the incident light is linearly polarised parallel to the director. This characteristic of the dye-doped nematic LCs provides a demonstration of the guest-host effect, where a mixture of E7 and 1 wt.% of DCM was capillary filled into a 5 µm anti-parallel rubbed Instec cell.

The absorbance parallel and perpendicular to the LC director can be approximately determined by using a linear polariser in conjunction with the UV-Vis spectrometer. This setup involves placing the polariser between the shutter and the sample, as shown in Fig. 3.8, and applying an electric field to the LC cell to manipulate the orientation of the director and the guest dye molecules. To determine the absorbance parallel to the director, the polariser was

first rotated to various angles until the maximum absorption was observed by the spectrometer, ensuring the polariser orientation aligned with the LC director. With this alignment, the absorbance spectra were measured both with and without the application of an electric field generated by a 20 Vpp voltage. The resulting spectra, presented in **Fig. 3.18**, reveal that the absorption of the dye reaches its maximum at 478 nm and significantly diminishes beyond 600 nm.

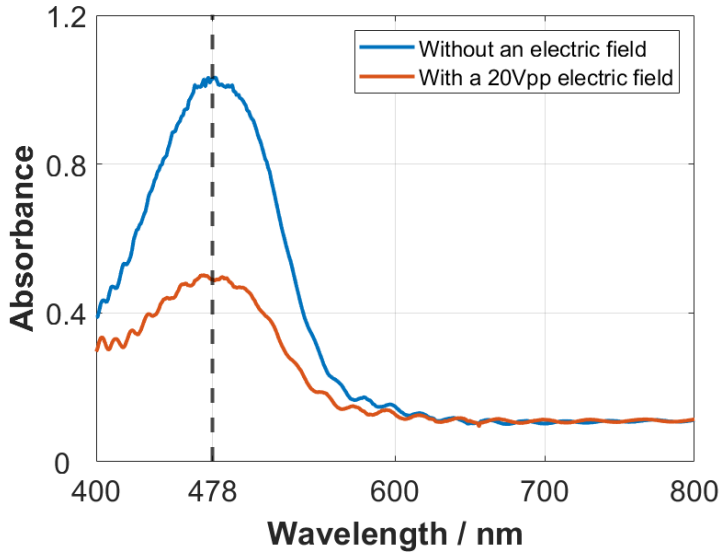

Figure 3.18: The absorption spectra of a dye-doped nematic LC, E7 + 1 wt.% DCM, were measured with and without an applied electric field of 20 Vpp. The results suggest that the absorption component of the dye perpendicular to the director is lower than that parallel to it. The incident light from the spectrometer was linearly polarised parallel to the director of the homogeneously aligned LCs. The absorption peak of the dye was observed at 478 nm, with a significant reduction above 600 nm. The LC layer thickness was 5 µm and measurements were conducted at a room temperature of 20°C.

The order parameter of the transition dipole moment of the dye in the nematic host, S_T, describes how well the dye molecules are aligned with the LC host. S_T can be defined by the following formula:

$$S_T = \frac{A_{\parallel} - A_{\perp}}{A_{\parallel} + 2A_{\perp}} \tag{3.9}$$

where $A_{\parallel}$ is the peak absorbance of the dye when the polarisation direction of incident light is parallel to the director (homogeneous alignment, without electric field), and $A_{\perp}$ is the peak absorbance of that perpendicular to the director (approximate homeotropic alignment, applied with 20 volts peak-to-peak). The value S_T ranges from 0 for complete disorder to 1 for complete order.

The spectra in Fig. 3.18 show that the cell reaches its absorption peak at 478 nm where $A_{\parallel}$ equals 1.06, $A_{\perp}$ equals 0.42, and S_T equals 0.32. A previous study has shown that the typical value

of S_T for the same dye and LC combination is 0.45 [152] which is higher than the experimental result presented here; however, these results demonstrate that the dye molecules have aligned well with the LC director. The difference in the value for S_T between the results presented here and the literature is perhaps expected as a perfect homeotropic alignment of the LC director was not obtained in the results presented above, which is due to the alignment layers on the substrates. For a more accurate measurement, the same mixture should be filled into a cell of the same thickness with homeotropic alignment layers so that a homeotropic alignment is formed.

For dyes such as DCM, fluorescence and absorption were observed. Since the sample shows the highest absorbance at 478 nm, blue light would be a good choice as the incident source so as to excite the dye-doped nematic LC sample. **Figure 3.19** shows examples of the fluorescence images recorded on a polarised fluorescence microscope (Axioplan2, Zeiss) equipped with a CCD camera (PL-B686CU, PixeLINK) with and without the electric field. A Stokes shift was observed when the dye molecules were excited by the blue incident light, and they produced an orange-coloured fluorescence. The left regions of the fluorescence images in Fig. 3.19 correspond to the area where an electric field was applied to the cell, while the right regions correspond to the area filled with dye-doped nematic LC but without electrodes. The left regions in Fig. 3.19(b) and Fig. 3.19(d) are darker than those in Fig. 3.19(a) and Fig. 3.19(c), respectively. This is because the component of the fluorescence parallel to the LC director is larger than that of the perpendicular component. Figure 3.19(e) and Fig. 3.19(f) show much darker images since the polariser is placed orthogonal to the director.

To measure the fluorescence spectrum from the dye-doped nematic LC sample, a fluorescence spectrometer system was assembled, as shown in **Fig. 3.20**. In this setup, the light emitting diode (LED) emission was coupled into a fibre and focused onto the LC cell using a lens with a focal length of 25.4 mm. The LC cell was positioned at an angle relative to the optical axis of the incident light, taking advantage of a non-coaxial optical system. This configuration effectively separated the excitation light from the fluorescence emission, preventing the spectrometer from capturing the incident light. To be specific, the excitation light passed directly through the sample along the incident optical axis, while the fluorescence emission from the sample, which is omnidirectional and always parallel to the helical axis of the LCs, was collected at an angle. The fluorescence emission was then gathered by a lens with a focal length of 35 mm and coupled

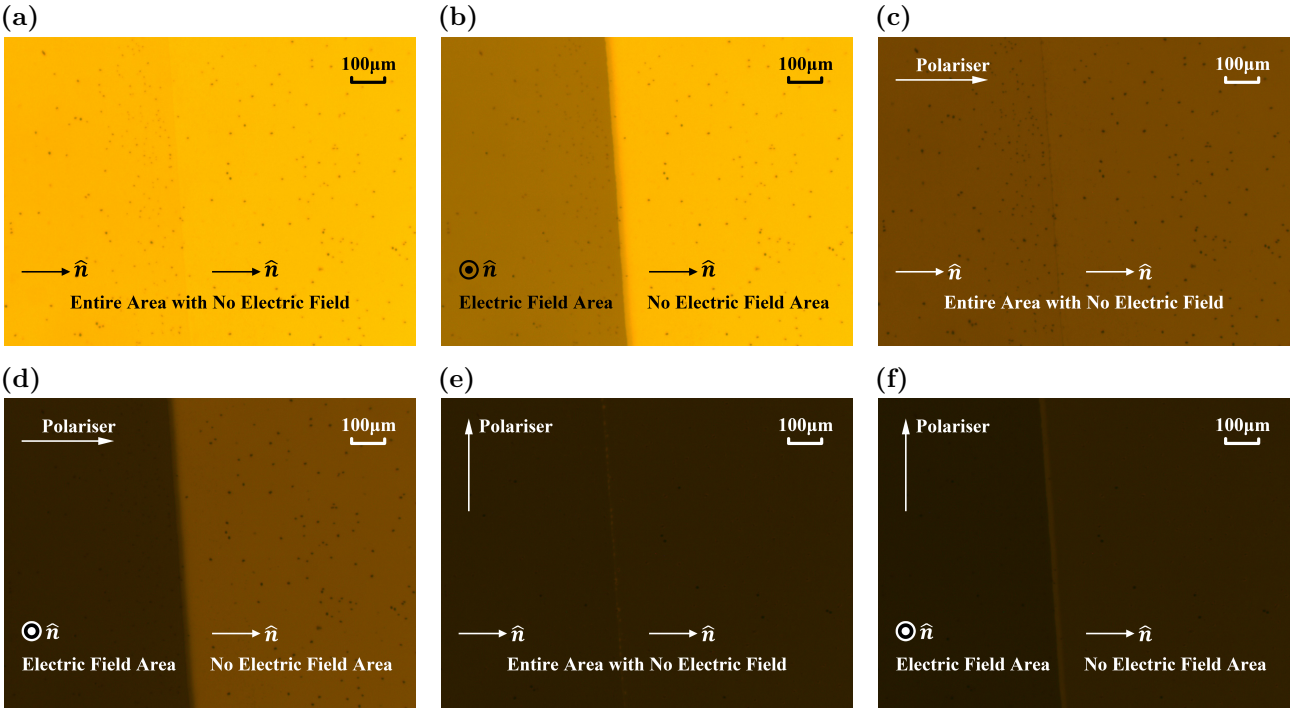

Figure 3.19: A dye-doped nematic LC cell, E7 + 1 wt.% DCM, with and without a polariser and an electric field was observed on an optical fluorescence microscope and a CCD camera. The observation of colour change with and without applied voltages demonstrates the guest-host effect, where the orientations of dye molecules rotate with external electric fields. The thickness of the cell was 5 µm and the observation was conducted at a room temperature of 20°C. (a) No electric field, no polariser; (b) An electric field of 20 Vpp, no polariser; (c) no electric field, a polariser parallel to the LC director; (d) An electric field of 20 Vpp, a polariser parallel to the LC director of the area with no electric field; (e) no electric field, a polariser perpendicular to the LC director; (f) An electric field of 20 Vpp, a polariser perpendicular to the LC director of the area with no electric field.

into a fibre connected to a USB spectrometer (USB2000, Ocean Optics). A polariser was placed after the LC cell to analyse the polarisation components of the fluorescence emission.

The fluorescence spectrum of the dye-doped nematic LC, E7 + 1 wt.% DCM, without a polariser, is shown in **Fig. 3.21**(a). The fluorescence emission from the cell spans approximately 500 nm to 750 nm, with a peak at 588.5 nm. When a polariser was introduced after the sample, the fluorescence component parallel to the polariser was collected. The peak intensity of the fluorescence spectrum was then plotted as a function of the angle between the polariser direction and the LC director, as shown in the polar plot in Fig. 3.21(b). The maximum intensity was observed when the polariser was aligned at 0° and 180°, corresponding to the polariser being parallel to the LC director. On the contrary, minimum intensity occurred at 90° and 270°, when the polariser was perpendicular to the director.

According to the literature, the order parameter can be equivalently defined using the same

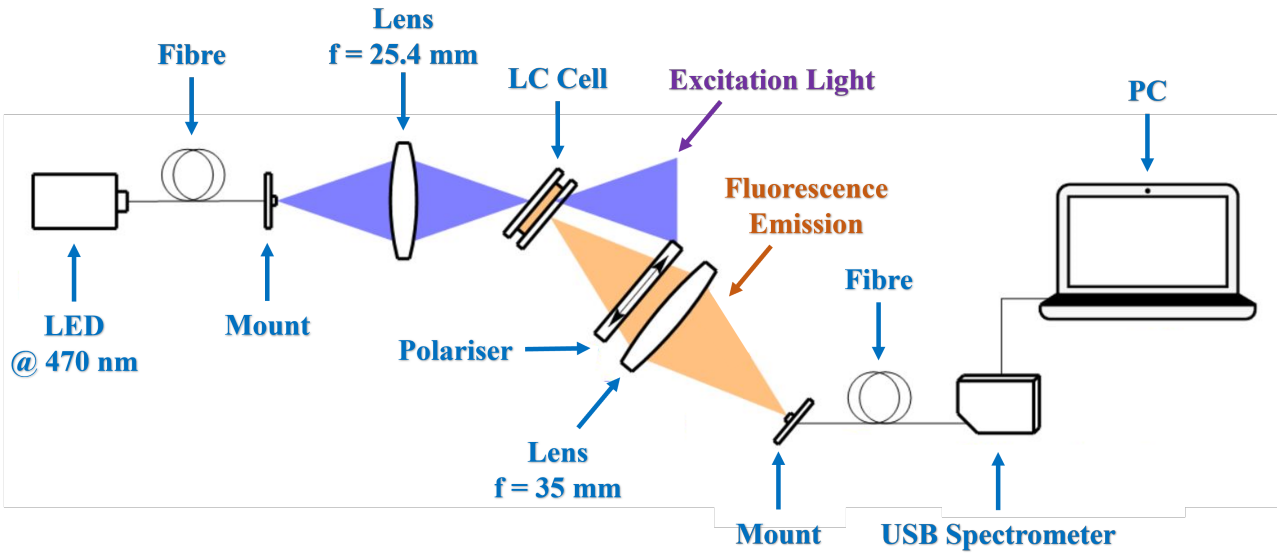

Figure 3.20: The system configuration of the fluorescence spectrometer for characterising the fluorescence emission from a dye-doped nematic LC cell, E7 + 1 wt.% DCM. The non-coaxial optical system can be achieved by rotating the LC cell by an angle so that its fluorescence emission is off-axis and the excitation light is then prevented from being collected by the USB spectrometer.

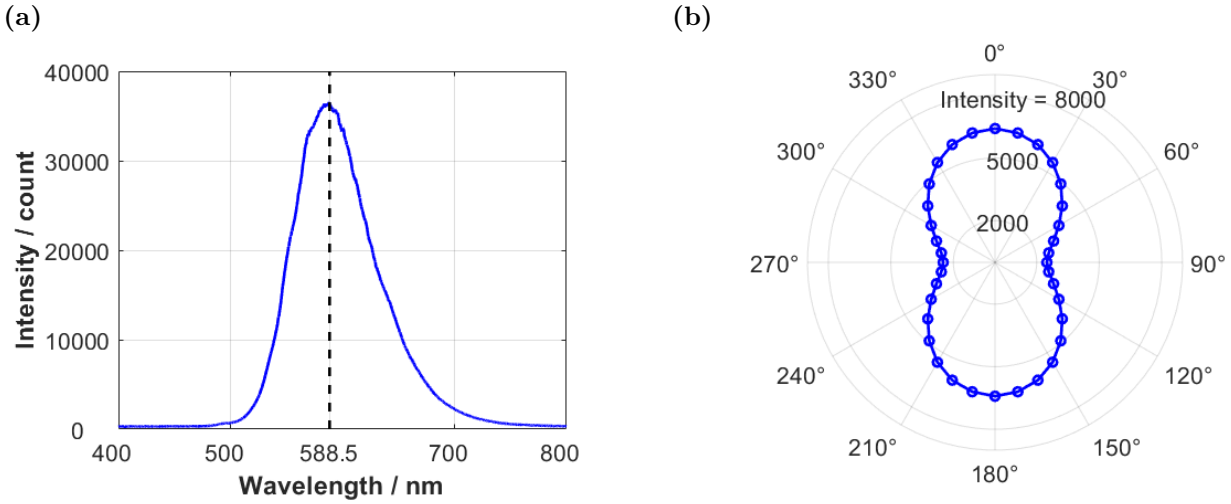

Figure 3.21: The fluorescence emission properties of a dye-doped nematic LC cell, E7 + 1 wt.% DCM. (a) Fluorescence spectrum of the cell under excitation from a 470 nm LED source, showing a fluorescence range from 500 nm to 750 nm with a centre wavelength of 588.5 nm. (b) Polar plot of peak fluorescence intensity along various polarisation directions, indicating maximum fluorescence parallel to the LC director and minimum fluorescence perpendicular to the director. The LC layer thickness was 5 µm and measurements were conducted at a room temperature of 20°C.

formulation in Eq. (2.1), substituting absorbance with fluorescence intensity [152, 153]. The fluorescence intensities for parallel and perpendicular polarisation components were measured to be 6413.74 and 2487.19, respectively, yielding an order parameter of $S_T = 0.34$. This value is in accordance with that determined from the absorbance measurements, where $S_T = 0.32$.

3.5.5 Fluorescence Emission from Dye-doped Chiral Nematic LCs

Dye-doped chiral nematic LCs combine the unique characteristics of both the dye and the chiral nematic LCs. According to a report by Morris et al [120], the optimal cell thickness for a mixture of DCM and E7 is approximately 12 µm, at which the laser threshold is minimised and the slope efficiency is maximised. In this study, a dye-doped nematic LC sample, E7 + 2.5 wt.% R5011 + 1 wt.% DCM, was prepared and initially filled into two Instec cells with thicknesses of 5 µm and 20 µm. R5011 is a similar right-handed chiral additive as BDH1281. After careful mixing and aligning, their optical textures were observed using a polarising optical microscope (BX51, Olympus), as shown in **Fig. 3.22**(a) and (b), respectively. However, these cells were found to be unsuitable, as no laser emission was observed for the 5 µm cell, and multi-mode lasing was observed for the 20 µm cell. The reason for the lack of LC laser emissions will be discussed in the next section. Consequently, another commercial glass cell sourced from LG Display was used, consisting of two glass substrates with anti-parallel rubbed polyimide alignment layers but without spacer beads distributed throughout the cell. The thickness at the centre of this cell was determined to be 8.4 µm, as shown in the measurement presented in Fig. 3.9. The optical texture of this glass cell after being capillary-filled with the same dye-doped chiral nematic LC mixture is shown in Fig. 3.22(c).

The absorption spectrum of the LG cell, with and without an electric field applied, corresponding to the optical texture shown in Fig. 3.22(c), was measured using the UV-Vis spectrometer, and the results are presented in **Fig. 3.23**(a). In the spectrum without an electric field, represented by the blue curve in Fig. 3.23(a), the wavelength range between 400 nm and 530 nm corresponds to the absorption spectra of the dye. The middle region between 530 nm and 610 nm represents the PBG that results from the LC helical structure. The absorption peak of the sample is in agreement with that measured for a dye-doped nematic LC without an electric field, as shown in Fig. 3.18; however, the absorption of the dye is overlapped by the PBG in the middle wavelength range, as shown in Fig. 3.23(a).

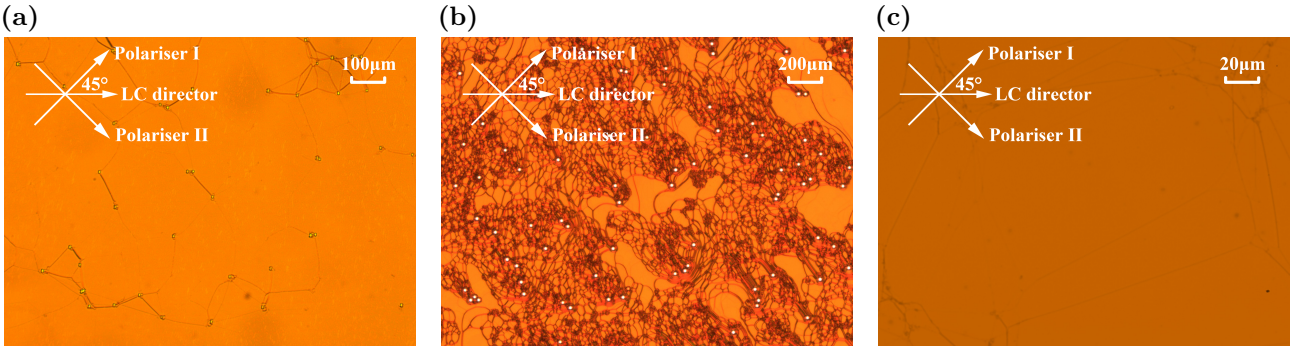

Figure 3.22: A dye-doped chiral nematic LC, E7 + 2.5 wt.% R5011 + 1 wt.% DCM, was capillary filled into several anti-parallel rubbed cells and their optical textures were observed on a polarising optical microscope and a CCD camera. The observation was conducted at a room temperature of 20°C. The mixture was filled into (a) a 5 µm Instec cell, (b) a 20 µm Instec cell with poor alignment as the spacer beads introduced defects for the alignment, and (c) an 8.4 µm LG Display cell. The first two cells were found to be inappropriate for generating LC laser emission while the third was used as the final choice.

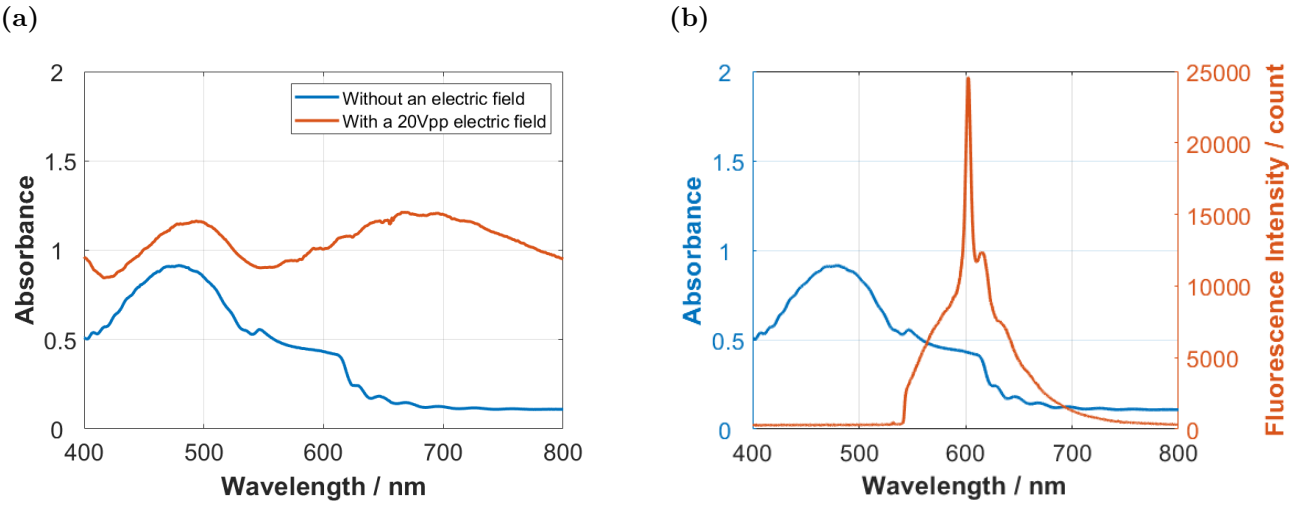

Figure 3.23: (a) The absorbance spectra of a dye-doped chiral nematic LC, E7 + 2.5 wt.% R5011 + 1 wt.% DCM, with and without an electric field generated by a voltage of 20 Vpp. The absorption of the DCM is overlapped by the PBG of the chiral nematic LCs, which can be removed by introducing an electric field to disrupt the helical structure. (b) The fluorescence spectrum of the dye-doped chiral nematic LC cell, shown by the orange curve, was measured by a fluorescence spectrometer. The fluorescence peak is located at 602.4 nm, attributed to the large photon density of states at the band-edge. The absorbance spectrum of the sample, illustrated by the blue curve, is provided for reference to the PBG. The LC layer thickness was 8.4 µm and measurements were conducted at a room temperature of 20°C.

When an electric field generated by a voltage of 20 Vpp was applied to the cell, its absorbance spectrum was measured as demonstrated by the red curve in Fig. 3.23(a). The electric field disrupts the helical structure of the LCs as it can be indicated by the disappearance of the PBG when the sample is subjected to a high voltage.

The corresponding fluorescence spectrum of the sample was measured using the fluorescence spectrometer setup shown in Fig. 3.20, and the results are presented in Fig. 3.23(b). For reference, the absorbance spectrum of the sample is also included in Fig. 3.23(b) as the blue curve. The orange curve represents the fluorescence emission spectrum of the cell. It can be observed that the fluorescence of the dye is suppressed by the PBG of the helical structure, compared to the spectrum shown in Fig. 3.21(a). The fluorescence peak is located at 602.4 nm. The fluorescence intensity at the band-edge, particularly at the long wavelength band-edge, is significantly enhanced, resulting in a much higher intensity compared to other wavelengths. This enhancement is due to the large photon density of states (DOS) at the band-edge, which provides potential gain for laser emission.

3.5.6 Laser Emission from Dye-doped Chiral Nematic LCs

Laser emission from dye-doped chiral nematic LCs occurs along the helical axis, irrespective of the optical geometry of the pump source. Typically, the glass substrates of the cell are positioned perpendicular to the incident light. In the following experiments, the LC cell being studied is a dye-doped chiral nematic LC, E7 + 2.5 wt.% R5011 + 1 wt.% DCM, housed in an anti-parallel rubbed 8.4 µm LG cell.

Laser emission can be observed using a nanosecond pulsed Nd:YAG laser as the optical pump source, with the system configuration shown in **Fig. 3.24**. The intensity of the pump beam was controlled by a variable neutral density filter, and the repetition rate was usually set at 10 Hz to prevent photo-bleaching of the dye. The Gaussian beam from the Nd:YAG laser was focused on the LC cell using a 75 mm lens, and the resulting LC laser emission was collected by a 10x objective lens and a 50 mm lens. After the LC cell was excited, the pump beam was filtered out by a long-pass edge filter, allowing only the laser emission from the sample to be collected by a mounted optical fibre connected to a USB spectrometer and a PC. If the PBG overlaps with the 532 nm wavelength of the Nd:YAG laser, an additional polariser and a quarter

waveplate working at 532 nm should be implemented to adjust the polarisation of the incident light to left circularly polarised, so as to provide effective optical pumping to the LC cell.

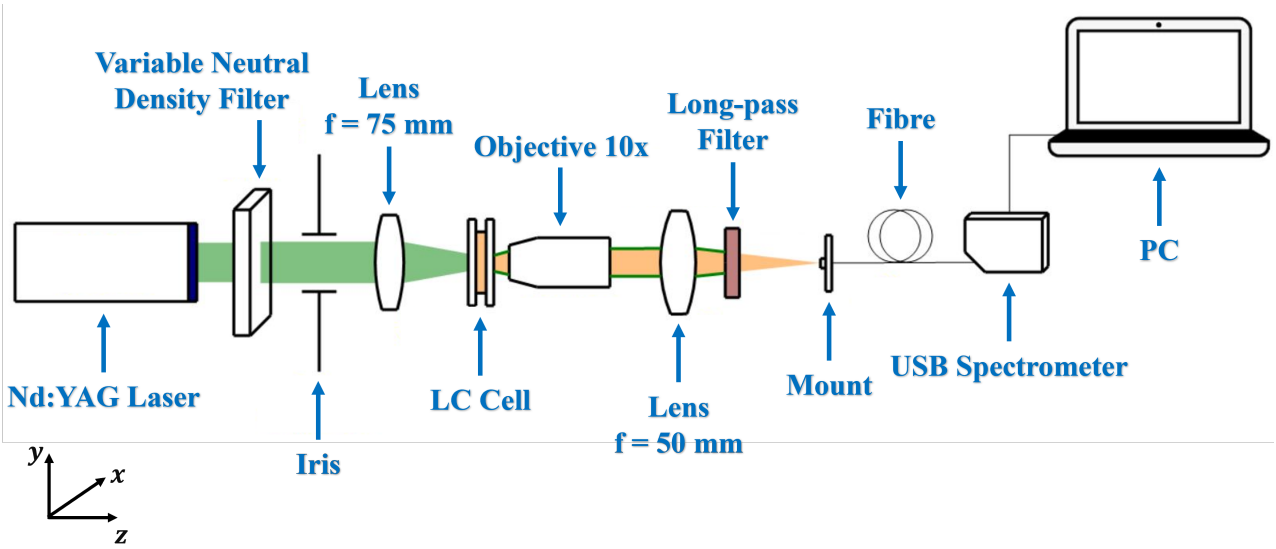

Figure 3.24: The system configuration for generating LC lasers using a nanosecond pulsed Nd:YAG laser as the pump source. The excitation light from the Nd:YAG laser was focused onto the LC cell and subsequently filtered out by a long-pass edge filter, while the laser emission from the LC cell was collected by an objective lens and a focusing lens before being coupled to a fibre and measured by a USB spectrometer.

In order to observe laser emission, the gain provided by the dye molecules has to overcome the losses. Since the gain is proportional to the concentration of dye in the mixture, a low concentration would produce no lasing, whilst a high concentration would cause aggregation and excimer formation which lowers the quantum yield. A previous report [81] claims that the lasing threshold power appears the lowest and linear in the dye concentration region from 0.25 wt.% to 2.5 wt.%. Thus, the concentration of DCM dye used here is 1 wt.% which falls into the suggested region. The report also suggests that the lasing threshold is also dependent on cell thickness and that it decreases to reach a minimum and then gradually increases while the cell thickness increases. If the cell is too thin, there will be insufficient gain resulting in no laser emission. On the contrary, if it is too thick, the alignment of the chiral nematic LC degrades resulting in unwanted scattering of light. This characteristic explains the lack of LC laser emission from the 5 µm Instec cell and the 20 µm Instec cell.

Thus, the thickness of the LC laser cell was chosen as 8.4 µm in which both the alignment is roughly uniform and the gain was sufficient to produce single-mode laser emission. The laser emission spectrum of the LC laser cell, E7 + 2.5 wt.% R5011 + 1 wt.%DCM, is shown

in **Fig. 3.25**. This band-edge LC laser has a wavelength of 605.1 nm, while the wavelength of the peak fluorescence emission in Fig. 3.23(b) is 602.4 nm. This offset is to be expected because the emitting laser mode is not exactly at the edge of the transmission spectrum for cells with finite thickness [6].

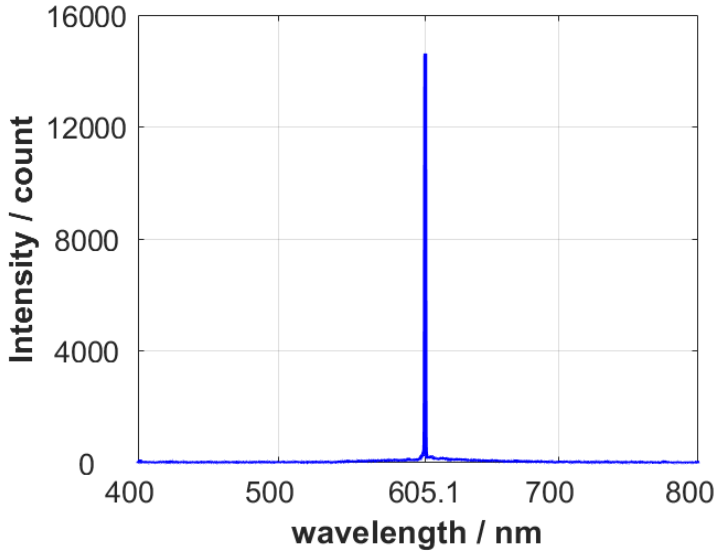

Figure 3.25: The spectrum of single-mode laser emission from a dye-doped chiral nematic LC, E7 + 2.5 wt.% R5011 + 1 wt.% DCM, excited by a 10 Hz Nd:YAG laser. The laser wavelength is 605.1 nm. The LC layer thickness was 8.4 µm and measurements were conducted at a room temperature of 20°C.

As discussed in Chapter 2, there exists an excitation threshold above which laser emission occurs. This threshold can be measured by rotating the variable neutral density filter to gradually increase the intensity of optical pumping until laser emission is observed. **Fig. 3.26**(a) presents the spectra recorded by the spectrometer for various excitation fluences of the incident Nd:YAG laser, while Fig. 3.26(b) illustrates the peak intensity of each spectrum. The excitation fluences were calculated by dividing the average pulse power of the Nd:YAG laser, measured by the pyroelectric power meter, by the beam waist area, which was determined using the knife-edge method described in Fig. 3.12.

The discontinuity in the differential when examining the output LC laser intensity as a function of the input Nd:YAG excitation fluence can be represented by two regression lines in Fig. 3.26(b), with their intersection indicating the threshold of this particular LC laser device. This threshold was found to be 671.9 µJ/cm^2/pulse. Above this threshold, lasing occurs, while only fluorescence emission can be observed below it. The threshold measured for this LC laser is lower than the typical value of approximately 1000 µJ/cm^2/pulse, as reported in the literature

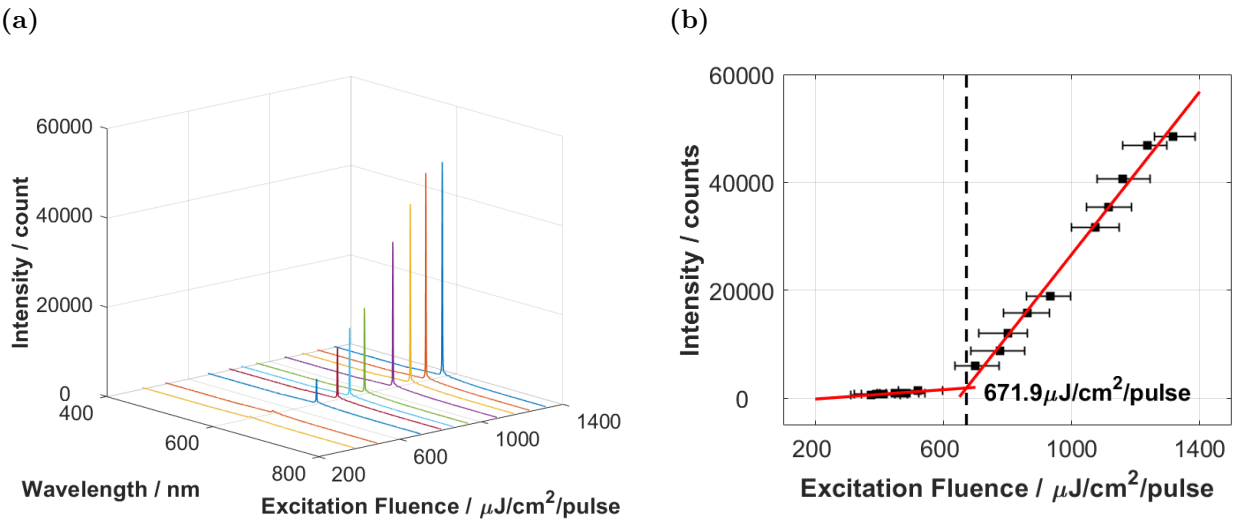

Figure 3.26: Excitation threshold measurements of a band-edge LC laser fabricated using a dye-doped chiral nematic LC, E7 + 2.5 wt.% R5011 + 1 wt.% DCM. (a) The laser emission sepctra were recorded at different excitation fluences. (b) The peak intensities of the laser emission spectra were plotted as a function of the corresponding excitation fluences. Two regression lines were applied to the data points where the intersection indicates that the excitation threshold of this LC laser is 671.9 μJ/cm^2/pulse.

[77]. This can be attributed to the shorter pulse length of the Nd:YAG laser, as research shows that pump sources with shorter pulse lengths lead to a lower lasing threshold in LC lasers [81].

3.6 Summary

In summary, this chapter has described the processes employed for preparing mixtures and fabricating LC glass cells. Typical commercial LC cells, such as the Instec cells and LG Display cells, consist of two glass substrates covered with anti-parallel rubbed alignment layers and spacers sandwiched between the substrates. LC mixtures can be capillary filled into the cell through the gaps between the spacers. Instec cells are equipped with ITO electrodes on both substrates, enabling the application of external voltages and the establishment of an electric field in the central region of the cell. Instec cells also contain spacer beads randomly distributed across the air gap to maintain uniform thickness; however, spacer beads can potentially disrupt the LC alignment, especially for thicker cells. In contrast, LG cells do not exhibit spacer beads, making them ideal devices for LC mixtures with requirements of precise alignment; for example, the LC laser cells where maintaining the homogeneous alignment of the dye-doped chiral nematic LCs is crucial for optimal cell performance.

LC cells were also fabricated by following a specific procedure. This process involved spin-coating an alignment layer onto a glass substrate, mechanically rubbing the alignment layer to achieve the desired alignment of the director, and attaching spacers to the substrate to control the cell thickness. The substrates were then assembled with UV glue, which was cured using UV light to form an empty cell. This method enabled the fabrication of LC cells with customised thicknesses, specific rubbing directions, and wedge cells with varied thicknesses, tailored to the needs of the experiment or application described later in the thesis.

Various optical characterisation techniques were employed in the experiments and investigations throughout this thesis. For instance, polarising optical microscopy and fluorescence microscopy are useful techniques for observing the optical texture and evaluating the alignment quality of LC samples. The transmission, absorption, and fluorescence emission properties of an LC cell were measured directly using a UV-Vis spectrometer, or alternatively a USB spectrometer when the LC cell was integrated into an optical system. Additionally, spectrophotometry was used for a precise measurement of the air gap in an empty cell.

The optical characteristics of chiral nematic LC hosts, dye-doped nematic LCs, and dye-doped chiral nematic LCs were investigated in detail. The concentration of chiral dopants determined the pitch and the wavelength range of the PBG. The laser dye molecules align with the director due to the guest-host effect, with an absorption peak at 478 nm for the DCM. The fluorescence emission from DCM molecules is anisotropic, with maximum intensity observed parallel to the long axis of the dye molecule. For dye-doped chiral nematic LCs, the absorbance spectrum of the dye overlaps with the PBG of the LCs, and the fluorescence peak is located at the band-edge due to the large photon density of states at that wavelength. This phenomenon provides potential gain for LC laser emission.

Band-edge LC lasers were generated using optical pumping with a nanosecond pulsed Nd:YAG laser onto a dye-doped chiral nematic LC cell when the PBG of the LC helical structure overlappedthe fluorescence spectrum of the organic dye. An LC laser was successfully achieved using an 8.4 µm LG Display cell capillary filled with a dye-doped chiral nematic LC mixture, specifically E7 + 2.5 wt.% R5011 + 1 wt.% DCM. The Nd:YAG pump source emits a Gaussian laser beam, and the diameter of its beam waist was measured using the knife-edge method. By combining this measurement with the average pulse power recorded by a pyroelectric power meter, the excitation fluence on the LC cell was calculated, which

further allows the determination of the excitation threshold and slope efficiency of the LC laser. This particular LC laser operated at a wavelength of 605.1 nm and had an excitation threshold of 671.9 µJ/cm^2/pulse. These parameters will be utilised in further studies, including an optical beam steering system discussed in Chapter 5.

4

Stokes Parameters Characterisation of Liquid Crystal Lasers

Contents

4.1 Introduction and Aims 78
4.2 Stokes Parameters Measurements and Calibration 80
4.2.1 Calibration 80
4.2.2 Stokes Imaging Polarimeter 83
4.3 Stokes Parameters of a Continuous-wave Laser 85
4.4 Stokes Parameters of a Pulsed Laser 90
4.5 Stokes Parameters of LC Lasers 93
4.5.1 Excitation Energy 96
4.5.2 LC Layer Thickness 100
4.5.3 Alignment Quality 103
4.6 Summary 105

4.1 Introduction and Aims

Controlling the polarisation of light plays an essential role in many applications, including 3D display technology, which benefits from enhanced image clarity and depth perception through polarisation control [154]. In virtual and augmented reality, polarisation manipulation is crucial for creating immersive experiences by optimising light propagation and minimising glare [155]. Polarimetric and holographic imaging leverage polarisation to improve contrast and extract additional information from observed scenes, thus enhancing image quality and detail [156, 157]. Microscopy techniques, particularly in three-dimensional imaging, utilise polarisation control to achieve higher resolution and better contrast, allowing for more precise and detailed observations

of microscopic structures [158, 159]. Furthermore, in optical communications, controlling polarisation is essential for reducing signal degradation and improving data transmission efficiency, especially in systems where birefringence and other polarisation-related issues can significantly impact performance [160, 161]. Thus, the ability to manipulate the polarisation state of light is indispensable across these diverse applications, driving innovation and improving performance in each domain.

As illustrated in Chapter 2, band-edge chiral nematic liquid crystal (LC) lasers are highly attractive light sources due to their ability to spontaneously emit circularly polarised light. For instance, it allows for a wide colour gamut and high contrast ratio in 3D displays, making them particularly suitable for advanced display technologies [9]. Additionally, their capability for direct beam-steering is crucial for optical communication links, navigation, tracking, and LiDAR applications [150]. Researchers have explored various methods to control the polarisation of band-edge LC lasers to further enhance their performance and application scope. For example, Ali et al. [149] implemented a nematic LC device with four in-plane electrodes to achieve on-demand polarisation control, showcasing a significant advancement in dynamic polarisation tuning for these lasers. Another approach involved applying an extra layer of nematic LC film within the cell, allowing for polarisation-tuneable lasing, which adds a layer of versatility to the laser's output characteristics [162].

Theoretically, considering the helical macroscopic structure of chiral nematic LCs, the electric field vector of the generated LC laser rotates with the helix across the LC layer leading to circularly polarised emission. Thicker LC layers could potentially lead to longer cavities and laser emissions with higher circularity. The handedness of the laser emission is the same as that of the helical structure. Experimentally, however, the polarisation states of band-edge LC lasers have been observed as not being perfectly circular by multiple researchers. To determine the polarisation state, different approaches have been considered including direct measurements by circular polarisers and a spectrometer [148], polarisation grating diffraction patterns [150], planar-aligned nematic LC polarisation controller [149], a combination of adjustable retarder with a mirror reflector [147], etc. The imperfect circular polarisation has been previously explained as being the result of Fresnel reflections from the cell boundaries due to the refractive index mismatch between the LC and glass substrates [147]. For instance, if the chiral nematic LC is right-handed, which generates a right-circularly polarised LC laser emission, the Fresnel

reflection from the glass substrates introduces a minor component of left-circularly polarised light, resulting in an elliptically polarised LC laser emission. However, despite the multitude of reports on band-edge LC lasers so far, there have been no reports focused on the factors that could affect the polarisation characteristics of the emission, nor considering the wavefront non-uniformity or pulse-to-pulse variations.

In this chapter, the polarisation states of band-edge chiral nematic LC lasers are characterised and analysed in terms of their Stokes parameters. Compared to other mathematical descriptions of polarisation (i.e., the Jones vector), Stokes parameters can account for partially polarised beams and their degrees of polarisation. Considering the non-uniform nature of these dye lasers between pulses and across the wavefront, a Stokes imaging polarimeter was implemented into the measurement system, which can specify the pixel-to-pixel information of the polarisation states of the propagation beam. Subsequently, the impact of various excitation fluences of the pump laser on the LC laser Stokes parameters was investigated, as well as how the LC layer thickness and alignment quality could affect the polarisation profiles. Such results could be of significant benefit to understanding the polarisation states and applications involving polarisation control of band-edge LC lasers.

4.2 Stokes Parameters Measurements and Calibration

4.2.1 Calibration

Measurement of the Stokes parameters of various laser sources requires precise control of the orientation of the components used, including a polariser and quarter waveplates (QWPs) designed for operation at different wavelengths. Specifically, the orientation of the polariser and the fast axes of the QWPs needed to be calibrated. The configuration for calibrating the polariser and QWPs is shown in **Fig. 4.1**. Since the purpose of further measurements is to indicate the polarisation states (e.g., linear, elliptical, circular, or partially polarised) of various laser sources, the absolute direction of each component with respect to the horizontal and vertical axes is not necessary, as long as they are all calibrated to a particular direction. This specific direction was determined by a film polariser mounted with its polarisation direction aligned vertically to the fixed platform on which the components were mounted.

(a)

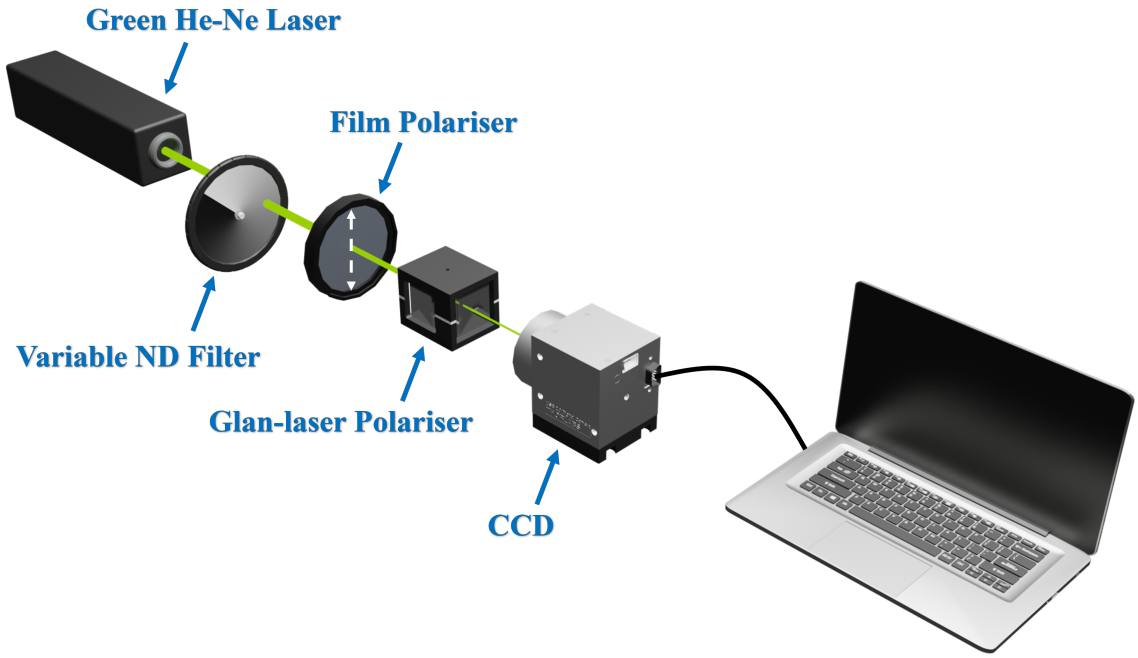

(b)

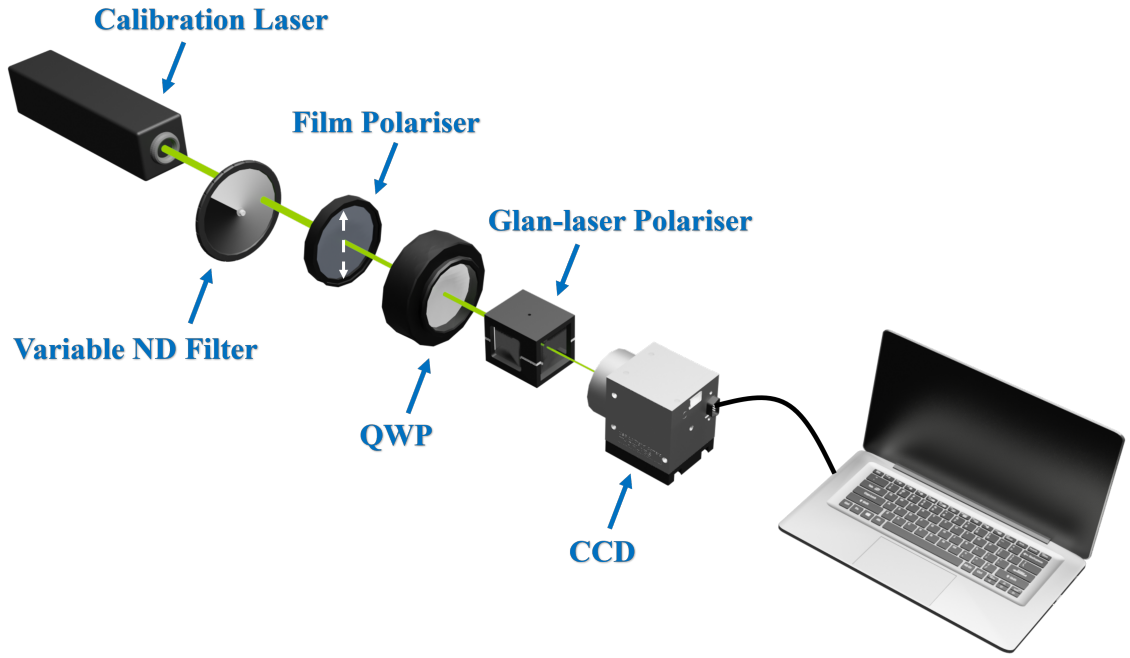

Figure 4.1: System configurations for calibration. (a) the Glan-laser polariser with a green He-Ne laser and (b) three QWPs designed for operation at 532 nm, 546 nm, and 633 nm with an Nd:YAG laser, a green He-Ne laser, and a red He-Ne laser, respectively, corresponding to the centre wavelengths of the QWPs. All components were calibrated using a thin-film linear polariser with its polarisation direction being aligned vertically with respect to the lab coordinate frame. Calibrated components were subsequently equipped with rotational mounts with their orientations recorded for future reference.

A Glan-laser calcite polariser (GL10-A, Thorlabs) was first calibrated according to the optical arrangement illustrated in Fig. 4.1(a). The polariser was mounted on a rotational mount with a Vernier scale (not shown in the configuration for simplicity) providing a resolution of 5 arcmin between consecutive marks. Note that the choice of the Glan-laser calcite polariser was due to its high extinction ratio of 100000:1 for the output beam, which operates by reflecting the ordinary and some of the extraordinary beam, with the remainder being a highly polarised extraordinary beam. The He-Ne laser propagated through a sequence containing the fixed film polariser and the Glan-laser polariser before the beam was collected by a CCD camera. The orientation of the Glan-laser polariser was first adjusted to be roughly perpendicular to the film polariser, then the rotational mount was slightly adjusted to minimise the intensity received by the CCD, where the orientation of the Glan-laser polariser was precisely calibrated perpendicular to the fixed film polariser, parallel to the optical bench. The rotational mount remained unchanged throughout the following experiments, leaving the Glan-laser polariser as a standard for other components to be calibrated relative to.

Subsequently, the optical arrangement was modified to be the configuration presented in Fig. 4.1(b) with the film polariser unchanged. Three QWPs at 532 nm, 546 nm, and 633 nm corresponding to measuring the polarisation of a green He-Ne laser (05-LGP-193, Melles Griot), an Nd:YAG laser (6FTSS355-Q4-S, CryLas), and LC lasers, respectively, were subsequently calibrated. The green He-Ne laser was first implemented in the system, propagating through the fixed film polariser, the 546 nm QWP, the calibrated Glan-laser polariser, and the CCD camera. Since the QWP can alter the polarisation of the laser, the intensity received by the CCD camera would reach a minimum when either the fast axis or the slow axis was parallel to the Glan-laser polariser. The specific axis could be determined by comparing with the fast-axis direction as labelled on the QWP. Even though the labelled directions were not precise, the deviation was found to be typically less than 20°, suggesting the possibility of distinguishing whether the fast or slow axis was parallel to the orientation of the Glan-laser polariser. Once the QWP was calibrated, its orientation was recorded for future reference. The same calibration method was repeated for the other two QWPs designed for use at 532 nm and 633 nm, where the green He-Ne laser was replaced with either an Nd:YAG laser or a red He-Ne laser, respectively.

4.2.2 Stokes Imaging Polarimeter

The Stokes parameters could be determined using a Stokes imaging polarimeter consisting of a QWP, a Glan-laser polariser, and a CCD camera, as illustrated in **Fig. 4.2**. Upon calibration of the fast axis of the QWP and orientation of the Glan-laser polariser, the respective Mueller matrices are then represented by M_P and M_{QWP} in Eq. (4.1) and Eq. (4.2).

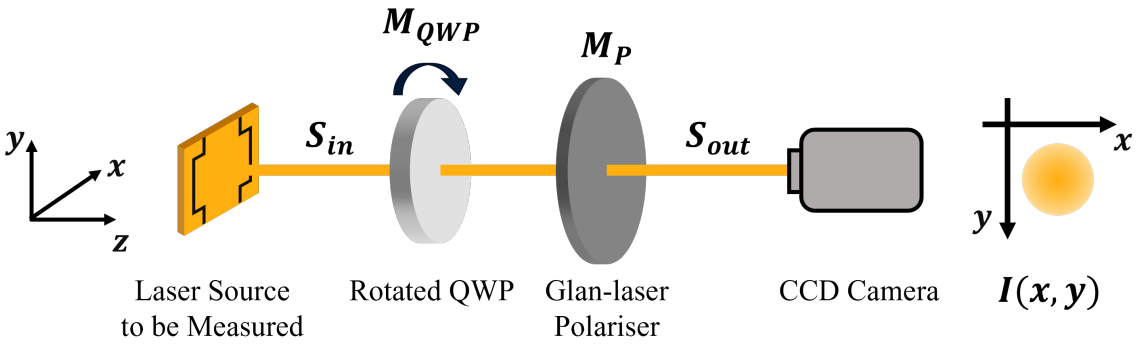

Figure 4.2: An illustration of the Stokes imaging polarimeter used for the measurement of the polarisation. The laser beam being measured was collimated before being received by a CCD camera where the pixel intensities could be extracted.

$$M_P = \frac{1}{2}\begin{pmatrix} 1 & \cos(2\theta) & \sin(2\theta) & 0 \\ \cos(2\theta) & \cos^2(2\theta) & \cos(2\theta)\sin(2\theta) & 0 \\ \sin(2\theta) & \cos(2\theta)\sin(2\theta) & \sin^2(2\theta) & 0 \\ 0 & 0 & 0 & 0 \end{pmatrix} = \frac{1}{2}\begin{pmatrix} 1 & 1 & 0 & 0 \\ 1 & 1 & 0 & 0 \\ 0 & 0 & 0 & 0 \\ 0 & 0 & 0 & 0 \end{pmatrix} \tag{4.1}$$

$$\begin{aligned} M_{QWP} &= \begin{pmatrix} 1 & 0 & 0 & 0 \\ 0 & \cos^2(2\theta) + \sin^2(2\theta)\cos(\delta) & \cos(2\theta)\sin(2\theta)(1-\cos(\delta)) & \sin(2\theta)\sin(\delta) \\ 0 & \cos(2\theta)\sin(2\theta)(1-\cos(\delta)) & \cos^2(2\theta)\cos(\delta) + \sin^2(2\theta) & -\cos(2\theta)\sin(\delta) \\ 0 & -\sin^2(2\theta)\sin(\delta) & \cos(2\theta)\sin(\delta) & \cos(\delta) \end{pmatrix} \\ &= \begin{pmatrix} 1 & 0 & 0 & 0 \\ 0 & \cos^2(2\theta) & \cos(2\theta)\sin(2\theta) & \sin(2\theta) \\ 0 & \cos(2\theta)\sin(2\theta) & \sin^2(2\theta) & -\cos(2\theta) \\ 0 & -\sin^2(2\theta) & \cos(2\theta) & 0 \end{pmatrix} \end{aligned} \tag{4.2}$$

where θ is either the orientation of the polariser or the fast axis of the QWP and δ is the phase difference between the fast and slow axis of the QWP.

The Stokes parameters of an incident beam S_{in} can be calculated according to the Stokes parameters received by the CCD camera S_{out} and the Mueller matrices of the Glan-laser polariser M_P and the QWP M_{QWP}:

$$S_{out} = M_P \cdot M_{QWP} \cdot S_{in} \tag{4.3}$$

Suppose the result of $M_P \cdot M_{QWP}$ can be represented by a 4×4 matrix A with its first row $B = (A_{11}, A_{12}, A_{13}, A_{14})$, and the four Stokes parameters received by the CCD can be denoted by $S_{out} = (S_{out_0}, S_{out_1}, S_{out_2}, S_{out_3})$, then

$$\begin{pmatrix} S_{out_0} \\ S_{out_1} \\ S_{out_2} \\ S_{out_3} \end{pmatrix} = \begin{pmatrix} A_{11} & A_{12} & A_{13} & A_{14} \\ A_{21} & A_{22} & A_{23} & A_{24} \\ A_{31} & A_{32} & A_{33} & A_{34} \\ A_{41} & A_{42} & A_{43} & A_{44} \end{pmatrix} \cdot S_{in} \tag{4.4}$$

$$S_{out_0} = B \cdot S_{in} \tag{4.5}$$

The first Stokes parameter represents the intensity of the beam, which can be extracted directly from the CCD camera, $I(x, y)$, as shown in Fig. 4.2. Thus, the Eq. (4.5) can be rewritten as $I(x, y) = B \cdot S_{in}(x, y)$ corresponding to each CCD pixel. To solve for the four Stokes parameters of the incident beam in $S_{in}(x, y)$, the QWP is rotated to four specific orientations 15.1°, 51.7°, 128.3°, and 164.9° to acquire four independent equations. In this chapter, we define an angle that is rotated anticlockwise to be positive, and clockwise to be negative. Notably, the selection of these orientation angles has been determined to be optimal, leading to an improved signal-to-noise ratio (SNR) compared to polarimeters utilising QWPs, as highlighted in a previous study [163].

$$\begin{cases} I_1(x, y) = B_1 \cdot S_{in}(x, y) \\ I_2(x, y) = B_2 \cdot S_{in}(x, y) \\ I_3(x, y) = B_3 \cdot S_{in}(x, y) \\ I_4(x, y) = B_4 \cdot S_{in}(x, y) \end{cases} \tag{4.6}$$

$$S_{in}(x, y) = \begin{pmatrix} S_0(x, y) \\ S_1(x, y) \\ S_2(x, y) \\ S_3(x, y) \end{pmatrix} = \begin{pmatrix} B_1 \\ B_2 \\ B_3 \\ B_4 \end{pmatrix}^{-1} \cdot \begin{pmatrix} I_1(x, y) \\ I_2(x, y) \\ I_3(x, y) \\ I_4(x, y) \end{pmatrix} \tag{4.7}$$

where $I_1(x, y)$, $I_2(x, y)$, $I_3(x, y)$, $I_4(x, y)$ are pixel intensities that can be extracted from four CCD images at four QWP orientations, and B_1, B_2, B_3, B_4 are known matrices from the calibration process given by Eq. (4.1) and Eq. (4.2).

As illustrated in Chapter 2, the Stokes parameters can be employed to represent the polarisation states of partially polarised sources, the degree of polarisation (DOP) of each pixel can be indicated using the formula $DOP(x, y) = \sqrt{S_1(x, y)^2 + S_2(x, y)^2 + S_3(x, y)^2}$ ranging from 0 to 1, with $DOP = 1$ indicating a polarised source and $DOP = 0$ being unpolarised. Linearity, L, and circularity, C, of the entire beam can be expressed as

$$L = \frac{\Sigma\sqrt{S_1(x, y)^2 + S_2(x, y)^2}}{\Sigma S_0(x, y)} \tag{4.8}$$

$$C = \frac{\Sigma|S_3(x,y)|}{\Sigma S_0(x,y)} \tag{4.9}$$

In terms of the following Stokes parameters measurements, only the polarisation profile was of interest, thus every Stokes parameter corresponding to each pixel was normalised by the corresponding $S_0(x,y)$ value so as to highlight only the polarisation profile. After normalisation, the first Stokes parameter which represents the total intensity, becomes uniformly equal to one for all pixels, i.e., $S_0(x,y)/S_0(x,y) = 1$. Since this parameter now only conveys the beam shape and provides no additional polarisation information, it was not considered in the analysis of the experimental results. The focus was instead placed on the other three normalised Stokes parameters to investigate the polarisation state across the beam profile.

4.3 Stokes Parameters of a Continuous-wave Laser

The Stokes imaging polarimeter was first used to measure the polarisation states of a commercially available continuous wave green Helium-Neon (He-Ne) laser, emitting at a wavelength of 534.5 nm, to verify the effectiveness and accuracy of the measurement system. The polarisation state of the He-Ne laser was deliberately converted to different polarisation states with the use of polarisers and waveplates in order to examine the reliability and accuracy of the Stokes parameters measurements.

The configuration for measuring the Stokes parameters of only the green He-Ne laser is demonstrated in **Fig. 4.3**(a) where a neutral density (ND) filter with optical density (OD) of 4 was introduced to the system to attenuate the beam intensity below the saturation level of the CCD camera. The rotatable QWP in the Stokes imaging polarimeter was designed for operation at 546 nm, where the slight difference in wavelength between it and the laser source was considered to be negligible. The impact of a larger wavelength mismatch on the measurement result will be discussed in detail later in this chapter.

Images were taken for each of the QWP orientations (15.1°, 51.7°, 128.3°, 164.9°). Note that the intensity received by the CCD camera changes for different orientations of the QWP. Therefore, to enhance the SNR, the exposure time of the CCD camera was adjusted to maximise the pixel intensity values while keeping them below the saturation level, specifically for the orientation of the rotated QWP that resulted in the highest intensity received by the CCD. This

particular exposure time for the current experiment was fixed during the entire measurement process. The Stokes parameters and the DOP for each pixel were calculated and presented in Fig. 4.3(b), along with a polarisation ellipse diagram sampled every 25 pixels to enable visualisation of the polarisation state of the beam. The result suggests that the green He-Ne laser was inherently linearly polarised which is in accordance with the profile provided by the supplier. The laser beam was regarded as possessing a Gaussian radial distribution, thus only the pixels that received at least 13.5% ($1/e^2$) of the maximum pixel intensity were taken into consideration.

Subsequently, the film polariser used for calibration was placed into the system as shown in Fig. 4.3(a). The orientation of the film linear polariser remained vertical (relative to the lab frame), and the CCD exposure time was adjusted similar to the previous experiment. The Stokes parameters results, shown in Fig. 4.3(c), indicate that the polarisation state of the beam after propagating through the film polariser was indeed vertical, consistent with the calibration of the film polariser. In both experiments, with and without the film polariser, the DOP was equal to unity across the wavefront, indicating that the beam was fully polarised. However, the linearity of the green He-Ne laser was 0.993 with the film polariser and 0.998 without it, indicating that the film polariser negatively impacted the linearity of the laser. Therefore, the film polariser was removed from the system for the subsequent experiments when manipulating and measuring the polarisation state of the green He-Ne laser. In this chapter, the linearity, circularity, and DOP for various lasers were kept for three significant figures, as they were derived from pixel values ranging from 0 to 255, measured by the Stokes imaging polarimeter.

The linear polarisation direction of the green He-Ne laser can be indicated from the Stokes parameters measurement results demonstrated in Fig. 4.3(b). The polarisation direction of the laser was then modulated to other orientations with a half waveplate (HWP) designed for a wavelength of 546 nm. The HWP introduced a relative phase difference of π between the fast and slow axes, which rotates light initially linearly polarised at an angle θ through a total angle of 2θ [139]. The system configuration is demonstrated in **Fig. 4.4**(a) where the HWP was placed with its fast axis at an angle of -45° with respect to the laser polarisation direction. Similar experimental procedures were conducted to measure the Stokes parameters of the modified beam with results presented in Fig. 4.4(b). The polarisation direction of the laser was rotated by 90° clockwise compared to that in Fig. 4.3(b), which was in agreement with the theoretical

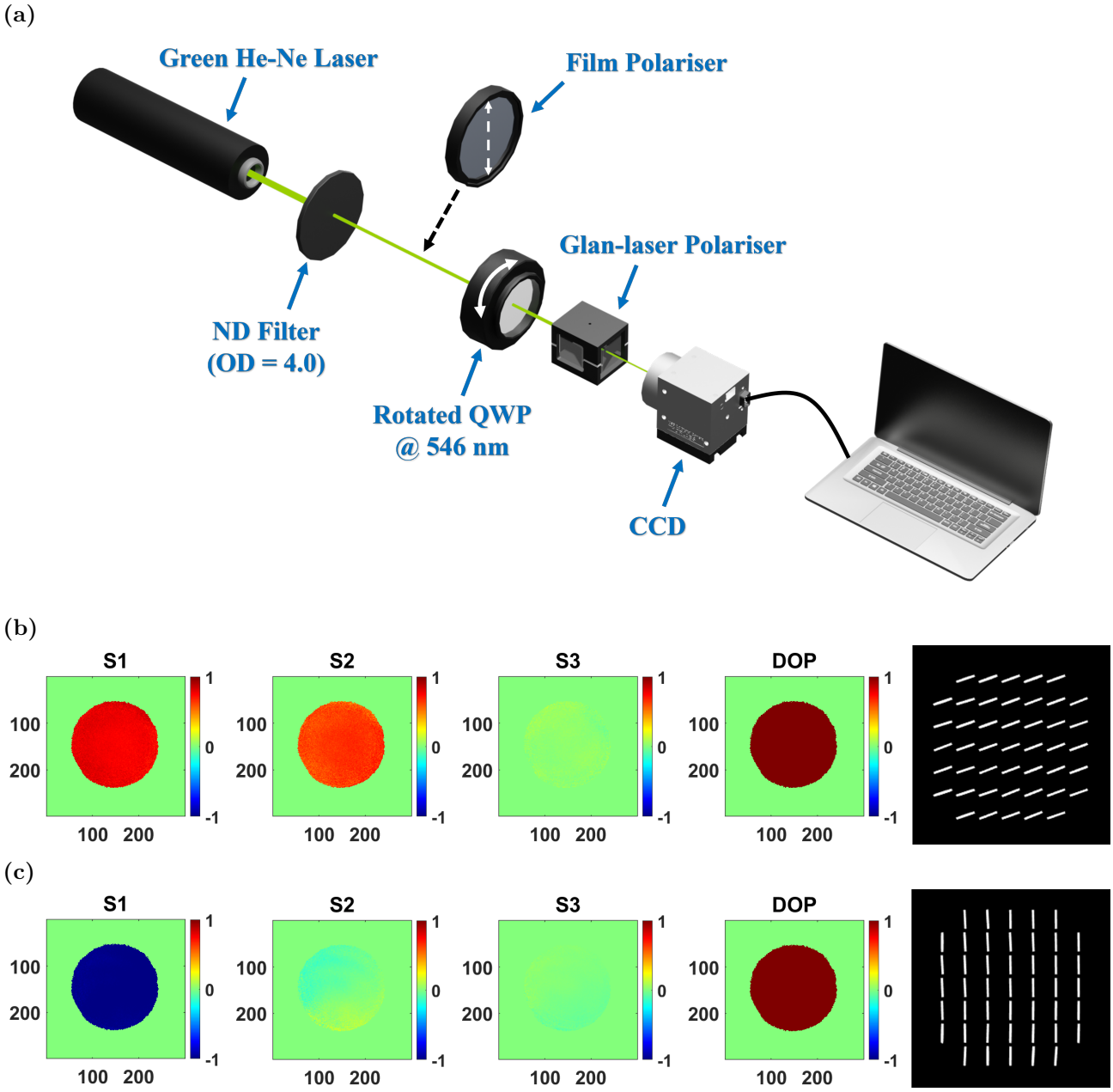

Figure 4.3: (a) The system configuration for measuring the Stokes parameters of the green He-Ne laser with and without a thin-film linear polariser. An ND filter was implemented to adjust the incident intensity within the exposure range of the CCD camera. The additional components and translation mounts for the polarisers and the QWP are not shown in the figure for simplicity. The normalised Stokes parameters and DOP of each pixel across the wavefront and polarisation ellipse diagrams with one of every 25 pixels are demonstrated in (b) for only the green He-Ne laser and (c) a combination of the laser and a film linear polariser. The first Stokes parameters are not shown as they provide only the beam shape information upon normalisation.

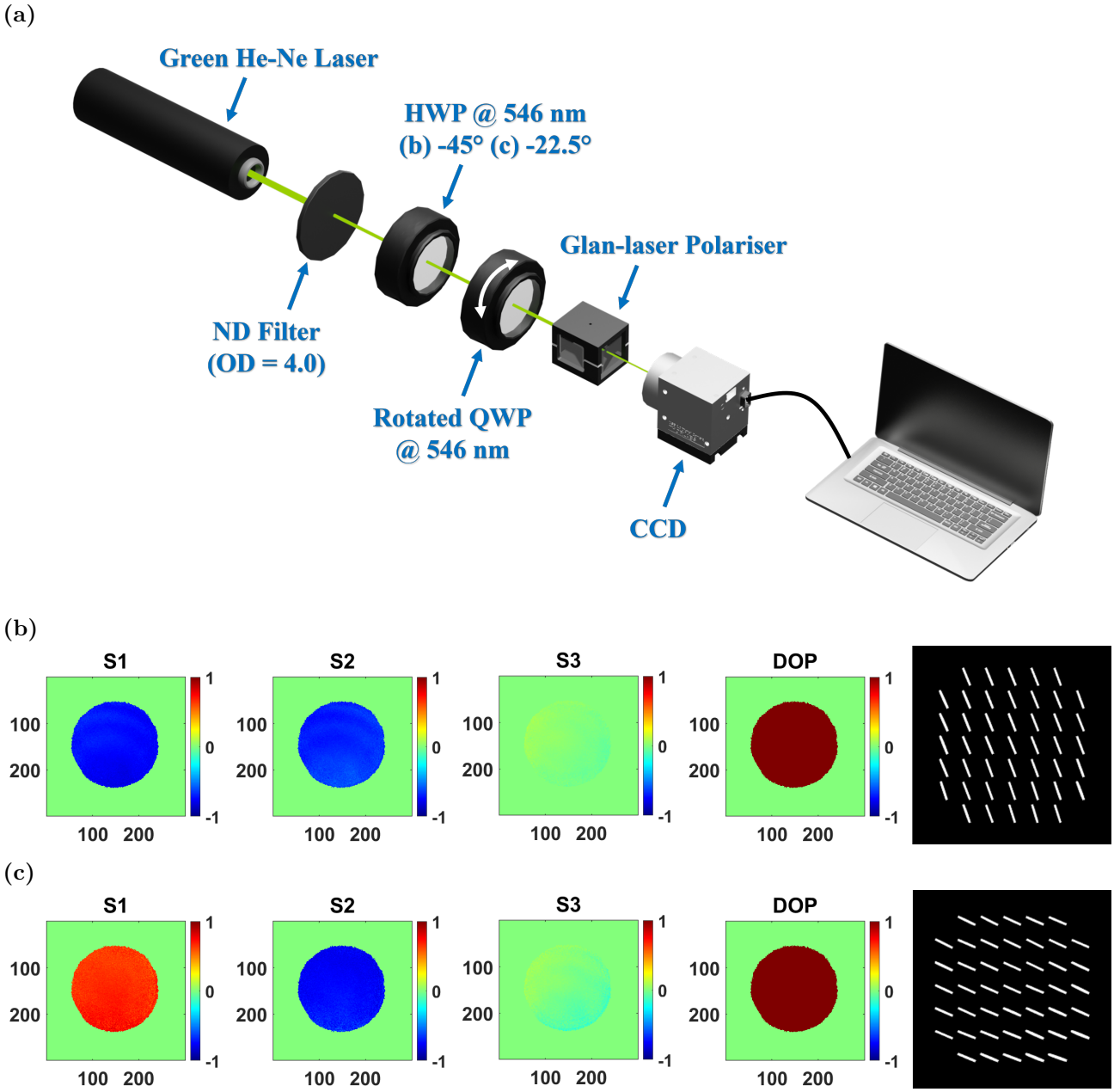

Figure 4.4: (a) The system configuration for measuring the Stokes parameters of a linearly polarised green He-Ne laser with its polarisation direction rotated with the addition of an HWP. An ND filter was included to adjust the incident intensity within the exposure range of the CCD camera. Additional components and translation mounts for the polariser and waveplates are not shown in the figure for simplicity. The normalised Stokes parameters and DOP of each pixel across the wavefront and polarisation ellipse diagrams with one of every 25 pixels are demonstrated for the HWP placed at (b) -45° and (c) -22.5°. The first Stokes parameters are not shown as they provide only the beam shape information upon normalisation.

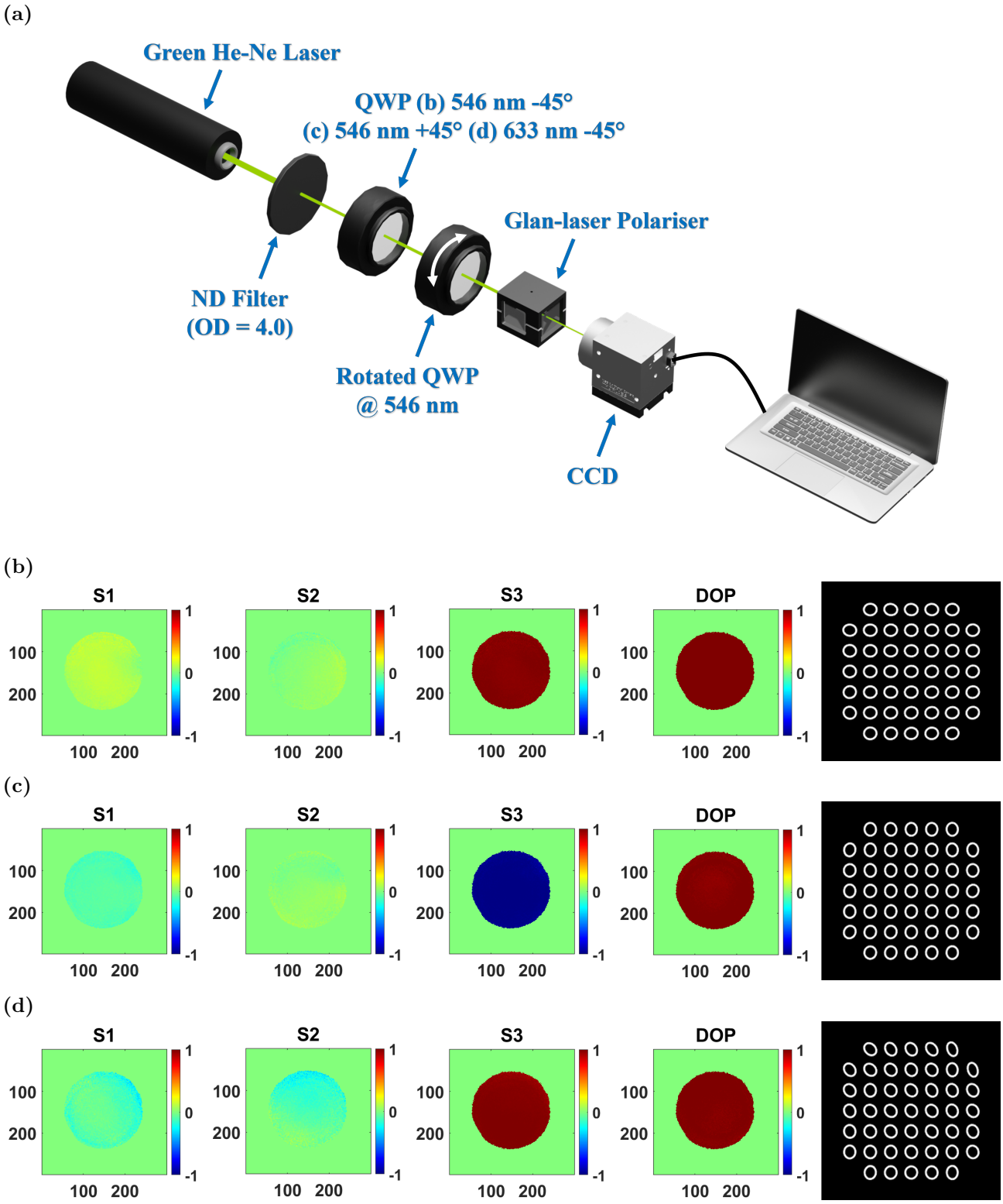

Figure 4.5: (a) The system configuration for measuring the Stokes parameters of a circularly polarised green He-Ne laser. An ND filter was implemented to adjust the incident intensity within the exposure range of the CCD camera. Additional components and translation mounts for the polariser and QWPs are not shown in the figure for simplicity. The normalised Stokes parameters and DOP of each pixel across the wavefront and polarisation ellipse diagrams with one of every 25 pixels are demonstrated for a 546 nm QWP placed at (b) -45°, (c) 45° and (d) a 633 nm QWP placed at -45°. The first Stokes parameters are not shown as they provide only the beam shape information upon normalisation.

properties of the HWP. Next, the HWP was adjusted to another angle of -22.5°, and the results in Fig. 4.4(c) suggested the polarisation direction of the laser was rotated by 45° clockwise.

Finally, the HWP was replaced with a QWP designed for 546 nm placed with its fast axis at -45° and 45° with respect to the polarisation direction of the laser, as illustrated in the system configuration in **Fig. 4.5**(a). The QWP can provide a relative phase difference of $\pi/2$ between the fast and slow axes, therefore it altered the linear polarisation of the green He-Ne laser to right circularly and left circularly polarised when it was placed at -45° and 45°, respectively. The results demonstrated in Fig. 4.5(b) and (c) are in accordance with the theoretical polarisation states upon propagation through QWPs, with the degree of circularity being respectively 0.989 and 0.990 demonstrating the effectiveness and accuracy of the Stokes imaging polarimeter system. The 546 nm QWP was then removed and another QWP designed for use at 633 nm was introduced which generated slightly elliptically polarised light. The measurement results for the green He-Ne laser and the 633 nm QWP are shown in Fig. 4.5(d) where the degree of circularity was found to be 0.985. The long axes of the polarisation ellipses are perpendicular to the intrinsic polarisation direction of the He-Ne laser, which can be indicated by comparing the S_1 and S_2 parameters demonstrated in Fig. 4.5(d) with that in Fig. 4.3(b). This is due to a retardance that is greater than $\pi/2$ provided by the 633 nm QWP for the laser beam emitting at centre wavelength of 543.5 nm.

4.4 Stokes Parameters of a Pulsed Laser

Unlike continuous wave laser sources that generate stable emission, pulsed laser sources possess slight pulse-to-pulse variations resulting in intensity fluctuations. Since the Stokes imaging polarimeter derives polarisation states of the beam from different intensities received by the CCD camera when the QWP is rotated, the intensity must remain stable over time for each QWP orientation. Employing beam splitters and four separate Stokes polarimeters for each QWP orientation can enable simultaneous measurements of a single pulse. However, it has been observed that beamsplitters can impact the polarisation states that are measured, particularly the retardance and diattenuation [164]. To address this challenge of measuring the Stokes Parameters of pulsed laser sources, several images were captured for each of the QWP orientations to determine an average intensity that does not vary regardless of the pulse-to-pulse intensity

fluctuation. The impact of the number of pulse averages on the Stokes parameters measurements was studied in detail on LC lasers illustrated in Section 4.5, where it has been found that an average over 10 pulses was sufficient to obtain a meaningful measurement of the polarisation state.

Prior to measuring the polarisation states of LC lasers, the Stokes imaging polarimeter was implemented to measure a pulsed Nd:YAG laser, with the configuration shown in **Fig. 4.6**(a). Note that the rotatable QWP in the polarimeter was replaced by another QWP working at 532 nm, the same as the wavelength of the laser emission. The exposure time of the CCD camera was set to 99.9 ms (maximum) and the repetition rate of the Nd:YAG laser was set at 10 Hz, so as to capture single pulses and the correct number of averages could be further conducted by taking the corresponding number of CCD images. Instead of adjusting the exposure time as it was for measuring continuous wave laser sources, a variable ND filter was introduced after the laser to enable an adjustment of the intensity so as to maximise the pixel intensity values while keeping them below the saturation level, specifically for the orientation of the rotatable QWP that resulted in the highest intensity received by the CCD. Due to the high pulse intensity and insufficient attenuation of the variable ND filter, another ND filter with an OD of 2.5 was also added to the Stokes imaging polarimeter. In addition, an iris was added to ensure the capture of a more circular beam profile.

The Nd:YAG laser was first tuned to be linearly polarised by employing a film polariser oriented vertically (relative to the lab frame) and the results are shown in Fig. 4.6(b). The linearity was calculated to be 1.00 with few circular components as can be identified from the S_3 parameter. Subsequently, the beam was modified to be left-handed circularly polarised by adding a QWP at 532 nm after the film polariser with its fast axis placed at an angle of 45°. The corresponding results are illustrated in Fig. 4.6(c) suggesting a circularity of 0.992. All images exclusively illustrate the central region of the beam, where intensities higher than 13.5% ($1/e^2$) of the maximum pixel value, based on the assumption that the Nd:YAG laser emission emits with a beam shape that resembles a Gaussian profile. Results in fig.4.6(b) and (c) align with the theoretical polarisation states of the incident beam, validating the preciseness of this Stokes parameters measurement method when used with pulsed laser sources.

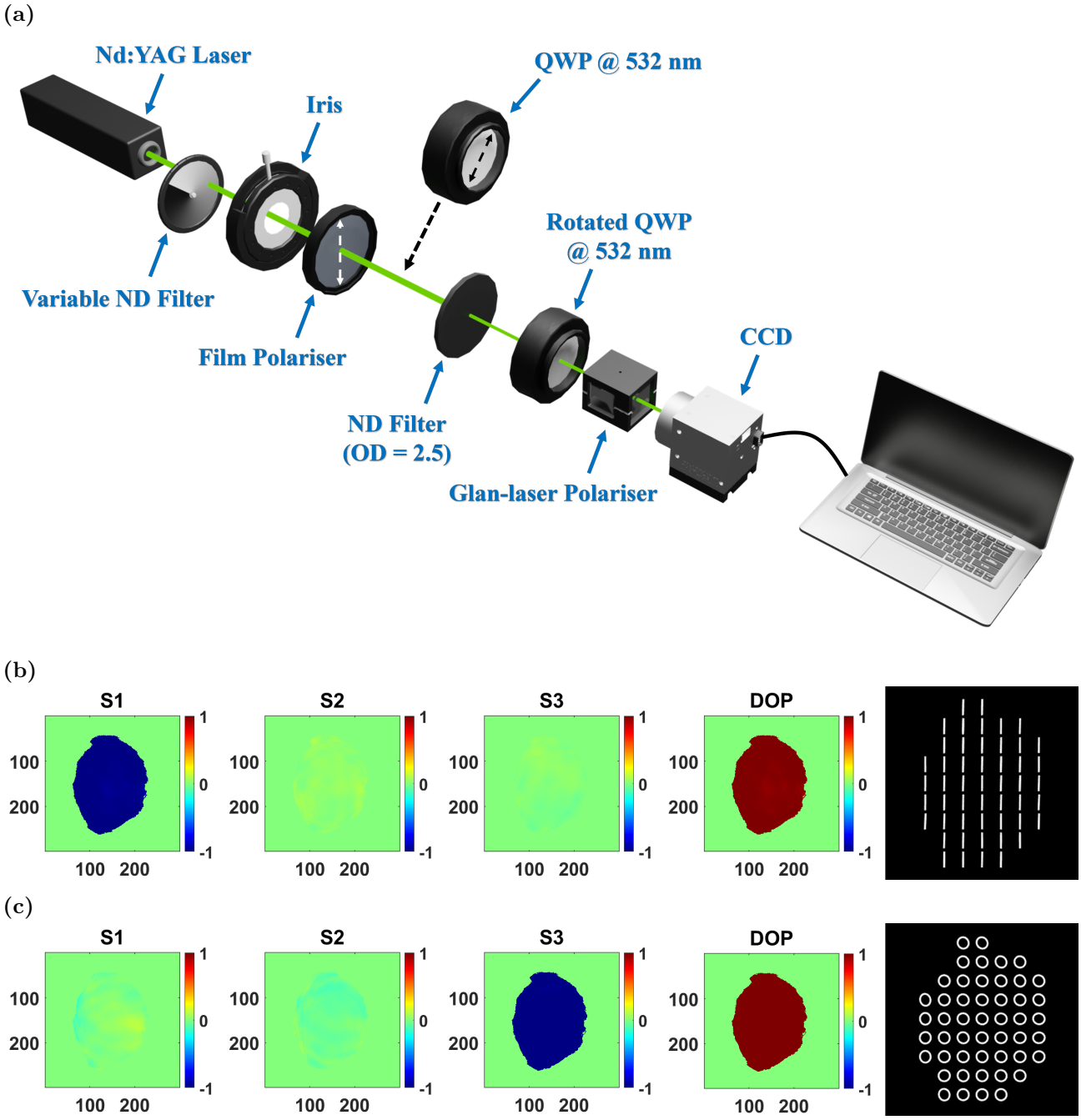

Figure 4.6: (a) System configuration for measuring the polarisation states of an Nd:YAG laser using a Stokes imaging polarimeter. The polarisation was tuned to be either linearly polarised or circularly polarised using a polariser and a QWP, respectively. ND filters were implemented to adjust the incident intensity to be within the exposure range of the CCD camera. Additional components and translation mounts for the polarisers and QWPs are not shown in the figure for simplicity. The normalised Stokes parameters and DOP of each pixel across the wavefront and polarisation ellipse diagrams with one of every 25 pixels are demonstrated for (b) linearly polarised and (c) left-handed circularly polarised Nd:YAG laser beam. The first Stokes parameters are not shown as they provide only the beam shape information upon normalisation.

4.5 Stokes Parameters of LC Lasers

The wavelengths of LC lasers can vary depending upon the combination of the pitch of the helix and the choice of laser dye/gain medium. They can also be tuneable in-situ using various external stimuli, leading to differences between the wavelengths of laser emissions and that of commercially available QWPs. This discrepancy necessitates an investigation into the potential impact of wavelength mismatch on the Stokes parameters measurements. Thus, the rotatable QWP in the Stokes imaging polarimeter was replaced with one designed for 633 nm and measurements were conducted for the linearly polarised Nd:YAG laser operating at 532 nm. The system configuration for investigating the wavelength mismatch is introduced in **Fig. 4.7**(a).

If the fast axis of the 633 nm QWP was calibrated using the Nd:YAG laser before measuring the Stokes parameters of the Nd:YAG laser, results in Fig. 4.7(b) show that the linearity of the beam was 0.990 and perceptible circular polarised components can be seen in S_3. On the contrary, if the QWP was calibrated to the red He-Ne laser operating at the same wavelength as the QWP, the measured linearity for the same Nd:YAG laser was 0.999 with results shown in Fig. 4.7(c). Therefore, compared to the Stokes parameters in Fig. 4.6(b) where the linearity was 1.00, the wavelength mismatch between the rotatable QWP in the Stokes polarimeter and the propagating beam does not significantly affect the measurement results, as long as the fast axis of the QWP was calibrated using a laser source with the same wavelength as that of the QWP. Note that the wavelength mismatch for this experiment was around 100 nm; however, when applying the same QWP to the LC lasers, the wavelength mismatch was only a few nm, exerting a minimal impact on the final polarisation measurement results.

The band-edge LC laser emission was generated using an Nd:YAG laser, directed onto an anti-parallel rubbed glass cell capillary filled with a dye-doped chiral nematic LC mixture. The fabrication process for manufacturing the glass cell has been illustrated in detail in Chapter 3. In this study, the LC mixture comprised of a nematic LC, E7, with 3.6% by weight of a chiral additive, BDH1281, and 1% by weight of an organic laser dye, DCM (4-(Dicyanomethylene)-2-methyl-6-(4-dimethylaminostyryl)-4H-pyran). This composition ensured that the fluorescence spectrum of DCM overlaps with the long photonic band-edge formed by the chiral nematic LC. The cell had an air gap of 20 µm, and the repetition rate of the Nd:YAG laser source was set to 10 Hz to achieve single pulse capture and prevent dye photo-bleaching. The polarisation state

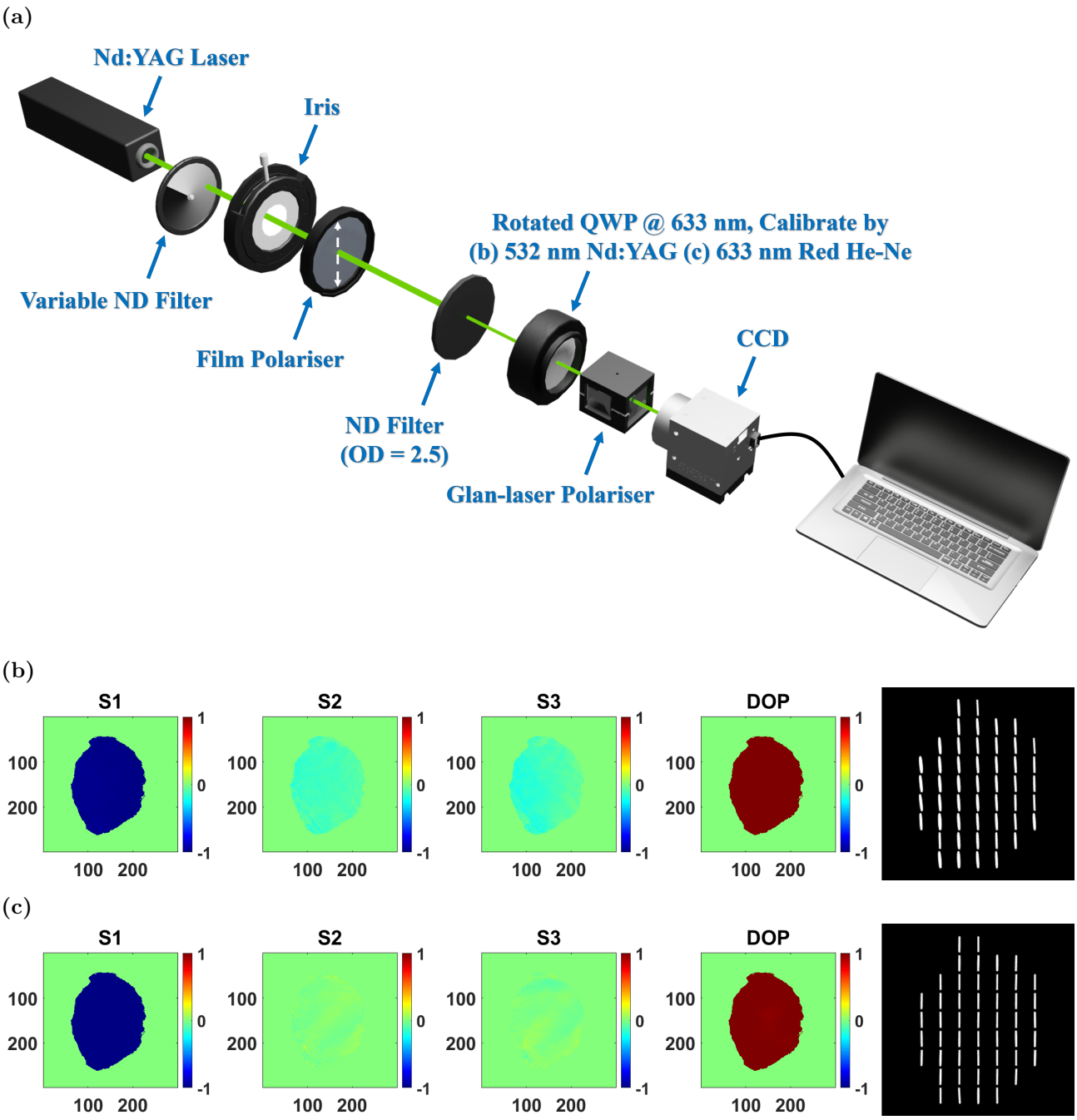

Figure 4.7: An investigation was conducted on the impact of wavelength mismatch, between the design wavelength of the rotatable QWP in the Stokes imaging polarimeter and the wavelength of the laser, on the Stokes parameters measurements. (a) System configuration for measuring a linearly polarised Nd:YAG laser using a Stokes imaging polarimeter designed for 633 nm. ND filters were implemented to adjust the incident intensity within the exposure range of the CCD camera. Additional components and translation mounts for the polarisers and QWPs are not shown in the figure for simplicity. The normalised Stokes parameters and DOP of each pixel across the wavefront and polarisation ellipse diagrams with increment of every 25 pixels are demonstrated, where the fast axis of the rotatable 633 nm QWP was calibrated using (b) a 532 nm Nd:YAG laser and (c) a 633 nm red He-Ne laser. The first Stokes parameters are not shown as they provide only the beam shape information upon normalisation.

of the Nd:YAG was adjusted to be left-circularly polarised, opposite to the handedness of the LC chirality. The Stokes parameters measurement system for the LC lasers, shown in **Fig. 4.8**, consists of components used for the optical pumping of the LC laser and a Stokes imaging polarimeter. To precisely control the excitation area of the LC laser, the cell was mounted on a two-dimensional translation mount, with each axis controlled by a Vernier scale providing 100 µm resolution. LC laser emission was collected by a 10x objective, and the Nd:YAG pump source was blocked by a long-pass edge filter. Before polarisation measurements, the beam spectrum was captured using a USB spectrometer (HR4000, Ocean Optics, not shown in the configuration), to confirm single-mode laser emission centred at 615.8 nm.

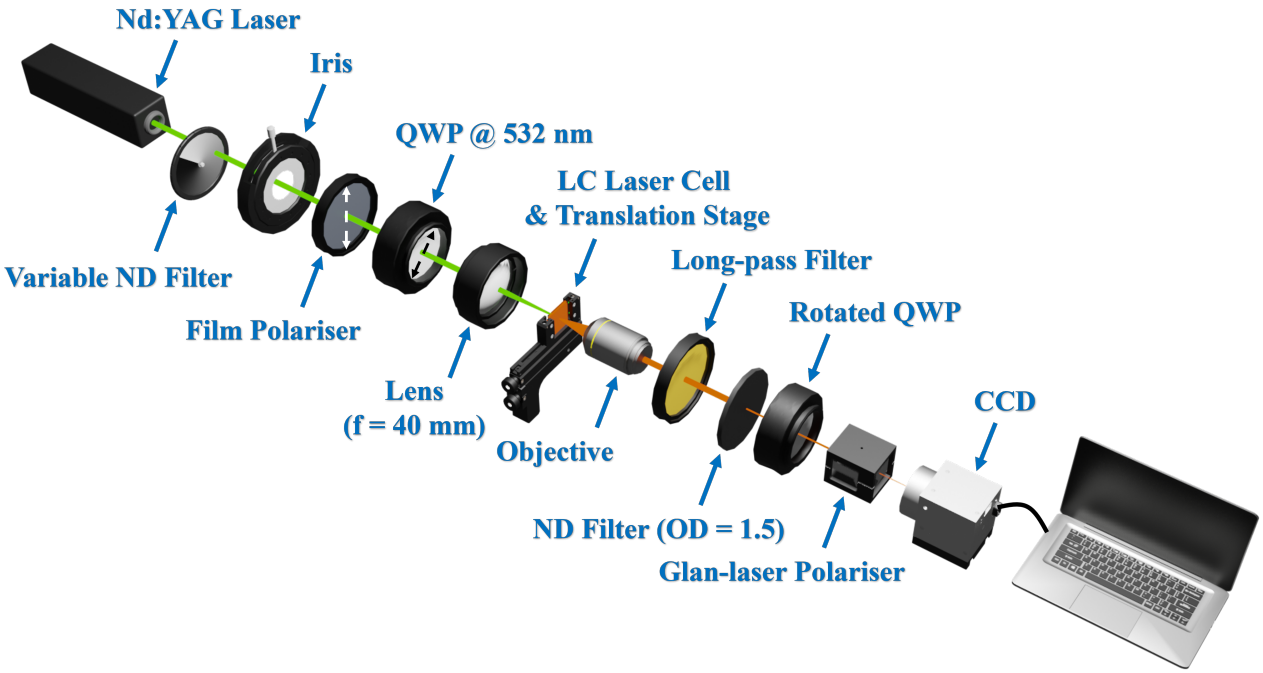

Figure 4.8: System configuration for measuring the Stokes parameters of LC lasers. Additional components and translation mounts for the polarisers and waveplates are not shown in the figure for simplicity.

Laser emission from band-edge LC lasers exhibits non-uniform behaviour across the wavefront, leading to slight intensity fluctuations between pulses. As mentioned previously, a method that involved taking the average of every 10 LC laser pulses for each QWP orientation was employed. Here, the impact of taking the average intensity for measurements involving a different number of pulses on the Stokes parameters was studied and illustrated in **Fig. 4.9**, presenting the measurement results for the same LC laser without any averaging, averaging over 2, 5, 10, and 20 pulses. The regions of the LC laser wavefront were manually extracted

from the CCD image background rather than implementing the 13.5% Gaussian beam diameter indication as employed for the Nd:YAG previously, considering that the intensity of the LC laser wavefront no longer exhibits a standard distribution. When there was no averaging over a number of pulses, only one image was taken for each QWP orientation and the plots for Stokes parameters in Fig. 4.9(a) exhibited a non-uniform colour, indicating potentially inaccurate measurements attributable to pulse-to-pulse variations of the LC laser. In comparison, the images in Fig. 4.9(b∼d) display a significantly higher level of uniformity as the number of averages increases, indicating that capturing a larger number of pulses substantially diminishes the speckle-like noise in the measurement results. In addition, the Stokes parameters measurement shown in Fig. 4.9(e) demonstrates that averaging over every 20 LC laser pulses results in a negligible deviation from the results obtained with 10 averages presented in Fig. 4.9(d). Consequently, a measurement approach involving averaging over 10 LC laser pulses was adopted in subsequent experiments for its practical efficacy.

4.5.1 Excitation Energy

The excitation fluence plays a crucial role in generating LC laser emission and determining its polarisation properties. The input-output characteristics of the LC laser cell, illustrated in **Fig. 4.10**, were measured by rotating the variable ND filter after the Nd:YAG laser and capturing the LC laser emission spectrum with a USB spectrometer (HR4000, Ocean Optics). A detailed experimental procedure has been provided in Chapter 3. As shown in Fig. 4.10, the threshold of the LC laser cell in this case was found to be 267.2 μJ/cm^2/pulse. Consequently, three excitation fluences were selected and applied to the LC cell by adjusting the variable ND filter to examine the impact on the polarisation states recorded for the LC laser emission. The lowest excitation chosen was just above the threshold to generate LC laser emission with minimal intensity, while the other two excitation fluences were achieved by setting the ND filter to give approximately half attenuation and no attenuation.

It has been observed that when the excitation from the pump source reached 364.8 μJ/cm^2/pulse, just above the threshold as shown in **Fig. 4.11**(a), the DOP was unity at the beam centre, indicating a well-defined polarisation state. However, the DOP gradually diminished to approximately 0.5 from the centre to the beam edge. This phenomenon can be attributed to the Gaussian distribution of the pump source wavefront, where higher intensity

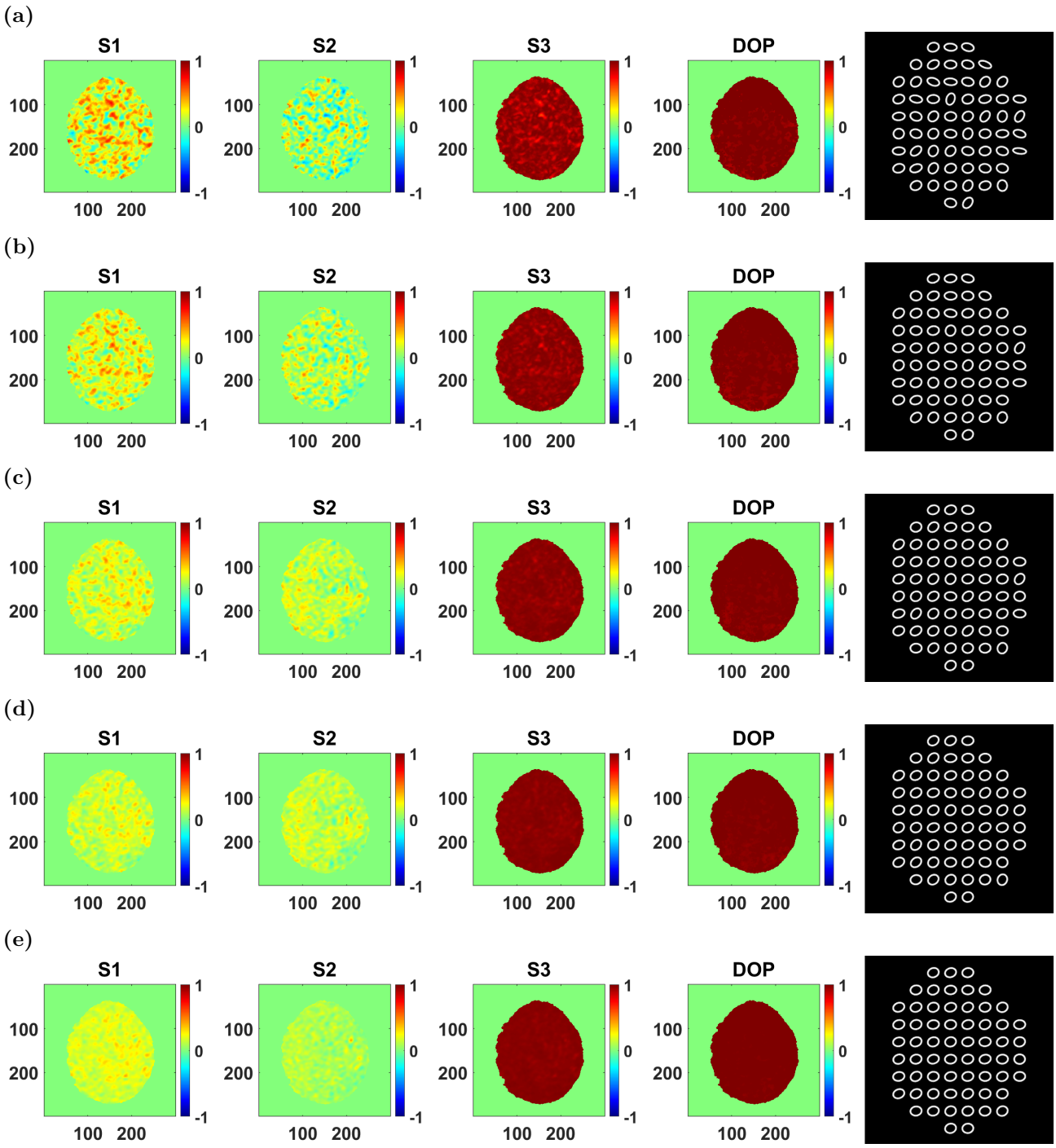

Figure 4.9: An investigation was conducted when averaging over a different number of pulses of the LC laser (E7 + 3.6 wt.% BDH1281 + 1 wt.% DCM) on the Stokes parameters measurements. Normalised Stokes parameters and DOP for each pixel across the wavefront and the polarisation ellipse diagrams with one of every 25 pixels are demonstrated, where (a) no average and averages of every (b) 2, (c) 5, (d) 10, (e) 20 pulses were conducted. The first Stokes parameters are not shown as they provide only the beam shape information upon normalisation. The thickness of the LC layer was 20 µm and the measurements were conducted at a room temperature of 20°C.

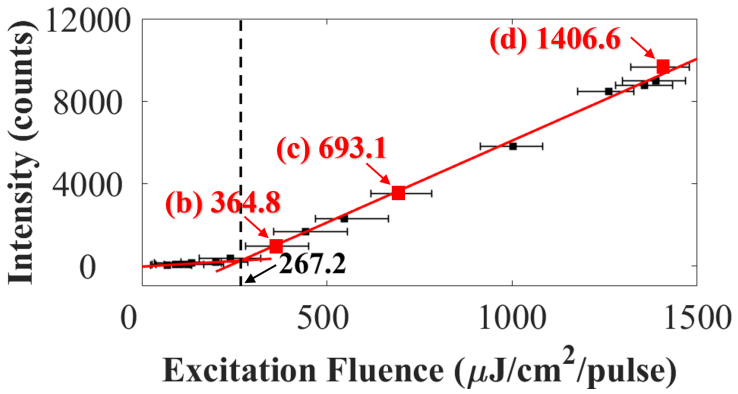

Figure 4.10: The output emission intensity of the LC laser (E7 + 3.6 wt.% BDH1281 + 1 wt.% DCM) as a function of the excitation fluence. The threshold is estimated to be at the location of the dashed black line. The thickness of the LC layer was 20 µm and the measurements were conducted at a room temperature of 20°C.

at the centre induces lasing from the LC cell, while lower intensity at the edge results in fluorescence generated by the DCM dye instead of lasing due to insufficient gain and feedback. The spectrum of this particular beam reveals a combination of a narrow LC laser spectrum intertwined with a DCM dye fluorescence spectrum. The right-handed helical structure of the LC acts as a one-dimensional Bragg reflector, theoretically capable of generating right-handed circularly polarised laser emission above the excitation threshold. However, due to the relatively low excitation fluence, the dye fluorescence at the beam edge exhibits partial elliptical polarisation and a lower DOP.

With an increase in the excitation fluence to 693.1 µJ/cm^2/pulse and 1406.6 µJ/cm^2/pulse, the DOP was largely improved, as evidenced in Fig. 4.11(b) and (c). Examination of the polarisation ellipses further revealed that the polarisation state became more uniform and less elliptical across the wavefront compared to that for the lower excitation fluence. The circularity, linearity, and DOP for the three excitation fluences are listed and compared in **Table 4.1**. This observed improvement can be considered to be due to an increase in the gain and feedback within the cell. Consequently, it is inferred that higher excitation fluence well above the excitation threshold enhances both the DOP and circular polarisation state of the band-edge LC laser emission.

While the system configuration and the excitation area of the LC laser cell remained unchanged throughout the measurements, the beam diameter of the LC lasers increased with higher excitation fluence. This phenomenon occurred because the increased excitation intensity caused a larger area around the centre to reach the lasing threshold. The Stokes parameters

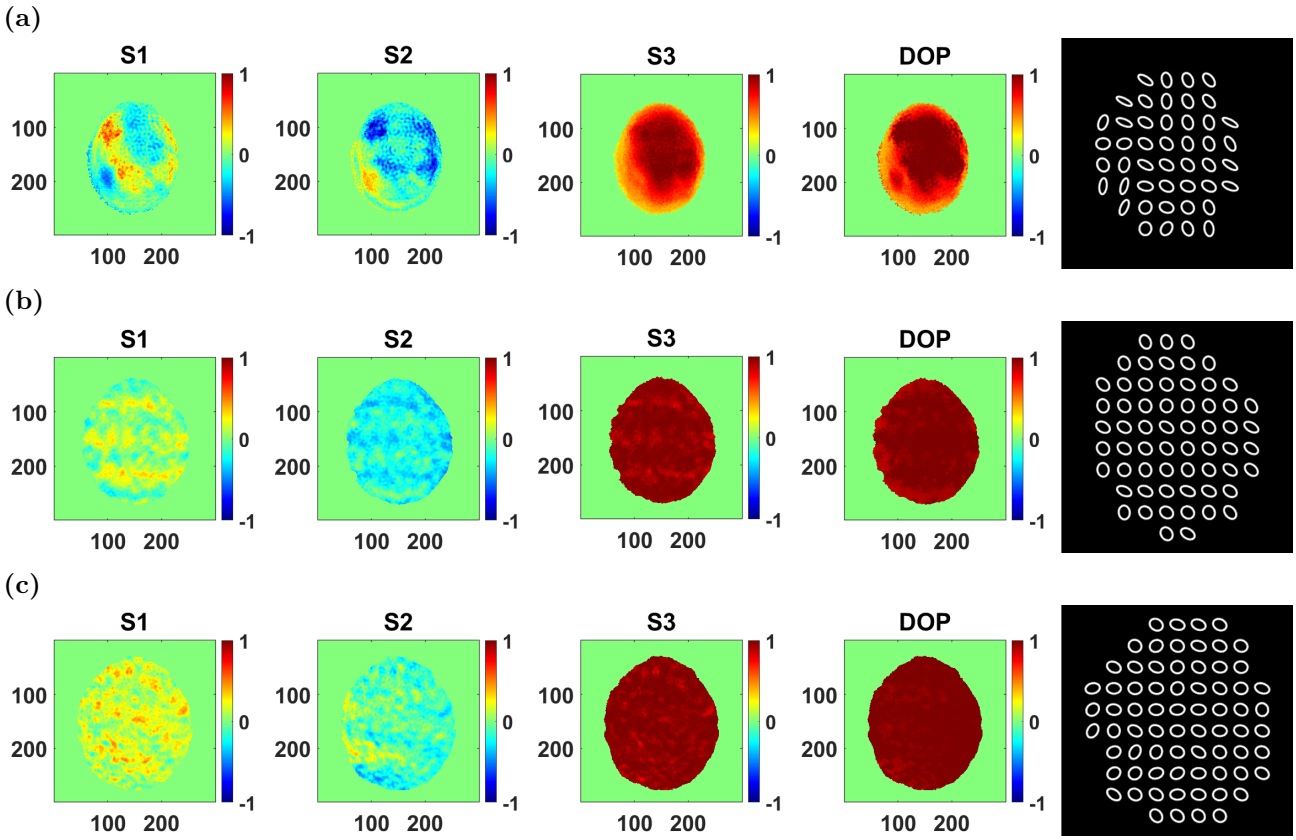

Figure 4.11: An investigation of the polarisation states of an LC laser (E7 + 3.6 wt.% BDH1281 + 1 wt.% DCM) with various excitation fluences. The normalised Stokes parameters and DOP of each pixel across the wavefront and polarisation ellipse diagrams with one of every 25 pixels are demonstrated, corresponding to three excitation fluences of (a) 364.8 µJ/cm^2/pulse, (b) 693.1 µJ/cm^2/pulse, and (c) 1406.6 µJ/cm^2/pulse. The first Stokes parameters are not shown as they provide only the beam shape information upon normalisation. The thickness of the LC layer was 20 µm and the measurements were conducted at a room temperature of 20°C.

Table 4.1: The circularity, linearity, and DOP of the LC laser (E7 + 3.6 wt.% BDH1281 + 1 wt.% DCM) with various excitation fluences. The thickness of the LC layer was 20 µm with a lasing threshold of 267.2 µJ/cm^2/pulse and the measurements were conducted at a room temperature of 20°C.

Excitation Fluence /(µJ/cm^2/pulse)	**Circularity**	**Linearity**	**DOP**
364.8	0.724	0.380	0.817
693.1	0.959	0.235	0.988
1406.6	0.968	0.172	0.984

demonstrated in Fig. 4.11(c) closely match the results presented in Fig. 4.9(d), as both were measured for the same LC laser cell with a thickness of 20 µm under excitation of 1406.6 µJ/cm^2/pulse without additional attenuation from the variable ND filter. The averaging was also taken every 10 pulses for both. However, the slight variation in the Stokes parameters across the wavefront was attributed to the different excitation areas on the LC cell. This consistency also indicated that the LC cell was not degraded over multiple experiments, and similar results could be obtained through repeated measurements.

4.5.2 LC Layer Thickness

An anti-parallel rubbed wedge glass cell with a thickness range from 0 to 23 µm was fabricated and was capillary filled with the same LC mixture (E7 + 3.6 wt.% BDH1281 + 1 wt.% DCM). The inner surfaces of the glass substrates were spin-coated with 1 wt.% PVA solution that acted as the alignment layer after being mechanically rubbed and a 23 µm spacer was placed at one edge of the cell to generate the thickness gradient. The thickness of the spacer was verified by measuring the thickness of another standard glass cell with two 23 µm spacers from the same supplier, following the experimental procedures outlined in Chapter 3.

The detailed fabrication process for wedge cells has been introduced in Chapter 3. The structure of this wedge cell is presented in **Fig. 4.12**(a), where three different thicknesses were selected by marking three distinct points on one edge of the glass substrate, labelled A to C in the figure, between the 'zero-thickness' edge of the cell (point O) and the spacer (point N). The distances of OA, OB, OC, and ON, were measured by a calliper as 6.92 mm, 9.97 mm, 13.34 mm, and 24.61 mm, respectively. Given that the spacer at point N is 23 µm thick, the corresponding LC layer thicknesses at points A to C were geometrically calculated as 6.47 µm, 9.32 µm, and 12.47 µm, respectively.

The transmittance spectra at three thicknesses were measured by placing the LC cell on a spectrometer (Cary 8454 UV-Vis, Agilent), such that the reference light from the spectrometer propagated through the three recorded LC cell regions being excited and further measured for the Stokes parameters. An extra position on the LC cell with a smaller thickness was measured, showing a spectrum corresponding to a region of the device which generated no LC laser emission. The transmission spectra are demonstrated in Fig. 4.12(b) where the band-edges

(a)

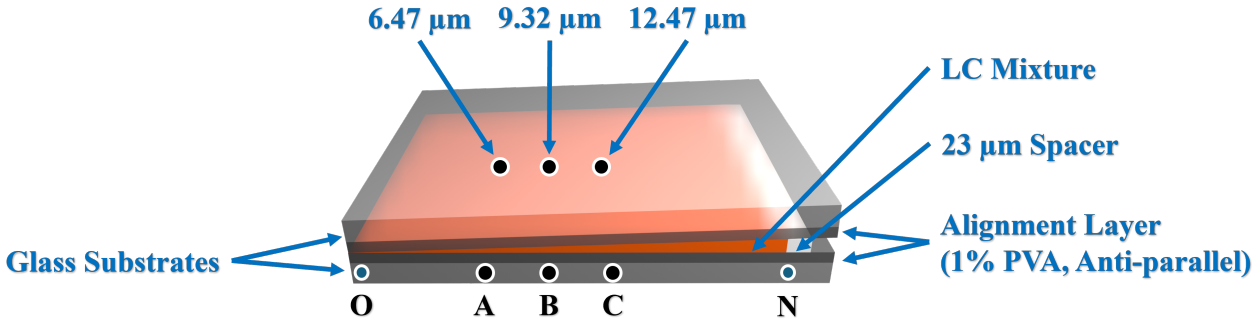

(b)

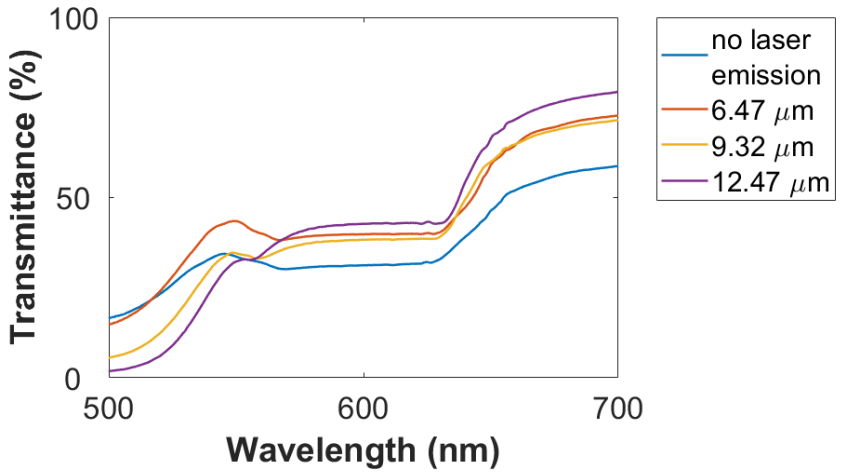

Figure 4.12: (a) The structure of a wedge cell fabricated for the investigation of the polarisation states of band-edge LC lasers of different thicknesses. The cell has a range of thickness from 0 to 23 µm and was filled with the same dye-doped chiral nematic LC mixture (E7 + 3.6 wt.% BDH1281 + 1 wt.% DCM). (b) The transmittance spectra for the LC cell at three selected thicknesses that generated single-mode LC lasers, 6.47 µm, 9.32 µm, and 12.47 µm, as well as a lower thickness where no laser emission was observed. The measurements were conducted at a room temperature of 20°C.

at thicker regions possess steeper gradients, following the theoretical analysis on the selective reflection from chiral nematic layers of various thicknesses introduced in Chapter 2.

Subsequently, the wedge cell was placed into the measurement system illustrated in Fig. 4.8 to investigate the impact of cell thicknesses on the polarisation state of LC lasers. Initially, the position of the LC cell was adjusted using the translation mount so that the Nd:YAG laser pump source was located at the thinner edge of the cell. The excitation fluence remained at 1406.6 µJ/cm^2/pulse. Subsequently, the cell was gradually moved horizontally so that thicker regions could be excited. A USB spectrometer (HR4000, Ocean Optics) was placed behind the long-pass edge filter in Fig. 4.8 to confirm the observation of 'single-mode' laser emission spectra, which appeared at the thicknesses of 6.47 µm, 9.32 µm and 12.47 µm.

Next, the USB spectrometer was removed and the polarisation state was measured using the Stokes imaging polarimeter, with the results presented in **Fig. 4.13**. At a thickness of 6.47 µm, as shown in Fig. 4.13(a), the visible linear components demonstrated in S_1 and S_2 suggest that the LC laser was elliptically polarised across the wavefront. In comparison, Fig. 4.13(b) and (c) indicate lower linear components in S_1 and S_2, resulting in higher circularity being observed with an increase in LC layer thickness. This phenomenon could be explained in such that thicker regions exhibited a greater number of pitches, leading to improved feedback. Additionally, the DOP for all three selected thicknesses was uniform and approximately one, consistent with the results in Fig. 4.11, indicating that higher excitation fluence can result in an almost fully polarised LC laser regardless of thickness. The circularity, linearity, and DOP for the three different LC layer thicknesses are listed and compared in **Table 4.2**.

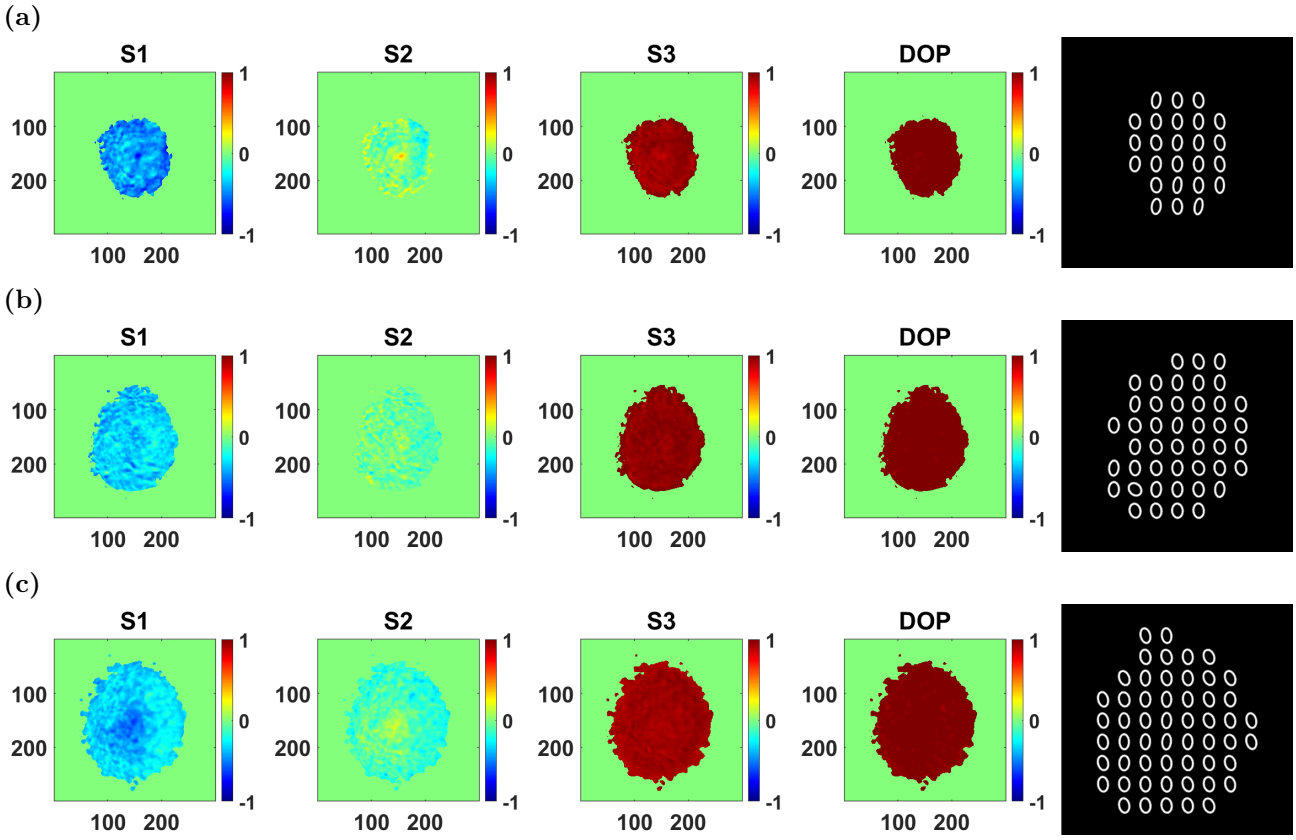

Figure 4.13: An investigation of the polarisation states of a wedge LC laser (E7 + 3.6 wt.% BDH1281 + 1 wt.% DCM) with different LC layer thicknesses. The normalised Stokes parameters and DOP of each pixel across the wavefront and polarisation ellipse diagrams with one of every 25 pixels are demonstrated, corresponding to three thicknesses of (a) 6.47 µm, (b) 9.32 µm, and (c) 12.47 µm. The first Stokes parameters are not shown as they provide only the beam shape information upon normalisation. The excitation fluence was 1406.6 µJ/cm^2/pulse and measurements were conducted at a room temperature of 20°C.

Table 4.2: The circularity, linearity, and DOP of a wedge LC laser (E7 + 3.6 wt.% BDH1281 + 1 wt.% DCM) with various LC layer thicknesses. Single-mode laser emissions were observed for all thicknesses. The excitation fluence was 1406.6 µJ/cm^2/pulse and measurements were conducted at a room temperature of 20°C.

LC Layer Thickness (µm)	Circularity	Linearity	DOP
6.47	0.890	0.436	0.991
9.32	0.937	0.334	0.995
12.47	0.929	0.365	0.999

4.5.3 Alignment Quality

Even though the larger LC layer thicknesses could lead to LC laser emission with higher circularity, they also could result in poorer alignment. The macroscopic one-dimensional Bragg reflector cannot be readily formed when the chiral nematic LCs are not planar aligned. In light of this, the impact of the alignment quality on the LC laser polarisation state was studied by fabricating another wedge cell with a thickness range from 0 to 50 µm. The glass substrates of the cell were spin-coated with 1 wt.% PVA and mechanically rubbed and assembled to give an anti-parallel configuration. The wedge cell was capillary filled with the same LC mixture (E7 + 3.6 wt.% BDH1281 + 1 wt.% DCM) with its structure presented in **Fig. 4.14**(a).

The cell was first observed on a polarised optical microscope (BX51, Olympus). Thinner regions of the cell exhibited well-defined Grandjean textures with few alignment defects, suggesting uniform alignment of the helix. In contrast, darker lines appeared in the thicker regions, especially near the spacer placed on one edge of the cell, indicating alignment defects where the LC did not align perfectly between the substrates. Subsequently, two regions, one with and one without alignment defects, were selected. The corresponding optical textures recorded on the polarised optical microscope are shown in Fig. 4.14(b) and (c), respectively. These regions were marked and recorded before being placed on the translation mount. The thicknesses were calculated to be 20.04 µm and 30.28 µm, respectively, using a similar method as that applied to the previous wedge cell.

The corresponding Stokes parameters for these two thicknesses were measured and the results are presented in **Fig. 4.15**(a) and (b). The circularity, linearity, and DOP are summarised in **Table 4.3**. Compared to previous measurements in Fig. 4.13(c), the Stokes parameters in

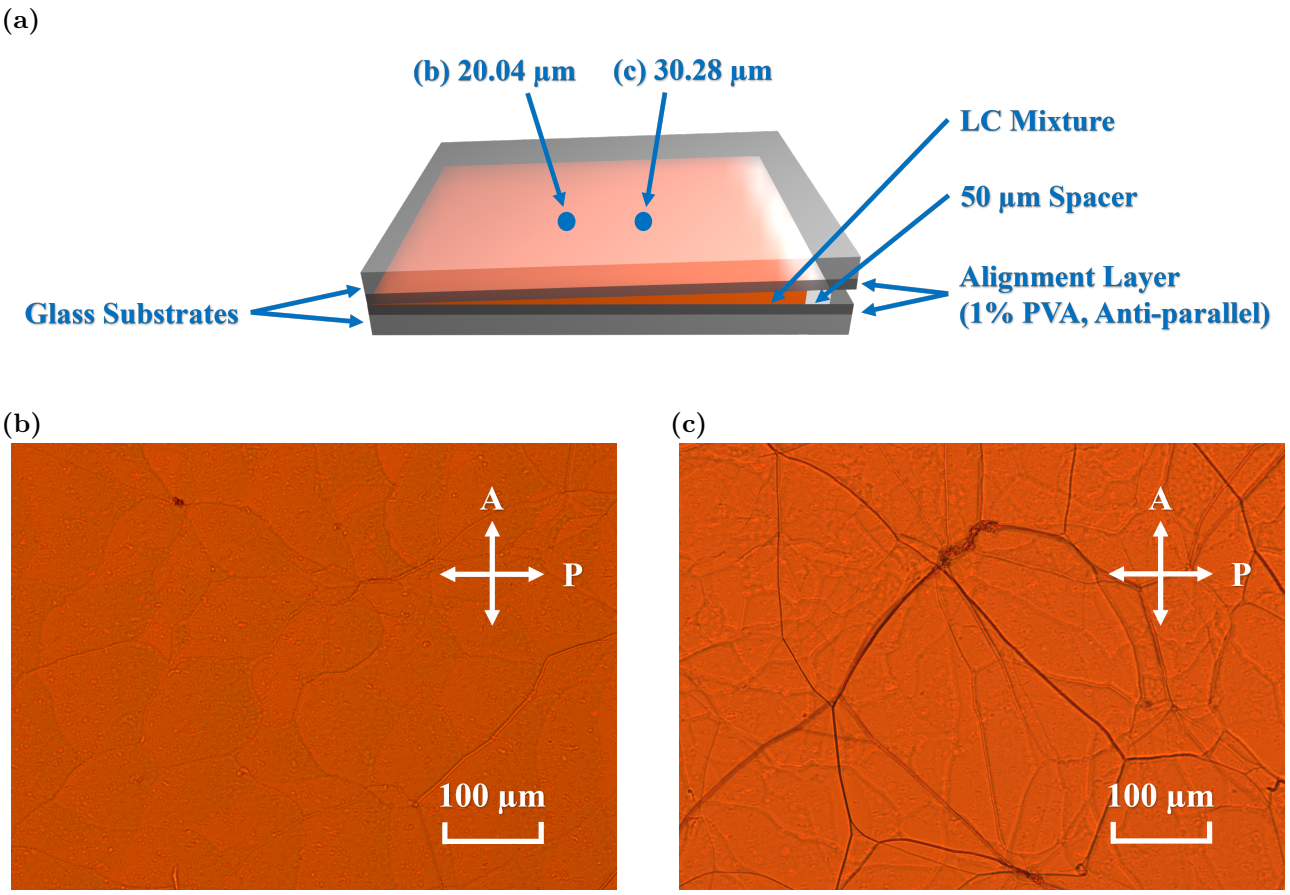

Figure 4.14: (a) The structure of a wedge cell fabricated for the investigation of the polarisation states of band-edge LC lasers with different alignment qualities. The cell has a thickness range from 0 to 50 µm and was filled with the same dye-doped chiral nematic LC mixture (E7 + 3.6 wt.% BDH1281 + 1 wt.% DCM). The optical texture of the cell was observed on an optical polarising microscope and the captured images are representative of the regions corresponding to thicknesses of (b) 20.04 µm and (c) 30.28 µm. The double-headed white arrows show the orientations of the polariser and analyser.

Fig. 4.15(a) show fewer linear components but more circular components, suggesting a higher thickness could further enhance the circularity as long as no alignment defects are formed across the excitation region. Although not substantial, a thicker LC layer typically leads to higher DOP, which can be observed by comparing Table 4.3 with Table 4.2. On the other hand, alignment defects appeared when the thickness of the LC layer reached 30.28 µm and the DOP of the LC laser noticeably decreased as is shown in Fig. 4.15(b). In this case, the Stokes parameters are not uniform across the wavefront. This phenomenon can be explained in such that alignment defects bring about poorer resonance in the LC cavity resulting in lower DOP and circularity.

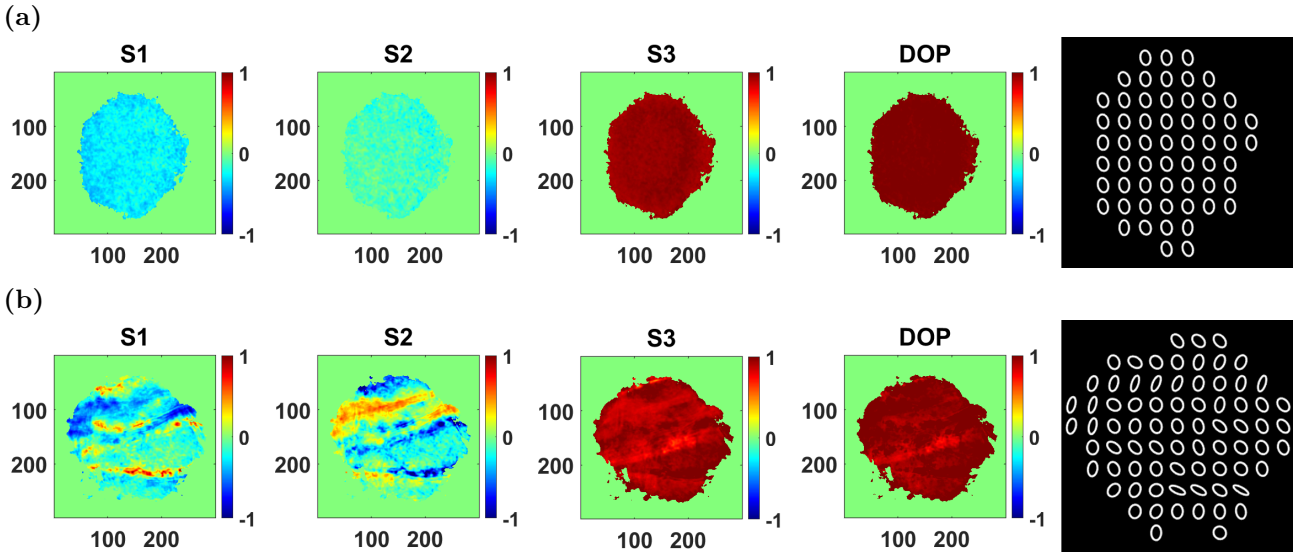

Figure 4.15: An investigation of the polarisation states of a wedge LC laser (E7 + 3.6 wt.% BDH1281 + 1 wt.% DCM) with and without alignment defects. The normalised Stokes parameters and DOP of each pixel across the wavefront and polarisation ellipse diagrams with one of every 25 pixels are demonstrated, corresponding to (a) 20.08 µm, where no alignment defects were observed across the region, and (b) 30.28 µm, where alignment defects (black lines on the corresponding microscope image) significantly reduce the DOP and circularity of the region.

Table 4.3: The circularity, linearity, and DOP of a wedge LC laser (E7 + 3.6 wt.% BDH1281 + 1 wt.% DCM) with and without alignment defects. The excitation fluence was 1406.6 µJ/cm^2/pulse and measurements were conducted at a room temperature of 20°C.

LC Layer Thickness (µm)	Circularity	Linearity	DOP
20.04 (planar aligned)	0.956	0.239	1.00
30.28 (defected aligned)	0.906	0.231	0.935

4.6 Summary

In conclusion, the polarisation states of band-edge LC lasers were measured and studied using a Stokes imaging polarimeter. By rotating the QWP to four distinct orientations, this polarimeter could reveal detailed Stokes parameters of the propagation beam, indicating the linearity, circularity, and DOP across the wavefront. Each polariser and waveplate combination was calibrated initially to minimise measurement error. To verify the effectiveness and accuracy of this measurement approach, both continuous wave and pulsed laser sources were measured (for different polarisation states), and the results were in good agreement with what was expected.

LC lasers emit wavelengths that are typically different from available commercial waveplates, However, the impact of this wavelength mismatch on Stokes parameter measurements was

found to be minimal, especially when the mismatch is only a few nanometres, provided the QWP of the Stokes imaging polarimeter was calibrated to a laser source matching the design wavelength of the QWP. To address the challenge of pulse-to-pulse variations in LC lasers, a technique of averaging over 10 pulses was employed, significantly reducing speckle-like noise in the measurement results and improving precision.

In general, it has been found that band-edge LC lasers are not perfectly, but nearly, circularly polarised with the same handedness as the LC helical structure. The polarisation states and DOP can be affected by multiple factors, including the excitation fluence of the pump source, the LC layer thickness, and alignment quality. Specifically, experiments suggest that higher excitation fluence correlates with an elevated DOP and fewer linear polarisation components at the beam edge, and thicker LC layers are associated with improved circularity, although the DOP of all thicknesses remains relatively similar. However, excessive thickness can lead to poor alignment quality and the appearance of alignment defects, which significantly reduce the DOP and circularity, especially around the defects. The highest circularity achieved was 0.956, with an excitation fluence of 1406.6 µJ/cm^2/pulse and a thickness of 20.04 µm. The slight ellipticity could be attributed to the refractive index mismatch between LCs and glass substrates.

The DOP of band-edge LC lasers can reach approximately one, suggesting the possibility of adjusting the polarisation state of LC lasers to be perfectly circular by adding a tuneable LC waveplate. Therefore, band-edge LC lasers become an ideal laser source to function with polarisation gratings, which are comprised of polymerisable LCs and can steer the propagating beam according to the incident polarisation state. In light of this, the next chapter will present the non-mechanical optical beam-steering of a band-edge LC laser, which exhibits multiple advantages compared to previous demonstrations of beam-steering of LC lasers.

5

Optical Beam-steering of a Liquid Crystal Laser

Contents

5.1 Chapter Introduction and Aims 107
5.2 Polarisation Gratings 110
5.3 Nematic LC Waveplates 113
5.4 Beam-steering Characterisation and Simulation 114
5.4.1 Characterisation of PGs 116
5.4.2 LC Laser Beam-steering 121
5.5 System Configuration and Experimental Results 124
5.6 Reconstructing the Jones Vector 131
5.7 Summary 133

5.1 Chapter Introduction and Aims

Steering a laser beam away from the original optical axis and directing it to a certain position in space is of considerable importance for numerous technological applications such as laser micromachining [165], microscopy [166] and optical wireless communications [167]. Conventional mechanical beam steering technology is typically based on macro-optical components, such as a Risley rotating prism [168], decentred lens [169] and reflective mirrors [170]. These achromatic optical devices can continuously deviate the primary beam within the whole field of view with a typical steering angle higher than 45° for the Risley prism and 25° for the decentred lens, whereas the challenge concerning these mechanical beam-steering methods is finding an appropriate combination of optical lenses and materials to ensure the wide-wavelength range of beam steering, especially in the infrared spectrum. Compared to the Risley prism, decentred

lenses for beam steering are not a practical approach, because the azimuth and elevation steering angles are linear to the displacement of the lenses requiring large overall dimensions. Reflective optical elements are the other choice in designing beam-steering systems. They possess the advantage of wavelength independence but are also limited with smaller field-of-view.

The above conventional mechanical beam steering approaches tend to be large, heavy and complex, thus non-mechanical, optoelectronic beam steering components are preferred (and sometimes essential) particularly for applications involving optical communications, navigation, or observation, where power, mass, and volume are primary drivers. Methods that have been developed so far include liquid crystal (LC) optical phased arrays [171], solid-crystal-based electro-optic modulators [172], acousto-optic modulators [173], and micro-electromechanical actuators [171]. An optical phased array steers the incident light by applying a linear phase shift across the wavefront so that the light would be steered propagating along an off-axis angle [174]. Furthermore, the ongoing developments of spatial light modulators (SLMs) include further functionality, such as beam shaping or splitting into multiple directions [175]. However, the use of an SLM is undesirable in some applications because of the cost and size of these systems. Apart from these approaches, researchers have also employed the use of passive [176] and active [177] thin-film LC polarisation gratings (PGs) to either mechanically [178] or nonmechanically [179] steer infrared laser sources (1064 nm and 1550 nm). PGs are particularly interesting for non-mechanical beam-steering systems because they are lightweight, compact, low-power, and inexpensive [180]. Combined with LC tuneable waveplates, a single PG device is capable of steering the beam to three diffraction orders according to the incident polarisation state, and further steering directions can be achieved by stacking multiple PGs or rotating the PGs with continuous scanning.

Apart from these beam steering technologies, researchers also have employed techniques to specifically steer the beam from LC lasers. In terms of the band-edge LC laser, recent reports focus on tuning the emission direction of a band-edge LC laser based on the engineered slanted helical structure so that the lasing occurs at a steered angle related to the helical axis [181]. A periodic dielectric tensor modulation is introduced along the direction perpendicular to the helical axis by a photoalignment method called "polarisation holography". The authors claim that they have achieved a horizontal patterning period of 620 nm within a left-handed dye-doped chiral nematic LC sample with a pitch of 400 nm, giving a slant angle of $\Lambda = 18°$ [148]. The

emission direction tunability is in the range of 27.4° to 31.3°. Inevitably, the wavelength of this LC laser also changes according to the relationship of $\theta_{lasing} = \sin^{-1}(\lambda_{lasing}/2\Lambda)$.

For defect mode lasers, beam steering has been demonstrated by mechanically bending a defect mode laser that consisted of two polymerised LC thin films separated by a dye-doped polymethylmethacrylate defect layer [182]. In this case, beam-steering of up to 42° with respect to the optical axis was demonstrated by mechanically deforming the device so as to vary the radius of curvature of the thin film from 0 mm to 5 mm. However, it was found that this process of LC laser beam-steering also resulted in an alteration of the laser wavelength together with a shift in the defect mode. In previous demonstrations, it is also likely that the emission intensity/efficiency was degraded during the process of beam-steering, although this was not discussed specifically.

This chapter demonstrates a non-mechanical method of steering a band-edge LC laser beam that takes place without deforming the LC macroscopic structure or the device architecture as well as not changing the laser wavelength or other emission characteristics such as the excitation threshold, slope efficiency, etc. This is achieved by adjusting the polarisation state of the LC laser based on the work presented in Chapter 4 using voltage-tuneable nematic LC devices and then steering the beam according to its current polarisation state by diffraction from PGs. This approach to non-mechanical beam-steering is based upon the concept proposed by Jihwan Kim et al. [176, 179]. Experimental results are presented, showing the optical steering of the LC laser emission to four separate discrete spatial positions and, using simulations based on Jones calculus, the appearance and relative intensities of other minor spots that appear around the primary beam are explained. Compared with other approaches of beam-steering an LC laser, this method does not result in an alteration of the laser wavelength, does not change the internal cavity structure of the laser, and has a minimal impact on the intensity of the laser emission. In addition, the entire system, except for the solid-state pump source, is comprised of thin films that are either liquid crystalline or polymers, which provides a tangible route towards a more compact and integrated optically steerable LC laser.

This work has been published in a peer-reviewed journal, Optics & Laser Technology, Volume 157, January 2023, 108623 (https://doi.org/10.1016/j.optlastec.2022.108623). A part of the work in this chapter was presented as an oral presentation at the SPIE Organic Photonics + Electronics 2023 and published in the conference proceedings, Liquid Crystals XXVII, September 2023, PC1265805 (https://doi.org/10.1117/12.2676363).

5.2 Polarisation Gratings

PGs, also known as Pancharatnam-Berry gratings, are space-variant polarisation devices with a periodic anisotropy across the plane which can change the phases of transmitted electric field components in one specific dimension. **Fig. 5.1** shows the detailed structure of a nematic LC and polymer-based PG [183] and the schematic diagram of the resulting diffraction. The LC director and its orientation in the cell are illustrated by the blue dashes and the spatial alignment of the LC is achieved by the photo-alignment layers attached to the glass substrates. Different from conventional phase or amplitude gratings, PGs divide a propagating plane wave into sub-waves and steer it to the +1 state and/or -1 state, which is dependent on the polarisation state of the wavefront. PGs combine numerous advantageous properties including a near-ideal diffraction efficiency of close to 100% and strong polarisation sensitivity in terms of the ± 1 diffraction states. These properties make PGs effective tools in spectral ellipsometers [184] and snapshot imaging polarimeters [185]. In addition, PGs have a wide range of other applications, such as in spatial heterodyne interferometers [186] and wavelength selective switches [187]. Research has also shown that PGs can be potentially used as polarisation-based multiplexers and demultiplexers, light modulators, or polarising beam splitters in optical data-transmitting communication systems [188]. A recent report introduces a novel approach to building a tuneable beam steering device based on Pancharatnam-Berry gratings using a linear array of phase control elements to control the in-plane alignment of LCs [189].

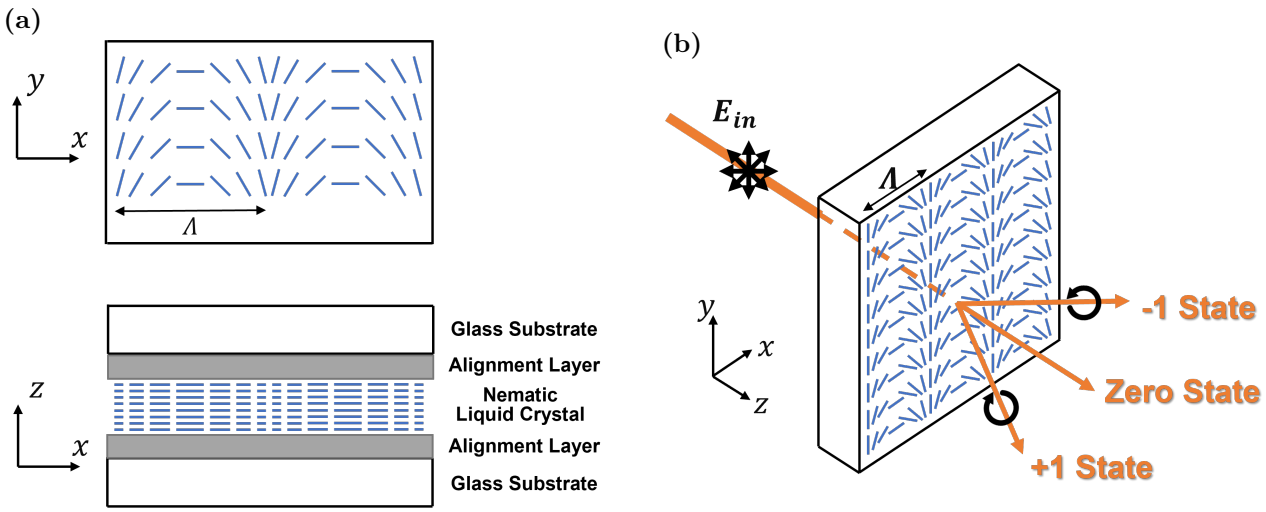

Figure 5.1: Illustration of the structure of a polymerisable LC PG. (a) The top view shows the alignment of the LC director, and the side view shows the device structure. (b) Illustration of the diffraction from the grating.

The PGs used in experiments mentioned in this chapter and the following experiments were sourced from Edmund Optics. They are designed for operation at a centre wavelength of 550 nm, and the retardance is quoted in the following analysis at this wavelength. These gratings are 0.45 ± 0.04 mm thick and 25.00 × 25.00 mm ± 0.25 mm in dimension with 286 grooves per millimetre. The diffraction angle and minimum diffraction efficiency are quoted as being 10° and 96%, respectively, resulting in a maximum of 4% light leakage into the zero-order (without being steered) regardless of the polarisation state of the incident light. The substrate of the PG is D263 glass with an anti-reflective coating. **Fig. 5.2** is a microscope image showing its internal texture. According to the measurement from this image, the period of this PG is about 3.3 µm, which is in agreement with the specification (3.5 µm) provided officially. Unpolarised light is diffracted evenly between the +1 and -1 orders while circularly polarised light is diffracted entirely into one specific order, depending upon the handedness of the polarisation. For convenience, the -1 state is defined as the diffraction state for left circularly polarised light, while the +1 state is defined as that for right circularly polarised light. The diffraction properties can be further illustrated by using Jones matrices [190].

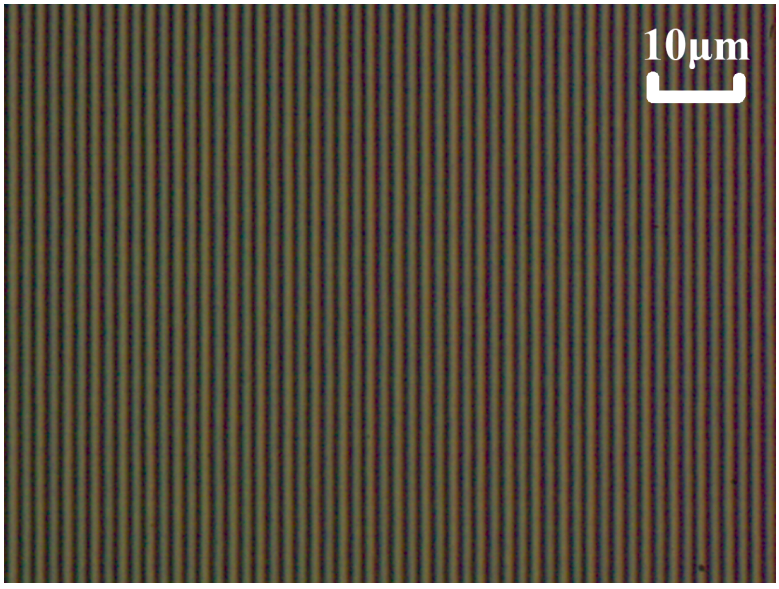

Figure 5.2: The PG used in this study was observed on an optical polarising microscope where the periodic anisotropy can be identified. The PG has 286 grooves/mm and is designed for a centre wavelength of 550 nm.

A recent report used a combination of the elastic continuum theory of LCs and Jones matrices to simulate the behaviour of light that was at oblique incidence to a series of cascaded PGs [191]. The Jones matrix for the PG can be determined by regarding it as a general retarder

with an arbitrary fast axis at an angle θ_P [185, 192] and a retardance of ϕ_P such that

$$J_P = \begin{bmatrix} \cos^2\theta_P + e^{i\phi_P}\sin^2\theta_P & \cos\theta_P\sin\theta_P - e^{i\phi_P}\cos\theta_P\sin\theta_P \\ \cos\theta_P\sin\theta_P - e^{i\phi_P}\cos\theta_P\sin\theta_P & e^{i\phi_P}\cos^2\theta_P + \sin^2\theta_P \end{bmatrix} \tag{5.1}$$

where θ_P is the spatial frequency term of the PG that represents the periodic rotation of the local fast axis in one dimension, and ϕ_P is the retardance of the PG that should be ideally π because the PG behaves as a half waveplate (HWP) at the designed wavelength. If the periodicity of the PG along the x-axis is Λ and the light is propagating along the z-axis, then the spatial frequency term can be expressed as

$$\theta_P = 2\pi x/\Lambda \tag{5.2}$$

For an ideal PG working at the centre wavelength, $\phi_P = \pi$, and therefore Eq. (5.1) can be further simplified to

$$J_P = \begin{bmatrix} \cos^2\theta_P - \sin^2\theta_P & 2\cos\theta_P\sin\theta_P \\ 2\cos\theta_P\sin\theta_P & \sin^2\theta_P - \cos^2\theta_P \end{bmatrix} \tag{5.3}$$

Suppose the incident light is right-handed circularly polarised, the Jones matrix for its two orthogonal electric field components can then be expressed as

$$E_{in} = \frac{1}{\sqrt{2}}\begin{bmatrix} 1 & -i \end{bmatrix}^T \tag{5.4}$$

The Jones matrix of the output electric field after the incident light has propagated through a PG is then given by:

$$\begin{aligned} E_{out} &= \begin{bmatrix} \cos^2\theta_P - \sin^2\theta_P & 2\cos\theta_P\sin\theta_P \\ 2\cos\theta_P\sin\theta_P & \sin^2\theta_P - \cos^2\theta_P \end{bmatrix} \frac{1}{\sqrt{2}}\begin{bmatrix} 1 & -i \end{bmatrix}^T \\ &= \frac{1}{\sqrt{2}}\begin{bmatrix} \cos^2\theta_P - \sin^2\theta_P - 2i\cos\theta_P\sin 2\theta_P \\ 2i\cos\theta_P\sin 2\theta_P - i(\sin^2\theta_P - \cos^2\theta_P) \end{bmatrix} \\ &= \frac{1}{\sqrt{2}}\begin{bmatrix} (\cos\theta_P - i\sin\theta_P)^2 \\ i(\cos\theta_P - i\sin\theta_P)^2 \end{bmatrix} \\ &= \frac{1}{\sqrt{2}}\begin{bmatrix} 1 & i \end{bmatrix}^T e^{-2i\theta_P} \end{aligned} \tag{5.5}$$

The derivation for left-handed circularly polarised incident light is similar. Considering Eq. (5.2), the $e^{-2i\theta_P}$ in Eq. (5.5) represents the phase shift as a function of the position along the x-axis introduced by the PG, which leads to beam steering. The $\frac{1}{\sqrt{2}}\begin{bmatrix} 1 & i \end{bmatrix}^T$ indicates that the output light is now left-handed circularly polarised. In other words, the PG would steer the beam totally to one particular diffraction direction, either the +1 state or -1 state, and convert the handedness of a circularly polarised beam having the same wavelength as the designed centre wavelength of the PG.

5.3 Nematic LC Waveplates

Waveplates, usually made of birefringent crystals, are widely used in the field of optical polarisation. This essential optical element contributes to a variety of applications in displacement measurements [193], coherence tomography [194], nonlinear optical system [195], etc. Waveplates change the phase and the polarisation state of the incident light depending on three key properties, the retardance and the orientation of the fast and slow axes. Retardance is the difference in optical phase shift between two polarisation components. The fast axis is the direction along which polarised light encounters the lowest refractive index and travels the fastest through the waveplate than light with other orientations of the polarisation. The slow axis lies along a direction perpendicular to the fast axis of the waveplate within the plane perpendicular to the propagation direction.

Suppose light with a vacuum wavelength of λ_0 is propagating through a waveplate with birefringence Δn and thickness L. The amount of relative phase difference, Γ, that arises between the two orthogonal components is calculated to be

$$\Gamma = \frac{2\pi \Delta n L}{\lambda_0} \tag{5.6}$$

that is, the waveplate introduces an extra phase difference of Γ to the polarisation component along the slow axis. The three most commonly used waveplates are quarter waveplates (QWPs), HWPs, and full waveplates (FWPs), with the relative phase differences (assuming zero-order) being $\pi/2$, π, and 2π, respectively.

Just like the PG, the Jones matrix method is also an effective mathematical tool to describe the change in polarisation for light propagating through waveplates. The Jones matrices for a QWP, HWP, and FWP, respectively, can be written as [139]

$$J_{QWP} = e^{-\frac{i\pi}{4}} \begin{bmatrix} \cos^2\theta + i\sin^2\theta & (1-i)\cos\theta\sin\theta \\ (1-i)\cos\theta\sin\theta & \sin^2\theta + i\cos^2\theta \end{bmatrix} \tag{5.7}$$

$$J_{HWP} = e^{-\frac{i\pi}{2}} \begin{bmatrix} \cos^2\theta - \sin^2\theta & 2\cos\theta\sin\theta \\ 2\cos\theta\sin\theta & \sin^2\theta - \cos^2\theta \end{bmatrix} \tag{5.8}$$

$$J_{FWP} = e^{-i\pi} \begin{bmatrix} \cos^2\theta + \sin^2\theta & 0 \\ 0 & \sin^2\theta + \cos^2\theta \end{bmatrix} = - \begin{bmatrix} 1 & 0 \\ 0 & 1 \end{bmatrix} \tag{5.9}$$

where θ is the angle of the fast axis with respect to the x-axis.

For instance, if linear polarised light in the y-axis (with Jones vector $\begin{bmatrix}0 & 1\end{bmatrix}^T$) propagates through a QWP with the orientation angle of $\theta = 45°$, then the Jones matrix of the output is

$$J_{out} = e^{-\frac{i\pi}{4}} \begin{bmatrix} \cos^2 45° + i\sin^2 45° & (1-i)\cos 45° \sin 45° \\ (1-i)\cos 45° \sin 45° & \sin^2 45° + i\cos^2 45° \end{bmatrix} \begin{bmatrix} 0 \\ 1 \end{bmatrix} = \frac{1}{\sqrt{2}} \begin{bmatrix} -i \\ 1 \end{bmatrix} \tag{5.10}$$

Here, the resulting vector of Eq. (5.10) represents that the output is left-handed circularly polarised light. The combination of linear polarised light and a QWP is therefore an effective tool for producing circularly polarised light.

Chapter 2 has introduced the dielectric anisotropy and birefringence properties of nematic LCs. Nematic LCs exhibit refractive indices of different values parallel and perpendicular to the optic axis, where the optic axis is defined to be colinear with the director $\hat{\boldsymbol{n}}$ of the uniformly aligned nematic LC. The director $\hat{\boldsymbol{n}}$ can be reoriented by applying an external electric field, and thus, the birefringence of a nematic LC cell can be changed with the electric field strength. When the incident light is polarised parallel to the slow axis (in the direction of $\hat{\boldsymbol{n}}$), the nematic LC cell can be used as a voltage-controllable phase modulator. It applies an extra phase delay depending on the voltage value when the light is transversing the cell. Alternatively, if the incident light possesses electric field components both parallel and perpendicular to the slow axis, the nematic LC cell functions as a continuously variable retarder. The Jones matrix for a nematic LC cell functioning as a tuneable wave plate can be expressed as

$$J_N = \begin{bmatrix} \cos^2\theta_N + e^{i\phi_N}\sin^2\theta_N & \cos\theta_N \sin\theta_N - e^{i\phi_N}\cos\theta_N \sin\theta_N \\ \cos\theta_N \sin\theta_N - e^{i\phi_N}\cos\theta_N \sin\theta_N & e^{i\phi_N}\cos^2\theta_N + \sin^2\theta_N \end{bmatrix} \tag{5.11}$$

where θ_N is the orientation angle of the fast axis with respect to the x-axis, and ϕ_N is the retardance of the LC wave plate introduced between the fast and slow axes.

The nematic LC waveplates used in later experiments were fabricated by capillary filling the nematic LC mixture, E7 (Synthon Chemicals Ltd), into commercially available 5 µm thick anti-parallel rubbed glass cells (LC-2, Instec) that are coated with indium-tin-oxide (ITO) electrodes and mechanically-rubbed polyimide alignment layers.

5.4 Beam-steering Characterisation and Simulation

Based on the working principles of PG diffractions and tunable nematic LC waveplates, Fig. 5.3 illustrates the concept and configuration of LC laser beam-steering. In this work, optical

beam-steering of an LC laser was demonstrated in both the horizontal and vertical directions. However, in principle, additional discrete positions could be achieved by incorporating extra tunable phase shifters and PGs, as demonstrated by Jihwan Kim et al. [176, 179, 196]. The steering of the beam occurs with minimal impact on the intensity of the laser beam because the helical structure of the chiral nematic LC remains unchanged.

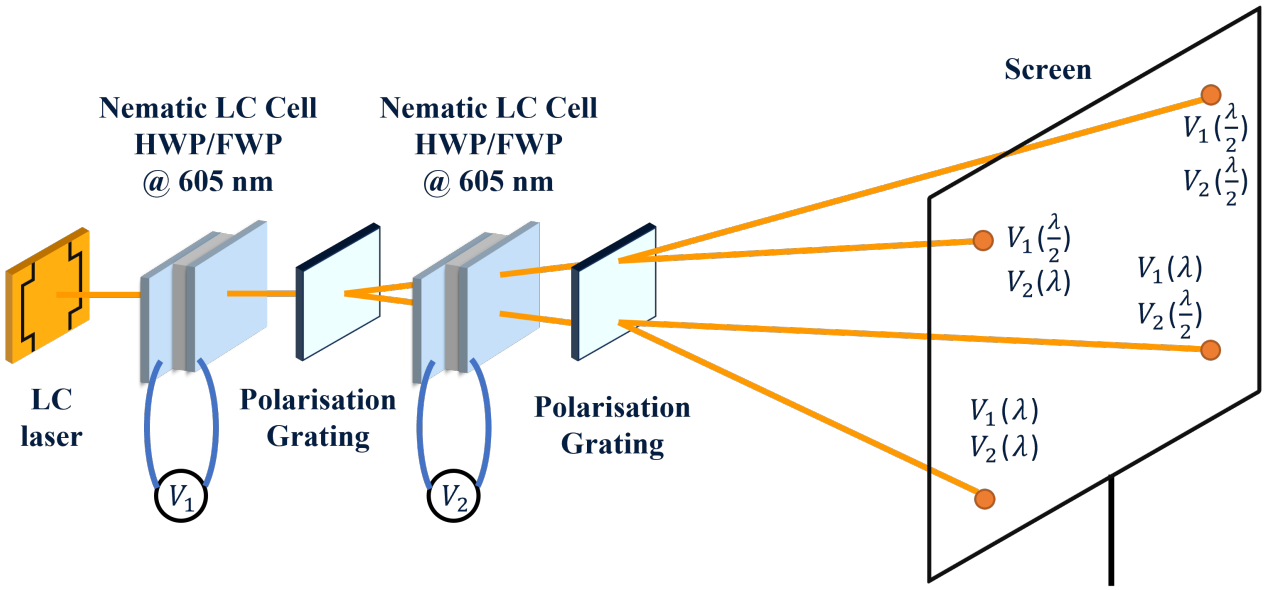

Figure 5.3: Optical beam-steering of an LC laser using tuneable nematic LC waveplates and PGs. By applying different voltages to the nematic LC cells so that they function as HWPs or FWPs, the beam can be steered to one of four different spatial locations as illustrated in the figure. V_1: the voltage applied to the first nematic LC cell; V_2: the voltage applied to the second nematic LC cell.

As discussed in Chapter 4, although not perfect, the polarisation states of band-edge LC lasers are nearly circular. This characteristic allows band-edge LC lasers to work directly with PGs, which require the incident beam to be circularly polarised for effective beam-steering. When two orthogonal PGs are implemented in the system, the LC laser can be steered horizontally and vertically. The beam-steering direction is controlled by the voltage applied to the nematic LC cells, which switches them between HWPs or FWPs, thereby altering or maintaining the handedness of the incident beam, respectively. However, further results revealed the presence of additional spots of much lower intensity surrounding the primary beam during beam-steering. This necessitates a calibration process before analysing the polarisation state and beam-steering of LC lasers. The commercial PGs used in the experiments do not exhibit ideal diffraction properties, resulting in multiple steered beams rather than just one. Additionally, numerical simulations based on Jones matrices were conducted to support the explanation of the PG diffraction patterns in the far field.

Specifically, the calibration of PGs was performed by investigating the diffraction pattern of a commercial laser source with known polarisation states and analysing the appearance of multiple steered beams, with the verification of a Jones matrix simulation method providing more accurate results. The characterisation of band-edge LC laser beam-steering was subsequently demonstrated, suggesting similar polarisation properties of the LC laser as those measured previously via its Stokes parameters.

5.4.1 Characterisation of PGs

A continuous-wave Helium-Neon (He-Ne) laser (05-LGP-193, Melles Griot) with an emission wavelength at 543.5 nm was used to initially characterise the PGs. First, the polarisation of the He-Ne laser was converted to be right circularly polarised by a combination of a polariser and a QWP (designed for operation at 546 nm). A CCD camera (DCU224C, Thorlabs) was used to capture the diffraction pattern on a screen placed in the far-field away from the PGs. The experimental system used to characterise the PG and the corresponding results are shown in **Fig. 5.4**(a) and (d) for either one PG or a combination of two PGs. Note that the intensity emitted from the He-Ne laser was above the saturation level for the CCD camera, thus an extra neutral density filter was placed after the laser; this component is not shown in the configuration for simplicity. When only one PG was placed in the system, the He-Ne laser with right-handed circular polarisation was steered vertically upwards to the (0, +1) position with the corresponding far-field pattern observed on the screen shown in Fig. 5.4(b). However, other minor spots are captured, as shown in Fig. 5.4(c), possessing significantly lower intensities compared to the primary beam at (0, +1) with a higher intensity input by removing the neutral density filter.

Similarly, when two PGs were placed such that they were aligned orthogonally in the system, the beam was first steered upwards and the circular polarisation was switched to the opposite handedness due to the retardance of the PG emphasised in Eq. (5.10), then steered leftwards to the (-1, +1) position. The system configuration and far-field pattern observed on the screen with a lower intensity below the saturation level, as well as that with a higher intensity input without the neutral density filter are shown in **Fig. 5.5**(d∼f), respectively.

The additional spots with minor intensities in Fig. 5.4(c) and Fig. 5.5(c), which also have been observed by other researchers [179, 197], can be divided into three categories: zero-order, sub-order, and opposite-order spots. The zero-order spots are non-diffracted spots (with zero

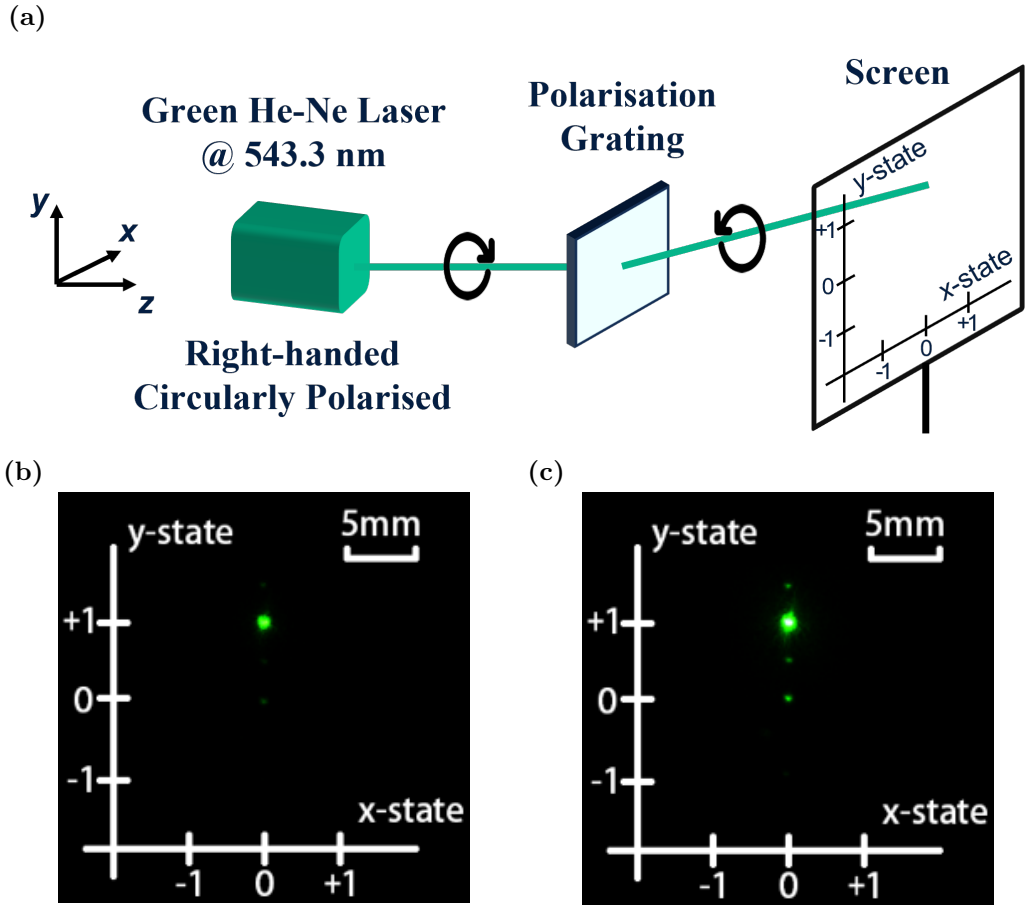

Figure 5.4: Experimental demonstration of one-dimensional beam-steering using a liquid crystalline polymer PG. (a) One-dimensional beam-steering of a He-Ne laser using a single PG and (b) the corresponding far-field pattern observed on a screen placed at a distance of 20 cm from the PGs. (c) The far-field pattern was recorded when the input laser intensity was increased so that the other weaker intensity spots can be observed on the screen. Here the primary spot saturates the camera.

diffraction angle) that appear at the zero position in the x and y-coordinates defined in this work. In addition to the inherent zero-order leakage that occurs due to imperfections in the PG, a mismatch in the wavelength between the emission wavelength of the laser and the design wavelength of the PG is another reason for the appearance of the zero-order spot. Specifically, the retardance of a PG, ϕ_P, is expected to be given by $\phi_P = 543.5\pi/550$ when working with the He-Ne laser. The spots that surround the primary beam with much weaker intensities, on the other hand, are defined as sub-order spots. The diffraction angles of these spots are at $\pm 5°$ and $\pm 15°$, which equals one-half or 1.5 times the designed diffraction angle of the PG. The appearance of these spots is assumed to be caused by a slightly asymmetrical periodic structure of the PGs. The so-called opposite-order spots, with the opposite diffraction angle to the primary beam, possess the opposite polarisation state to that of the primary beam. There

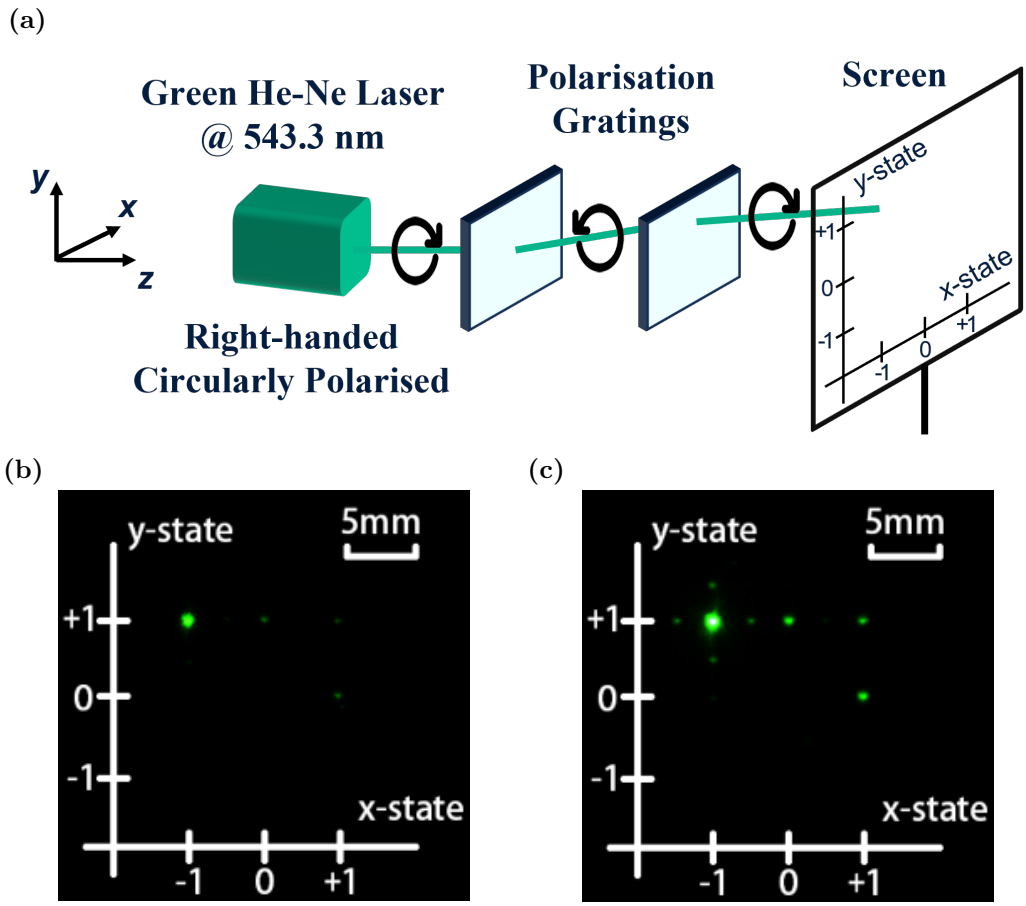

Figure 5.5: Experimental demonstration of two-dimensional beam-steering using liquid crystalline polymer PGs. (a) Two-dimensional beam-steering of a He-Ne laser using two PGs placed with their axes orthogonal to one another and (b) the corresponding spot pattern on the screen. (c) The far-field pattern is recorded with increased input intensity so that the other weaker spots can be observed on the screen.

are two reasons why opposite-order state spots might appear: one reason could be that there is a slight residual birefringence introduced by the PG substrates and the other reason is that the incident light does not have an ideal circular polarisation state. All these characteristics can be accounted for with simulations carried out based on Jones matrices (vide infra).

According to the Huygens-Fresnel principle and scalar diffraction theory, the diffraction of light can be derived using Fresnel and Fraunhofer approximations, respectively [198]. The critical conditions of these two diffraction regimes depend on the value of the Fresnel number, F, which is defined as

$$F = a^2/\lambda z \tag{5.12}$$

where a is the characteristic size of the aperture (e.g., the radius), λ is the incident light wavelength and z is the distance of the screen from the aperture. As for the PG diffraction

in the experiments, a is treated as the radius of the LC laser beam which is of the order of 0.1 mm (measured in Chapter 3), and z is of the order of 10 cm. Thus, the Fresnel number here satisfies $F \gg 1$ which indicates that the propagating beam can be described as far-field Fraunhofer diffraction, in which

$$U(x,y) = \frac{e^{ikz}e^{i\frac{k}{2z}(x^2+y^2)}}{ikz}\iint_{-\infty}^{+\infty} U(\xi,\eta)\exp\left[-i\frac{2\pi}{\lambda z}(x\xi+y\eta)\right]d\xi\,d\eta \tag{5.13}$$

where (ξ,η) and (x,y) are the coordinates of the aperture plane and screen plane, respectively, while $U(\xi,\eta)$ and $U(x,y)$ represent the optical fields at the aperture and where the screen is placed in the far-field, respectively. k is termed the wave number given by $k = 2\pi/\lambda$. Aside from the multiplicative phase factor before the integral sign, Eq. (5.13) indicates that the complex disturbance of the light on the screen is simply the Fourier transform of the aperture (PG) distribution, evaluated at frequencies

$$\begin{cases} f_x = x/\lambda z \\ f_y = y/\lambda z \end{cases} \tag{5.14}$$

To investigate the slight asymmetrical periodic structure of the PGs, each birefringence period Λ is divided into two parts with unequal lengths $k\Lambda$ and $(1-k)\Lambda$, where k is a constant parameter less than 0.5. The fast axis angle θ_P rotates by π within $k\Lambda$ and $(1-k)\Lambda$, respectively. That is, in each birefringence period, the angle θ_P takes the form

$$\begin{cases} \theta_P = \pi x/\Lambda', & \text{when } x \le \Lambda' \\ \theta_P = \pi + \pi x/\Lambda', & \text{when } x > \Lambda' \end{cases} \tag{5.15}$$

Finally, the intensity of light on the screen is calculated as the squared magnitude of the electric field complex phasor.

$$I_{screen} = |E_{screen}|^2 = E_{screen}\cdot E^*_{screen} \tag{5.16}$$

Applying the Jones matrices of PGs and nematic LC waveplates according to Eq. (5.1) and Eq. (5.11), as well as the Fourier transform derivation above, the diffraction simulations for one and two-dimensional beam-steering of the He-Ne laser with the PGs were carried out and the relative intensities for each spot are shown in Fig. 5.6. In addition, the laser intensities of all orders on the screen were measured using a photodiode (PD) (PDA36A-EC, Thorlabs) connected to an oscilloscope (TBS1052C, Tektronix). A PD is a semiconductor device with a

P-N junction that converts light (photons) into an electrical current. Within the response range, the PD generates a linear voltage response according to the intensity of the incident light. For the incident pulsed light, the peak-to-peak value of the voltage signal generated by the PD is proportional to the intensity of the pulsed light. The neutral density filter after the Nd:YAG laser and the gain of the PD was adjusted to avoid over-saturation of the detector.

Fig. 5.6(a) and (b) are the simulation and experimental results for one-dimensional beam-steering. The primary beam appears at the +1 state while minor sub-order spots are observed at the (0, +0.5) position and (0, +1.5) position. There is also a zero-order at the centre in Fig. 5.6(b), which can be considered to be entirely from intrinsic zero-order leakage with a value of 1.6% of the total incident power. Similarly, Fig. 5.6(c) and (d) are the simulation and experimental results for two-dimensional beam-steering, where the primary beam is located at the (-1, +1) position surrounded by four minor sub-order spots. Two spots are found at the (0, +1) and (+1, 0) positions as well as an opposite-order spot at the (+1, +1) position. The primary beam has a relative intensity of 0.91 while that of the zero-order spot at (0, +1) is 0.02 which is the highest of all the spots excluding the primary beam. This result is similar to that found in another study that employed a ray-tracing tool to simulate two-dimensional beam-steering achieved by a 1550 nm laser and corresponding PGs [197]. The main spot had a relative power of 87% of the total power and any of the highest intensity single side spots were still lower than 1.5% of the total power (these side spots were claimed to be caused mainly by the zero-order leakage of the PGs).

The value of the asymmetrical period parameter k and the additional residual birefringence introduced by the PG substrates can be estimated by adjusting their values so that the simulation results are close to the experimental measurements. Specifically, it was found that the simulations closely matched the experiments when the asymmetrical period parameter k was set to 0.46 and the additional residual birefringence introduced by the PG substrates was set to 0.05π. The similarity between Fig. 5.6(a) and (b), together with Fig. 5.6(c) and (d) suggests that the asymmetrical periodic structure of the PG results could indeed be the reason for the appearance of the sub-order spots and that the residual birefringence of the substrates gives rise to spots with the opposite handedness polarisation on the screen. In most previous reports the focus has been on the investigation of the first and zeroth order spots [197, 199, 200], while this work also presents an explanation for the appearance of sub-order and opposite-order spots.

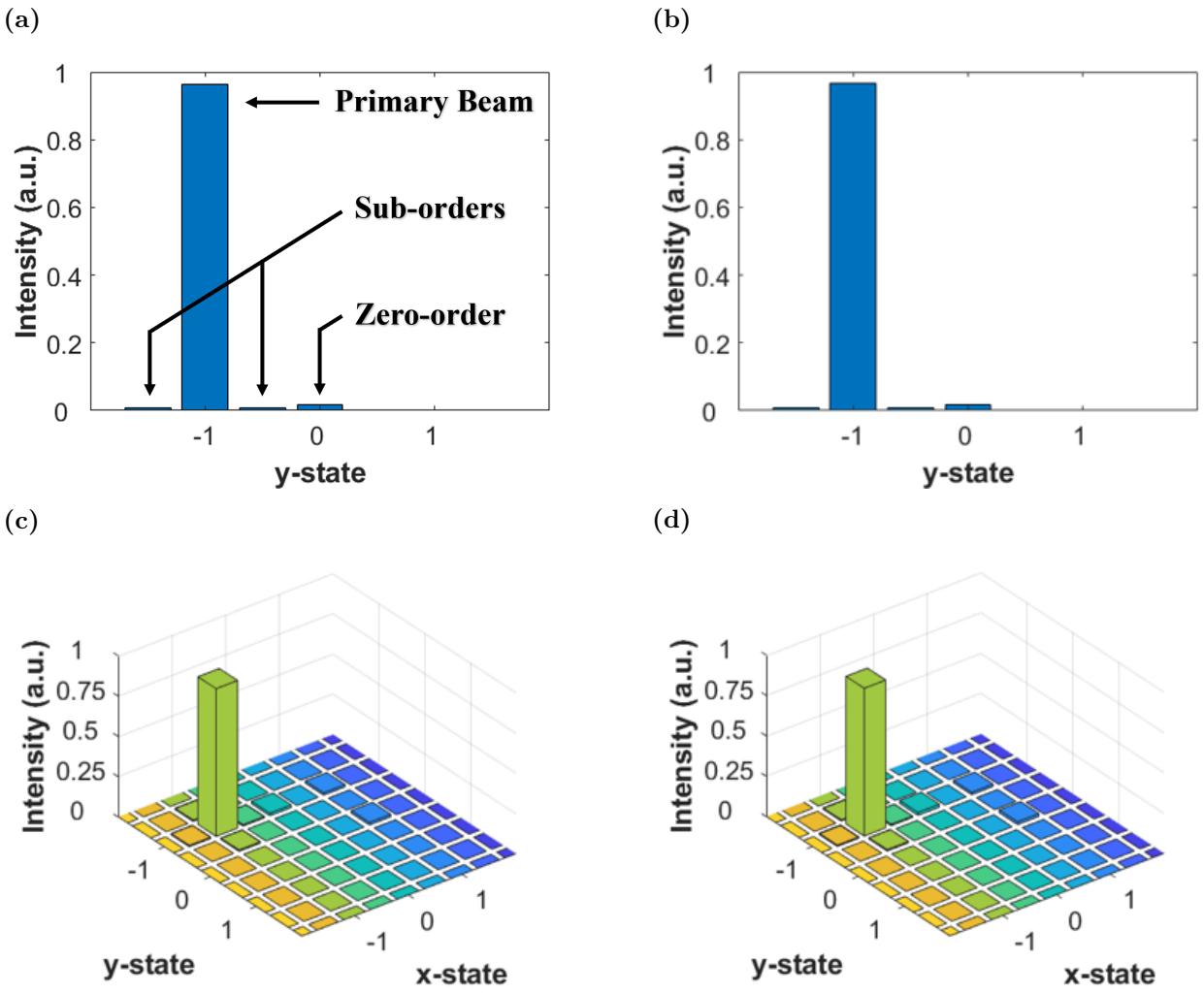

Figure 5.6: Simulations and experimental results for the relative intensity of each spot observed (primary beam, zero-order, sub-order spots) in the far-field pattern for both one and two-dimensional beam-steering of a He-Ne laser. (a) Simulation result for one-dimensional beam-steering and the corresponding (b) experimental result for one-dimensional beam-steering using a single PG. (c) Simulation result for two-dimensional beam-steering and (d) the corresponding experimental result for two-dimensional beam-steering.

5.4.2 LC Laser Beam-steering

The LC laser used in this study was fabricated from a dye-doped chiral nematic LC mixture of E7, 2.5 wt.% R5011 and 1 wt.% of the laser dye DCM (4-(Dicyanomethylene)-2-methyl-6-(4-dimethylaminostyryl)-4H-pyran). E7 is a well-known nematic LC mixture (Synthon Chemicals ltd), R5011 is a right-handed chiral dopant (Merck KGaA), and DCM (Exciton) is a commonly used laser dye with a typical lifetime in an LC host of 2 ns and a quantum efficiency of 45% [77]. The concentration of the chiral dopant was chosen so that the long-wavelength band-edge approximately coincided with the gain maximum of the DCM laser dye. The mixture was then

capillary filled into a glass cell with anti-parallel rubbed polyimide alignment layers and spacer beads dispersed in the glue walls that resulted in a cell gap of 8.4 µm.

The optical pump source for this LC laser was a solid-state frequency-doubled Nd:YAG laser (6FTSS355-Q4-S, CryLas) with a wavelength of 532 nm and a pulse length of 1 ns. The emission energy of the pump beam was controlled using a manually controlled neutral density filter. To minimise photo-bleaching of the sample [120], the repetition frequency was set to 10 Hz. The Nd:YAG laser output was converted to left-handed circularly polarised light by a combination of a polariser and a QWP. This laser beam was used to excite the dye-doped chiral nematic LC cell to produce an LC laser output with a near right-handed circularly polarisation state, which was then collected by a microscope objective with a magnification of 4 times and a numerical aperture of 0.1. The 532 nm pump laser radiation was removed from the detection system using a long-pass edge filter. The LC laser had a wavelength of 605.1 nm and an excitation threshold of 671.9 µJ/cm^2/pulse. Results for the characterisation of the LC laser, in terms of the emission wavelength and the excitation threshold, are presented in Chapter 3.

When only one PG is placed in the system, the LC laser with right-handed circular polarisation is steered vertically upwards to the (0, +1) position. The experimental configuration and the far-field pattern observed on the screen are shown in **Fig. 5.7**(a) and (b), respectively. Fig. 5.7(c) shows an example image captured with a higher intensity input so that the zero-order and opposite-order spots can be clearly seen. Compared to the beam-steering results obtained for the He-Ne laser, this LC laser produces a slightly stronger zero-order spot because of the larger wavelength mismatch (605 nm for the LC laser compared with the design wavelength of the PG of 550 nm). In addition, the opposite-order spot for this LC laser in Fig. 5.7(c) also possesses a higher relative intensity compared with that observed for the circularly polarised He-Ne laser in Fig. 5.4(c), which indicates that the residual birefringence of the PG substrates is not the only reason for the appearance of the opposite-order spots and the incident LC laser beam is not purely circularly polarised in this case. This observation is in accordance with the study on band-edge LC laser polarisation states presented in Chapter 4.

When a second identical PG is added to the system, the configuration and spot pattern are shown in Fig. 5.8(a) and (b). Fig. 5.8(c) is another example of an over-exposed image to demonstrate the appearance of the secondary lower-intensity spots. The primary beam at (0, +1) in Fig. 5.7(c) exhibits a right-handed circular polarisation state before diffraction and is

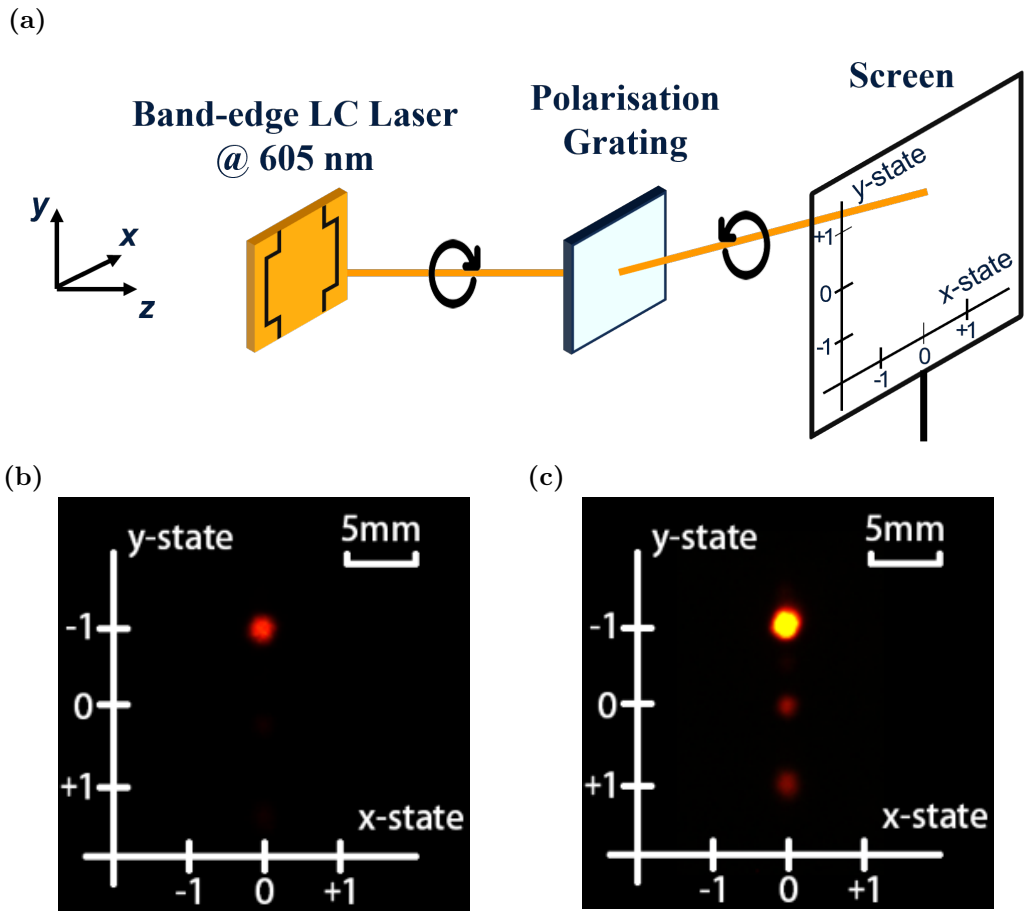

Figure 5.7: Demonstration of (a) one-dimensional beam-steering of an LC laser using one PG and (b) the corresponding diffraction pattern recorded on the screen. (c) The primary beam is allowed to saturate the camera so that the other spots can be seen on the screen. The thickness of the LC layer was 8.4 µm while the measurement were conducted at a room temperature of 20°C.

nearly left-handed circularly polarised after the diffraction from the first PG (with a phase delay of $605\pi/550$ introduced by the PG). Consequently, the diffraction by the second PG steers it to (-1, +1) leaving a zero-order spot at (0, +1) due to the wavelength mismatch. The other two spots in Fig. 5.8(c), at (+1, 0) and (+1, -1), are correspondingly diffracted from the two spots in Fig. 5.7(c), at (0, 0) and (0, -1), respectively.

Since the LC laser is not purely circularly polarised, it is simulated by an elliptically polarised source with an initial phase difference of 0.3π between the x and y components of the electric field vectors. This initial phase difference will be optimised by reconstructing the Jones vector for the LC laser according to the Stokes parameters measured in Chapter 4. The simulation results for one- and two-dimensional beam-steering of an LC laser are shown in **Fig. 5.9**(a) and (c), respectively. The location and corresponding intensities of the primary beam, zero-order and opposite-order spots are labelled in Fig. 5.9(a). These simulation results are in good agreement

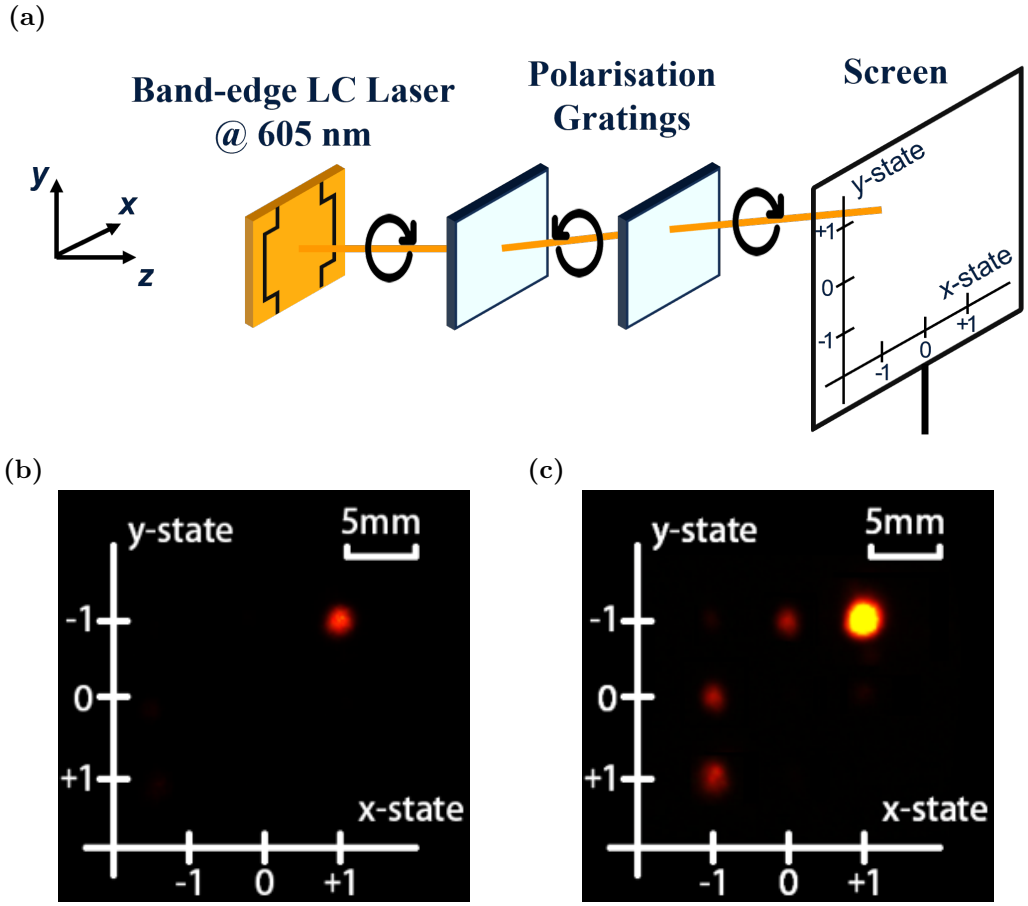

Figure 5.8: Demonstration of (a) two-dimensional beam-steering of an LC laser using two PGs placed with their axes orthogonal to one another and (b) the corresponding diffraction pattern observed on the screen. (c) The primary beam saturated the camera in order to see the other weaker intensity spots on the screen. The thickness of the LC layer was 8.4 µm while the measurement were conducted at a room temperature of 20°C.

with the experimental results as shown in Fig. 5.9(b) and (d). This demonstrates the validity of the Jones matrix simulation as well as the modelling of the LC laser and the PGs.

5.5 System Configuration and Experimental Results

The next step is to demonstrate the dynamic steering of the LC laser to any one of four spatial locations (-1, +1), (+1, +1), (+1, -1), and (-1, -1) through the introduction of tuneable nematic LC wave plates in accordance with previous studies [176, 179, 197]. The experimental configuration used in this study to dynamically steer the beam is illustrated in **Fig. 5.10**. The Nd:YAG laser produced a pulsed laser output with a frequency of 10 Hz, which was converted by a polariser and a QWP into left-handed circularly polarised light. This laser beam excites the dye-doped chiral nematic LC cell to produce an LC laser output with a

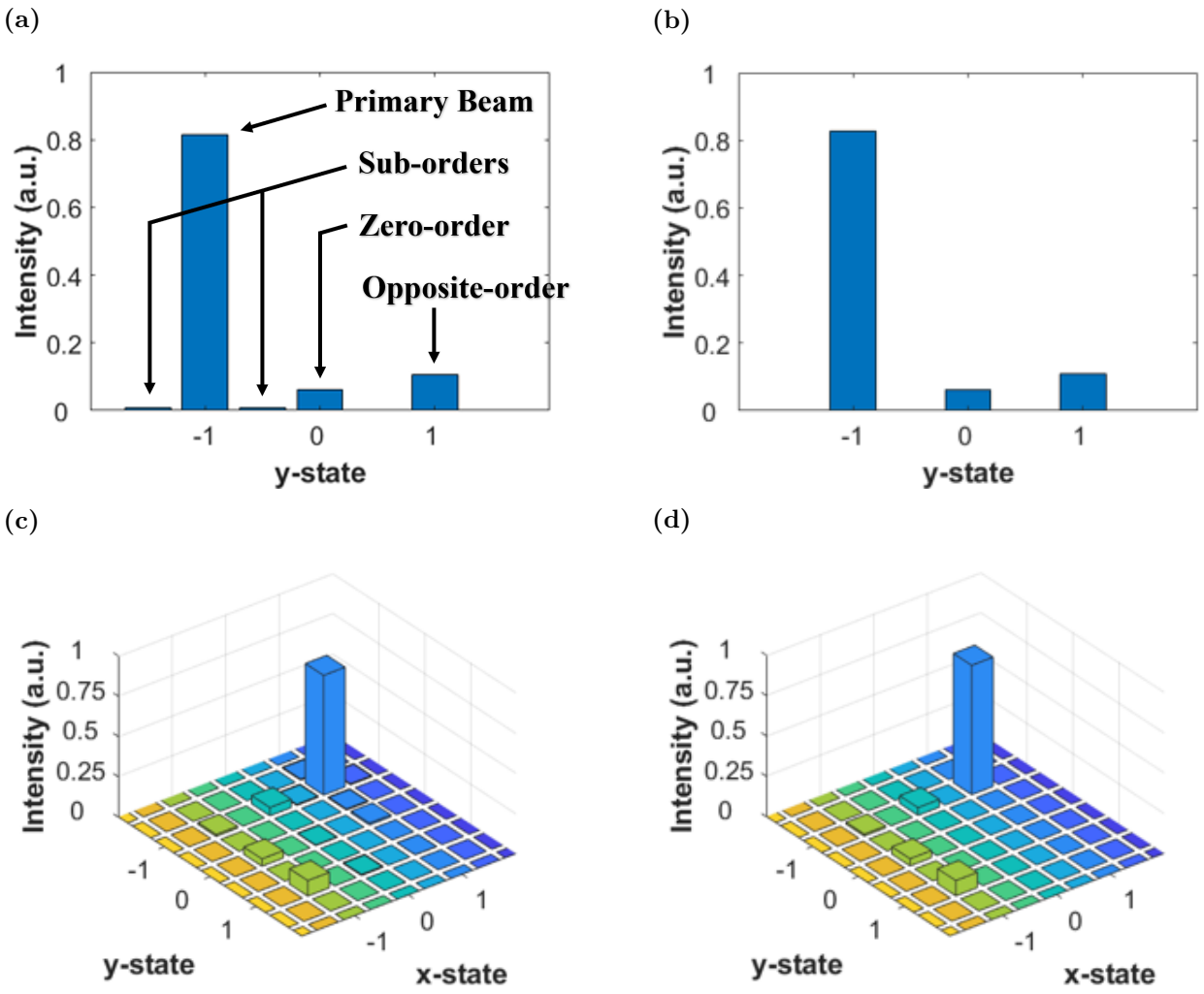

Figure 5.9: Simulation and experimental results for the relative intensity of each spot observed in the far-field when steering emission from the LC laser. (a) Simulation results for one-dimensional beam-steering and (b) the corresponding experimental results for one-dimensional beam-steering. (c) Simulation results for two-dimensional beam-steering and (d) the corresponding experimental results for two-dimensional beam-steering.

near right-handed circularly polarisation state, which is collected by the objective lens. The Nd:YAG laser was filtered out by a long-pass edge filter.

Since the nematic LC cells can work as tuneable waveplates at different voltages, it becomes possible to switch the polarisation state of the LC laser. The nematic LC cell alters the handedness of the LC laser when the correct voltage is applied so that it behaves as a half-waveplate at the wavelength of the LC laser. The beam would then be steered in the opposite direction by the PG. When two nematic LCs and two PGs are placed behind the laser, four directions of beam steering (left-top, right-top, left-bottom and right-bottom) in the $x-y$ plane can be achieved. If the first nematic LC cell acts as an FWP, the LC laser polarisation state

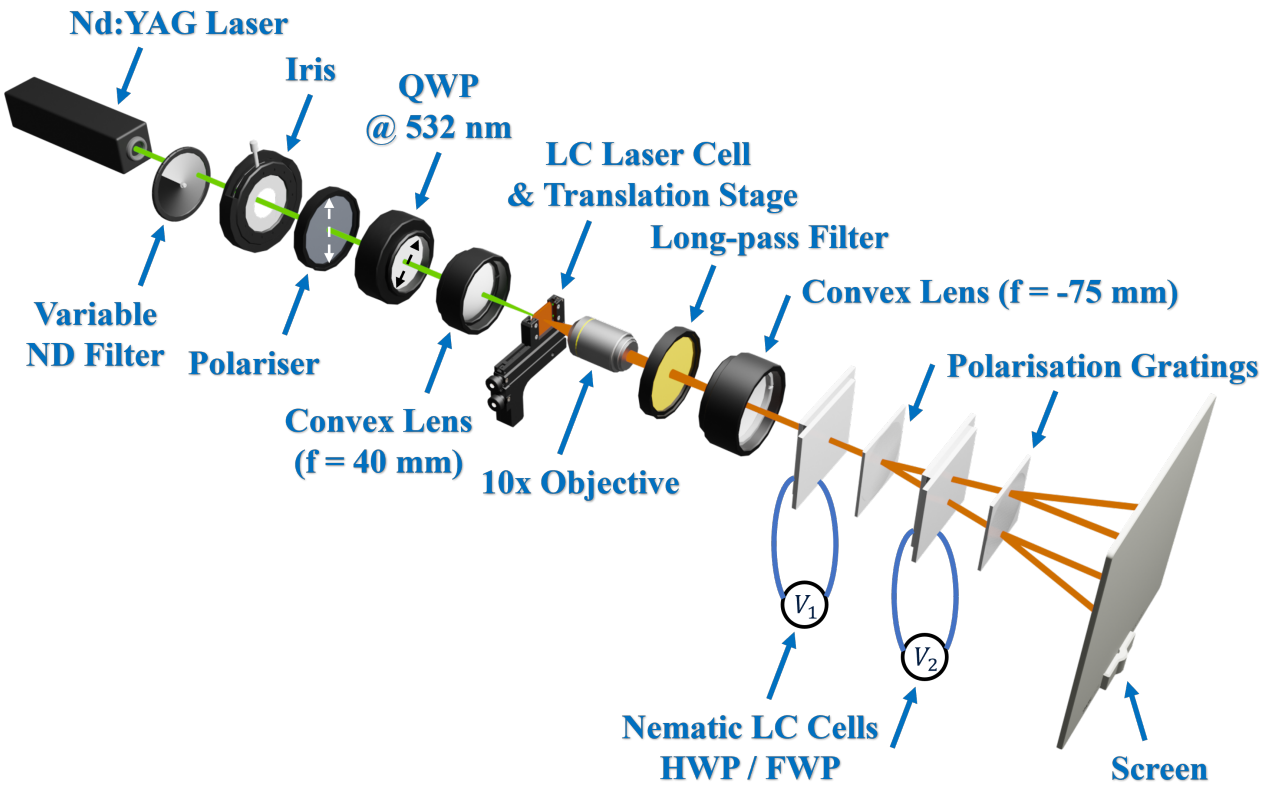

Figure 5.10: The system configuration used to demonstrate dynamic optical beam-steering of an LC laser. QWP: QWP; V_1: the voltage applied to the first nematic LC cell; V_2: the voltage applied to the second nematic LC cell.

is maintained and is diffracted to the +1 state (in the y-direction) by the first PG. When the nematic LC is used as an HWP, on the other hand, the LC laser is reversed to the opposite handedness, which is then diffracted to the -1 state (in the y-direction). In the same way, the second nematic LC cell can also maintain or alter the handedness of the LC laser by controlling the magnitude of the voltage V_2, so as to switch the beam-steering direction between the +1 state (x-direction) and the -1 state (x-direction). The combination of the two PGs and two nematic LC devices means that the beam can be switched from say the (+1, +1) position to the (-1, -1) position by changing the waveplate conditions of the nematic LC devices.

The voltages at which the nematic LC cell behaves as an HWP or FWP are specified by initially removing the second set of nematic LC cell and PG from the system leaving only one nematic LC cell and one PG to steer the beam in the vertical direction. When the voltage applied to the first nematic LC cell was 3.06 V, the top diffracted spot at (0, +1) reached its maximum intensity (measured by the same PD as before) suggesting that the nematic LC cell was now working as an FWP. Alternatively, when the applied voltage was set to 2.14 V, the

laser beam was steered to the bottom position at (0, -1) with maximum intensity. Thus, the first nematic LC cell behaved as an HWP when this voltage amplitude is applied.

Subsequently, the second nematic LC cell and PG in Fig. 5.10 were placed back into the system. When V_1 (the voltage applied to the first LC cell) was equal to 3.06 V and by adjusting the value of V_2 (the voltage applied to the second LC cell) to be either 1.84 V or 1.24 V, the LC laser beam can be steered either to the top-left (-1, +1) or top-right (+1, +1) quadrants, respectively, with the highest intensities. Alternatively, setting $V_1 = 2.14$ V, the LC laser beam can then be steered to either the bottom-left (-1, -1) or bottom-right (+1, -1) quadrants when V_2 was set to either 1.36 V or 2.10 V, respectively. Note that the variation in voltages is caused by different cell thicknesses due to manufacturing variation and different incident angles due to the action of the first PG.

The four sets of voltages that were applied to the nematic LC cells demonstrate the operating principle of the device whereby the primary beam was steered to one of four different spatial directions. When the nematic LC cells were subjected to voltages that did not match these conditions, the LC cells no longer behaved as HWPs or FWPs and therefore the intensity of the primary beam was reduced, and the opposite order spots appeared as the LC laser beam will not be circularly polarised. As the difference between the actual applied voltage and the required voltage increases, the brightness of the opposite-order spots increases.

The photographs in **Fig. 5.11** demonstrate that the beam was successfully steered to four separate directions when the appropriate voltages were applied to the nematic LC cells. Unlike other LC laser beam-steering approaches [148, 181, 182] where the laser wavelength changes with the structural variation of the LC laser, this method of LC laser beam-steering does not change the wavelength. A spectrometer (USB2000, Ocean Optics) was used to measure the spectrum of the steered beam at each of the four separate locations and these are shown in **Fig. 5.12**. The wavelength of the laser remained at 605.1 nm regardless of the steering direction.

The drive voltages required for each beam-steering direction and the voltage response measured by a PD are presented in **Table 5.1**. Subsequently, the PD voltage response was further normalised to acquire the relative intensity of each spot in the four spatial quadrants with respect to the primary beam by dividing the measured voltage response for each spot by the highest voltage response among the four spots. The results for the corresponding relative intensities and drive voltages required are presented in **Table 5.2**. Even though additional

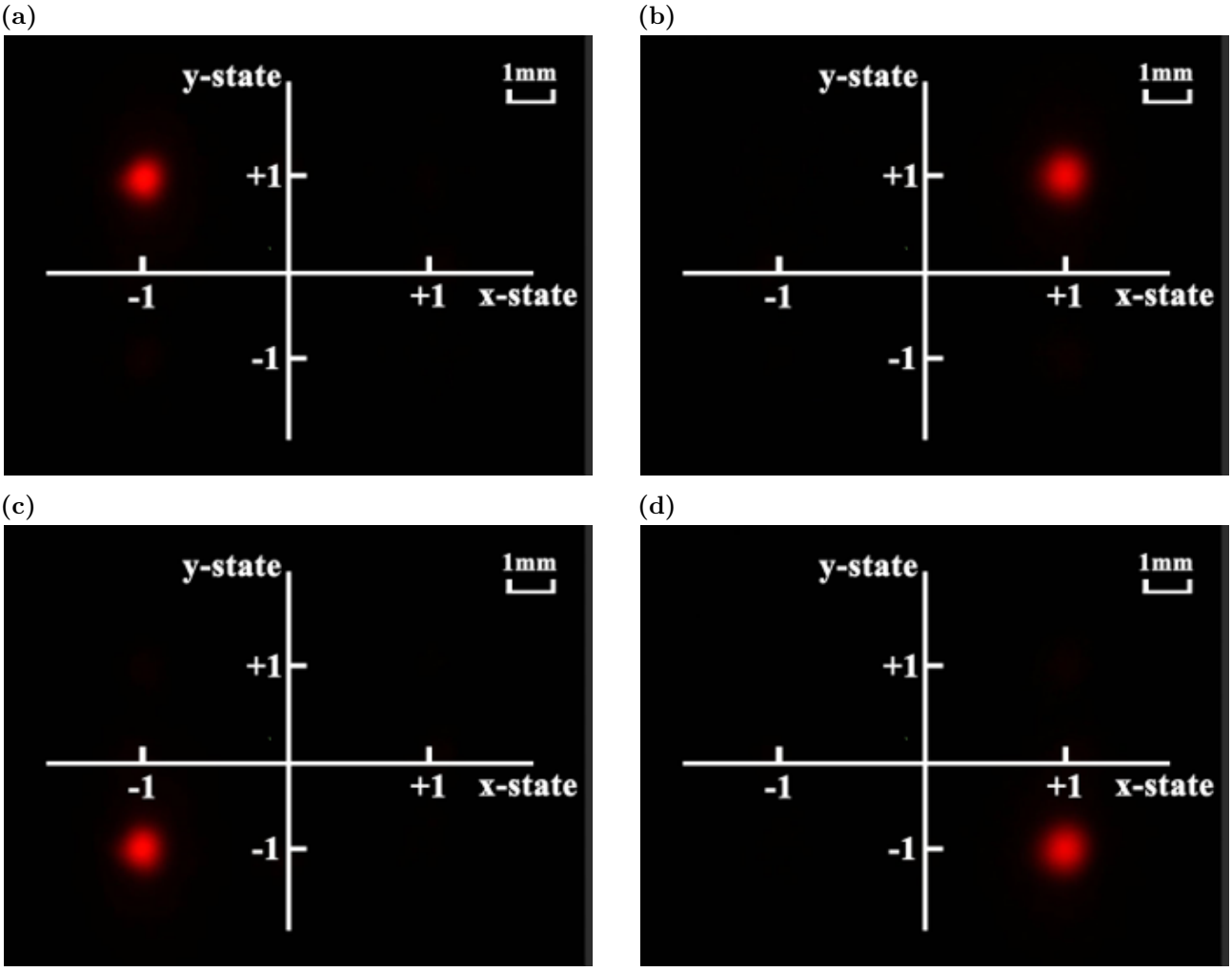

Figure 5.11: Experimental results of the far-field pattern of a non-mechanical LC laser beam-steering. The thickness of the LC layer in the laser cell was 8.4 µm, which was optically pumped by an Nd:YAG laser with a repetition rate of 10 Hz. The thicknesses of the nematic LC layers used as tuneable wave plates were 5 µm and were driven by a 1 kHz square-wave electric field. By applying the appropriate voltage amplitudes, the LC laser beam was steered to (a) top-left (-1, +1), (b) top-right (+1, +1), (c) bottom-left (-1, -1), or (d) bottom-right (+1, -1). The voltages applied to the nematic LC cells are overlaid on the figures, respectively. The emission spectrum next to each diffraction pattern demonstrates the relative intensity (with respect to the original laser beam) and the wavelength of the steered laser beam.

beams appear, the relative intensities of these 'residual' spots at the other three locations are less than a tenth of the intensity of the primary beam. Therefore, for most potential applications such as in optical communications and light detection and ranging (LiDAR), these additional beams would have little influence on the resulting performance of the beam-steering system.

The overall response time of the system was measured to be 170 ms when the voltage applied to the second LC cell was switched from 1.24 V to 1.84 V, which caused the beam to be steered from the top-left (-1, +1) location to the top-right (+1, +1) position. The response time for switching

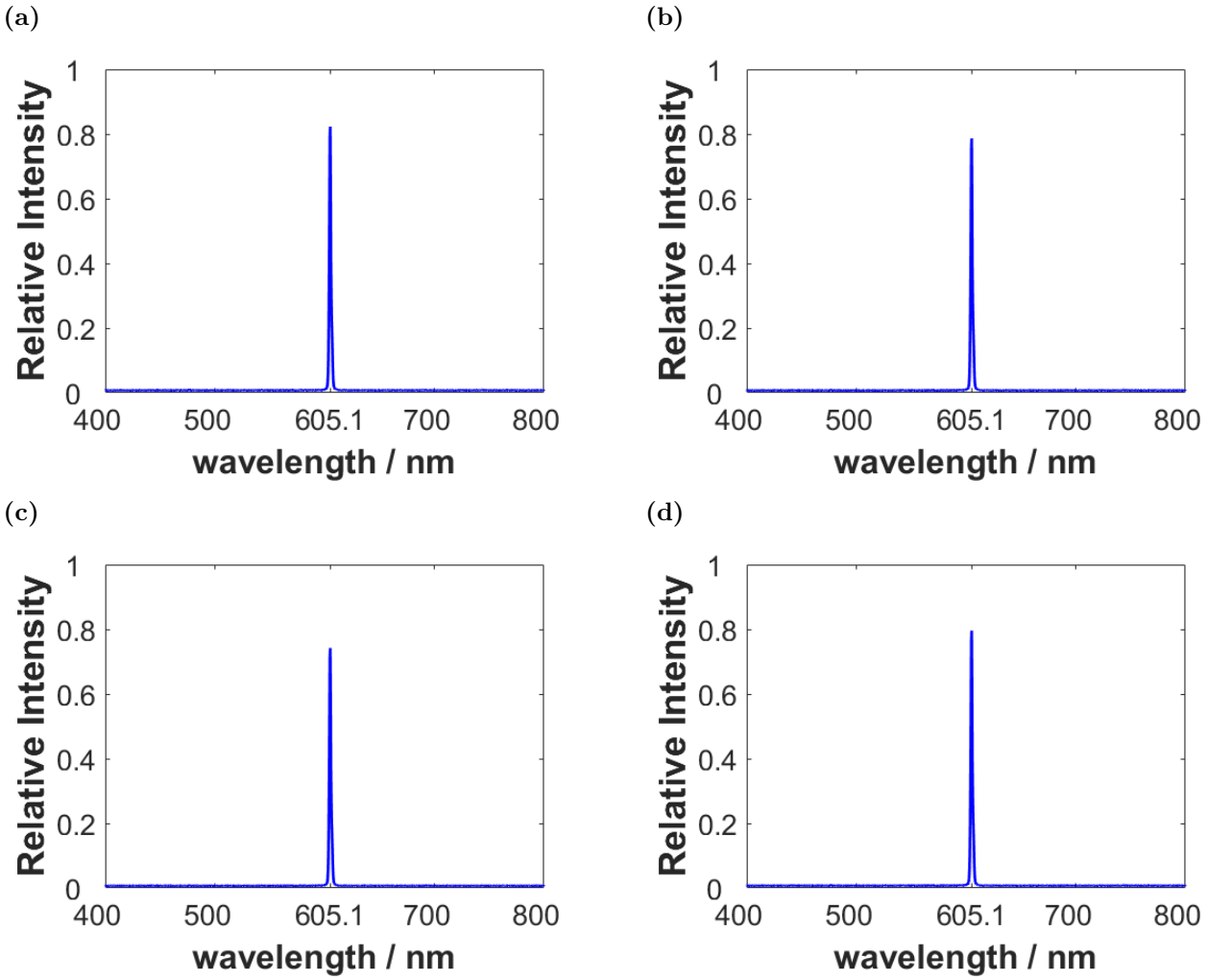

Figure 5.12: The relative intensity spectra of the LC laser beam after been steered to (a) top-left (-1, +1), (b) top-right (+1, +1), (c) bottom-left (-1, -1), and (d) bottom-right (+1, -1). The LC laser spectra were measured and demonstrated normalised to the laser beam intensity before being steered. The beam-steering does not alter the laser wavelength and has a minimal impact on the laser intensity.

Table 5.1: Voltage response of each spot of the beam-steering when the nematic LC cells were subjected to different voltages to switch between the HWP and FWP conditions.

Voltage on Nematic LC Cells (square wave, 10 kHz)		**Voltage Response of Each Spot**			
V_1	V_2	top-left	top-right	bottom-left	bottom-right
3.06 Vpp	1.84 Vpp	17.3 Vpp	1.339 Vpp	1.45 Vpp	0.981 Vpp
3.06 Vpp	1.24 Vpp	1.325 Vpp	16.53 Vpp	0.707 Vpp	1.447 Vpp
2.14 Vpp	1.36 Vpp	1.47 Vpp	0.744 Vpp	15.6 Vpp	1.25 Vpp
2.14 Vpp	2.10 Vpp	1.325 Vpp	949.3 mVpp	934.7 mVpp	16.73 Vpp

Table 5.2: Relative intensities of each spot of the beam-steering when the nematic LC cells were subjected to different voltages to switch between the HWP and FWP conditions.

Voltage on Nematic LC Cells (square wave, 10 kHz)		**Relative Intensity of Each Spot**			
V_1	V_2	top-left	top-right	bottom-left	bottom-right
3.06 Vpp	1.84 Vpp	1	0.077	0.084	0.057
3.06 Vpp	1.24 Vpp	0.080	1	0.043	0.088
2.14 Vpp	1.36 Vpp	0.094	0.048	1	0.080
2.14 Vpp	2.10 Vpp	0.079	0.057	0.050	1

between the other locations was found to be shorter since higher applied voltages are required.

The measurement method for the response times was as follows. A nematic LC cell was placed between crossed polarisers on an optical polarising microscope and the optic axis of the LC was aligned at an angle of 45° to the transmission axes of the polarisers. The nematic LC was then subjected to an electric field. The voltage waveform applied to the LC was a 1 kHz square wave that was modulated by a 1 Hz square wave with an amplitude that increased from 0.62 Vrms and 0.92 Vrms (1.24 Vpp and 1.84 Vpp). These voltage amplitudes correspond to those that need to be applied to the second LC cell to steer the primary beam between the top-left (-1, +1) and top-right (+1, +1) positions. The intensity propagated through the LC cell was captured by a PD mounted on the top of the microscope, which was then connected to an oscilloscope.

The blue curve in **Fig. 5.13** shows an example response of the nematic LC from which a response time of 170 ms was extracted while the orange curve represents the signal that was applied to the LC. Note that the case presented in Fig. 5.13 represents the slowest and limiting response time of the beam-steering system. Switching between the other spatial positions occurs on faster timescales as larger driving voltages are required. For further potential applications that require shorter response times, for instance, in optical communications and LiDAR, thinner LC cells and higher voltages can be implemented so that the cells work as zero-order HWPs or FWPs. Previous work has shown that the response time for nematic LCs can be as low as a few milliseconds when the material and cell thicknesses are carefully selected [201].

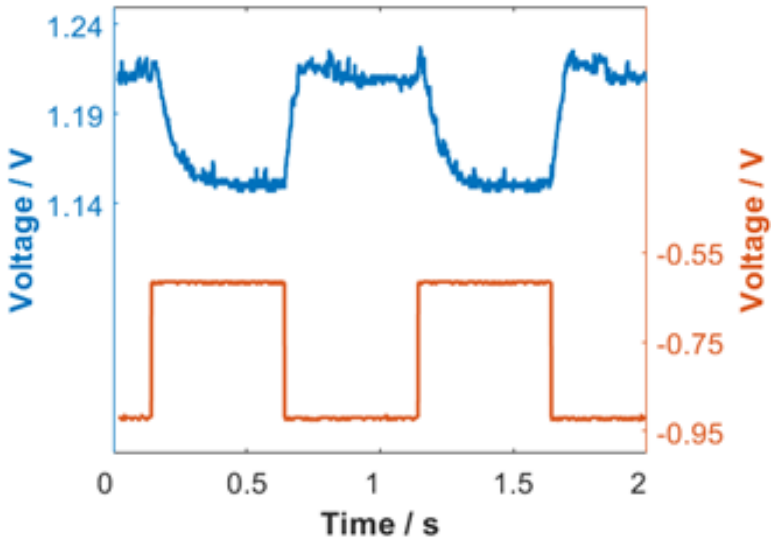

Figure 5.13: An example of the response time measurement of the nematic LC phase shifters. The blue curve represents the response of the nematic LC recorded by a fast PD while the orange curve is the modulation signal that was applied to the LC.

5.6 Reconstructing the Jones Vector

It has been found that the polarisation states of the band-edge LC lasers are not purely circular by characterising its Stokes parameters in Chapter 4. This is in accordance with the beam-steering result for the LC laser shown in Fig. 5.7(c) with the appearance of the opposite-order diffraction. For the previous simulation on the LC laser beam-steering, the LC laser was simulated by an elliptically polarised source with an initial phase difference of 0.3π between the x and y components of the electric field vectors, such that the simulation results aligned with the measured intensities for each diffraction order. Here, the simulation can be optimised by converting the Stokes parameters to the corresponding Jones vector which was then taken as the input (E_{in}) for the previous simulation method. The Stokes parameters can also be represented in terms of the amplitudes and relative phases of the two complex components of the incident electric field ($\langle E_x \rangle, \langle E_y \rangle$) [142]. The polarised part of the Stokes parameters (normalised) can then be recast as

$$\begin{aligned} I &= S_0/S_0 = E_x^2 + E_y^2 \\ Q &= S_1/S_0 p = E_x^2 - E_y^2 \\ U &= S_2/S_0 p = 2E_x E_y \cos\delta \\ V &= S_3/S_0 p = 2E_x E_y \sin\delta \end{aligned} \tag{5.17}$$

where δ is the phase difference between the two components. If $I + Q = 0$, then $E_x = 0, E_y = 1$. Otherwise,

$$\begin{aligned} E_x &= \sqrt{\frac{I+Q}{2}} \\ E_y e^{i\delta} &= \frac{U}{\sqrt{2(I+Q)}} - i\frac{V}{\sqrt{2(I+Q)}} \end{aligned} \tag{5.18}$$

The absolute phase for the electric field vector is not of concern when evaluating only the polarisation of the beam, thus the polarised part of the Stokes parameters can be converted to the corresponding Jones vector by Eq. (5.17) and assigning an arbitrary phase which is chosen to make the x-component of the Jones vector purely real. To simulate the LC laser beam-steering, the Jones vector for each pixel captured by the CCD camera was taken as an independent input electric field. Each diffraction result corresponding to a pixel was then further weighted and summed based on their relative intensities. Unpolarised light, denoted by intensity $I(1 - p)$, diffracts into both directions during the propagation through a PG. Finally, the far-field diffraction intensity distribution was simulated by combining the polarised and unpolarised parts of the LC laser emission.

This optimisation for the beam-steering simulation was verified for the one-dimensional LC laser beam-steering. Note that the LC laser cell used for the previous beam-steering experiments was found to have degraded over time, thus a new cell was fabricated with the same mixture and an LC thickness of 7.9 µm. The cell was first placed in the Stokes parameters measurement system and the results are presented in **Fig. 5.14**. Following this, the components for polarisation measurements were then replaced with the beam-steering components including the PGs and tuneable LC waveplates. This procedure was taken to ensure that the the Stokes parameters were measured for the same excitation location of on the LC cell as that used for beam-steering since the polarisation profile of an LC laser could vary across different spatial regions.

Simulation results of the relative intensities of each diffraction order based on the Jones Matrix model and the converted Jones vector are presented in **Table 5.3**. The results are compared with the experimental measurements by the same PD and all intensities were normalised by the total intensity after propagation through the PG. These results reveal consistency between the simulation and measurements, suggesting that this LC laser is partially and not purely circularly polarised.

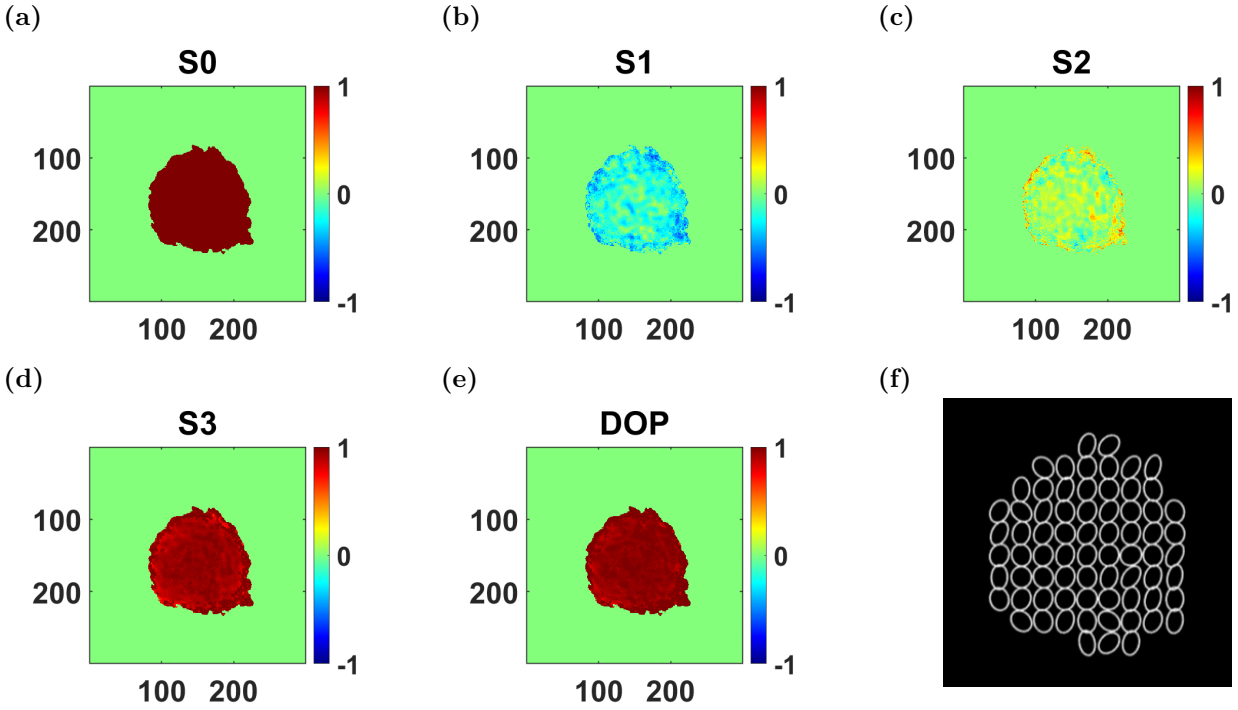

Figure 5.14: The Stokes parameters measurement results for the LC laser (E7 + 2.5 wt.% R5011 + 1 wt.% DCM) used for beam-steering with four normalised Stokes parameters demonstrated in (a∼d) and its (e) DOP as well as (f) polarisation ellipses. The cell has a thickness of 7.9 µm and measurements were conducted at a room temperature of 20 °C.

Table 5.3: The one-dimensional beam-steering diffraction intensities of the primary beam, zero-order, and the opposite order. Results include simulations based upon reconstructing the Jones vector from the measured Stokes parameters and direct intensity measurement using a PD.

	Primary beam	**zero-order**	**opposite-order**
Simulation results	0.9289	0.0238	0.0295
Measurement results	0.9176	0.0209	0.0355

5.7 Summary

In summary, optical beam steering of a band-edge LC laser to four separate spatial positions in two dimensions has been demonstrated using two PGs and two nematic LC cells functioning as tuneable waveplates. This method of beam-steering for LC lasers has the advantages of not altering the laser wavelength, not changing the characteristics of the laser itself, and having minimal impact on the intensity of the laser. In addition, The combination of this all-LC system comprising an LC laser, tuneable LC waveplates, and LC PGs provides a route towards a very compact system that could be deployed as a complete laser source-beam steering system for potential use in optical communications, navigation and tracking, and LiDAR applications. The

steering angle is fixed according to the diffraction angle of the PGs, as though more steering directions can be achieved by applying extra PGs and LC waveplates on demand.

Additional spots at other diffraction orders were observed on the screen beside the primary beam. These minor spots possess much lower intensities and can be categorised as zero-order, sub-order, and opposite-order spots. The appearance of each can be explained and supported by a simulation technique using the Jones matrix method and the principle of far-field Fraunhofer diffraction, which numerically indicates the intensity distribution of diffraction orders upon PGs and allows imperfections in the PG structure to be modelled. In terms of the zero-order spots, in addition to the inherent zero-order leakage that occurs due to imperfections in the PG, a mismatch in the wavelength between the propagation beam and the designed centre wavelength for the PG is another reason for their appearance. The sub-order spots are assumed to be the consequence of the asymmetrical birefringence period of the PG. Subsequently, the opposite-order spots can be explained by the imperfect circular polarisation state of the LC laser, as has been characterised in detail in the previous chapter, and the additional residual birefringence introduced by the PG substrates. Even though the laser beam is not steered entirely in one specific direction due to multiple factors, the intensity of the desired beam can reach more than ten times the intensity of other minor diffraction beams, which is not an issue for many applications.

The Stokes parameters of the LC laser were measured by a Stokes imaging polarimeter and the method illustrated in the previous chapter. By assigning an arbitrary phase to its Stokes parameters, the corresponding Jones vector for the polarised part of the LC laser was reconstructed and used as the electric field vector for the beam-steering simulations. The unpolarised part, on the other hand, led to an intensity split between the +1 and -1 orders. The optimised LC laser beam-steering simulation provides consistent results regarding the intensity distribution for one-dimensional diffraction, suggesting the validity of both the LC laser polarisation measurement results and the simulation method.

Besides LC lasers, this optical beam-steering approach based on PG diffractions can also be applied to other laser sources, and a free-space optical communication link can be subsequently established when the propagating light is modulated with transmitted signals. The simulation and analysis of the far-field PG diffraction pattern, as well as the electrical control of the beam-steering system introduced in this chapter, provide a foundation for the establishment of the optical communication link that will be introduced in the next chapter.

6

Liquid Crystal Beam-steering for Optical Communications

Contents

6.1 Introduction and Aims 135
6.2 Optical Characterisation of Diffusers 138
6.3 Free-space Optical Communications Link 144
6.3.1 Communications Link without Diffuser 147
6.3.2 Communications Link with a Diffuser 149
6.4 Signal-to-noise Ratio Optimisation 150
6.4.1 Fibre-coupled Laser Diode 151
6.4.2 Amplified Differential PIN Photodiode 156
6.5 Optimised Free-space Optical Communications Link 159
6.6 Summary 163

6.1 Introduction and Aims

The increasing demand for higher transmission rates in modern communication systems necessitates innovative approaches to address the limitations of the traditional radio frequency (RF) spectrum. The RF spectrum, which is both licensed and expensive to use, has become saturated, pushing researchers to explore alternative technologies [202]. One promising solution is the use of free-space optical links and visible light communication (VLC), particularly in indoor environments. VLC, utilising the visible light spectrum, offers several advantages over RF communication, including a larger available spectrum and immunity to electromagnetic interference, making it suitable for environments where RF congestion is a problem [203]. VLC systems have demonstrated the ability to achieve transmission rates exceeding 1 Gbps,

as shown by multiple studies [204–206]. These high transmission rates make VLC a viable solution to meet the growing demand for high-speed data transmission. Reports have been published to demonstrate VLC applications in different scenarios, such as integrated sensing, lighting and communication [3,4], free-space optical communication [207, 208], underwater communication [209, 210], optical camera communication [211, 212], and visible light positioning [213, 214], etc. There also have been promising expectations that VLC can be an applicable candidate for the 6G mobile networks[215].

Recent research has focused on developing new detectors and schemes to further push the boundaries of VLC transmission limits, especially the narrow modulation bandwidth of the optical light sources. For instance, Hsu et al. [216] demonstrate a 3×3 imaging multiple-input multiple-output system with orthogonal frequency division multiplexing on three white-light LEDs which reaches a 1.1 Gbps transmission rate. Cossu et al. [217] report a VLC communication system using discrete multi-tone modulation on red, green, and blue (RGB) LEDs which achieves a single-channel data rate of 1.5 Gbps and 3.4 Gbps by implementing wavelength division multiplexing. Separately, Yoshida et al. [218] and Hu et al. [219] have explored advanced photodetectors capable of higher sensitivity and faster response times, thereby improving the overall efficiency of VLC systems. Additionally, hybrid systems combining WiFi and VLC are being explored to leverage the strengths of both technologies, providing a robust solution for indoor communication needs [220]. These hybrid systems aim to combine the ubiquity and flexibility of WiFi with the high-speed and interference-free characteristics of VLC.

For VLC systems to perform optimally, they require both high bandwidth and a high signal-to-noise ratio (SNR). A key strategy to achieve higher SNR for a fixed bandwidth is to reduce the size of the illuminated area. Besides, in order to increase data rates above Gbps, optical wireless links must operate with a relatively narrow field of view (FOV), and in these circumstances, beam-steering is required to maintain a link over a wide coverage area. This underscores the significance of optical alignment between the transmitter and receiver to enhance SNR. For instance, Gunawan et al.[221] demonstrate a 21.01 Gbps optical VLC system with vibration mitigation based on orthogonal frequency division multiplexed and non-orthogonal multiple access signals using RGB laser diodes. The beam-steering of the system was achieved by implementing fast-steering mirrors. Theoretically, beam-steering employed at both the transmitter and receiver can maximise the performance of the link. At

the transmitter, beam-steering ensures the narrow beam of light reaches the receiver, and at the receiver, beam-steering steers the incoming light back onto the optical axis. This allows the receiver to be designed with a large collection area and a narrow FOV.

Notable beam-steering technologies include mechanical fast steering mirrors and lenses; for example, Singh et al.[222] discuss the design and implementation of prisms and fast steering mirrors, which provide dynamic adjustment of the light beam direction with high speed and continuous steering angles. These mirrors offer significant advantages in terms of rapid beam adjustment, but they also introduce complexity in the system design and typically have larger footprints compared to other beam-steering technologies. Recently, new micro-opto-electro-mechanical-system-based approaches have been demonstrated [223, 224] which can reach up to 10 Gbps and a 3 dB optical bandwidth covering the infrared bands (1530 nm to 1625 nm) for more than 1-metre free-space link distance and lower than 10^{-10} bit error rate (BER). Non-mechanical techniques include variable focus lenses [225], passive diffractive optics [226], integrated optical phased arrays [227] and/or tuneable lasers [228]. A literature review of these non-mechanical approaches has been illustrated in Chapter 5. These approaches typically offer beam-steering over a continuous set of angles and therefore require complex control and tracking arrangements to optimise alignment and achieve minimum link loss.

In this chapter, a simpler approach [161] is illustrated, inspired by prior research [179] that focused on discrete position beam-steering using polarisation gratings (PG) and liquid crystal (LC) polarisation shifters. Building upon this foundation and the previous work introduced in Chapter 5, a diffuser was employed at the transmitter to achieve continuous angular coverage. Additionally, beam-steering at both the transmitter and receiver was implemented, significantly improving the overall FOV compared to a system that only uses beam-steering at the transmitter. Although the steering positions are discrete, the diffused beam can be steered separately or simultaneously to all positions, and the power distribution at these positions can be tuned continuously. Experimental results on pseudo-random binary sequence (PRBS) data transmission and reception are presented, as well as eye diagrams, indicating that the communication link can reach over 1 metre with a BER lower than 10^{-3}. This approach is lightweight, low-cost, and not limited to any operational wavelength or bandwidth due to the inherent properties of the PGs and LC waveplates. Moreover, it offers the potential for bidirectional communication

links since beam-steering is conducted for both the transmitter and receiver, ensuring that the transmission is no longer dependent on direction.

This work has been published in a peer-reviewed journal, IEEE Photonics Technology Letters, Volume 35, Issue 22, November 2023.

6.2 Optical Characterisation of Diffusers

Compared to the optical system introduced in the previous chapter, where an LC laser could be steered in four directions controlled by voltages applied to switchable LC waveplates and PGs, the proposed communications link discussed in this chapter requires the propagation beam to fully cover a two-dimensional space. To achieve this, light-shaping diffusers were implemented into the system to expand the beam, allowing for large area coverage while meeting eye-safety requirements even at higher optical powers. The diffuser used is made of polycarbonate film, which creates a pseudo-random, non-periodic surface resembling a combination of randomised micro-lenses. It generally behaves like a negative lens, diverging the propagation beam within a defined angle regardless of its wavelength or coherence, with its random structure eliminating Moiré patterns and dispersion.

The diffuser was designed to work with the beam-steering method presented in Chapter 5 and it is therefore crucial that the polarisation properties of the diffuser do not adversely impact the steered beam otherwise it will not be compatible with the polarisation-sensitive beam-steering system. The optical texture and characteristics of the diffusers were first investigated using an optical polarised microscope (BX51, Olympus). It was found that diffusers could change the polarisation state of the incident beam since their textures could be observed between crossed polarisers. The extinction of the microscope image was seen upon every 90° rotation of the diffuser, suggesting that the diffuser exhibited uniformly aligned birefringence of an arbitrary value. For instance, the bright and dark states of a 10° full width at half maximum (FWHM) diffuser film (P1, Luminit) on the microscope are shown in **Fig. 6.1**(a) and (b), respectively. The films did not display clear Michel-Levy colours, indicating they possess high birefringence that strongly depends on the incident angle, with the ideal performance achieved with collimated perpendicular incident light.

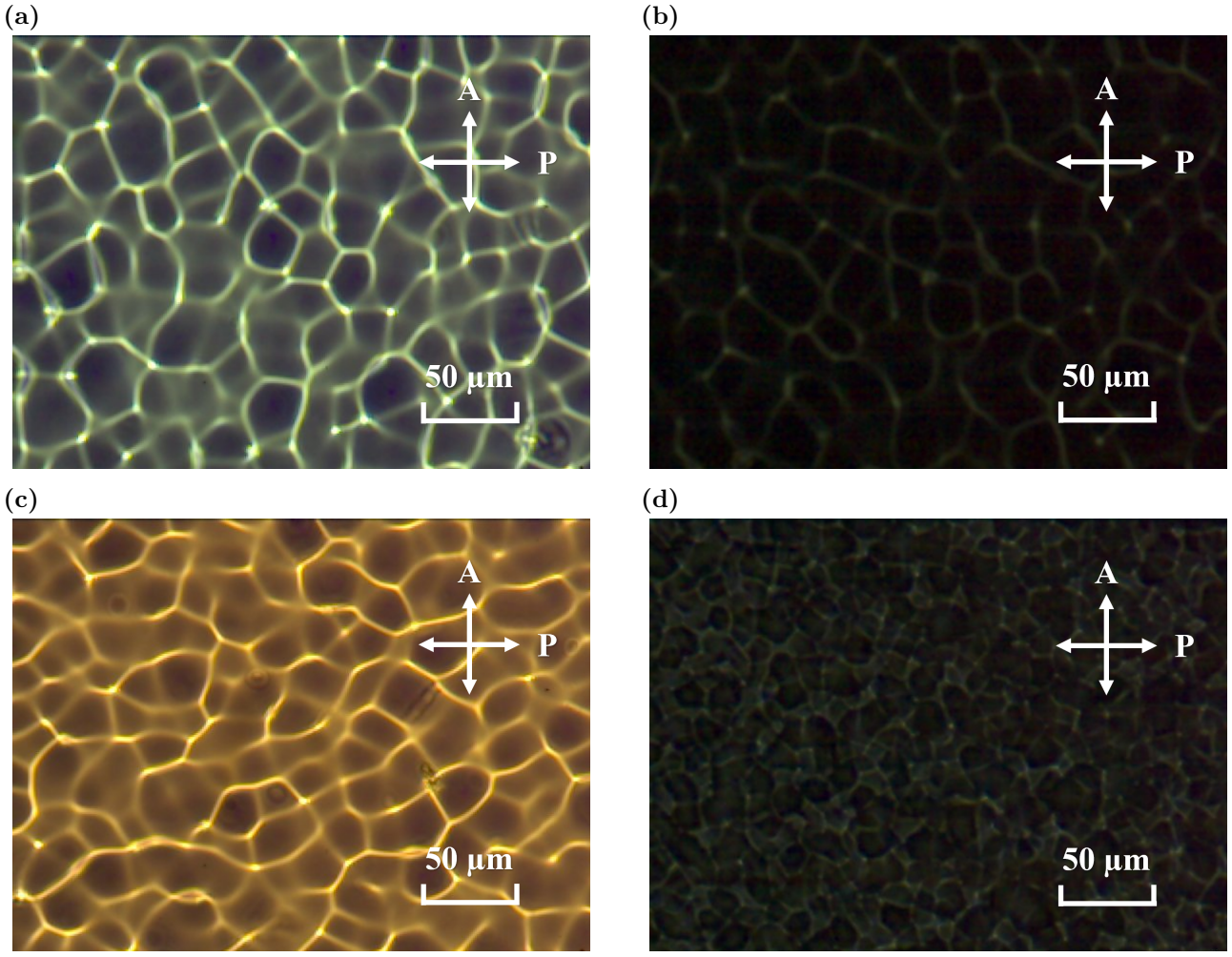

Figure 6.1: The optical textures of the diffusers when viewed on an optical polarising microscope. The micro-lenslet texture of a 10° FWHM diffuser was placed between the crossed polarisers of the microscope where the (a) bright and (b) dark state was observed upon rotating the diffuser. (c) The optical texture of the diffuser without the analyser in the microscope. (d) The texture of a 30° FWHM diffuser between crossed polarisers of the microscope where smaller micro-lenslets were observed. The double-headed white arrows show the orientations of the polariser and analyser.

In addition, the diffuser can function regardless of the incident polarisation state. This was examined by removing the analyser from the microscope, and the image intensity remained unchanged with the rotation of the diffuser, as shown in Fig. 6.1(c). Furthermore, Fig. 6.1(d) displays the optical texture of a 30° diffuser with smaller micro-lenslet divisions, which can be explained by the larger curvature required for higher diffraction angles.

The transmitter for the communications link was proposed consisting of two switchable LC waveplates and two orthogonal PGs to achieve two-dimensional beam-steering as has been demonstrated in Chapter 5, as well as a diffuser to establish an entire space light coverage. Similar to the components used in the previous chapter, the LC cells consisted of a nematic

LC mixture (E7, Synthon Chemicals Ltd) capillary filled into commercially available anti-parallel rubbed glass cells (LC-2, Instec) coated with indium-tin-oxide electrodes and polyimide alignment layers. The LC layer was 5 μm thick. The PGs (Edmund Optics) were designed to operate at 550 nm with a diffraction angle of $\pm 10°$.

To begin with, the sequence of the diffuser and other beam-steering components for the transmitter was studied to maximise the functionality of the free-space optical communications link. Even though placing a diffuser after the LC waveplates and PGs can ensure easier control of the beam diverging and steering, it eliminates the possibility of bi-directional reciprocal communication, since the inverse light path would propagate through the diffuser first, leading to excess geometrical loss. Therefore, the approach of placing the diffuser before the beam-steering components for the transmitter was proposed and tested.

The system configuration for one-dimensional beam-steering with a diffuser is illustrated in **Fig. 6.2**(a). A laser diode working at 520 nm (PL520, Thorlabs) was employed, which was driven by a current controller (LDC205C, Thorlabs) and its diverging emission was focused by a collimating lens. The laser beam then propagated through a film polariser and an iris, before being steered by a horizontally aligned PG. The diffraction pattern was detected by a screen and captured by a digital single-lens reflex (DSLR) camera, as shown in Fig. 6.2(b), where the beam was steered into the -1 and +1 states, accompanied by zero-order leakage and sub-orders, with reasons for their appearance illustrated in Chapter 5.

Next, a 10° diffuser was inserted before the PG, and the diffraction pattern is presented in Fig. 6.2(c). Two diffused spots appeared, corresponding to the -1 and +1 states, respectively. The change in the intensity ratio between the two states compared to that in Fig. 6.2(b) indicated the diffuser introduced extra retardance, altering the polarisation state of the incident beam. This is in accordance with the findings from observations made on a polarised optical microscope. Note that the background light was switched off compared to that shown in Fig. 6.2(b) for better visualisation. Furthermore, the diffraction pattern varied with the orientation of the diffuser, as shown in Fig. 6.2(d) where the diffuser was rotated by some arbitrary angle. This indicated that the diffuser behaves similar to a waveplate, with its orientation affecting the retardance. The orientation of the diffuser was adjusted until the spots at the -1 and +1 states possessed equal intensities. In this case, the diffuser would not introduce any phase difference between the x- and y-component of the electric field vectors of the propagation beam.

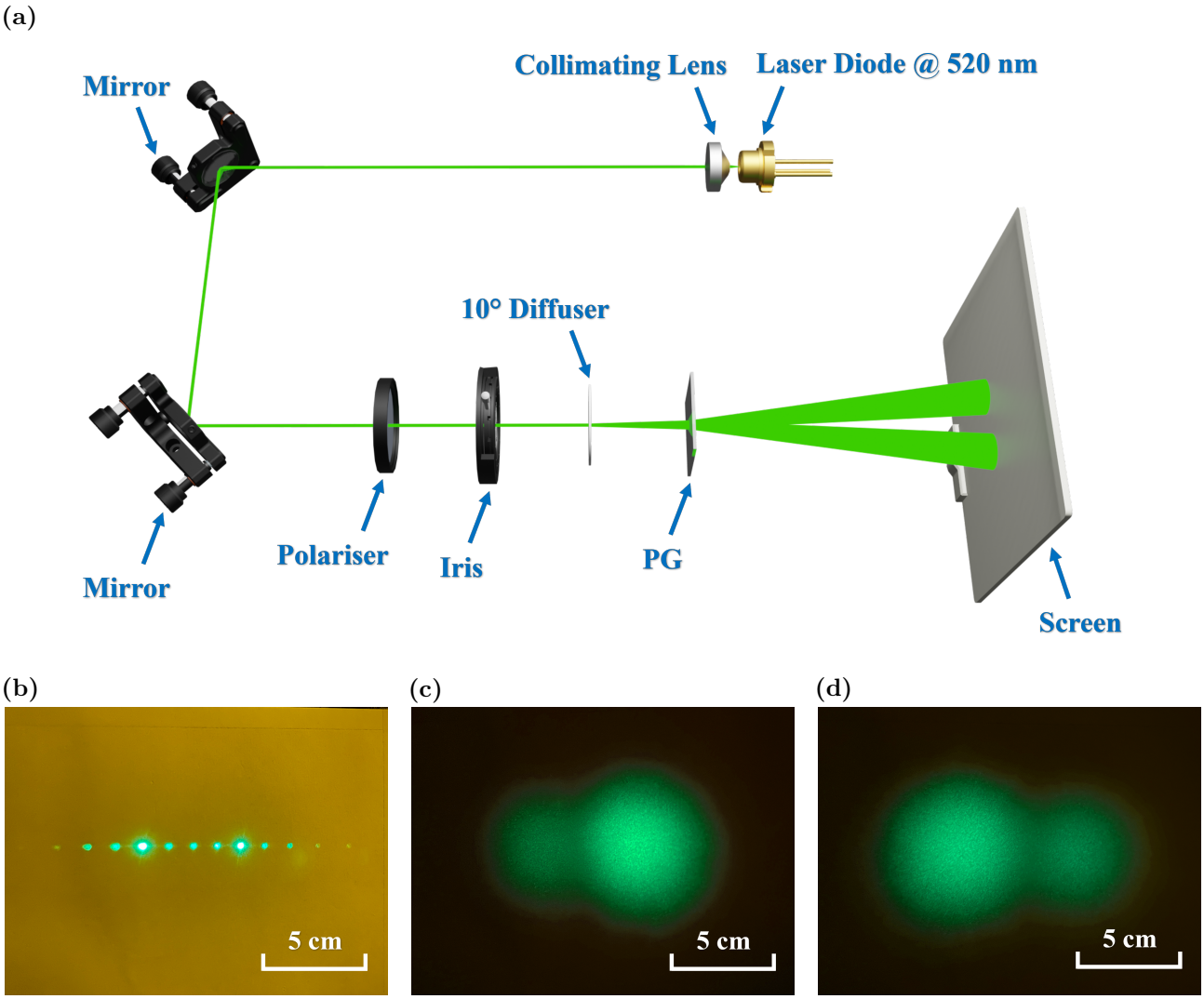

Figure 6.2: (a) The system configuration for investigating the impact of introducing the diffuser on the PG beam-steering. The laser driver is not shown in the figure for simplicity. (b) Diffraction patterns on the screen without the 10° diffuser, showing the linearly polarised beam split into the +1 and -1 states. Zero-order and sub-order diffraction spots also appeared on the screen due to wavelength mismatch and intrinsic properties of the PG. (c) Diffraction pattern on the screen with the 10° diffuser placed before the PG, showing diffused spots at the +1 and -1 states with different intensities due to the retardance introduced by the diffuser. (d) Variation of diffused spot intensities with the orientation of the diffuser.

As introduced in Chapter 2, nematic LC cells can function as continuous variable waveplates depending upon the applied voltages. Therefore, they can be applied to offset the extra retardance introduced by the birefringence of the diffuser when voltages are applied appropriately. This enables the possibility of placing the diffuser before the LC waveplates and PGs in the transmitter to achieve entire space coverage upon diffused beam-steering.

The design for the transmitter with two-dimensional beam-steering and light diffusion is illustrated in **Fig. 6.3**(a). Initially, the collimated beam from the laser diode propagated through a polariser and an iris, before its polarisation was altered to be right-handed circularly polarised by a nematic LC waveplate and steered to the +1 state by a horizontal PG. The diffraction pattern on the screen is shown in Fig. 6.3(b), where the primary beam upon diffraction was located at the +1 state, accompanied by the appearance of other minor spots. The LC director in the waveplate was aligned at a 45° angle with respect to the direction of the polariser.

Subsequently, the 10° diffuser was inserted before the nematic LC cell and the PG. The voltage applied to the LC cell was adjusted to offset the retardance introduced by the diffuser, resulting in right-handed circularly polarised emission. The diffraction pattern on the screen is demonstrated in Fig. 6.3(c), where the centre of the diffused primary beam is located at the +1 state, with other minor spots appearing as noise. Finally, two sets of nematic LC waveplates and PGs, along with the 10° diffuser, were implemented into the system, as illustrated in Fig. 6.3(a). The second LC cell functioned as a half-waveplate (HWP) or full-waveplate (FWP) depending on the applied voltages, and the second PG correspondingly vertically steered the beam to the -1 and/or +1 state, enabling two-dimensional beam-steering. With appropriate voltages applied to the LC waveplates, the diffused beam was steered to the top-left, top-right, bottom-left, and bottom-right, with their patterns on the screen captured and shown in Fig. 6.3(d∼g). The noise beside the primary beam was due to the other diffraction orders upon propagation through PGs.

The dimension of the PGs used was 25.00 × 25.00 mm, with a radius of 12.50 mm for the circular active area. Since the diffraction angle of the PG and the FWHM of the diffuser were both 10°, the distance between the diffuser and the second PG in Fig. 6.3(a) should be within $12.5/\tan 15° = 46.65$ mm; otherwise, the beam would propagate outside the PG, leading to geometrical loss and a lower SNR eventually. The requirement in practical applications is stricter when the beam diameter is taken into consideration. This observation underscores the need to

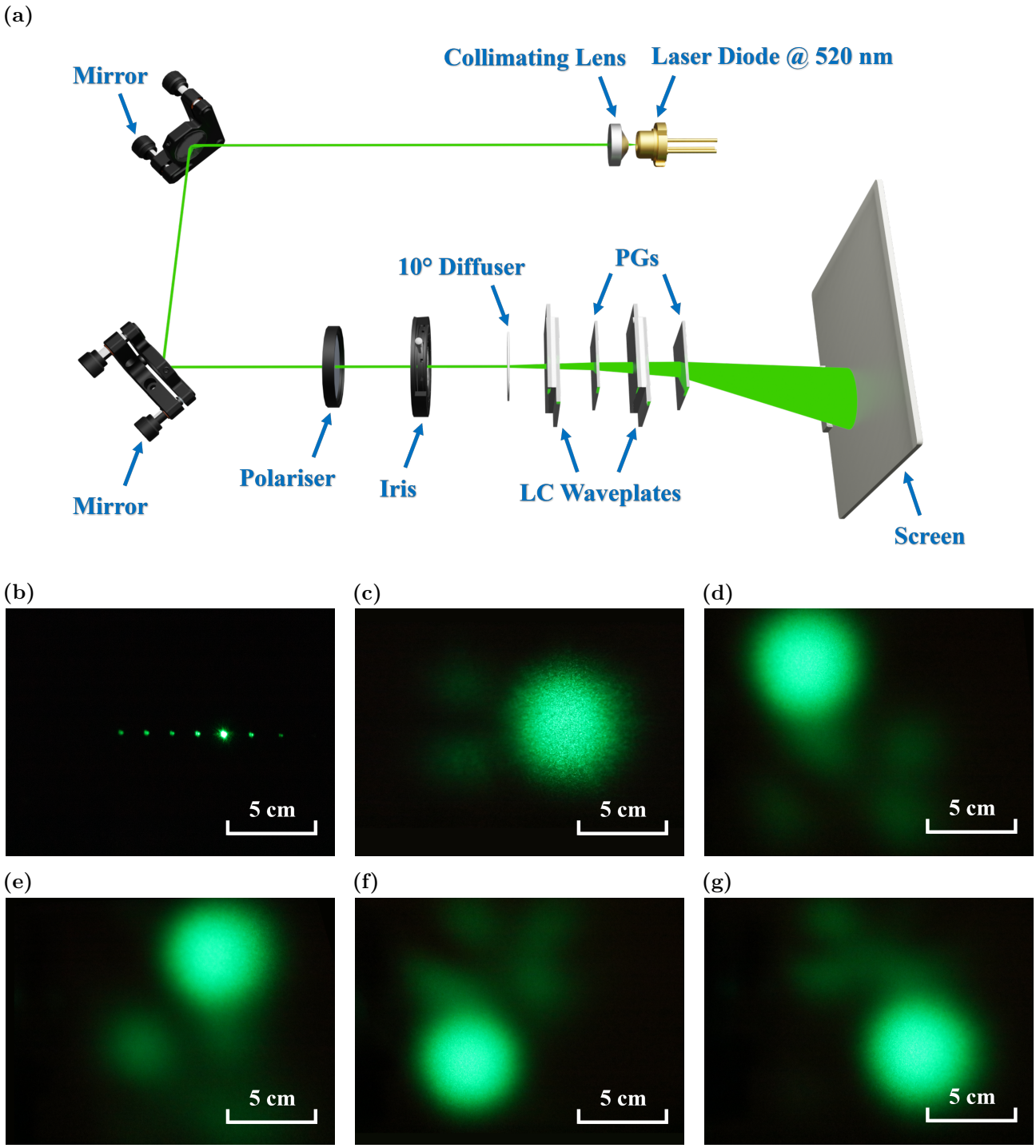

Figure 6.3: (a) The system configuration for the transmitter of the optical communications link. The laser driver is not shown in the figure for simplicity. Diffraction patterns were first recorded for the one-dimensional beam-steering circumstances where (b) the diffuser was removed from the system and the beam was adjusted to be right-handed circularly polarised and steered horizontally, and (c) the diffuser was employed before the LC waveplate and PG so that the diffused beam was adjusted to be right-handed circularly polarised and steered horizontally. The diffused beam was then steered in two dimensions to four separate directions: (d) top-left, (e) top-right, (f) bottom-left, and (g) bottom-right, where minor diffraction spots appeared as surrounding noise.

stack all components tightly instead of having them on individual posts. In light of this, a 3D-printed rack was fabricated to position the components closely together with minimal gaps, with its structure demonstrated in **Fig. 6.4**. Note that the diffuser was cut into the same dimension as the PG so that it can be inserted into either side of the beam-steering stack on demand.

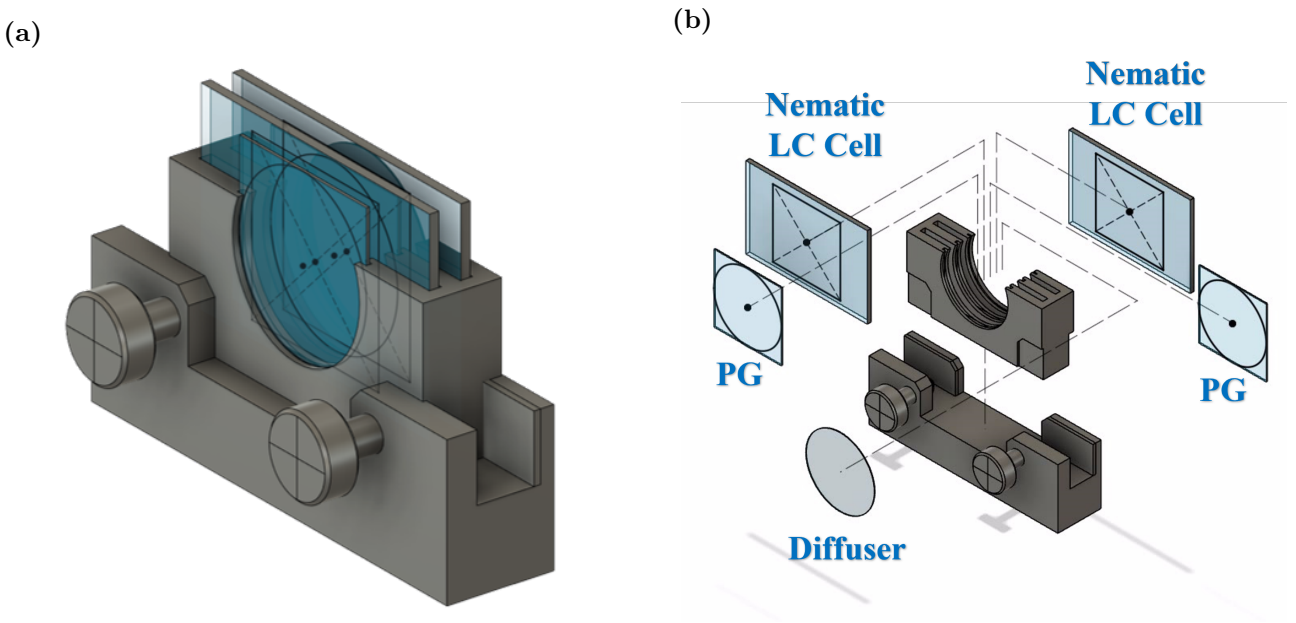

Figure 6.4: The structural representation of the 3D-printed rack for stacking the beam-steering components and the diffuser. (a) The appearance of the 3D-printed rack with the components mounted. (b) The decomposition of the component rack structure, showing how components can be inserted into the mount sequentially, minimising gaps between them and ensuring alignment of their geometric centres with the optical axis.

6.3 Free-space Optical Communications Link

The design for the transmitter has been illustrated in the previous section, where the diffuser was placed before the nematic LC cells and PGs. An optical communications link can be further established by introducing similar arrangements for the receiver and applying non-return-to-zero on-off-keying modulation to the transmitted light. As shown in **Fig. 6.5**, the receiver could comprise two sets of LC waveplates and PGs placed before a detector, steering the beam parallel to the optical axis. Specifically, light from the diffuser propagated to the receiver, and an LC waveplate was used to convert the beam to be either left or right circularly polarised. The beam was then steered by the first PG of the receiver so that the angle it subtended with the optical axis was reduced, effectively reversing the steering effect of the corresponding transmitter PG. It then passed through the second LC waveplate and PG, where

it was steered in the other axis by the same process, again reducing the angle it subtended with the optical axis. The steered beam was then collected by a photodetector. The receiver could be removed from the configuration so as to demonstrate the proof of principle of the beam-steering and the realisation of transmitting data to four separate regions in space, either simultaneously or independently, according to requirements.

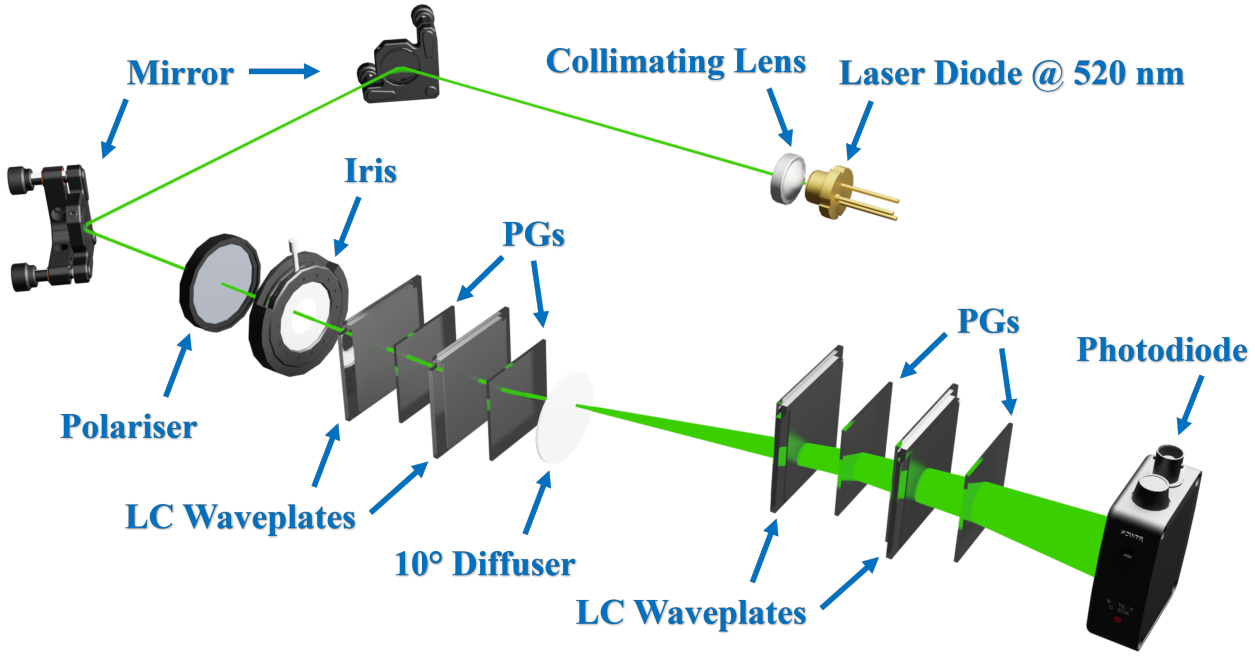

Figure 6.5: The system configuration of a proposed prototype of the free-space optical communications link using LC beam-steering. The laser driver is not shown in the figure for simplicity. The receiver consists of a similar component arrangement as the transmitter to steer the diffused beam back to the optical axis and onto the photodetector. Although shown separately, the beam-steering components for both the transmitter and receiver were closely mounted on the 3D-printed rack to minimise the geometrical loss. The functionality of communications can then be achieved by modulating data information on the transmitted light.

There are substantial benefits to the approach described above, even for modest numbers of steering positions. Firstly, the approach is, in principle, agnostic to the transmission rate and the wavelength, as long as the PG is designed for operation at the desired wavelength. Thus, there is no transmission bandwidth for the beam-steering system. In terms of the steering bandwidth, it is a function of the LC response time, where the LC waveplates used were measured to be 170 ms with details presented in Chapter 5. As each of the steered positions covers an angular range of 10°, this response time would support rates of 58.82°/sec, sufficient for many situations with mobile terminals. Besides, through careful choice of the LC and using techniques such as polymer stabilisation, a response time of the order of a few milliseconds could be

obtained [201] which would lead to a higher steering bandwidth. Secondly, the approach requires no mechanical components, is lightweight and compact, and can provide full space coverage. Thirdly, for a system where the desired angular coverage is $\psi \times \psi$ degrees, the transmitter and receiver would be optimally designed with the same FOV. If the transmitter steers the beam to $N \times N$ positions, then the intensity received by the receiver will increase by N^2 compared with a non-steered system with the same overall FOV and transmitter power if all the light is diverted to a single position. If the receiver beam-steering is implemented, then the required FOV of the receiver is $(\psi/N) \times (\psi/N)$ degrees. This allows an increase in receiver collection area by a factor of N^2 if the design is étendue-limited, representing the best possible receiver design. Combining the effects of both transmitter and receiver steering leads to a potential overall N^4 gain in system link margin. This increased margin can be used to increase the link rate or range, or both, compared with the nonsteered link.

The focus of the demonstration of this free-space optical communications link is the novel technique used to direct the radiation, rather than tracking. Tracking can be implemented using a number of methods. For the system reported here a possible method is as follows: steering light equally to all output positions, and then maximising the received signal by selecting the best receiver position. This determines the angle of arrival of the radiation. The receiver can then transmit a return signal at that same angle and the transmitter can determine the angle of arrival using its receiver, before then optimising its transmitter. There are other potential sequences that allow links to be established, and these are the subject of future research.

Despite the potential for bidirectional communications, the link is first investigated for unidirectional operation where the diffuser could be placed after the LC waveplates and PGs of the transmitter to minimise the geometrical loss. In the following sections, the unidirectional communications link is then examined through demonstrations of data transmission and reception, both with and without the diffuser. Subsequently, the insertion loss for the beam-steering components and the geometrical loss for diffused beam propagation in free space are measured and analysed. Finally, multiple optimisation approaches were taken for the system configuration and components to enhance the SNR and extend the link length, leading to a robust free-space optical communication link with the PG and LC beam-steering. A bidirectional link can be achieved by making minor modifications to the beam-steering components for the transmitter

and receiver, using the same PGs and LC waveplates combination. A potential arrangement for a bidirectional communications link will be introduced in Chapter 8.

6.3.1 Communications Link without Diffuser

The initial system without the diffuser allowed for a direct assessment of the system performance for the communications link, focusing on the fundamental data modulation, transmission, and reception without the complexity of beam diffusion or geometrical loss.

Besides the removal of the diffuser in Fig. 6.5 from the transmitter, the laser diode was driven by a 30 mA current and modulated by a 10 MHz, 700 mVpp square wave from an arbitrary waveform generator (AWG) (33500B, Keysight). The selection of the driving current and modulation voltage ensured that the laser diode operated within its linear output power range, as specified by the profile provided by the supplier. With appropriate voltages applied to the four LC cells of the transmitter and receiver, the beam was steered to the top-left direction and finally collected by a photodiode (PD) (PDA36A-EC, Thorlabs). The modulation signal and the received signal were captured by an oscilloscope (MSO9254A, Agilent) and the waveform is demonstrated in **Fig. 6.6**(a). The insertion loss of the beam-steering system was 3.8 dB measured by a power meter (1830-C, Newport), given by the beam power ratio before the first LC cell of the transmitter and after the second PG of the receiver. This loss was predominantly caused by Fresnel reflections between the components and could be significantly reduced by index matching between the elements. The link distance in free-space was 35 cm, although theoretically there was no limitation for the link distance since the beam was collimated. The laser diode was subsequently modulated by a 10 Mbps, 700 mVpp PRBS signal, with the corresponding modulation and received signal captured and demonstrated in Fig. 6.6(b). As suggested by the corresponding signals highlighted in the black rectangles, the delay between the transmitted and received signals is approximately 6.5 µs which represents the system round trip time.

The successful reception of the correct waveform through the optical communications link without the diffuser indicates the effectiveness of modulating the propagation light, directing it to the desired direction, and detecting the received signal using the PD. This configuration serves as a crucial reference for subsequent experiments involving the diffuser, where additional challenges such as geometrical loss and signal dispersion need to be addressed.

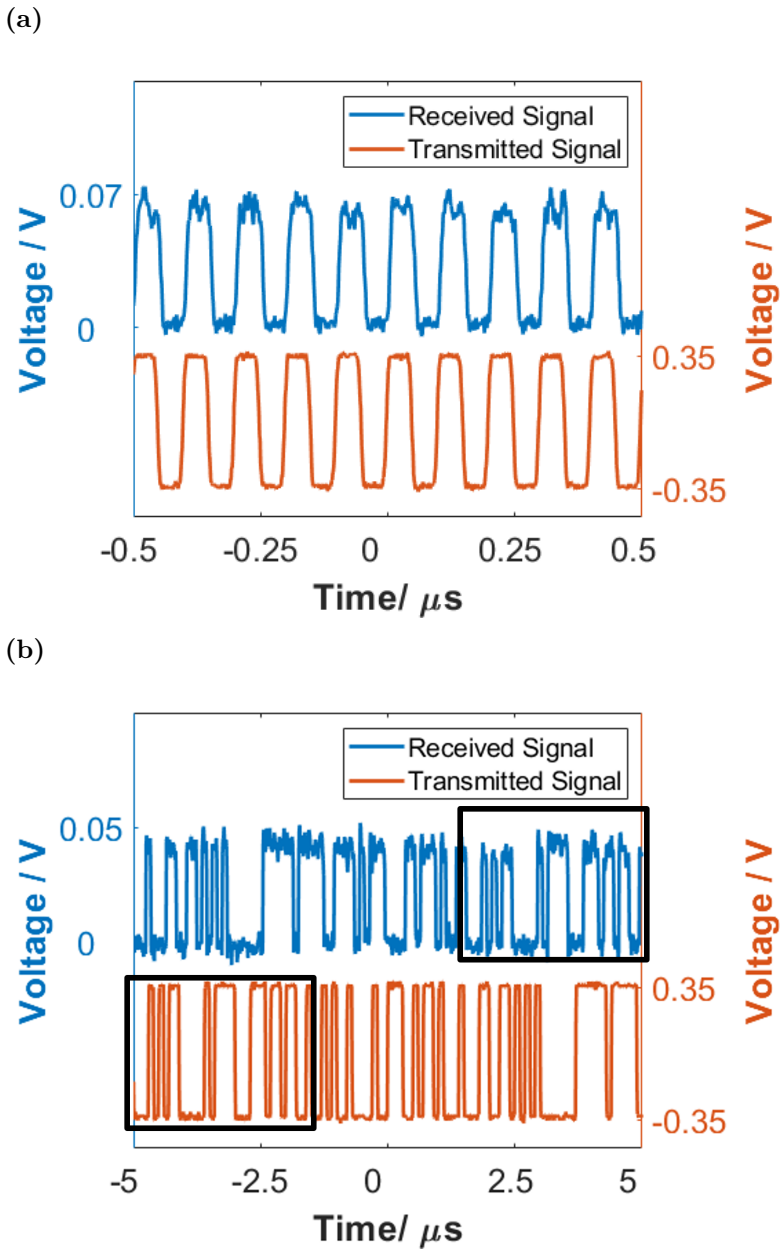

Figure 6.6: The transmitted and received signals for a 35 cm communications link without the diffuser. The light was modulated by (a) a 10 MHz, 700 mVpp square wave and (b) a 10 Mbps, 700 mVpp PRBS signal. The black rectangles highlight the corresponding transmitted and received signals, suggesting a transmission delay of 6.5 µs for the current system.

6.3.2 Communications Link with a Diffuser

The 10° diffuser was then inserted into the transmitter after the beam-steering components with the system configuration illustrated in Fig. 6.5. The employment of the diffuser scatters the propagation beam and largely reduces the irradiance at the receiver. For instance, the irradiance for a 3 mm diameter laser after propagating 1 metre will be reduced to $1.5^2/(10^3 \tan 5° + 1.5)^2 = 1/3519$, equivalent to an extra 35.5 dB geometrical loss. Additionally, only a proportion of the diffused beam could be detected by the PD, limited by the dimensions of the beam-steering components and the effective detection area.

The noise equivalent power (NEP) is a straightforward and necessary metric for quantifying the sensitivity and performance of photodetectors. It is defined as the optical input power that results in an SNR of 1 in a 1 Hz output bandwidth. The PD used in the experiments has a NEP of 29.2 pW/Hz$^{0.5}$ and a bandwidth of 150 MHz, leading to the minimum detectable power for the device being $29.2 \times 10^{-12} \times \sqrt{150 \times 10^6} = 0.36$ µW, assuming the entire bandwidth was utilised. Therefore, a minimum power of 1∼2 µW, which is slightly larger than the NEP, was expected at the PD to achieve a distinguishable received signal with a decent SNR.

It was observed that when the link distance was reduced to 15 cm, the power measured after the fourth PG of the system (the second PG of the receiver) was 0.464 µW, slightly above the calculated NEP for the PD. The power measured after the first, second, and third PGs was 17.46 µW, 12.14 µW, and 0.561 µW, respectively. The driving current was adjusted to 40 mA, and the modulation voltage applied to the laser diode was increased to 1 Vpp to enhance the received signal while remaining within its linear output power range. Additionally, the received signal needed to be averaged 4096 times by the oscilloscope to stabilise the waveform due to insufficient SNR, with the results demonstrated in **Fig. 6.7**.

The peak-to-peak voltage of the received signal was 0.8 mV, significantly reduced compared to 50 mV for the communications link without the diffuser, as shown in Fig. 6.6(a). This reduction is attributable to the substantial geometrical loss of optical power due to beam diffusion and the limited effective detection area of the photodetector. Moreover, distinguishable high and low voltage levels could only be observed with a large number of averages because of the high noise power of the photodetector and the inadequate SNR of the system. Despite these challenges, the demonstration of modulated waveform transmission and reception illustrates

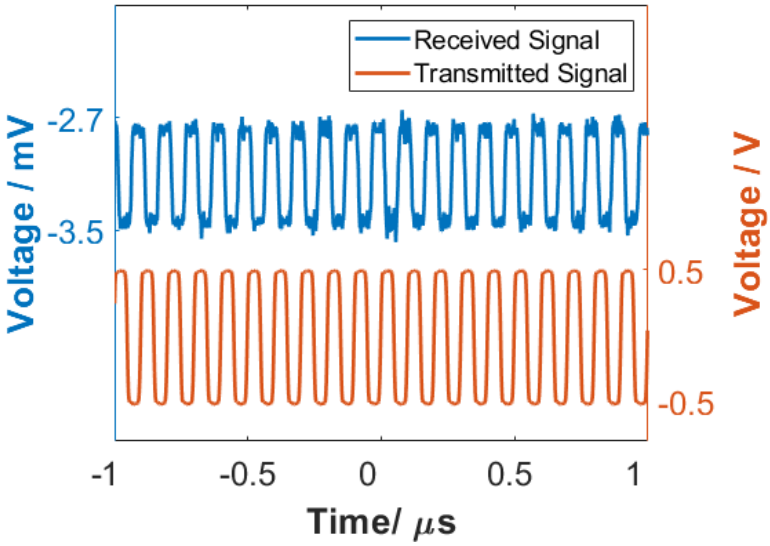

Figure 6.7: The transmitted and received signals for a 15 cm communications link where the diffuser was placed as the last component of the transmitter and the light was modulated by a 10 MHz, 1 Vpp square wave. An averaging of 4096 was implemented by the oscilloscope to acquire a stable square waveform generated by the PD.

the feasibility of applying the PG and LC beam-steering to a free-space communications link, provided that further geometrical and SNR optimisation approaches are implemented.

6.4 Signal-to-noise Ratio Optimisation

Despite the employment of a collimating lens after the laser diode, there was an unavoidable divergence angle of the laser emission, leading to extra optical power loss upon propagation. Currently, the optical power emitted from the transmitter is 12.14 µW, which is much lower than the eye-safe requirement of 0.2 mW for optical communications systems. Therefore, the first approach to enhance the SNR of the system is to replace the light source with a fibre-coupled laser diode that generates higher output power and a lower divergence angle. In addition, the laser was reflected twice from mirrors before being steered and diffused by the transmitter components, which could lead to unnecessary propagation distance and optical power loss. To address this, the mirrors were removed and the laser source was placed directly before the transmitter to further minimise the geometrical optical power loss.

Another possible optimisation is to implement a photodetector with a lower NEP, such as a differential PD with balanced photodetection to cancel out common noise or an avalanche photodiode with internal gain. This could also open up the opportunity to increase the receiver

bandwidth and therefore the maximum transmission rate of the system for further experiments. Besides, employing a focusing lens over the receiver could improve detection, as the diffused beam had an approximate maximum entrance angle of 0.1 radians. Finally, the desired photodetector should possess a larger effective detection area.

6.4.1 Fibre-coupled Laser Diode

The laser source for the free-space optical communications link was replaced with a single-mode fibre-pigtailed laser diode (LP520-SF15A, Thorlabs) operating at a centre wavelength of 520 nm and an output power of 15 mW. The laser beam was coupled into an optical fibre, which ran through a polarisation controller (FPC030, Thorlabs) before being connected to an integrated collimator (F810FC-543, Thorlabs). The laser beam had a diameter of 6.4 mm and a divergence of 0.1°, and the output was adjusted to be linearly polarised using a polariser. The transmitter and receiver configuration remained the same as shown in Fig. 6.5

The driving current applied to the fibre-coupled laser diode was increased until a 0.2 mW power emission was reached after the polariser, which met the threshold of eye safety requirements. Without the diffuser in the transmitter, the power measurements after the first, second, third, and fourth sets of LC waveplates and PGs were 143.6 µW, 98.6 µW, 77.6 µW, and 62.4 µW, respectively. These correspond to losses of 28.2%, 48.3%, 61.2%, and 68.8%, respectively. The losses can be attributed to PG diffraction leakage into other orders and Fresnel reflections between the components.

When the diffuser was placed as the last component of the transmitter, the power measured after the diffuser without additional propagation through space was 95.8 µW, indicating a transmission rate of 97.2% for the diffuser. However, after 20 cm of light propagation, the optical power was reduced to 7.0 µW and finally to 6.3 µW after the fourth set of LC waveplates and PGs. This reduction was due to the limited detection area of the power meter, which had a diameter of 11.3 mm and could only capture a proportion of the diffused light.

The beam diameter at the polariser D_P can be calculated given the distance between the collimator where the laser was emitted and the polariser was 160 cm:

$$D_P = 6.4 + 1600 \times \tan(0.05^\circ) \times 2 = 9.19 \text{ (mm)} \tag{6.1}$$

consequently, the irradiance at this position E_{diff} and before the receiver can be denoted by:

$$E_P = 0.2 \times 10^{-3} \div (\frac{\pi}{4} \times (9.19 \times 10^{-3})^2) = 3 \times 10^{-6} \text{ (W/mm}^2\text{)} \tag{6.2}$$

$$\frac{E_P}{E_{Rx}} = E_{Rx} = 6.3 \times 10^{-6} \div (\frac{\pi}{4} \times (11.3 \times 10^{-3})^2) = 6.3 \times 10^{-8} \text{ (W/mm}^2\text{)} \tag{6.3}$$

therefore, the total loss for this 20 cm free-space optical communications link can be estimated by:

$$10 \log \frac{3 \times 10^{-6}}{6.3 \times 10^{-8}} = 16.8 \text{ (dB)} \tag{6.4}$$

The laser diode was then modulated by a 10 MHz, 1 Vpp square wave generated by the AWG, and the received signal, averaged 8 times by the oscilloscope, is shown in **Fig. 6.8**(a) and (b), with link distances of 10 cm and 20 cm, respectively. Compared to the received waveform in Fig. 6.7, the SNR was substantially improved as the number of averages was significantly reduced from 4096 to 8, and the peak-to-peak voltage increased from 0.8 mV to 4 mV, even with the link distance extended by 5 cm. The improvement in SNR and signal strength demonstrates the effectiveness of the fibre-pigtailed laser diode setup, which optimises the beam collimation and alignment, ensuring more efficient propagation and detection of the transmitted signal. The results indicate that the fibre-coupled laser diode provides a more robust and reliable performance for the free-space optical communications link, especially for longer transmission distances.

In an application scenario, users would only be exposed to the light propagating in free space. Therefore, the laser power can be further increased, as the transmitter components could attenuate around 50% of the power indicated by previous measurements, as long as it meets eye safety requirements after the transmitter. To maximise the modulation voltage and utilise the entire operating range of the laser diode, the voltage-current-power curves were measured by sweeping the driving current from 0 to 95 mA, considering the maximum laser diode current of 102 mA specified by the supplier. As shown in **Fig. 6.9**, the threshold current for lasing is approximately 20 mA, corresponding to a voltage of 4.27 V. If the entire operating range is used for modulation, the driving current and modulation voltage should be 47 mA and 1.4 Vpp, respectively. This suggests an operating range of 20 mA to 94 mA and 4.27 V to 5.67 V, represented by the purple dashed lines in Fig. 6.9. The optical output power after the diffuser was measured to be 6 dBm, meeting the eye safety requirements.

This approach ensures that the laser diode operates efficiently within its linear output power range, maximising the transmitted optical power and thus enhancing the performance of the

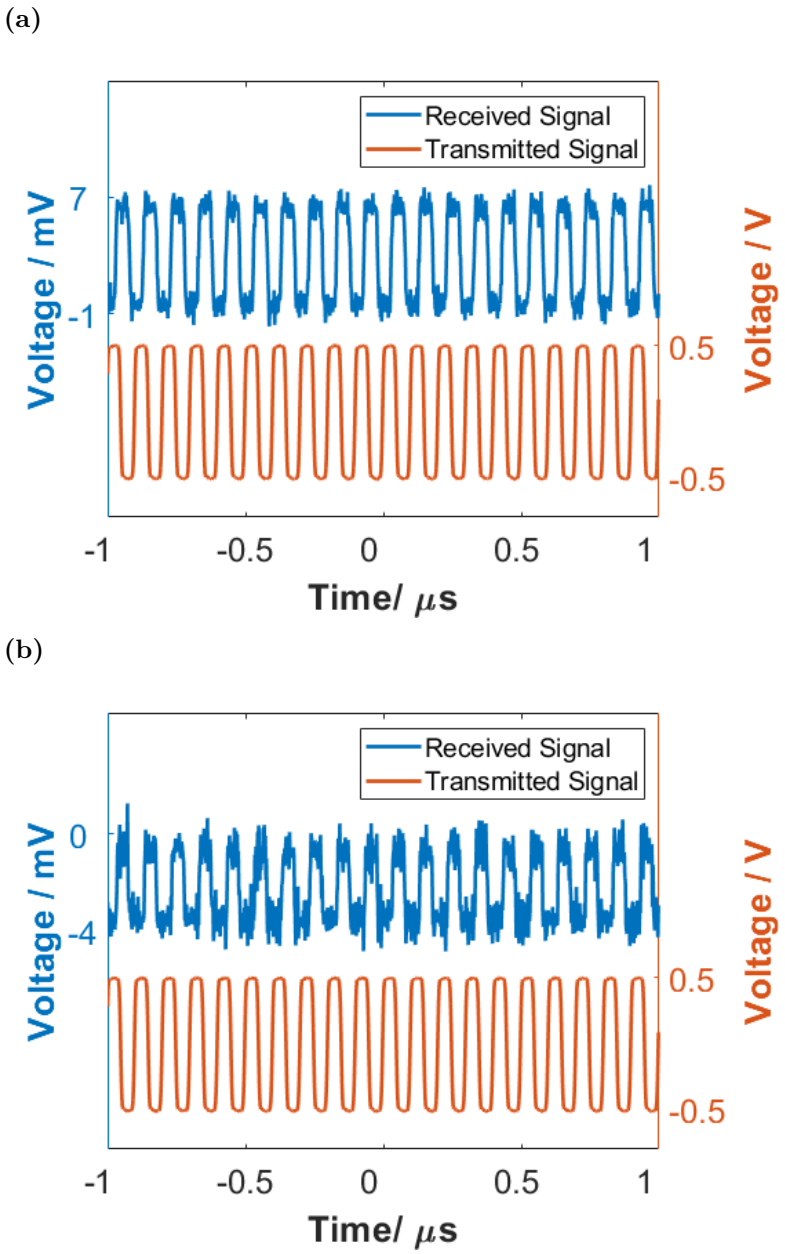

Figure 6.8: The transmitted and received signals for (a) a 10 cm and (b) a 20 cm communications link where the light was modulated by a 10 MHz, 1 Vpp square wave. An averaging of 8 was implemented by the oscilloscope to both measurements to acquire stable square waveforms generated by the PD.

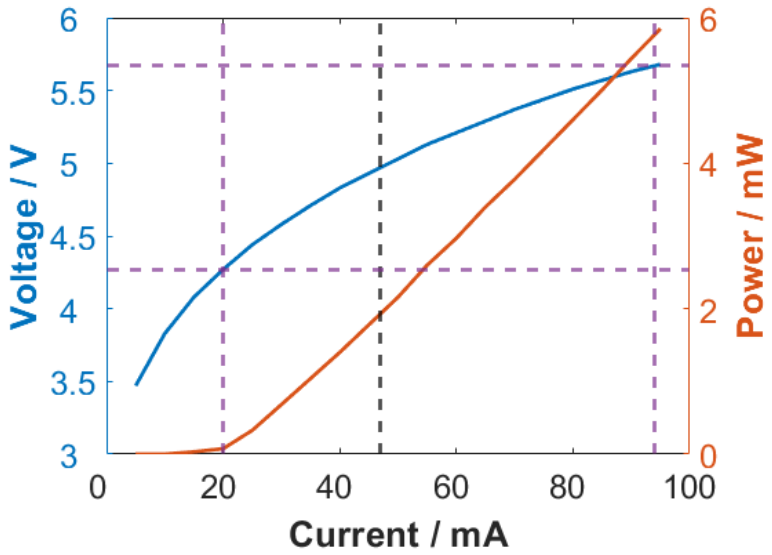

Figure 6.9: The voltage-current-power curves measured for the fibre-coupled laser diode. The current lasing threshold is 20 mA, above which a linear output-input relationship can be observed. The driving current was set to 47 mA, as represented by the black dashed line. The peak-to-peak modulation voltage was 1.4 V, with the modulation range for voltages and currents represented by the purple dashed lines.

optical communications link with higher SNR and longer link distances. The modulation signals and received signals for link distances of 40 cm and 80 cm are demonstrated in **Fig. 6.10**(a) and (b), respectively. Averaging of 1024 was taken for both experiments, whereas 64 averages were sufficient for acquiring a distinguishable received signal for the 40 cm link. Note that the modulation frequency was increased to 50 MHz, which was the maximum capability of the AWG. Higher frequencies were limited by the bandwidth of the experimental equipment, although theoretically, the system is agnostic to the transmission rate. In addition, the peak-to-peak voltages received by the PD were measured to be 780 µV and 300 µV for link distances of 60 cm and 1 metre, respectively.

In the above data transmission experiments, the laser beam was steered entirely to one of the four directions, positioning the receiver at the centre of the diffused beam where the intensity was highest. To explore the spatial coverage of the system and investigate the peak-to-peak voltages of the received signals at locations with lower beam intensities, the transmitted beam was initially steered to the bottom-left position and the receiver, including the beam-steering components and the PD, was then manually displaced and scanned horizontally across the beam diffraction pattern. The received signals were then captured and necessary averaging was conducted. As illustrated by the blue curve in **Fig. 6.11**, the highest peak-to-peak voltage

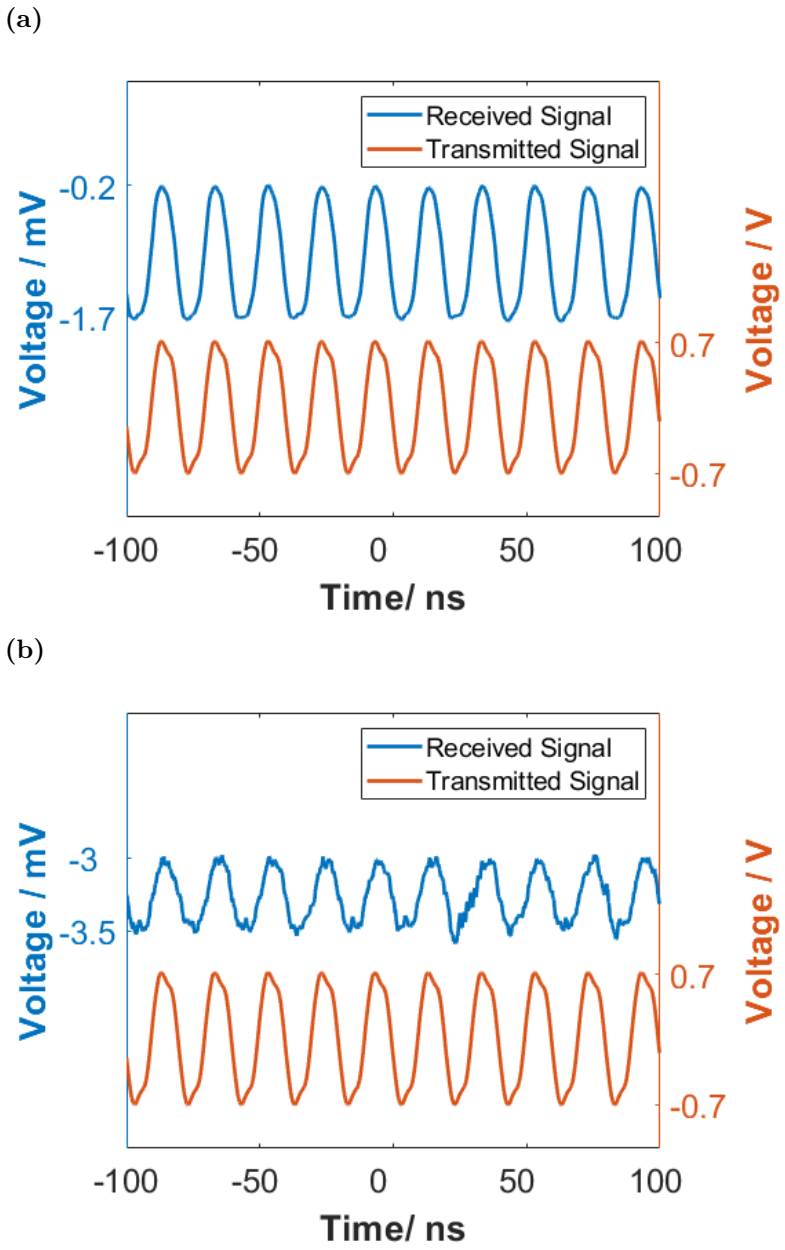

Figure 6.10: The transmitted and received signals for (a) a 40 cm and (b) an 80 cm communications link where the light was modulated by a 50 MHz, 1.4 Vpp square wave. An averaging of 1024 was implemented by the oscilloscope to both measurements to acquire stable square waveforms generated by the PD.

was observed at a displacement angle of 10°, corresponding to the centre of the diffused beam, and it decreased at surrounding displacement angles, suggesting a Gaussian-like distribution. In addition, since the laser beam has a lower intensity at the edge, the minimum intensity was located at 0° of the steering angle.

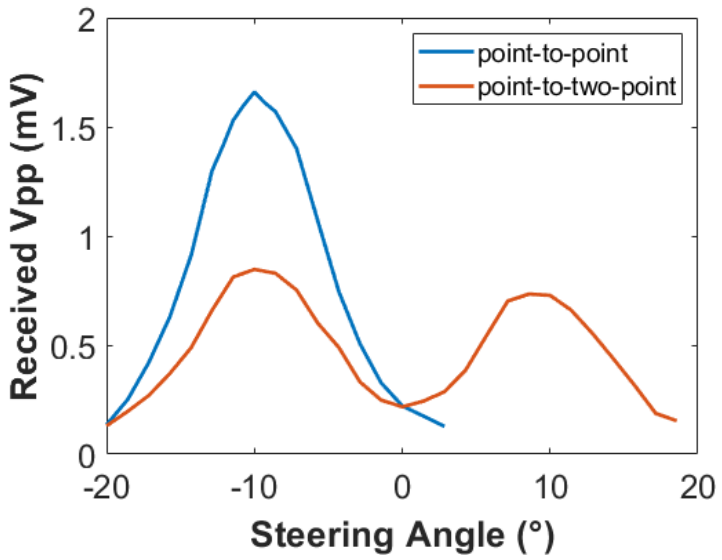

Figure 6.11: Displacement measurement results for the point-to-point scenario where the beam was steered entirely to the bottom-left position, as represented by the blue curve, and the point-to-two-point scenario where the beam was steered simultaneously to the bottom-left and bottom-right positions, as represented by the orange curve. Both curves were measured by scanning the receiver horizontally while recording the received peak-to-peak voltages throughout the scanning locations.

Subsequently, when the transmitted beam was steered simultaneously to the bottom-left and bottom-right positions, the peak-to-peak voltages of the received signals were recorded, as shown by the orange curve in Fig. 6.11. The dip in the received signal along the scanning direction can be mitigated by optimising the relative receiver FOV, the diffuser beam angle, and the diffraction angle of the PG. For instance, a diffuser with a larger diffusion angle can increase the intensity at the 0° steering angle, overlapping the beam at the bottom-left and bottom-right positions, although it also decreases the intensity at the centre of the beams due to energy conservation.

6.4.2 Amplified Differential PIN Photodiode

The current optical communications link using LC beam-steering is capable of transmitting and receiving square waves of up to 1 metre of free-space propagation. However, the system SNR was inadequate, necessitating substantial averaging, especially for longer link distances. This was predominantly due to the high NEP of the photodetector. Consequently, PRBS

modulation was not feasible, limiting the potential for real communications applications for the system. To address this challenge, a photodetector with a larger active detection area (currently 0.08 mm^2) could be employed. Additionally, incorporating a focus lens would help concentrate the diverged beam received by the detector, enhancing the SNR and enabling more robust communications capabilities.

As a result, the PD was replaced by an amplified differential PIN PD [229], which has three plano-convex lenses providing an effective focal length of 13.7 mm and a collection diameter of 20 mm. The optical lenses were simulated in Zemax, where results suggested that it has a FOV of at least 7° (half-angle) providing a reasonable match to the diffuser and PG angular characteristics. The photodetector was a 3.8 × 3.8 mm silicon PIN photodiode and the transimpedance pre-amplifier circuit had a built-in direct current cancellation loop with an open loop bandwidth of 590 MHz. Other characteristics of the PIN PD are detailed in [229]. Upon receiving a transmitted signal, the detector can generate two balanced outputs with one inverted, therefore the common mode noise can be cancelled by subtracting the two optical output signals so that measurements with an improved SNR ratio can be carried out.

Received signals that were distinguishable were observed for longer link distances without the need for averaging, which enables PRBS modulation for data transmission applications. The results of transmitting a 50 MHz, 1.4 Vpp PRBS signal with 60 cm link distance are demonstrated in **Fig. 6.12**, where the negative channel with inverted waveform and the positive channel are illustrated in Fig. 6.12(a). The time delay between the differential outputs is due to the different cable lengths feeding the oscilloscope. Upon subtracting the signals of the negative channel from the positive channel, the received signal was acquired and presented in Fig. 6.12(b) together with the transmitted signal. The delay between the transmitted and received signals is approximately 0.03 µs which represents the system round trip time.

By implementing the optimisation of the laser diode and photodetector, PRBS signals can be transmitted and received through the free-space optical communications link for over 60 cm of transmission, even with a diffuser in place to achieve full spatial coverage. Compared to the received signal with only 0.8 mVpp and 4096 averages for a 15 cm link distance, the optimisation for SNR results in extended link distances with prominent increases in peak-to-peak voltages and no need for averaging. For instance, a 40 mVpp signal can be achieved for a 60

(a)

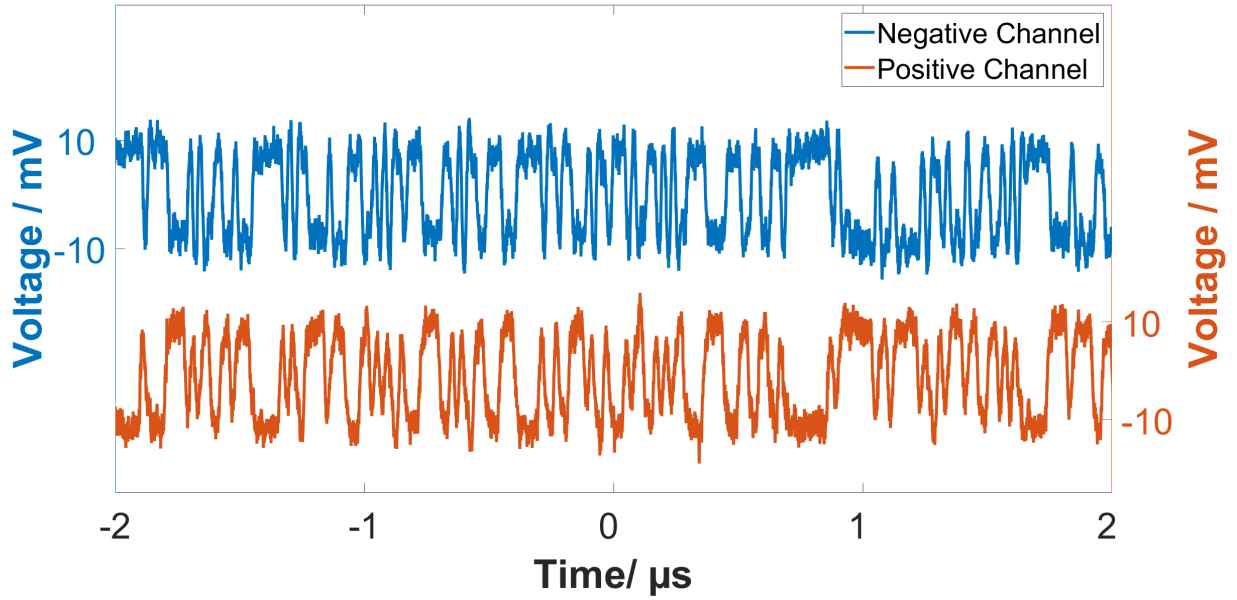

(b)

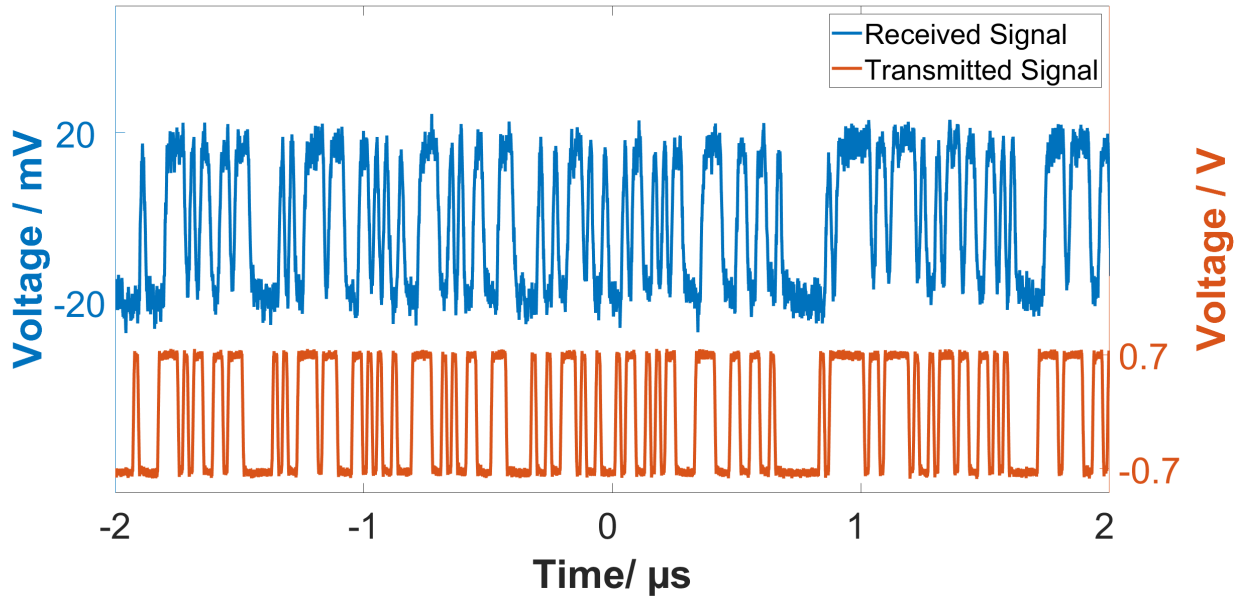

Figure 6.12: Demonstration of 50 MHz, 1.4 Vpp PRBS data transmission and reception for a 60 cm communications link using a differential PIN PD as the photodetector where no averaging was needed. (a) The received signals were generated by the negative and positive channels of the differential PIN PD. (b) The received signal was acquired by subtracting the positive and negative channel waveforms, and the result is accompanied by the transmitted signal for comparison. The delay between the transmitted and received signals represents the system round trip time.

cm link distance. The link distance can be further extended, considering that typically a few millivolts are expected for an optical receiver.

6.5 Optimised Free-space Optical Communications Link

Following the optimisation discussed previously, the mirrors were removed from the system, and the final configuration for the free-space communications link using LC waveplates and PG beam-steering is illustrated in **Fig. 6.13**. The 520 nm laser diode was powered by a laser driver and modulated by an AWG, with its laser emission coupled into a fibre connected to a polarisation controller and a collimating lens. The fibre and polarisation controller are not shown in the figure for simplicity. The laser beam was then switched to linearly polarised using a polariser and subsequently passed through the first LC cell of the transmitter.

Four LC cells of the transmitter and receiver were individually driven by four channels of the second AWG, which altered the polarisation states of the propagation beam, leading to beam-steering upon propagating through the PGs to the desired direction. The beam was eventually collected by the differential PIN photodiode, with the received signal displayed on an oscilloscope. Fig. 6.13 illustrates the scenario where the diffused beam was steered entirely to the top-left, however, setting the appropriate voltages of the LC cells allows for the control of the power distribution of each steering direction individually and simultaneously. For instance, **Fig. 6.14** demonstrates the far-field diffraction pattern captured by a CCD camera (DCU224C, Thorlabs) when the diffused beam was steered simultaneously to all four directions. Diffusers with larger diffusing angles could be employed to reduce the gap between each region.

The experimental apparatus limited the modulation index to 25%, where the modulation index is defined as the magnitude of the optical power modulation relative to the maximum optical power. Combined with the modulation depth available, this resulted in a mean modulated power; that is, a useful communications power of -12 dBm. The insertion loss of the transmitter steering elements after the initial polariser that controls the polarisation from the laser to after the diffuser at the output of the transmitter components stack was measured to be 3.07 dB.

Measurements were taken to demonstrate the benefits of active steering at both the transmitter and receiver. The transmitter beam was steered separately to the bottom-left and bottom-right positions, and in each case, the receiver was manually displaced and scanned across

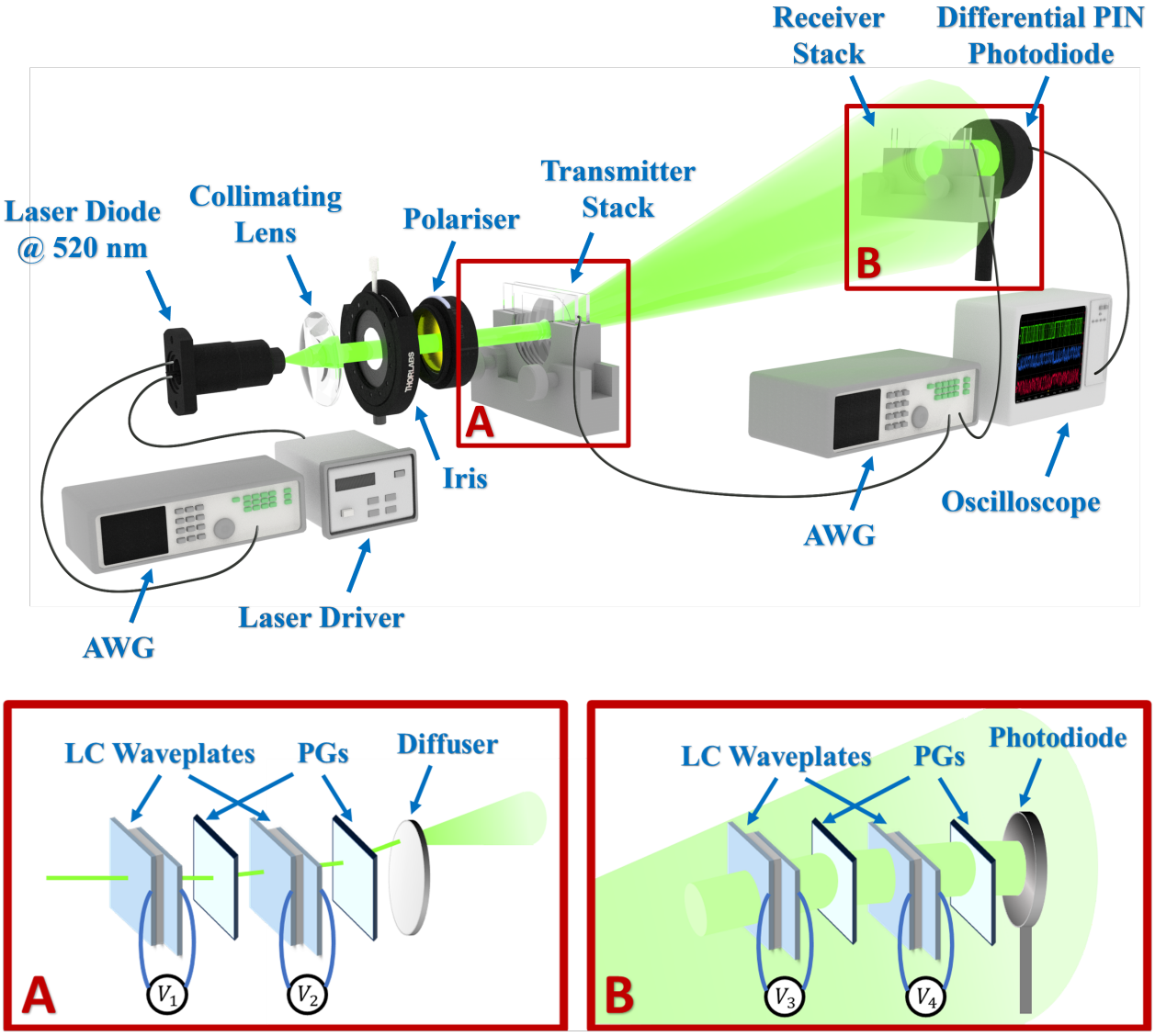

Figure 6.13: Schematic diagram of the free space optical communications link. All electrical connections are represented by black lines and the optical path is illustrated in green. The components of the transmitter and receiver beam-steering stack as well as the light propagation are included in the red boxes A and B, respectively, below the system configuration. Each of the first PG of the component stacks steers the beam horizontally and the second PG vertically.

the centre of the received pattern, as indicated by the dashed line in Fig. 6.14. The received signals were recorded for each position across the scanning. The displacement measurement results are shown in **Fig. 6.15**, where the received power was normalised to the power measured after the diffuser, providing an indication of the geometric loss of the link. For a 40 cm link, it is expected to have a loss of -8.91 dB (12.8%) according to geometrical considerations, which is consistent with the normalised intensity at 10° of steering as represented by the dotted line in Fig. 6.15.

In the case of the solid lines, it can be seen that the overall FOV was limited by the 7.5°

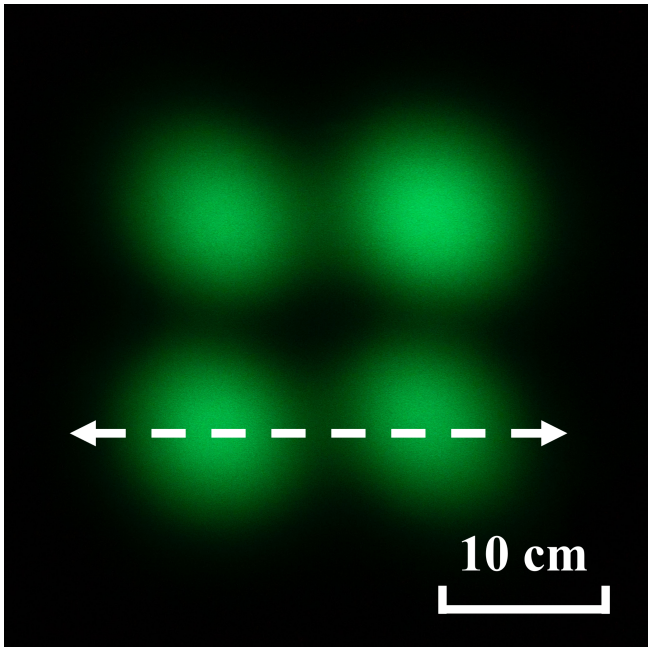

Figure 6.14: The beam profile of all four beam-steered states at the output of the transmitter was recorded on a screen by a CCD camera. Setting the voltage of the LC cells accordingly allows for control of the power distribution of each steering region individually and simultaneously. The white dashed line represents the direction in which the receiver was translated for the displacement measurement when the beam was steered to the bottom-left and bottom-right simultaneously.

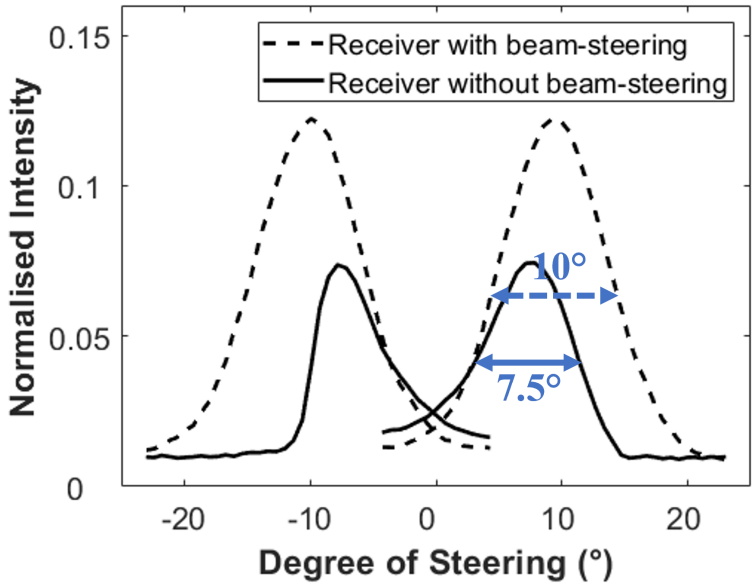

Figure 6.15: Displacement measurements with and without the beam-steering stack at 40 cm distance from the transmitter. Both curves have been normalised to the transmitter output power after the diffuser allowing for an estimate of the geometrical link loss. The FOV labelled on the figure was estimated by measuring the FWHM of the normalised intensity curves. Results show that the beam-steering stack increases the effective detection angles and intensities of the received signal.

FOV of the differential PIN photodiode. The dotted lines illustrate the benefit of receiver beam-steering, showing significant increases in signal power and FOV. The FOV with receiver beam-steering reached 10°, equivalent to the full angle of the diffuser, suggesting it was no longer constrained by that of the photodetector. At the centre position with zero degrees of steering, the beam-steering stack has a slight negative impact on the intensity of the received signal because any beam-steering would prevent the zero-order spot from reaching the photodiode. However, this disadvantage is generally minor, therefore, applying a beam-steering stack in the receiver can effectively enhance signal detection.

A 50 Mbps non-return to zero on-off-keying PRBS signal was used to test the link. Data transmission experiments were conducted over various link distances, and the corresponding received signals were captured by the oscilloscope. The corresponding BER was estimated using the complementary error function and the Q factor, with μ_0, μ_1 representing the mean voltages associated with the transmission states, and σ_0, σ_1 the corresponding standard deviations of the noise.

$$\text{BER} = 0.5 \ \text{erfc}(Q/\sqrt{2}) \tag{6.5}$$

$$Q = \frac{\mu_1 - \mu_0}{\sigma_1 + \sigma_0} \tag{6.6}$$

Fig. 6.16 presents the eye diagram of the transmitted signal for the communications link, illustrating the noise distribution, where the histograms of logical 0s and 1s are shown to visualise the SNR. The parameters for calculating the BER, μ_0, μ_1, σ_0, and σ_1, are labelled on the histograms and can be derived from fitting the histograms into normal distributions. The eye diagrams for the received signals of the 50 Mbps PRBS data transmission over link distances of 40 cm, 60 cm, and 80 cm are shown in **Fig. 6.17**. Besides the point-to-point scenario where the beam was steered entirely to the bottom-left, the transmitter was also set to a point-to-two-point scenario, in which the output power was split 50/50 between the bottom-left and bottom-right regions, with the receiver placed in one of the regions to detect the received signal. The point-to-two-point scenario simulates the circumstance when multiple users within two spatial regions, the bottom-left and bottom-right, are sharing the link simultaneously. The corresponding eye diagrams for the point-to-two-point scenario at various link distances are also presented in Fig. 6.17. Additionally, the eye diagrams for both data transmission scenarios at a 100 cm link distance are shown in **Fig. 6.18**.

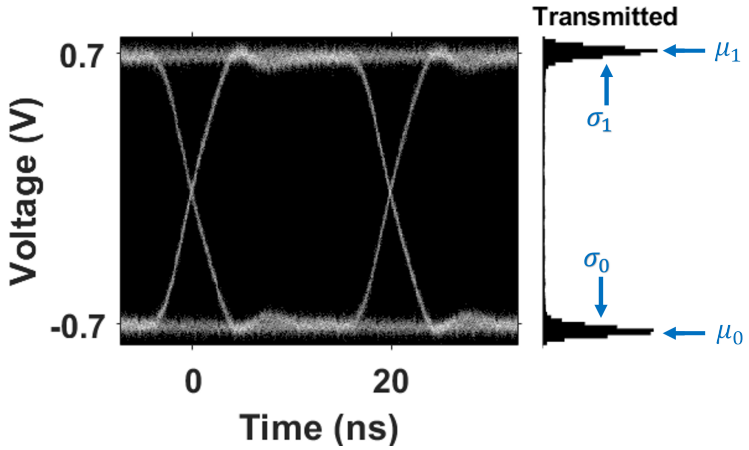

Figure 6.16: The eye diagram for the transmitted signal, 50 Mbps PRBS, of the free-space optical communications link. The parameters used to calculate the BER are labelled on the logical 0 and 1 histograms.

The eye height is approximately half in the point-to-two-point scenario compared to the point-to-point scenario, regardless of the link distance, due to the splitting of the optical power between two transmitted directions. Besides, the SNR decreases and the BER increases with the link distance, as indicated by the eye-opening of the graphs in Fig. 6.17 and Fig. 6.18.

Upon extracting the necessary parameters for calculating the BER from the eye diagrams, the relationship between the BER and the received power at different link distances in both scenarios is indicated by the results presented in **Fig. 6.19**(a). To meet the requirement of a BER lower than 10^{-3} for most applications, the proposed free-space optical communications link can achieve a 1-meter transmission distance for the point-to-point scenario. This distance is reduced to 80 cm for the point-to-two-point scenario. The difference in the received modulation power between the two scenarios with the same BER is 3 dB, corresponding to the split in energy between the two spatial regions. In addition, the geometrical loss of the link can be calculated given the dimensions of the components, the distances between the components, and the beam diffraction angles. Therefore, the results for the BER as a function of the link geometrical loss at different link distances in both scenarios are presented in Fig. 6.19(b).

6.6 Summary

In summary, a free-space optical communications link was demonstrated based on a non-mechanical beam-steering method, consisting of PGs and tuneable LC waveplates as illustrated

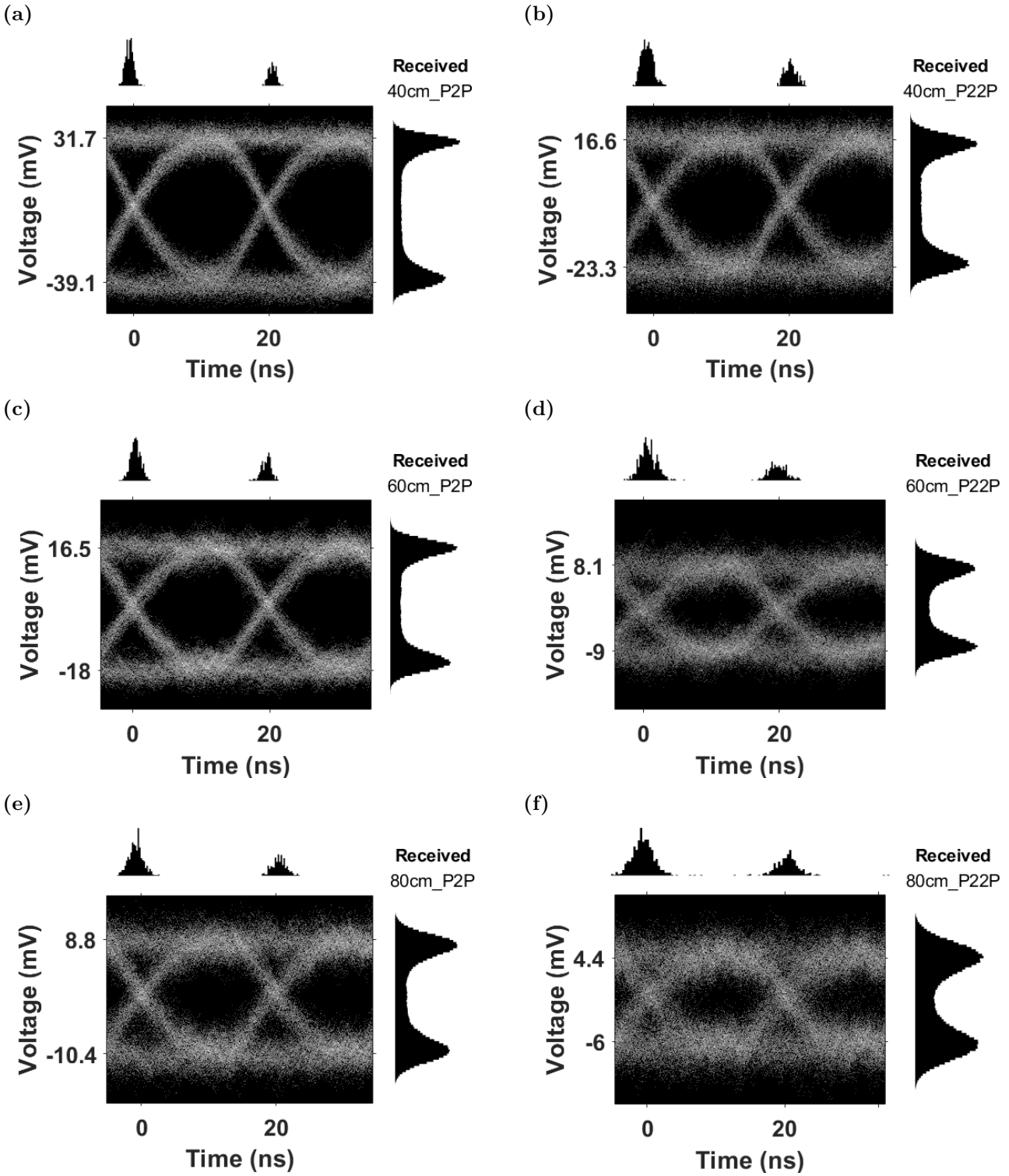

Figure 6.17: The eye diagrams and logical 0 and 1 histograms for the received signals of the free-space optical communications link for (a) 40 cm link distance and point-to-point scenario, (b) 40 cm link distance and point-to-two-point scenario, (c) 60 cm link distance and point-to-point scenario, (d) 60 cm link distance and point-to-two-point scenario, (e) 80 cm link distance and point-to-point scenario, (f) 80 cm link distance and point-to-two-point scenario. The transmission rate was fixed to 50 Mbps.

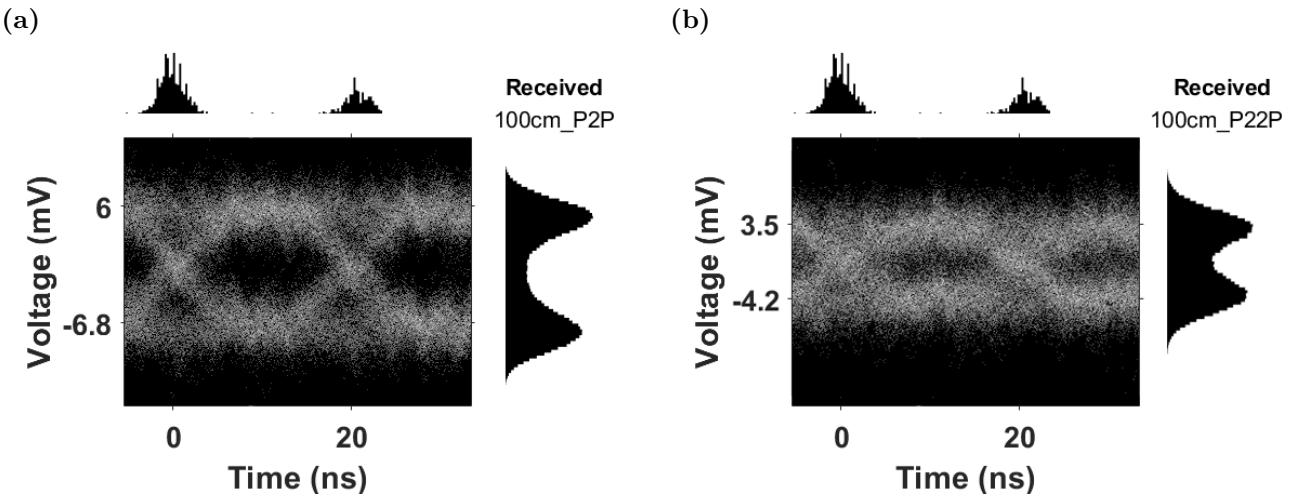

Figure 6.18: The eye diagrams and logical 0 and 1 histograms for the received signals of the free-space optical communications link for (a) 100 cm link distance and point-to-point scenario, (b) 100 cm link distance and point-to-two-point scenario. Longer link distance could result in indistinguishable logical 0s and 1s with high BER. The transmission rate was fixed to 50 Mbps.

in Chapter 5, where a diffuser was additionally employed in the transmitter so as to achieve an entire space coverage. The optical properties of the diffusers were studied, from which it was found that they possess birefringence and act similarly to arbitrary waveplates. The retardance introduced by the diffuser can be offset by the subsequent tuneable LC waveplate with the application of an appropriate voltage. Beam-steering was implemented for both the transmitter and the receiver of the link, to direct the beam to desired locations separately or simultaneously and steer the beam back to the optical axis to achieve orthogonal incidence into the photodetector of the receiver, respectively. Experimental results show that this approach offers a substantial increase in the FOV and link margin over using transmitter beam-steering alone.

In principle, the beam-steering system can be designed for any transmission rate and wavelength, since they are not limited by the physical properties of the PGs and the diffuser. This offers a considerable degree of application flexibility. The steering bandwidth is a function of the LC response time, and so far, the system can achieve a rate of 58.82°/sec, sufficient for many situations with mobile terminals. A response time of the order of a few milliseconds could be obtained leading to higher steering bandwidth through careful choice of the LC mixture and using a polymer stabilisation technique. For the purposes of demonstration, a link transmitting 50 Mbps PRBS signals for over 1 meter with a BER lower than 10^{-3} for the point-to-point scenario has been presented, accompanied with eye diagrams to demonstrate the SNR.

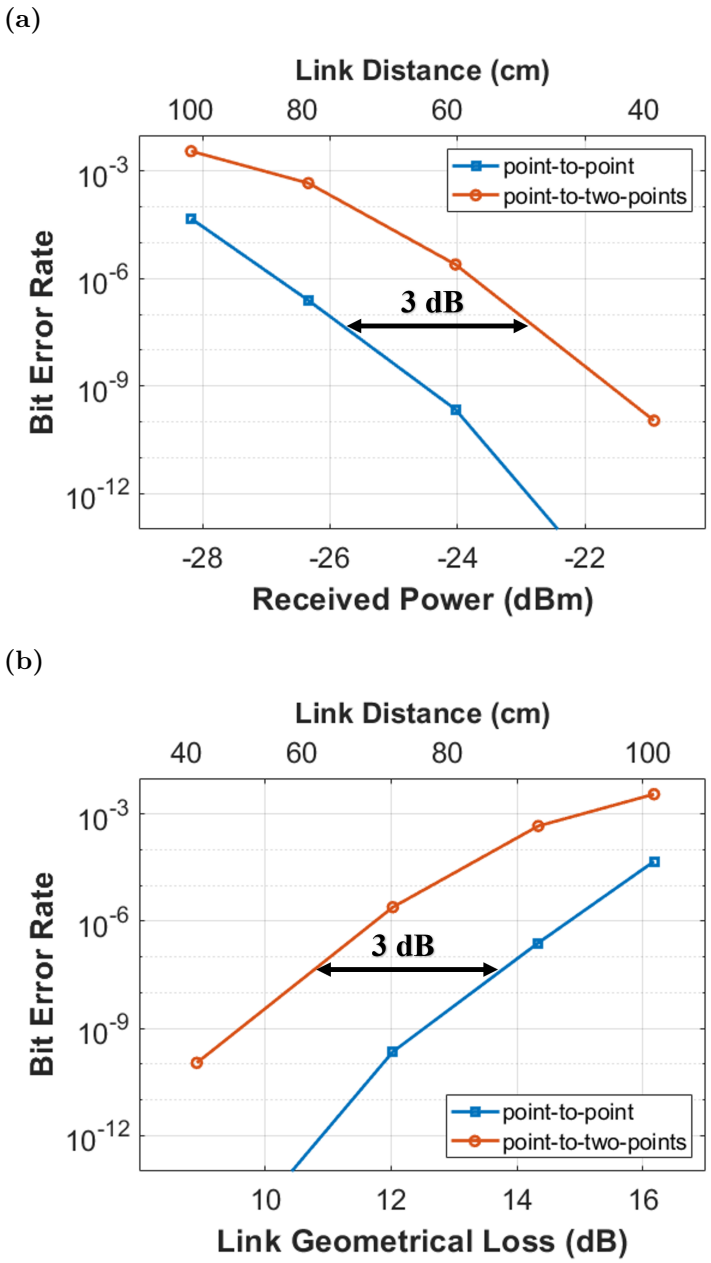

Figure 6.19: The BER measured as a function of (a) the average of the modulated power after the beam-steering and link distances, and (b) the link geometrical loss and the link distances in the point-to-point and point-to-two-point scenarios. The transmission rate was fixed to 50 Mbps.

Overall this beam-steering approach for optical communications offers substantial improvements in link performance using low-cost compact components that can be integrated to create a lightweight high-performance steering subsystem potential for a wide range of applications. Only simple voltage control of the LC waveplates is required to steer the beam to the different spatial locations. This can be contrasted with other solid-state steering methods, for instance, spatial light modulators which require full control of millions of LC pixels. Besides, continuous angular coverage lowers the tolerance of the tracking and pointing, thus reducing complexity when compared with a continuous beam-steering system. This lowered tolerance comes at the cost of higher link loss compared with a system with continuous steering, but the focus of the work here is to show that even steering to a few points offers a substantial gain in link margin compared with the more complex alternatives.

The link distance could be further increased by employing a post amplifier or a fixed gain amplifier to the receiver. Furthermore, a higher transmission rate can be achieved by using a decision feedback equaliser since the receiver bandwidth limits the maximum transmission rate. Finally, the beam-steering elements offer the potential for a bidirectional free-space optical communications link using the same LC cell and PG combination, with only minor modifications.

7

Coherence Measurements of Liquid Crystal Lasers

Contents

7.1 Chapter Introduction and Aims 168
7.2 Temporal Coherence Measurements 170
7.2.1 Michelson Interferometer 170
7.2.2 Coherence Length of a Pulsed laser 171
7.2.3 Coherence Length of LC lasers 174
7.3 Summary 180

7.1 Chapter Introduction and Aims

Coherence is a fundamental property of light referring to the correlation between the phases of a light wave at different points in space and time, which significantly impacts the performance of optical systems and applications. The coherence properties of light can be broadly divided into temporal and spatial coherence, usually characterised by the coherence length and coherence area of the light source, respectively [139]. Temporal coherence refers to the degree of correlation between light emitted from the same point at different times and is associated with the monochromaticity of light, while spatial coherence refers to the correlation between light waves at different spatial locations, usually separated by a distance larger than the wavelength.

Understanding and controlling the coherence of light is critical for a wide range of optical applications, from imaging systems [230, 231] to communication technologies [232, 233] and quantum optics [234, 235]. For example, high temporal coherence is essential to achieve

constructive interference, which is crucial for applications such as precision metrology [236] and holography [237]. In telecommunications, optical coherence plays a vital role in fibre-optic systems [238], where maintaining phase stability is essential for transmitting information over long distances with minimal signal degradation. On the contrary, reducing coherence can minimise speckle noise and enhance image contrast in applications such as optical coherence tomography [239] and microscopy [240], where the use of light with low temporal coherence improves axial resolution by reducing interference artefacts caused by scattering, offering better discrimination between sample features. These varied applications highlight the importance of manipulating the coherence properties of light to meet specific operational requirements of the optical system.

Various methods have been developed to control the coherence of light and optimise its behaviour for different application scenarios. For temporal coherence, the most common approach is to manipulate the spectral width of the light source. Narrowband light sources, such as lasers, exhibit high temporal coherence, making them ideal for interferometric applications. However, in applications such as optical coherence tomography, broadening the spectrum of the light source through the use of superluminescent diodes or broadband lasers results in lower temporal coherence, leading to enhanced axial resolution [241]. In recent years, researchers have demonstrated using a chiral nematic liquid crystal (LC) dispersed with zwitterionic dopants to combat laser speckle noise [242], where both temporal and spatial coherence were reduced. Spatial coherence can be controlled by adjusting the spatial characteristics of the light source. In optical lithography and microscopy, spatial coherence is often reduced by expanding the size of the light source or using spatial filters to mitigate speckle noise and improve image quality [231]. Other approaches include implementing deformable mirrors [243] or spatial light modulators [239] in adaptive optics to dynamically adjust the wavefront of the light.

Although the coherence length of a light source can be estimated from its spectral linewidth and the coherence area from its divergence angle, there has been no direct research on measuring the coherence length or coherence area of LC lasers, nor detailed studies of their coherence characteristics. However, understanding these properties is crucial for employing LC lasers in various application scenarios. On the other hand, due to the relatively small linewidth of LC lasers, the accuracy of most commercial spectrometers is insufficient to give precise measurement results, thus measuring the coherence length of LC lasers directly would be more desirable. These factors motivate the exploration of the coherence properties of LC lasers.

In this chapter, a Michelson interferometer was assembled and first employed to measure the coherence length of the Nd:YAG laser. The measurement result shows consistency with that published in the literature which reaffirms the accuracy of the measurement system. Subsequently, the coherence length of LC lasers is measured and investigations on how it varies for different LC layer thicknesses and excitation fluences are conducted. Such results could be of significant benefit to understanding the temporal coherence of these band-edge LC lasers. This chapter focuses on studies related to the temporal coherence measurements of band-edge LC lasers, while spatial coherence measurements are a subject for future research.

7.2 Temporal Coherence Measurements

7.2.1 Michelson Interferometer

The coherence length of a laser beam can be measured using a Michelson interferometer, where the beam is split by a beamsplitter, sending one part to a fixed mirror and the other to a movable mirror. The split beams are then superposed and directed to a photodetector, where interference fringes are observed when the mirrors are perfectly aligned. If the electric field vectors and intensities of the separated beams are represented as $\mathbf{E_1}$, $\mathbf{E_2}$, and I_1, I_2, respectively, then the received intensity of light can be expressed as

$$I = \langle \mathbf{E_1} + \mathbf{E_2} \rangle^2 = I_1 + I_2 + 2|\gamma|\sqrt{I_1 I_2}\cos\phi \tag{7.1}$$

where ϕ is the phase difference between $\mathbf{E_1}$ and $\mathbf{E_2}$ ($\phi = \arg\langle \mathbf{E_1 E_2^*} \rangle$) and the angle brackets represent time averaging of the quantities inside them. The degree of temporal coherence between the two beams, γ, can be further defined as

$$\gamma = \frac{\langle \mathbf{E_1 E_2^*} \rangle}{\sqrt{\langle |\mathbf{E_1}| \rangle \langle |\mathbf{E_2}| \rangle}} \tag{7.2}$$

The quality of the interference fringes is typically described by their interferometric visibility, which is given by

$$V = \frac{I_{max} - I_{min}}{I_{max} + I_{min}} \tag{7.3}$$

where I_{max} and I_{min} are the maximum and minimum intensity across the interference pattern, respectively. According to Eq. (7.1), constructive and destructive interference occur when ϕ

equals $2k\pi$ and $(2k+1)\pi$, respectively, where k is an arbitrary integer. Therefore,

$$\begin{cases} I_{max} = I_1 + I_2 + 2|\gamma|\sqrt{I_1 I_2} \\ I_{min} = I_1 + I_2 - 2|\gamma|\sqrt{I_1 I_2} \end{cases} \tag{7.4}$$

If the beamsplitter divides the incident energy equally between the two paths, then $I_1 = I_2$, and the visibility in Eq. (7.3) directly represents the degree of temporal coherence, since

$$V = \frac{2|\gamma|\sqrt{I_1 I_2}}{I_1 + I_2} = |\gamma| \tag{7.5}$$

In this case, complete coherence corresponds to $V = 1$ or $|\gamma| = 1$, partial coherence to $0 < V < 1$ or $0 < |\gamma| < 1$, and complete incoherence to $V = 0$ or $|\gamma| = 0$.

7.2.2 Coherence Length of a Pulsed laser

Prior to investigating the temporal coherence of LC lasers, the coherence length of a commercially-sourced pulsed Nd:YAG laser (6FTSS355-Q4-S, CryLas) was measured to validate the effectiveness and accuracy of the measurement method. The experimental setup is illustrated in **Fig. 7.1**, where the movable mirror was mounted on a piezoelectric stage (17TFC001/MD, Melles Griot) and a manual translation stage. The stages were equipped with micrometres, offering fine (1 µm) and coarse (10 µm) control over the position of the movable mirror, respectively. The piezoelectric stage was also connected to a piezoelectric controller (17PCW011, Melles Griot) for finer displacement control by adjusting the applied voltage. Prior to the measurements, the intensities of two split beams after the beamsplitter were measured by a photodiode (PD) (PDA36A-EC, Thorlabs) connected to an oscilloscope (TBS1052C, Tektronix) to confirm that they exhibited the same intensity.

Subsequently, the interference pattern was detected by another PD (DET10A/M, Thorlabs) connected to the same oscilloscope, which had a smaller detecting area of 0.8 mm^2 to capture a single interference fringe at a time. By adjusting the voltages applied to the piezo stage, the optical path difference between the two split beams was gradually varied, causing the intensity at the PD to periodically switch between maxima and minima. These intensity variations occurred as constructive and destructive interference fringes were detected. For example, when a voltage of 1.5 V was applied to the piezoelectric stage, the PD recorded maximum intensity, generating a signal with a 6.62 V peak-to-peak value. The next maximum occurred

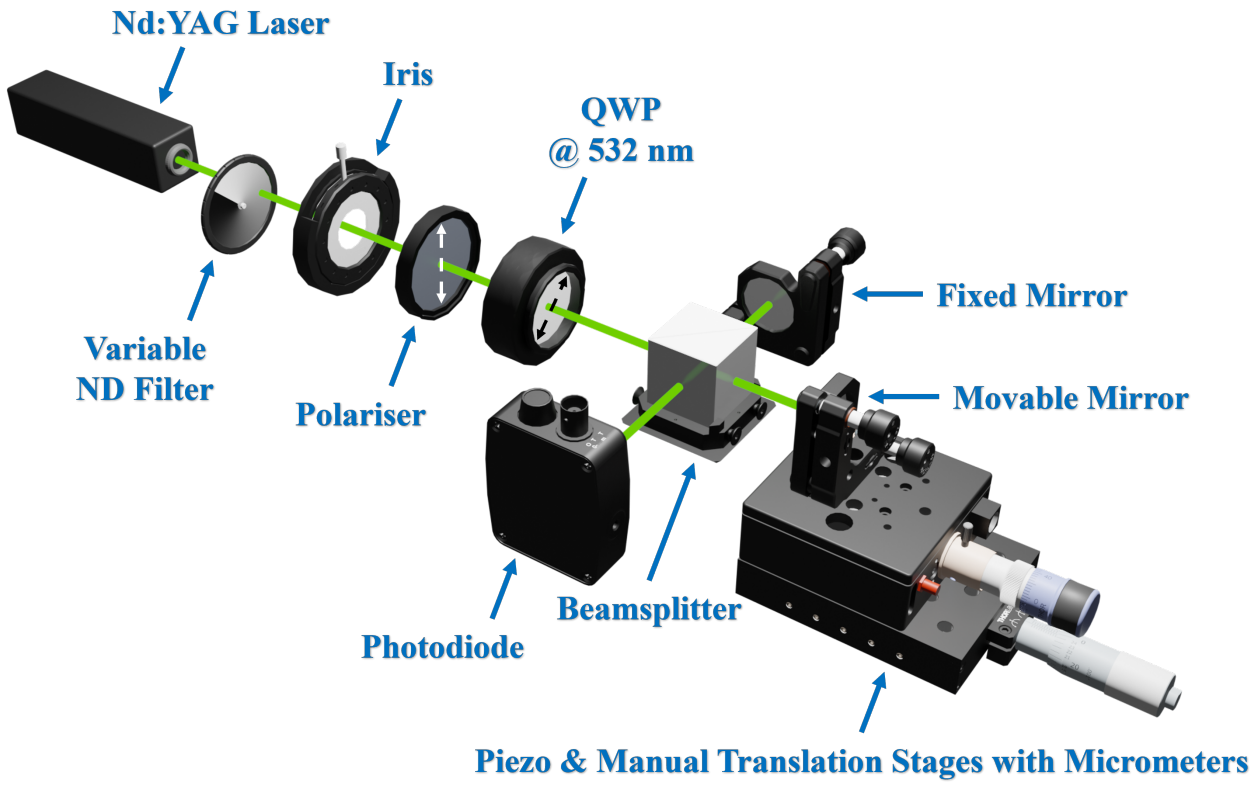

Figure 7.1: System configuration for measuring the coherence length of a commercial pulsed Nd:YAG laser using a Michelson interferometer. The light under investigation was split into two beams by a beamsplitter. The movable mirror was mounted on a piezoelectric and a manual translation stage which were equipped with micrometers to provide coarse and fine control of the optical path difference between the two split beams, respectively. The interference pattern was detected by a PD. Additional components and translation mounts for the polarisers and QWPs are not shown in the figure for simplicity.

at 2.9 V. Given that the laser wavelength was 532 nm, this indicated that the piezoelectric controller provided a displacement control of approximately 190 nm/V to the piezoelectric stage suggesting a resolution of approximately 19 nm. This level of control was sufficient for measuring the coherence length of the Nd:YAG and LC lasers. The combination of the piezoelectric controller and the PD allows for precise measurements of I_{max} and I_{min} in Eq. (7.3) leading to the calculation of the visibility of the interference fringes. Additionally, the micrometers on the translation stages enable accurate displacement scanning across the coherent range so that coherence length can be further measured.

The alignment of components is essential for the accuracy of the Michelson interferometer. Initially, the beamsplitter and fixed mirror were positioned in the system to ensure that the reflection from the fixed mirror was precisely superimposed with the incident beam. After that, the movable mirror mounted on translation stages was added to the system, and its reflection

was aligned to overlap with the incident beam as well. The position of the movable mirror was adjusted so that the distance between it and the beamsplitter was close to the distance between the fixed mirror and the beamsplitter, corresponding to zero optical path difference. Furthermore, the optical paths of the split beams were minimised to reduce divergence due to the non-collimated nature of the Gaussian beam.

The maximum and minimum voltages received by a PD were recorded when adjusting the voltage applied to the piezo translation stage. The measurement was repeated for different positions of the movable mirror and the results are demonstrated in **Fig. 7.2**, where the maxima and minima at each position are illustrated by the dotted and solid blue lines, respectively. Using Eq. (7.3), the corresponding visibility of the interference fringes was calculated and is represented by the orange solid line in the figure. The coherent range is defined as the distance between the positions that correspond to $1/e$ fringe visibility [244]. Since the optical path is a roundtrip, the coherence length is calculated as twice this coherent range. As indicated by Fig. 7.2, the coherence length of the Nd:YAG laser was measured to be 16.38 mm, where the repetition rate was set to 10 Hz. This result aligns well with values reported in the literature for the similar type of Q-switched Nd:YAG lasers [245, 246].

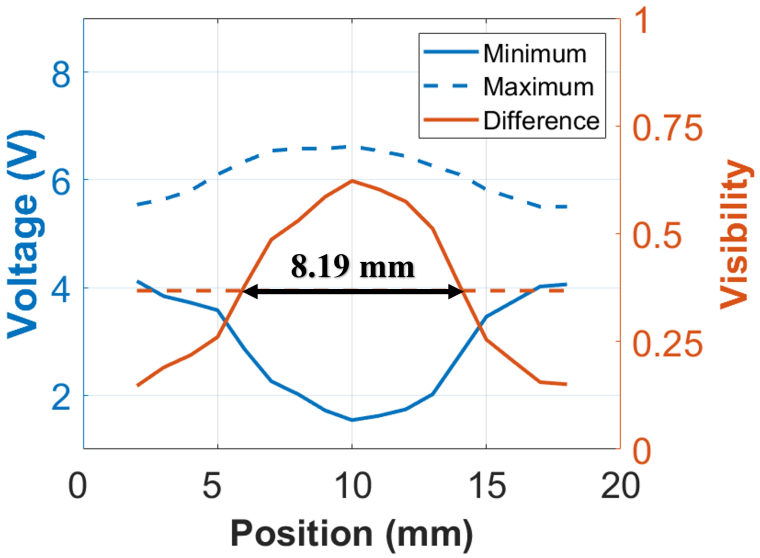

Figure 7.2: Measurement of the coherence length of the Nd:YAG laser. The repetition rate of the Nd:YAG laser was set to 10 Hz. The maximum and minimum intensities across the interference pattern at different positions of the movable mirror were measured by a PD and are represented by the dotted and solid blue lines on the graph, respectively. The corresponding visibility was calculated and is shown by the orange line, plotted on the secondary y-axis. The coherent range is defined as the distance between the positions that correspond to $1/e$ fringe visibility. From these measurements, the coherence length is determined to be 16.38 mm.

7.2.3 Coherence Length of LC lasers

Similar to the Nd:YAG laser, the coherence lengths of LC lasers were measured using the optical system shown in **Fig. 7.3**. The laser emission from the LC cell was collected by a 10x microscope objective lens and a concave lens with a focal length of -75 mm, to collimate the beam and minimise the disturbance of the spatial coherence on the measurement results.

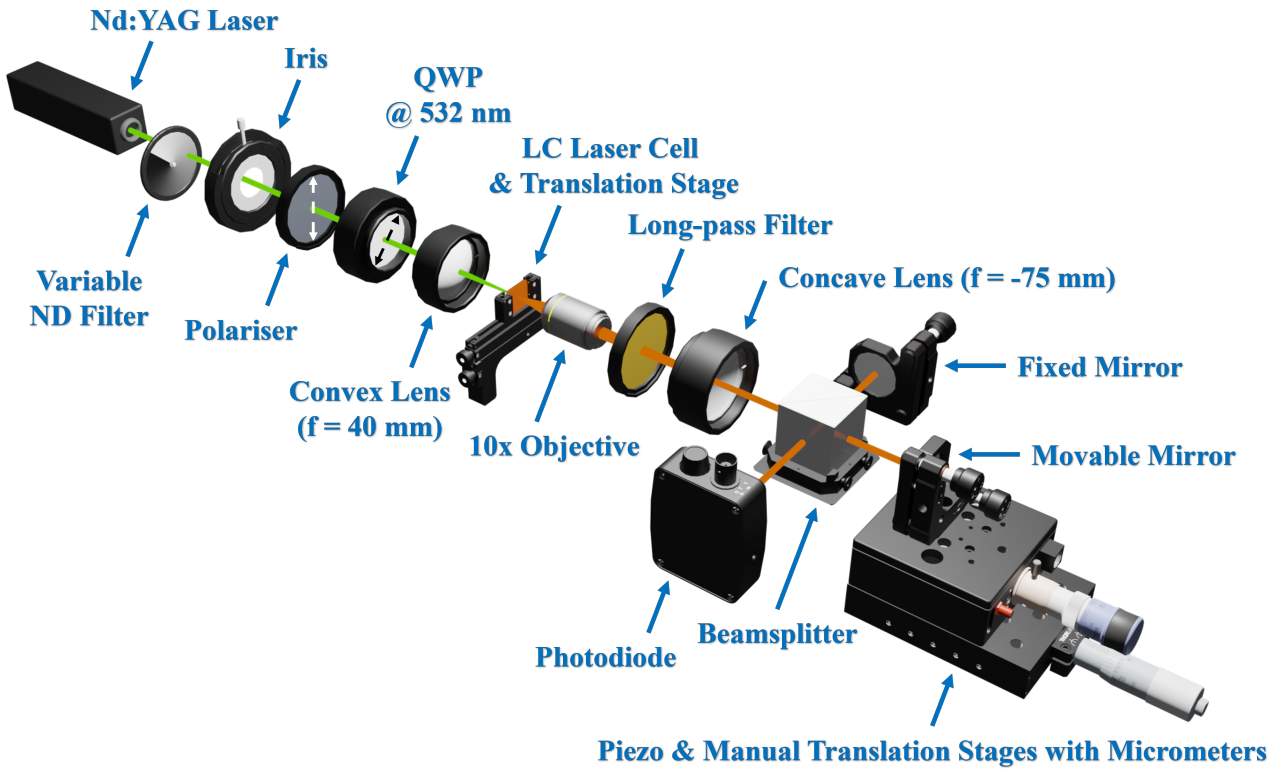

Figure 7.3: System configuration for measuring the coherence length of LC lasers using a Michelson interferometer. The LC laser emission was collected and collimated by an objective and a concave lens, before being split into two beams by a beamsplitter. The movable mirror was mounted on a piezoelectric and a manual translation stage which were equipped with micrometers to provide coarse and fine control of the optical path difference between the two split beams, respectively. The interference pattern was detected by a PD. Additional components and translation mounts for the polarisers and QWPs are not shown in the figure for simplicity.

The LC cell used in this experiment was a wedge cell fabricated following the procedure introduced in Chapter 3 with a thickness gradient of 0 to 23 µm and filled with a mixture of E7 + 3.8 wt.% BDH1281 + 1 wt.% DCM. This LC device has a similar threshold as that demonstrated in Fig. 4.10, with a slightly higher concentration of the chiral additive leading to laser emission with a lower wavelength. The emission profile of this LC laser will be presented later in the chapter. Initially, a screen was used in place of the PD, and the repetition rate of the Nd:YAG laser was set to 100 Hz for the convenience of observing the interference pattern

on the screen. The position of the movable mirror was adjusted using the coarse and fine micrometers on the translation stages so that the interference fringes reached their highest visibility. After achieving this, the repetition rate of the Nd:YAG laser was reset to 10 Hz, and the screen was replaced with the PD for further measurement.

The use of the wedge cell facilitates an investigation into the impact of cell thickness on the coherence length of LC lasers. The structure of the LC cell is illustrated in **Fig. 7.4**, where six different thicknesses were selected by marking six distinct points on one edge of the glass substrate, labelled A to F in the figure, between the 'zero-thickness' edge of the cell (point O) and the spacer (point N). The distances of OA, OB, OC, OD, OE, OF, and ON, were measured by a calliper as 5.70 mm, 8.90 mm, 12.24 mm, 16.11 mm, 19.26 mm, 22.71 mm, and 25.80 mm, respectively. Given that the spacer at point N is 23 µm thick, the corresponding LC layer thicknesses at points A to F were geometrically calculated as 5.08 µm, 7.93 µm, 10.91 µm, 14.36 µm, 17.17 µm, and 20.25 µm, respectively.

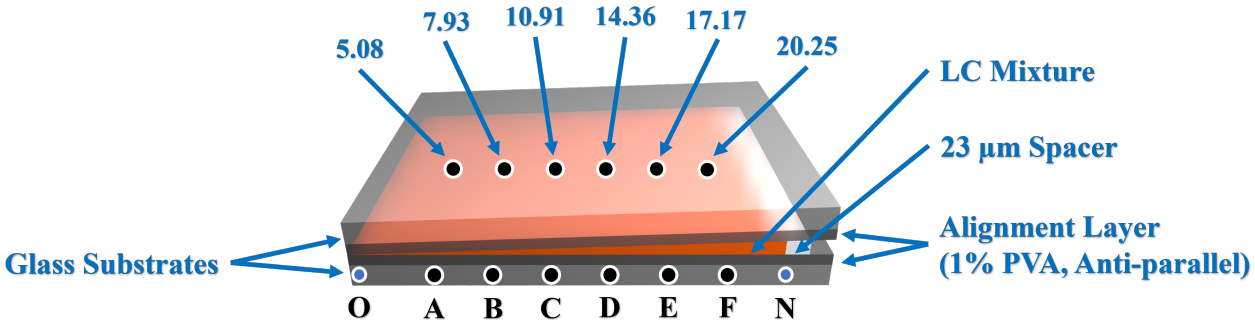

Figure 7.4: The structure of a wedge cell fabricated for the investigation of the coherence length of band-edge LC lasers of different thicknesses. The cell has a range of thicknesses from 0 to 23 µm and was filled with a dye-doped chiral nematic LC mixture (E7 + 3.8 wt.% BDH1281 + 1 wt.% DCM). Six points were selected for the measurements as illustrated by the blue dots on the figure, and their thicknesses were calculated by geometry.

In the experiments carried out to measure coherence length at these thicknesses, the LC cell was first mounted on an XY-translation stage as shown in Fig. 7.3. The translation stage was adjusted in both the x- and y-directions so that the Nd:YAG laser beam was directed to one of the marks on the substrate edge. The cell was then moved vertically to ensure that the centre of the LC sample with the corresponding thickness was illuminated by the Nd:YAG laser, as indicated by the blue points in Fig. 7.4. Similar to the experimental approach for the Nd:YAG laser, the coherence lengths of LC lasers with six LC layer thicknesses were measured subsequently and the results are presented in **Fig. 7.5**.

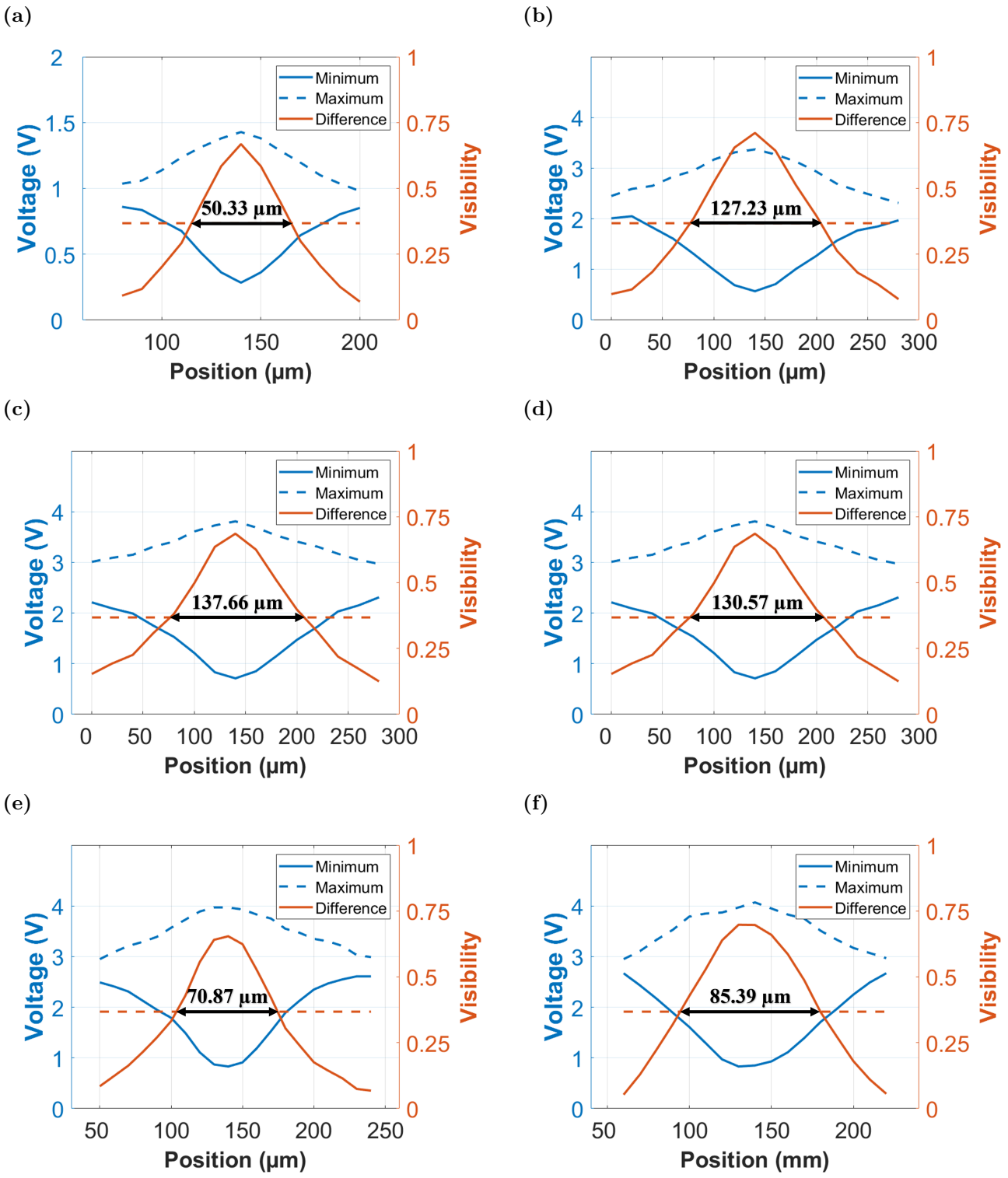

Figure 7.5: Measurement of the coherence length of a band-edge LC laser (E7 + 3.8 wt.% BDH1281 + 1 wt.% DCM) with thicknesses of (a) 5.08 μm, (b) 7.93 μm, (c) 10.91 μm, (d) 14.36 μm, (e) 17.17 μm and (f) 20.25 μm. The maximum and minimum intensities across the interference pattern at different positions of the movable mirror were measured by a PD and are represented by the dotted and solid blue lines on the graph, respectively. The corresponding visibilities were calculated and are shown by the orange line on the secondary y-axis. The coherent range is defined as the distance between the positions that correspond to $1/e$ fringe visibility. The measurements were conducted at a room temperature of 20°C.

The results in Fig. 7.5 suggest that the coherence length of LC lasers varies with the thickness of the LC layer, with the longest coherence length observed for a 10.91 µm thick device. This phenomenon can be explained by the variation in the LC laser spectrum as the LC layer thickness changes, due to the relationship between the degree of temporal coherence and the spectral irradiance distribution of a light source, as described by the Wiener-Khinchin theorem [247]. In terms of a Michelson interferometer, where two split beams originate from a light source with intensity, I, and spectral intensity distribution, $I(\omega)$, the degree of temporal coherence between the split beams, after propagating for t_1 and t_2 ($t_2 > t_1$) can be given by

$$|\gamma(\tau)| = \frac{\langle \mathbf{E_1} \mathbf{E_2^*} \rangle}{I} = \frac{\int I(\omega) \exp(iw\tau)\, d\omega}{I} \tag{7.6}$$

where $\tau = t_2 - t_1$ and ω is the angular frequency of the light.

Eq. (7.6) suggests that the degree of temporal coherence is the inverse Fourier transform of the spectral distribution of the beam [198]. If $I(\omega)$ is broad in frequency, then $|\gamma(\tau)|$ will be narrow in time, and vice versa. The temporal width, $\Delta\tau$, also known as the coherence time, represents the maximum time range over which the beam remains coherent with itself. Suppose the spectrum distribution of the beam has a width of $\Delta\omega$ in angular frequency and $\Delta\lambda$ in wavelength, centred at λ, then the coherence length, l_c, can be given by

$$l_c = c\Delta\tau = \frac{2\pi c}{\Delta\omega} = \frac{\lambda^2}{\Delta\lambda} \tag{7.7}$$

where $\Delta\lambda$ is typically indicated by the full width at half maximum (FWHM) of the beam spectrum. It is important to note that Eq. (7.7) only provides an estimation for calculating the coherence length of a beam from its spectrum, as it is subject to various limitations, such as the resolution of the spectrometer, the spectral distribution of the beam, and the number of laser modes, etc.

The spectra of LC lasers at different thicknesses were measured using a USB spectrometer (HR4000, Ocean Optics), with the results presented in **Fig. 7.6**. Due to the imperfect alignment of the LCs in this device, a slight wavelength variation of approximately 1 nm was observed across different regions. This could be attributed to multiple possible lasing modes in various regions, with one mode dominating the others, as suggested by the variation in emission spectra presented in Fig. 7.6. Subsequently, the coherence length of LC lasers measured previously can be compared with the estimation calculated from the corresponding centre wavelength

and spectral width using Eq. (7.7). For example, as shown in Fig. 7.6(c), the LC laser with a thickness of 10.91 µm has a centre wavelength of 587 nm and a spectral width of 0.68 nm, giving an estimated coherence length of 506.7 µm. Although not identical, this estimation is of the same order as the measured coherence length of 275.32 µm obtained using the Michelson interferometer, as shown in Fig. 7.5(c). The measured coherence length and spectral width of LC laser emission at various thicknesses are summarised in **Table 7.1**.

Table 7.1: The LC layer thickness, spectral width (FWHM) measured by the HR4000 spectrometer, and coherence length measured by the interferometer system of a wedge LC laser (E7 + 3.8 wt.% BDH1281 + 1 wt.% DCM). The measurements were conducted at a room temperature of 20°C.

LC Layer Thickness	Spectral Width (FWHM)	Coherence Length
5.08 µm	0.60 nm	100.66 µm
7.93 µm	0.65 nm	254.46 µm
10.91 µm	0.68 nm	275.32 µm
14.36 µm	0.69 nm	261.14 µm
17.17 µm	0.80 nm	141.74 µm
20.25 µm	0.90 nm	163.06 µm

The shortest coherence length was observed at an LC layer thickness of 5.08 µm, where the emission spectrum spanned approximately from 585.4 nm to 590.1 nm, as shown in Fig. 7.5(a). This broader spectrum, compared to those at higher thicknesses, can be attributed to a combination of fluorescence and weak laser emission, as suggested by Fig. 7.6(a). The coherence length of the LC laser increases with LC layer thickness up to 10.91 µm, where the emission spectrum spans from 585.5 nm to 588.7 nm, before decreasing for greater thicknesses as the spectral width of the LC lasers simultaneously broadens. Notably, the smallest spectral width does not necessarily correspond to the longest coherence length, which can be misleading if based solely on the FWHM metric. This discrepancy arises from the non-Gaussian nature of the emission spectra in this type of LC laser, which often exhibits a sharper peak but includes broader wavelength components at lower intensities. Consequently, the FWHM indication may underestimate the true spectral span, especially for components at lower intensities. For example, in Fig. 7.6(d), the FWHM width is represented by the red arrow, but a broader range of approximately 3 nm is observed for the weaker intensity components, as indicated by the

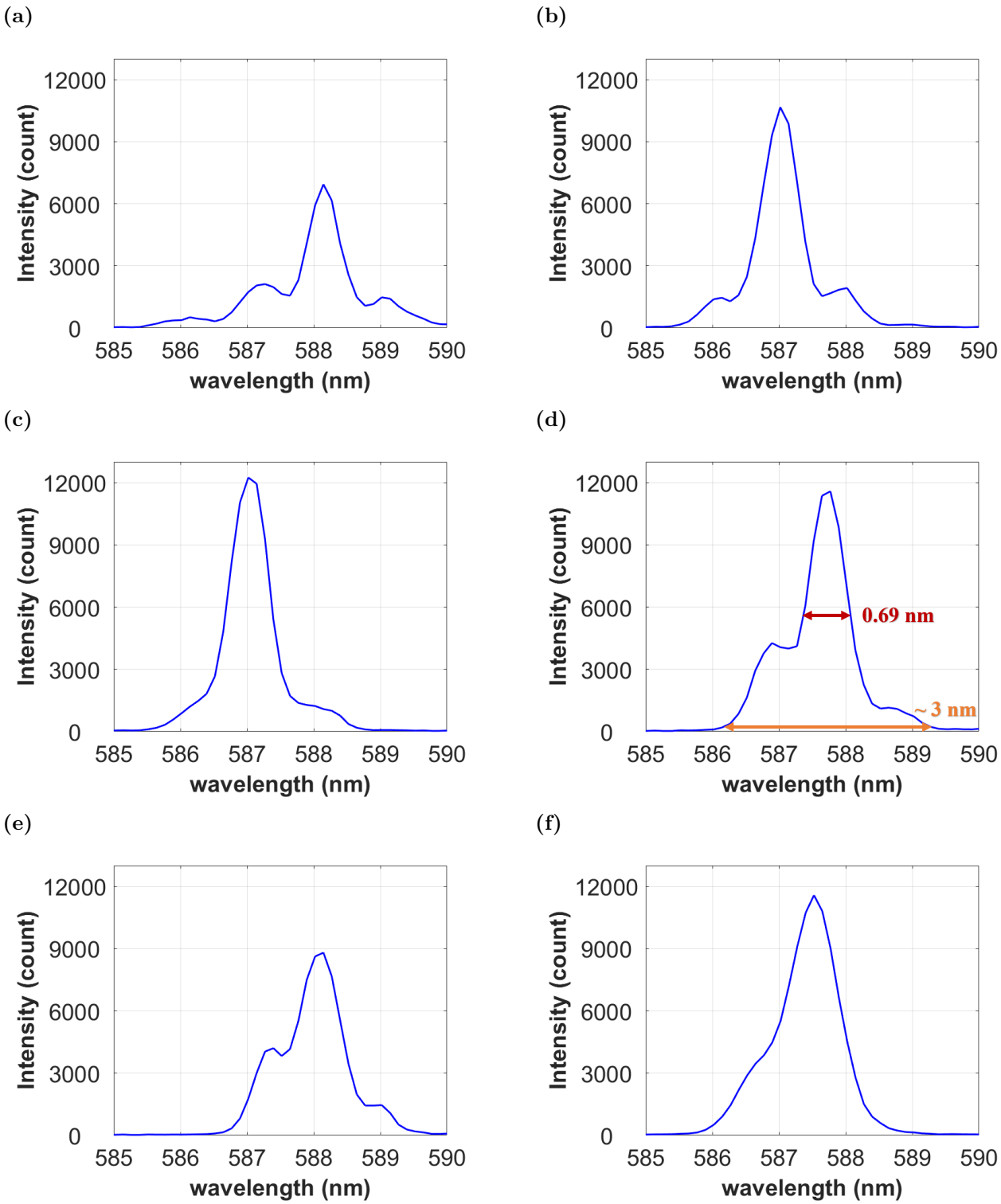

Figure 7.6: The emission spectra of band-edge LC lasers (E7 + 3.8 wt.% BDH1281 + 1 wt.% DCM) with thicknesses of (a) 5.08 µm, (b) 7.93 µm, (c) 10.91 µm, (d) 14.36 µm, (e) 17.17 µm and (f) 20.25 µm. The resolution of the spectrometer is 0.03 nm and the measurements were conducted at a room temperature of 20°C.

orange arrow. This highlights that relying on FWHM alone could misrepresent the spectral width and coherence properties of the laser, particularly for non-Gaussian emission profiles.

Another investigation into the coherence length of LC lasers involved examining the impact of excitation fluence on the LC cell. The XY-translation stage was fixed to excite a thickness of 20.25 µm, while the excitation fluence of the Nd:YAG source was varied by rotating a variable ND filter. Four different excitation fluences were selected, including 326.4 µJ/cm^2/pulse, 589.0 µJ/cm^2/pulse, 1174.5 µJ/cm^2/pulse, 1262.0 µJ/cm^2/pulse. The coherence lengths of the LC lasers were measured, with the results shown in **Fig. 7.7**(a)∼(d), respectively. Additionally, the emission spectra were observed to verify the occurrence of 'single-mode' LC laser emissions under these excitation conditions. From Fig. 7.7, it can be observed that the coherence lengths under different excitation fluences remain relatively consistent around 180 µm. Therefore, it can be concluded that the excitation fluence of the Nd:YAG laser does not significantly influence the coherence length of the LC laser.

7.3 Summary

In conclusion, the coherence length of band-edge LC lasers was investigated using a Michelson interferometer. By measuring the maximum and minimum intensities of the interference fringes, the visibility was calculated, providing an indication of the coherence length. To verify the effectiveness and accuracy of this measurement approach, a commercial pulsed Nd:YAG laser was measured and the results were in good agreement with what was published in the literature for the similar type of Q-switched Nd:YAG lasers.

It has been found that the coherence length of band-edge LC lasers can be affected by the LC layer thickness, which can be attributed to variations in the lasing modes at different thicknesses due to the non-uniform alignment of the macroscopic helical structure, as confirmed by the emission spectra measured for each thickness. The longest coherence length of 275.32 µm was observed at a thickness of 10.91 µm. Shorter or thicker LC layer thicknesses were found to be associated with broader spectral linewidths and reduced coherence lengths of the laser emission. Additionally, experimental results suggested that the excitation fluence of the Nd:YAG laser had little impact on the coherence length of LC lasers. The directly measured coherence length of LC lasers was compared with those estimated from calculations

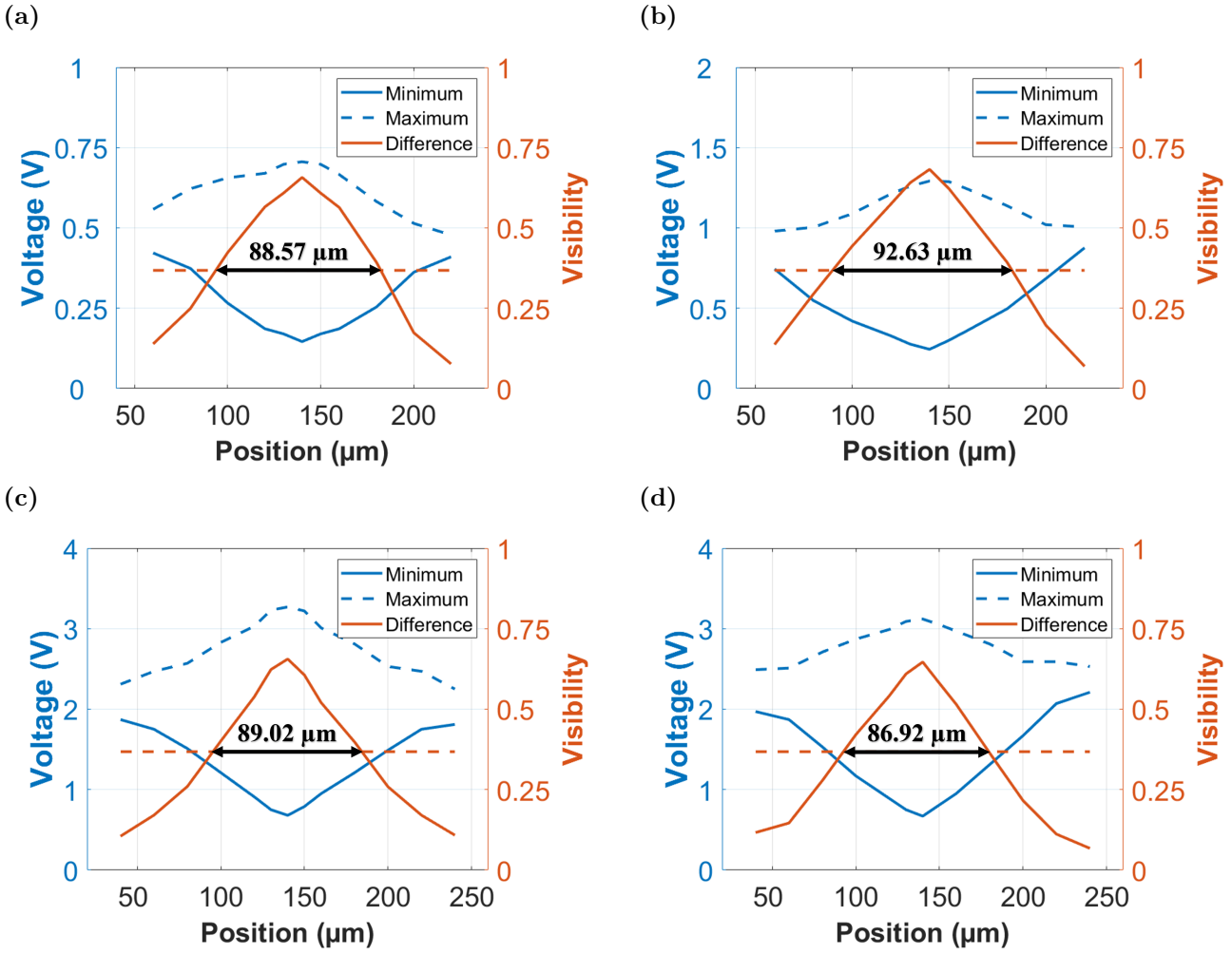

Figure 7.7: Measurement of the coherence length of a band-edge LC laser under excitation fluences of (a) 326.4 μJ/cm^2/pulse, (b) 589.0 μJ/cm^2/pulse, (c) 1174.5 μJ/cm^2/pulse, and (d) 1262.0 μJ/cm^2/pulse. The maximum and minimum intensities across the interference pattern at different positions of the movable mirror were measured by a PD and are represented by the dotted and solid blue lines on the graph, respectively. The corresponding visibilities were calculated and are shown by the orange line on the secondary y-axis. The coherent range is defined as the distance between the positions that correspond to $1/e$ fringe visibility. The measurements were conducted at a room temperature of 20°C.

involving the spectral linewidth of the beam measured by a USB spectrometer, where both approaches show coherence length results of the same order.

In addition to the temporal coherence study, future work could investigate the spatial coherence properties of LC lasers, with a proposed experimental method outlined in the next chapter. These findings will enhance the understanding of LC laser coherence and benefit applications where coherence is an essential factor to be considered.

8

Conclusions and Future Work

Contents

8.1 Conclusion to Thesis 182
8.2 Stokes Parameters Measurements of Left-handed Band-edge LC Lasers 184
8.3 Spatial Coherence Study of LC Lasers 187
8.4 Polarisation States and Coherence of Polymerised Blue Phase LC Lasers 188
8.5 Bidirectional Optical Communication Link Using LC Beam-steering 192
8.6 Advanced LC Laser Device Architectures 193

8.1 Conclusion to Thesis

This thesis investigates various liquid crystal (LC) devices for laser and optical beam-steering technologies and applications. Building upon the research motivation outlined in Chapter 1, the theoretical background and literature review presented in Chapter 2, and the experimental techniques and fabrication of band-edge LC lasers described in Chapter 3, this work first studies the polarisation states and temporal coherence of band-edge LC lasers, fabricated from dye-doped chiral nematic LCs. It also explores factors that can influence these emission characteristics, such as excitation fluences, LC layer thicknesses, and alignment quality.

In terms of the polarisation state, as discussed in Chapter 4, the laser emissions from these LC devices are close to circularly polarised with the same handedness as the helical structure of LCs. The highest degree of circularity observed is 0.956 for an LC layer thickness of 20.04 µm, with a degree of polarisation (DOP) of 1.00. Thinner LC layers or lower excitation fluences above

the threshold lead to a reduction in the circularity and DOP. Additionally, larger thicknesses could potentially result in poor alignment qualities with defects appearing across the LC cell, such that the corresponding laser emission exhibits lower circularity and DOP. Regarding the temporal coherence investigated in Chapter 7, the longest coherence length measured is 275.32 µm, corresponding to an LC layer thickness of 10.91 µm and spectral width (full width at half maximum) of 0.68 nm. Experiments indicate that varying the excitation fluence has minimal effect on the coherence length of these LC lasers. Commercial laser sources were also measured to validate the accuracy and reliability of the employed measurement systems.

These fundamental studies of band-edge LC lasers provide further information in terms of their emission characteristics, which were then utilised to develop a non-mechanical two-dimensional beam-steering system as demonstrated in Chapter 5. The beam-steering direction was controlled by adjusting the voltages applied to LC tunable waveplates such that the polarisation state of the propagation beam was altered between left and right circular and was subsequently steered by polymerisable LC polarisation gratings (PG). This approach has the advantages of not altering the laser wavelength, not changing the characteristics of the laser itself, and having minimal impact on the intensity of the laser. Along with the Jones matrix simulation, the appearance of other diffraction orders (zero-orders, sub-orders, and opposite-orders) aside from the primary beam were explained and characterised. The intensity distribution of the diffraction pattern of this system served as another indication of the polarisation state of an LC laser, with results further verifying the polarisation states characterised in earlier chapters.

Finally, Chapter 6 demonstrated a free-space optical communication link employing the same beam-steering components alongside a diffuser for full spatial coverage. This system successfully transmitted 50 Mbps pseudo-random binary sequence signals over a distance of more than 1 meter, with a bit error rate lower than 10^{-3} in point-to-point scenarios. The system also achieved a steering bandwidth of 58.82°/sec, making it suitable for mobile terminals in various applications. The beam-steering system can, in principle, accommodate any transmission rate or wavelength, as the performance is independent of the physical properties of the beam-steering components and the diffuser. This approach offers a substantial increase in the field of view and link margin over using transmitter beam-steering alone and implements low-cost compact components that can be integrated to create a lightweight high-performance steering subsystem potential for a wide range of applications.

The subsequent sections outline potential future work that could build upon the research introduced in this thesis. These include proposed directions for further investigations, supported by some preliminary experimental results that provide insight and justification for these research proposals.

8.2 Stokes Parameters Measurements of Left-handed Band-edge LC Lasers

The Stokes parameters measurements introduced in Chapter 4 were conducted on LC lasers fabricated from dye-doped chiral nematic LC mixtures with a right-handed helical structure. LC laser emissions can also be generated from left-handed mixtures at either band-edge of the photonic bandgap. Therefore, the impact of the helical handedness on the Stokes parameters and polarisation states of LC lasers could be further investigated.

The concentration of a left-handed chiral additive, S811, was first examined to ensure that the fluorescence spectrum of DCM overlaps with the long wavelength photonic band edge formed by the chiral nematic LC. S811 has a lower helical twisting power compared to BDH1281 used previously, so another nematic LC, BL006, was used due to the greater solubility of S811 in BL006. Initially, a mixture of BL006 + 20 wt.% S811 was prepared and capillary filled into an anti-parallel rubbed cell (Instec) with a thickness of 5 µm. The detailed mixture preparation procedure was described in Chapter 3. The transmittance spectrum for the mixture was measured with the UV-Vis spectrometer, as shown in **Fig. 8.1**, indicating a bandgap of 720 to 810 nm. The concentration of S811 was then increased, and an organic laser dye, DCM, was added at approximately 1% by weight of the total mixture to create two mixtures: BL006 + 24.1 wt.% S811 + 1 wt.% DCM and BL006 + 28.7 wt.% S811 + 1 wt.% DCM. Both mixtures were capillary filled into 5 µm Instec cells, and their spectra were measured and are shown in Fig. 8.1.

The long wavelength band-edge of the mixture BL006 + 28.7 wt.% S811 + 1 wt.% DCM was located at 626 nm, allowing for the possibility of LC laser generation if the mixture is filled into thicker cells with sufficient gain within the cavity. Therefore, this particular mixture was filled into another anti-parallel rubbed cell (LG) with a thickness of 8.18 µm and placed into the LC laser system illustrated in Fig. 4.8. The direction of the fast axis of the 532 nm QWP was rotated 90° anti-clockwise to adjust the polarisation state of the Nd:YAG laser to be right

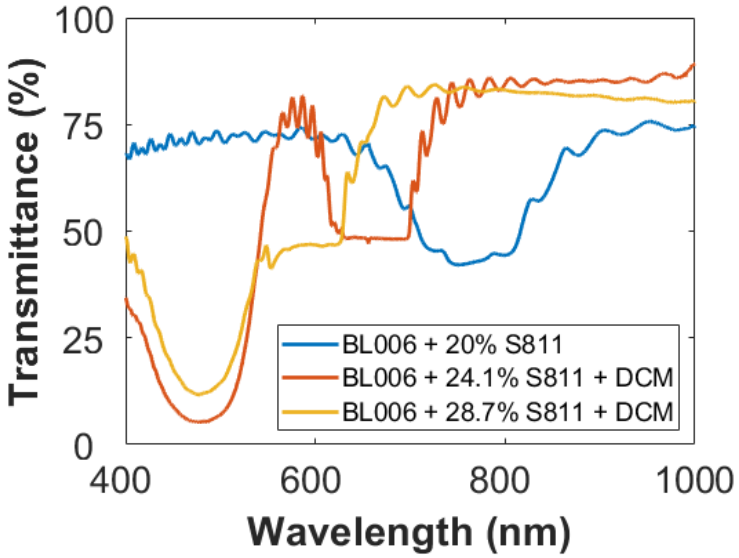

Figure 8.1: The transmittance spectra for three different left-handed chiral nematic LC mixtures with various concentrations of the chiral additive, BL006 + 20 wt.% S811, BL006 + 24.1 wt.% S811 + 1 wt.% DCM, and BL006 + 28.7% S811 + 1 wt.% DCM, capillary filled in 5 µm anti-parallel rubbed cells. The measurements were conducted at a room temperature of 20°C.

circular, opposite to the handedness of the LC helix. A USB spectrometer was placed after the long-pass filter to collect the propagation beam, and a single-mode LC laser was observed. However, the spectrum disappeared after a few seconds and did not reappear, even when other regions of the cell were excited. The cell was heated to the isotropic phase and then cooled to room temperature, yet no further laser emission was observed.

To investigate the reason for the disappearance of the left-handed LC laser, the texture of the LC cell was observed under a polarised optical microscope after being heated to the isotropic phase and cooled to room temperature again. Interestingly, the colour of the cell varied from dark orange to yellow over time, as shown in **Fig. 8.2**, where three images were captured at 30 seconds, 1 minute, and 2 minutes after the cell was cooled to room temperature. The optical texture of the LC was further stabilised, and the current transmittance spectrum was measured. Results showed that the photonic bandgap immediately after cooling was approximately 553∼626 nm, while it slightly shifted to longer wavelengths of 590∼650 nm after the stabilisation of the LC texture.

Although the reason for the bandgap shift in the LC mixture was unclear, it could account for the disappearance of the LC laser emission, as the fluorescence spectrum of DCM no longer overlapped with the long wavelength band edge when the bandgap shifted to longer wavelengths. Additionally, experiments found that the shift in band-gap was more substantial for another

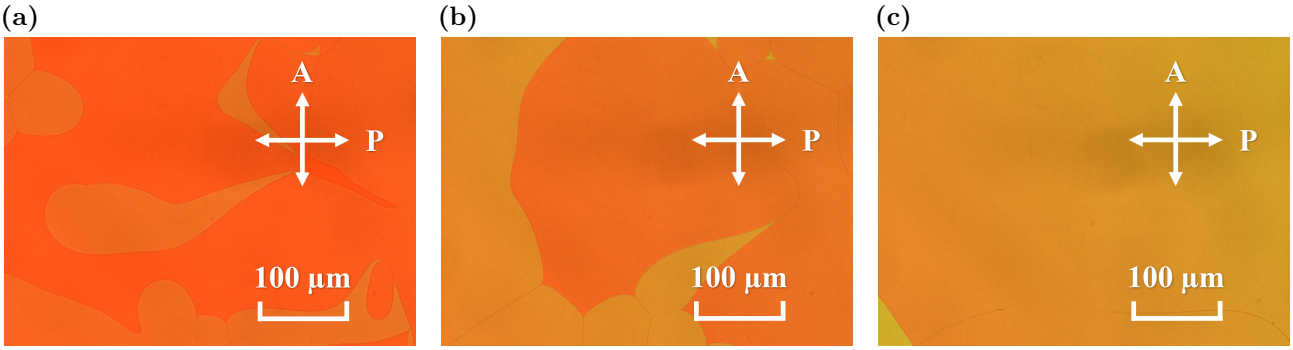

Figure 8.2: The optical textures of a left-handed LC cell (BL006 + 28.7 wt.% S811 + 1 wt.% DCM) on a polarising optical microscope. The colour of the textures altered over time from (a) to (b) and (c) suggesting the transmission spectra were shifted. The thickness of the LC cell was 5 µm and the measurements were conducted at a room temperature of 20°C.

LC mixture, BL006 + 30 wt.% S811 + 1 wt.% DCM, which had a higher concentration of the left-handed chiral additive. This mixture was capillary filled into a 5 µm Instec cell, and its transmittance spectra were measured using a UV-Vis spectrometer. The long wavelength band edge shifted from approximately 609 nm to the infrared, as illustrated in **Fig. 8.3**.

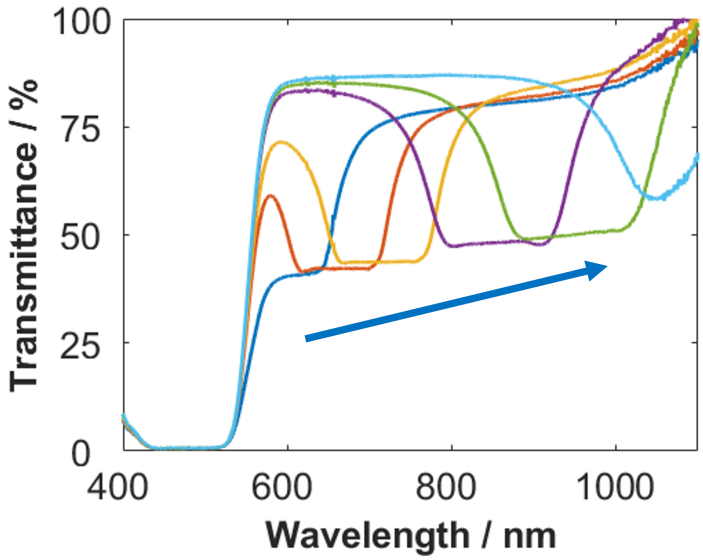

Figure 8.3: The transmittance spectra for the left-handed LC cell (BL006 + 30 wt.% S811 + 1 wt.% DCM) altered over time with the photonic bandgap blue-shifting to longer wavelengths. The thickness of the LC cell was 5 µm and the measurements were conducted at a room temperature of 20°C.

A series of varied microscope optical textures of the cell after being cooled to room temperatures were captured and are shown in **Fig. 8.4**. Additionally, multiple mixtures with 29 wt.% $\sim$ 31 wt.% S811 and cells with various thicknesses were experimented with, where similar behaviour was observed and no laser emission was achieved. Although the photonic

bandgap did not shift for LC mixtures with lower concentrations of S811, the long wavelength band edge did not match the fluorescence emission spectrum of the laser dye, resulting in no LC laser generation from these cells as well. Therefore, a left-handed chiral nematic LC laser could not be fabricated using a combination of BL006 and S811. The Stokes parameters of left-handed LC lasers were not investigated further due to the lack of left-handed chiral additives with high-twisting power. However, similar experimental results to those of right-handed LC lasers regarding excitation fluence, LC layer thickness, and alignment quality were expected, as the handedness of the LC helices should only alter the handedness of the LC emission, but not the circularity and DOP theoretically.

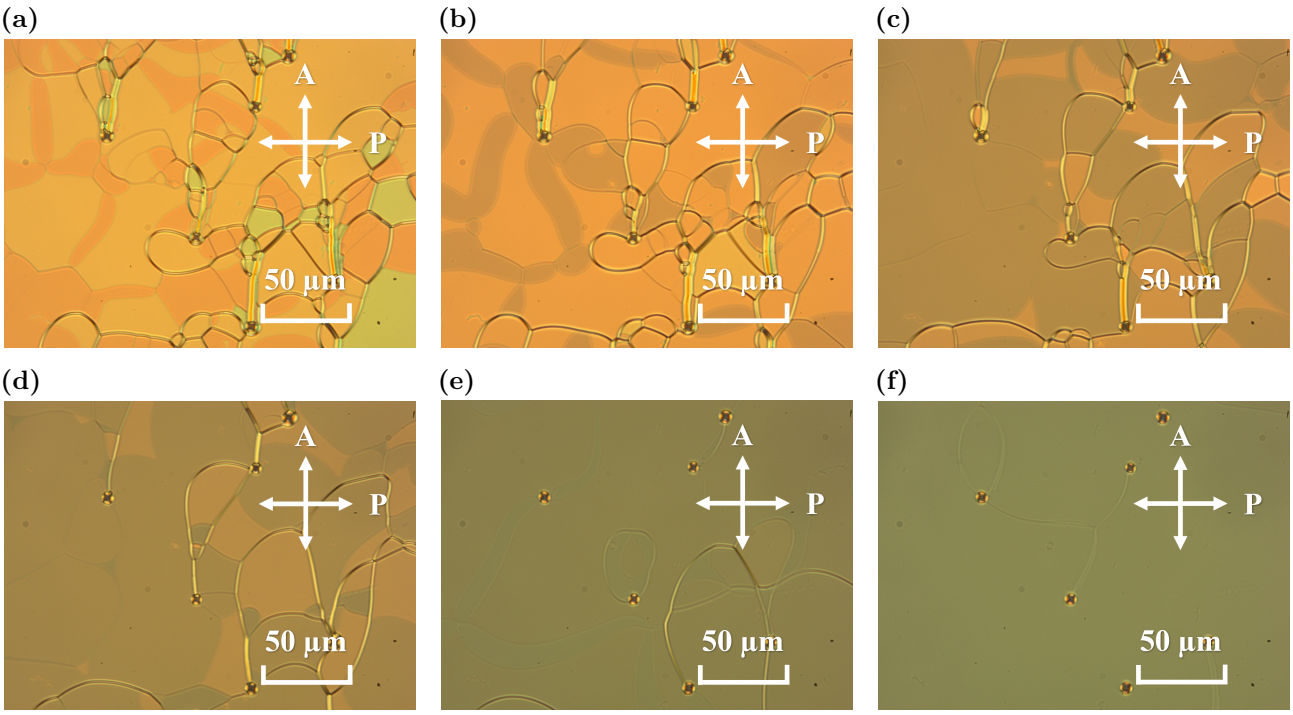

Figure 8.4: The optical textures of another left-handed LC cell (BL006 + 30% S811 + 1 wt.% DCM) on a polarising optical microscope. The colour of the textures altered over time from (a) to (b) and (c) suggesting the transmission spectra were shifted. The thickness of the LC cell was 5 µm and the measurements were conducted at a room temperature of 20°C. The double-headed white arrows show the orientations of the polariser and analyser.

8.3 Spatial Coherence Study of LC Lasers

As mentioned in Chapter 7, few studies have focused on the direct measurement of the coherence area of band-edge LC lasers, which is a key parameter for characterising their spatial coherence. An initial approach for measuring the coherence area could involve an optical system similar to

Young's double-slit experiment, where the interference fringes are detected by a photodiode or CCD camera, as illustrated in **Fig. 8.5**. The coherence area, A_c, can be indicated by observing the visibility of the interference fringes under various slit widths of the tunable double-slit, and the results can be compared to theoretical estimations using the relation $A_c = \lambda^2/\Delta\theta^2$, where $\Delta\theta$ is the divergence half-angle of the light source. This method could also serve as an indirect way of determining the divergence angle of band-edge LC lasers.

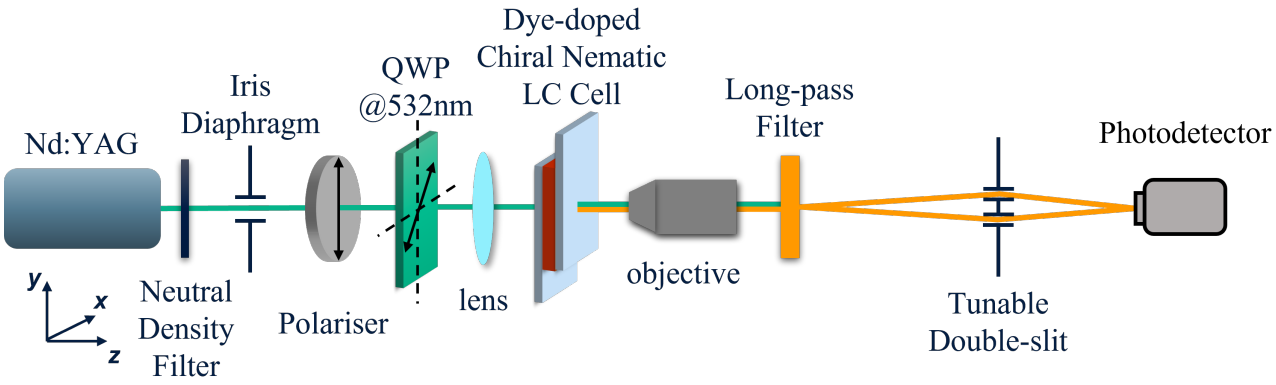

Figure 8.5: A proposed system configuration for measuring the coherence area of LC lasers using a similar arrangement as Young's double-slit experiment. The distance between the slits in this configuration is tunable such that the coherence of beams at two separate locations across the wavefront can be investigated by measuring the visibility of the interference pattern by a photodetector.

Further investigations can explore how the coherence area varies under different experimental conditions, such as changes in LC layer thickness, excitation fluence, or laser dye concentration. However, it is important to note that temporal and spatial coherence are often intertwined in experimental setups, such as the Michelson interferometer or Young's double-slit experiment, where both coherence properties can influence the results. To separate these two types of coherence, advanced experimental designs could be employed, such as using pinholes to isolate spatial coherence and narrowband filters or temporal modulators to isolate temporal coherence. These methods would potentially enable a more precise characterisation of the distinct coherence properties of LC lasers.

8.4 Polarisation States and Coherence of Polymerised Blue Phase LC Lasers

Besides dye-doped chiral nematic LCs studied in Chapter 4 and Chapter 7, band-edge LC lasers can also be fabricated from blue phase (BP) LCs, which offer significant advantages, despite

the challenges in achieving laser emission from such structures. The BP is an intermediate LC mesophase that exists between the isotropic and chiral nematic phases, with strict formation conditions and narrow temperature ranges. For conventional compounds, this phase can be achieved by slowly cooling a chiral nematic LC from its isotropic state. The most commonly observed BP phases are BP I, which has a body-centred cubic structure, and BP II, characterised by a simple cubic structure.

One notable benefit of BPLC lasers is the potential for simultaneous laser emission in three orthogonal directions, owing to the double-twist LC structure along with three-dimensional photonic bandgaps of BP II [70]. Researchers have reported successful laser emission from polymer-stabilised BP I LCs [248] as well as from wide-temperature BP I LCs [120]. In these studies, it has been found that the excitation threshold for BPLC lasers is lower than that of corresponding chiral nematic LC lasers using the same mixtures and similar experimental setups. This lower threshold, combined with the unique optical properties of BPLCs, presents exciting prospects for the future development of BPLC lasers. In recent years, reports have demonstrated a tunable lasing wavelength range of 30 nm in BP II as a function of temperature [249], as well as tunability from single- to quadruple-wavelength lasing over a broad range of 60 nm achieved by manipulating factors such as the photonic bandgap, the order parameter of the laser dye, the resonance cavity quality, and the pump energy [250]. Additionally, a wider operating temperature range, spanning over 15°C and including room temperature, has been reported in a dye-doped polymer-stabilised BP II LC laser [251].

Investigating the polarisation and coherence properties of BPLC lasers could further enhance the physical understanding and development of band-edge LC lasers. **Fig. 8.6** demonstrates a formation of BPLC from a mixture of BL006 + 44.6 wt.% R811, which was capillary filled into a 5 µm Instec cell. R811 is a chiral additive with low twisting power. The optical textures were observed using a polarising optical microscope (BX51, Olympus) and captured by an attached CCD camera (Retiga R6, Teledyne Photometrics). The sample was initially heated to the isotropic phase at 65°C by a hot stage, followed by a cooling process at 0.2°C/min until BP phase platelets began to appear at 58.7°C, as shown in Fig. 8.6(a). The cooling rate was then reduced to 0.1°C/min, and the platelet texture was observed to completely form across the cell between 51.7°C and 48.5°C, as demonstrated in Fig. 8.6(b). Finally, Fig. 8.6(c) illustrates the optical texture of the cell when the BP phase fully disappeared at 44.6°C.

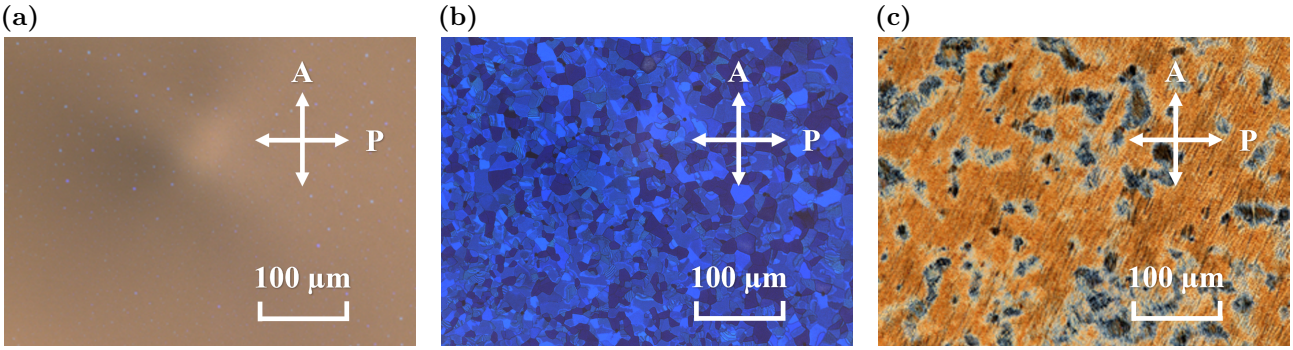

Figure 8.6: The textures of a BPLC cell (BL006 + 44.6 wt.% R811) on a polarising optical microscope during the formation of a BPLC. The sample was heated to 65°C by a hot stage and was cooled at a rate of 0.2°C/min until (a) the appearance of BP phase platelets at 58.7°C. The cooling rate was decreased to 0.1°C/min and (b) the platelet texture entirely covered the cell between 51.7°C and 48.5°C. (c) The BP fully disappeared at 44.6°C. The thickness of the LC cell was 5 µm and the double-headed white arrows show the orientations of the polariser and analyser.

The BPLC temperature range for the device described is relatively narrow, making the development of a polymer-stabilised BPLC cell crucial for practical BPLC lasers, ideally operating at room temperature. This can theoretically be achieved by incorporating a small fraction of monomers and a photoinitiator into the LC mixture. Under UV irradiation, these monomers polymerise, forming a polymer network that stabilises the BPLC lattice structure, thereby extending the BP temperature range.

Fig. 8.7 illustrates the formation of the BP phase and the subsequent UV curing process applied to another 5 µm LC cell, filled with a mixture of BL006 + 44.6 wt.% R811 + 5 wt.% RM257 + 1 wt.% IR819, where RM257 is a bi-functional monomer and IR819 is a photoinitiator. The sample was first heated to the isotropic phase at 65°C using a hot stage, followed by a cooling process at 0.2°C/min until BP platelets started forming at 56.5°C, as shown in Fig. 8.7(a). To block UV spectrum components, an orange long-pass filter was placed between the LC sample and the microscope illumination during observation. The cooling rate was reduced to 0.1 °C/min, resulting in a complete platelet texture at 50.8°C, as shown in Fig. 8.7(b).

Subsequently, the sample was transferred to a UV light source for curing at 1 mW/cm^2 for 60 seconds. The optical texture post-UV curing is shown in Fig. 8.7(c). The sample was then cooled further to 48°C at 0.1°C/min and subjected to a second round of UV curing with the same irradiance for 120 seconds, as shown in Fig. 8.7(d). A final cooling process to 44°C at 0.1°C/min was followed by UV curing for 180 seconds, with the optical texture demonstrated in Fig. 8.7(e). The curing rates and times were chosen based on optimal conditions reported

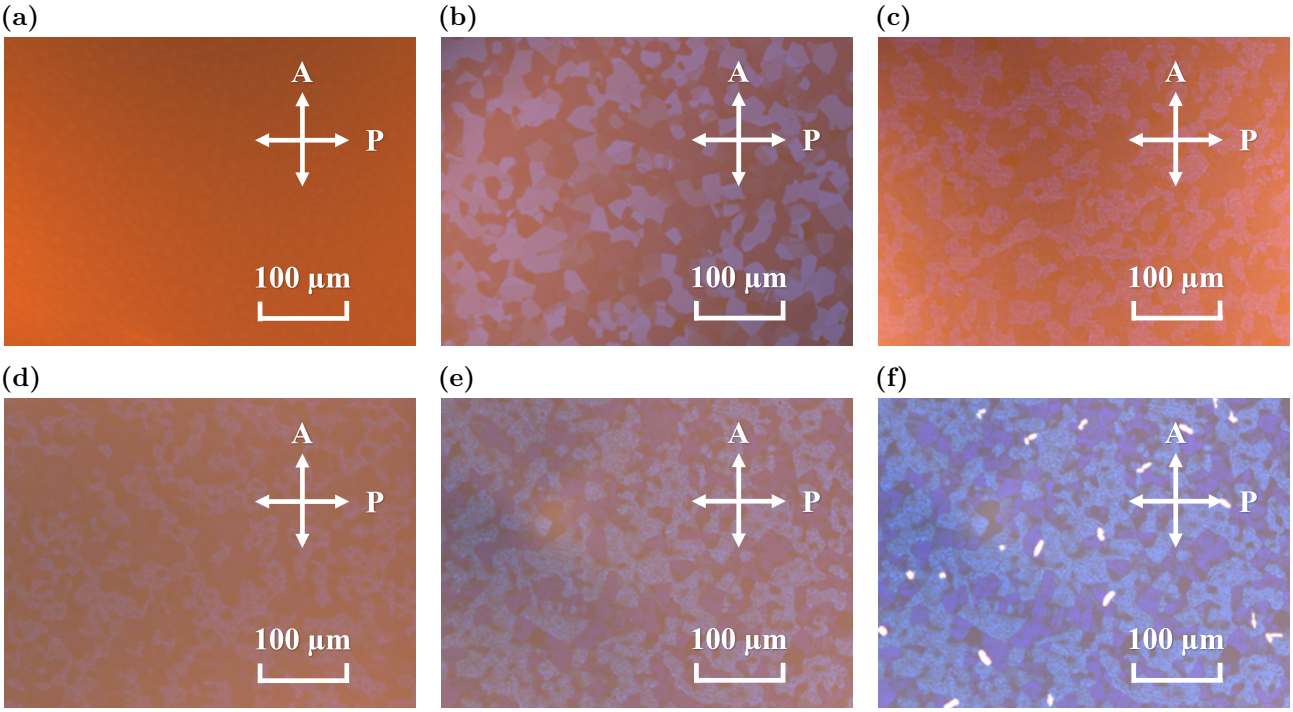

Figure 8.7: The textures of a polymerisable BPLC cell (BL006 + 44.6 wt.% R811 + 5 wt.% RM257 + 1 wt.% IR819) on a polarising optical microscope during the formation and UV curing of a BPLC. The UV components of the microscope illumination were filtered to prevent undesirable UV polymerisation. The sample was heated to 65°C by a hot-stage and was cooled at a rate of 0.2°C/min until (a) the appearance of BP platelets at 56.5°C. The cooling rate was decreased to 0.1°C/min and (b) the platelet texture entirely covered the cell at 50.8°C. (c) The cell was first transferred to a UV curing at 1 mW/cm^2 for 60 seconds. (d) Subsequently, the cell was cooled to 48°C at a rate of 0.1°C/min and experienced another UV curing process at 1 mW/cm^2 for 120 seconds. (e) Finally, the cell was cooled to 44°C at a rate of 0.1°C/min followed by UV curing at 1 mW/cm^2 for 180 seconds. (c) The BP platelet texture fully disappeared at 42.8°C. The thickness of the LC cell was 5 µm and the double-headed white arrows show the orientations of the polariser and analyser.

in the literature for similar LC samples. The lower temperature limit for the BP phase was ultimately found at 42.8°C, approximately 6°C lower than that of the non-polymerised sample. Fig. 8.7(f) illustrates the optical texture at the moment the BP disappeared.

Although polymer-stabilised BPLC was not achieved at room temperature in this study, the UV curing procedure effectively extended the temperature range. Some reports suggest the use of two monomers [252, 253], one mono-functional (e.g., EHA or C12A) and one bi-functional (e.g., RM257), for further optimisation. Therefore, future work could explore new combinations involving both mono-functional and bi-functional monomers to achieve more stable and room-temperature-operable BPLC devices, such that the polarisation states and coherence of these band-edge BPLC lasers can be further investigated.

8.5 Bidirectional Optical Communication Link Using LC Beam-steering

The arrangement of the beam-steering elements introduced in Chapter 6 offers the potential for bidirectional operation with minimal modifications, using the same combination of LC tunable waveplates and PGs. **Fig. 8.8** proposes a system configuration that could establish a bidirectional communication link utilising LC-based beam-steering. A key advantage of this design is that the same polarisation beam-steering assembly (the stack of PGs and their associated LC waveplates) can be used for both the transmitter and receiver, requiring only minimal additional components.

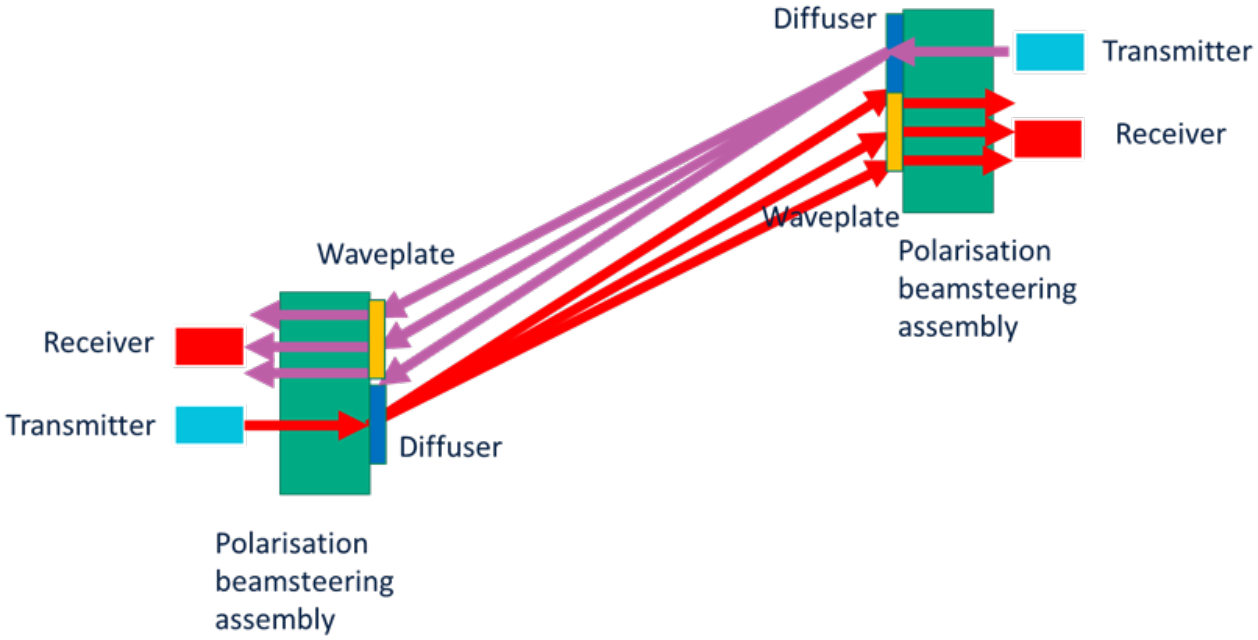

Figure 8.8: A proposed system design for a bidirectional free-space optical communication link using similar components as illustrated in Chapter 6, requiring only minimal additional components.

In the experiments detailed in Chapter 6, the data rates were limited by the transmitter modulator and receiver photodetector, both of which performed below the capabilities of current Li-Fi products. However, addressing this limitation was not the focus, as the study primarily aimed to demonstrate the beam-steering technique at both the transmitter and receiver, combined with a diffuser for full spatial coverage. The beam-steering components, offering an increased field of view and improved link margin, are independent of data rate and wavelength, meaning that the proposed bidirectional communication link can operate with multiple wavelengths and higher data rates when equipped with more advanced transmitter and receiver hardware.

8.6 Advanced LC Laser Device Architectures

To enhance the performance of LC lasers, particularly in reducing the excitation threshold, a primary challenge is to minimise various forms of loss. These losses come in various forms including fluorescence emission along directions that are orthogonal to the helix axis for which there is no band gap. Furthermore, the photonic bandgap is only partial as it affects light of one sense of circular polarisation only. Therefore, reducing the excitation threshold necessitates innovative approaches to improve photon confinement within the laser device. One possible solution is to explore new device architectures and geometries that could enhance photon confinement, such as utilising direct laser writing to lock in refractive index profiles that reduce losses along directions that are perpendicular to the helix.

As a preliminary step, a mixture containing nematic LC, a chiral dopant, laser dye, polymer, and photoinitiator could be prepared and capillary-filled into an Instec cell. The next phase would involve polymerising a small, central region of the LC cell using direct laser writing technology. The optimal size for this polymerised region would need further exploration to maximise performance. Subsequently, a high voltage would be applied between the two substrates of the cell to unwind the remaining unpolymerised LC region, transforming it into a near-homeotropic alignment. After this, the entire cell would be polymerised using UV curing to lock the internal structure in place.

When this device is excited with a suitable pump source, such as an Nd:YAG laser, lasing would be confined to the central area where the helical structure and PBG exist, while the surrounding regions would not produce sufficient gain for effective laser oscillation. In contrast to conventional LC lasers, which typically exhibit a divergence angle of 20 to 30 degrees and are dependent on the excitation spot size, the divergence angle in this novel architecture is theoretically largely reduced. This design promises improved photon confinement and reduced losses, potentially leading to a reduction in the excitation threshold and improved overall performance of the LC laser system.

References

[1] Wenqi Ouyang et al. “Ultrafast 3D nanofabrication via digital holography”. In: *Nature Communications* 14.1 (Mar. 2023), p. 1716.

[2] X.F. Yang et al. “Laser spectroscopy for the study of exotic nuclei”. In: *Progress in Particle and Nuclear Physics* 129 (Mar. 2023), p. 104005.

[3] Dong Liang et al. “Evolution of laser technology for automotive LiDAR, an industrial viewpoint”. In: *Nature Communications* 15.1 (Sept. 2024), p. 7660.

[4] Youting Liang et al. “Monolithic single-frequency microring laser on an erbium-doped thin film lithium niobate fabricated by a photolithography assisted chemo-mechanical etching”. In: *Optics Continuum* 1.5 (May 2022), p. 1193.

[5] Olivier Spitz et al. “Private communication with quantum cascade laser photonic chaos”. In: *Nature Communications* 12.1 (June 2021), p. 3327.

[6] Harry Coles and Stephen Morris. “Liquid-crystal lasers”. In: *Nature Photonics* 4.10 (Oct. 2010), pp. 676–685.

[7] Jaroslaw Mysliwiec et al. “Liquid crystal lasers: the last decade and the future”. In: *Nanophotonics* 10.9 (July 2021), pp. 2309–2346.

[8] Philip J. W. Hands et al. “Liquid-Crystal Lasers: Recent Advances and Future Opportunities”. In: *SID Symposium Digest of Technical Papers* 53.1 (June 2022), pp. 440–443.

[9] Xiuqin Zhan et al. “3D Laser Displays Based on Circularly Polarized Lasing from Cholesteric Liquid Crystal Arrays”. In: *Advanced Materials* 33.37 (Aug. 2021).

[10] Longwu Li. “Random lasers tuning by combining a dye-doped liquid crystal and CdS nanoparticles”. In: *Optik* 134 (Apr. 2017), pp. 1–8.

[11] Margaret C. Normand et al. “Overcoming repetition rate limitations in liquid crystal laser systems”. In: *Optics Express* 26.20 (Oct. 2018), p. 26544.

[12] Diederik S. Wiersma. “The physics and applications of random lasers”. In: *Nature Physics* 4.5 (May 2008), pp. 359–367.

[13] Rui Duan et al. “Real-time, quantitative and sensitive detection of urea by whispering gallery mode lasing in liquid crystal microdroplet”. In: *Talanta* 209 (Mar. 2020), p. 120513.

[14] Long-Wu Li, Zhen-Zhen Shang, and Luogen Deng. “Random lasing from dye-doped negative liquid crystals using ZnO nanoparticles as tunable scatters”. In: *Chinese Physics B* 25.9 (Sept. 2016), p. 090301.

[15] Friedrich Reinitzer. “Contributions to the knowledge of cholesterol”. In: *Liquid Crystals* 5.1 (1989), pp. 7–18.

[16] Michel Mitov. “Liquid-Crystal Science from 1888 to 1922: Building a Revolution”. In: *ChemPhysChem* 15.7 (May 2014), pp. 1245–1250.

[17] Peter J. Collings and Michael Hird. *Introduction to Liquid Crystals Chemistry and Physics*. CRC Press, Sept. 2017, pp. 1–2.

[18] Patrick Garidel et al. “Self-Organisation, Thermotropic and Lyotropic Properties of Glycolipids Related to their Biological Implications”. In: *The Open Biochemistry Journal* 9.1 (Sept. 2015), pp. 49–72.

[19] J. W. Goodby. "Materials and Phase Structures of Calamitic and Discotic Liquid Crystals". In: *Handbook of Visual Display Technology*. Berlin, Heidelberg: Springer Berlin Heidelberg, 2012, pp. 1243–1287.

[20] Miha Škarabot et al. "Flexoelectric Polarization in a Nematic Liquid Crystal Enhanced by Dopants with Different Molecular Shape Polarities". In: *ACS Omega* 7.11 (Mar. 2022), pp. 9785–9795.

[21] Yaohao Song, Satoshi Aya, and Mingjun Huang. "Updated view of new liquid-matter ferroelectrics with nematic and smectic orders". In: *Giant* 19 (Aug. 2024), p. 100318.

[22] F. Castles et al. "Blue-phase templated fabrication of three-dimensional nanostructures for photonic applications". In: *Nature Materials* 11.7 (July 2012), pp. 599–603.

[23] S. M. Wood et al. "Wavelength-tuneable laser emission from stretchable chiral nematic liquid crystal gels via in situ photopolymerization". In: *RSC Advances* 6.38 (2016), pp. 31919–31924.

[24] Bohan Chen et al. "Laser Written Stretchable Diffractive Optic Elements in Liquid Crystal Gels". In: *Crystals* 12.10 (Sept. 2022), p. 1340.

[25] Kunihiro Ichimura. "Photoalignment of Liquid-Crystal Systems". In: *Chemical Reviews* 100.5 (May 2000), pp. 1847–1874.

[26] Takahiro Seki. "New strategies and implications for the photoalignment of liquid crystalline polymers". In: *Polymer Journal* 46.11 (Nov. 2014), pp. 751–768.

[27] Yuan Chen et al. "High Performance Negative Dielectric Anisotropy Liquid Crystals for Display Applications". In: *Crystals* 3.3 (Sept. 2013), pp. 483–503.

[28] Haiguang Chen et al. "Negative Dielectric Anisotropy Liquid Crystal with Improved Photo-Stability, Anti-Flicker, and Transmittance for 8K Display Applications". In: *Molecules* 27.21 (Oct. 2022), p. 7150.

[29] Hyang Yul Kim, Sang-Hee Nam, and Seung Hee Lee. "Dynamic Stability of the Fringe-Field Switching Liquid Crystal Cell Depending on Dielectric Anisotropy of a Liquid Crystal". In: *Japanese Journal of Applied Physics* 42.Part 1, No. 5A (May 2003), pp. 2752–2755.

[30] Volodymyr Borshch et al. "Nanosecond electro-optics of a nematic liquid crystal with negative dielectric anisotropy". In: *Physical Review E* 90.6 (Dec. 2014), p. 062504.

[31] Stephen G. Lipson and Henry Lipson. *Optical Physics*. Cambridge University Press, 1981, pp. 58–60.

[32] Pilar García Parejo and Alberto Álvarez-Herrero. "Liquid crystals for space instrumentation: optical properties of liquid crystal mixtures for polarimeters". In: *Optical Materials Express* 9.6 (June 2019), p. 2681.

[33] John Gustav Delly. "The Michel-Lévy interference color chart–microscopy's magical color key". In: *Modern Microsc. J* (2003).

[34] Satyendra Kumar. *Liquid Crystals: Experimental Study of Physical Properties and Phase Transitions*. Dec. 2001, pp. 12–13.

[35] F. Grandjean. "The existence of equidistant layers normal to the optic axis in anisotropic liquids (liquid crystals)". In: *C.R. Hebd. Seances Acad. Sci.* 172 (1921), pp. 71–74.

[36] P. G. de Gennes. *The Physics of Liquid Crystals*. Oxford University Press, 1974, pp. 216–220.

[37] Charles Mauguin. "Sur les cristaux liquides de M. Lehmann". In: *Bulletin de Minéralogie* 34.3 (1911), pp. 71–117.

[38] Frederick C Frank. "I. Liquid crystals. On the theory of liquid crystals". In: *Discussions of the Faraday Society* 25 (1958), pp. 19–28.

[39] H L De Vries. "Rotatory power and other optical properties of certain liquid crystals". In: *Opticals Effects in Liquid Crystals*. Springer, 1951, pp. 31–38.

[40] Sjoerd Stallinga. "Berreman 4× 4 matrix method for reflective liquid crystal displays". In: *Journal of applied physics* 85.6 (1999), pp. 3023–3031.

[41] Jun Li and Shin-Tson Wu. "Extended Cauchy equations for the refractive indices of liquid crystals". In: *Journal of Applied Physics* 95.3 (Feb. 2004), pp. 896–901.

[42] T. H. Maiman. "Optical and Microwave-Optical Experiments in Ruby". In: *Physical Review Letters* 4.11 (June 1960), pp. 564–566.

[43] Wolfgang Osten et al. "Recent advances in digital holography". In: *Applied Optics* 53.27 (Sept. 2014), G44.

[44] P. Campbell, I.D. Moore, and M.R. Pearson. "Laser spectroscopy for nuclear structure physics". In: *Progress in Particle and Nuclear Physics* 86 (Jan. 2016), pp. 127–180.

[45] You Li and Javier Ibanez-Guzman. "Lidar for Autonomous Driving: The Principles, Challenges, and Trends for Automotive Lidar and Perception Systems". In: *IEEE Signal Processing Magazine* 37.4 (July 2020), pp. 50–61.

[46] Jesús del Barrio and Carlos Sánchez-Somolinos. "Light to Shape the Future: From Photolithography to 4D Printing". In: *Advanced Optical Materials* 7.16 (Aug. 2019).

[47] Taofiq K. Paraïso et al. "Advanced Laser Technology for Quantum Communications (Tutorial Review)". In: *Advanced Quantum Technologies* 4.10 (Oct. 2021).

[48] Stephen M. Morris et al. "Polychromatic liquid crystal laser arrays towards display applications". In: *Optics Express* 16.23 (Nov. 2008), p. 18827.

[49] Fa Feng Xu et al. "Flat-Panel Laser Displays Based on Liquid Crystal Microlaser Arrays". In: *CCS Chemistry* 2.6 (Dec. 2020), pp. 369–375.

[50] Rui Duan et al. "Detection of heavy metal ions using whispering gallery mode lasing in functionalized liquid crystal microdroplets". In: *Biomedical Optics Express* 10.12 (Dec. 2019), p. 6073.

[51] Ziyihui Wang et al. "Bio-electrostatic sensitive droplet lasers for molecular detection". In: *Nanoscale Advances* 2.7 (2020), pp. 2713–2719.

[52] P. J. W. Hands et al. "Wavelength-tuneable liquid crystal lasers from the visible to the near-infrared". In: ed. by Iam Choon Khoo. Sept. 2011, 81140T.

[53] Ji-Liang Zhu et al. "Random laser emission in a sphere-phase liquid crystal". In: *Applied Physics Letters* 106.19 (May 2015).

[54] Rina Wu et al. "Random lasing in dye-doped chiral nematic liquid crystal". In: *Optik* 202 (Feb. 2020), p. 163616.

[55] Zhiwen Wang et al. "Coherent Random Lasing in Colloidal Quantum Dot-Doped Polymer-Dispersed Liquid Crystal with Low Threshold and High Stability". In: *The Journal of Physical Chemistry Letters* 11.3 (Feb. 2020), pp. 767–774.

[56] A. Chiasera et al. "Spherical whispering-gallery-mode microresonators". In: *Laser & Photonics Reviews* 4.3 (Apr. 2010), pp. 457–482.

[57] Chengkun Yang et al. "Electrically tunable whispering gallery mode microresonator based on a grapefruit-microstructured optical fiber infiltrated with nematic liquid crystals". In: *Optics Letters* 42.15 (Aug. 2017), p. 2988.

[58] Maruša Mur et al. "Magnetic-field tuning of whispering gallery mode lasing from ferromagnetic nematic liquid crystal microdroplets". In: *Optics Express* 25.2 (Jan. 2017), p. 1073.

[59] Rupert F. Oulton et al. “Plasmon lasers at deep subwavelength scale”. In: *Nature* 461.7264 (Oct. 2009), pp. 629–632.

[60] Kunal Tiwari, Ankit K. Singh, and Suresh C. Sharma. “Evidence for surface plasmons in a liquid crystal containing gold nanoparticles”. In: *Applied Physics Letters* 101.25 (Dec. 2012).

[61] Hao-Chi Cheng et al. “Liquid-Crystal Active Tamm-Plasmon Devices”. In: *Physical Review Applied* 9.6 (June 2018), p. 064034.

[62] Jung-Min Seo, Waliullah Khan, and Soo-Young Park. “Protein detection using aqueous/LC interfaces decorated with a novel polyacrylic acid block liquid crystalline polymer”. In: *Soft Matter* 8.1 (2012), pp. 198–203.

[63] Chih-Hsin Chen and Kun-Lin Yang. “A liquid crystal biosensor for detecting organophosphates through the localized pH changes induced by their hydrolytic products”. In: *Sensors and Actuators B: Chemical* 181 (May 2013), pp. 368–374.

[64] Yan Wang et al. “Detecting enzymatic reactions in penicillinase via liquid crystal microdroplet-based pH sensor”. In: *Sensors and Actuators B: Chemical* 258 (Apr. 2018), pp. 1090–1098.

[65] L Goldberg and J Schnur. *Tunable internal-feedback liquid crystal-dye laser*. Nov. 1973.

[66] V. I. Kopp et al. “Low-threshold lasing at the edge of a photonic stop band in cholesteric liquid crystals”. In: *Optics Letters* 23.21 (Nov. 1998), p. 1707.

[67] Victor I. Kopp, Zhao-Qing Zhang, and Azriel Z. Genack. “Lasing in chiral photonic structures”. In: *Progress in Quantum Electronics* 27.6 (Jan. 2003), pp. 369–416.

[68] Alison D. Ford, Stephen M. Morris, and Harry J. Coles. “Photonics and lasing in liquid crystals”. In: *Materials Today* 9.7-8 (July 2006), pp. 36–42.

[69] A. Muñoz F., P. Palffy-Muhoray, and B. Taheri. “Ultraviolet lasing in cholesteric liquid crystals”. In: *Optics Letters* 26.11 (June 2001), p. 804.

[70] Wenyi Cao et al. “Lasing in a three-dimensional photonic crystal of the liquid crystal blue phase II”. In: *Nature Materials* 1.2 (Oct. 2002), pp. 111–113.

[71] M. Ozaki et al. “Mirrorless Lasing in a Dye-Doped Ferroelectric Liquid Crystal”. In: *Advanced Materials* 14.4 (Feb. 2002), pp. 306–309.

[72] Jonathan P. Dowling et al. “The photonic band edge laser: A new approach to gain enhancement”. In: *Journal of Applied Physics* 75.4 (1994), pp. 1896–1899.

[73] H. Kogelnik and C. V. Shank. “Coupled-Wave Theory of Distributed Feedback Lasers”. In: *Journal of Applied Physics* 43.5 (May 1972), pp. 2327–2335.

[74] J. Schmidtke and W. Stille. “Fluorescence of a dye-doped cholesteric liquid crystal film in the region of the stop band: theory and experiment”. In: *The European Physical Journal B - Condensed Matter* 31.2 (Jan. 2003), pp. 179–194.

[75] William P. Partridge et al. “Performance of Pyrromethene 580 and 597 in a commercial Nd:YAG-pumped dye-laser system”. In: *Optics Letters* 19.20 (Oct. 1994), p. 1630.

[76] Mark D. Rahn and Terence A. King. “Comparison of laser performance of dye molecules in sol-gel, polycom, ormosil, and poly(methyl methacrylate) host media”. In: *Applied Optics* 34.36 (Dec. 1995), p. 8260.

[77] Carrie Mowatt et al. “Comparison of the performance of photonic band-edge liquid crystal lasers using different dyes as the gain medium”. In: *Journal of Applied Physics* 107.4 (2010).

[78] Yuko Matsuhisa et al. “Low-threshold and high efficiency lasing upon band-edge excitation in a cholesteric liquid crystal”. In: *Applied Physics Letters* 90.9 (Feb. 2007).

[79] Calum M. Brown, Daisy K.E. Dickinson, and Philip J.W. Hands. "Diode pumping of liquid crystal lasers". In: *Optics & Laser Technology* 140 (Aug. 2021), p. 107080.

[80] Calum M. Brown, Daisy K. E. Dickinson, and Philip J. W. Hands. "Advancing multi-wavelength liquid crystal laser microcavities in a compact prototype device using a laser diode pump source". In: *Laser Resonators, Microresonators, and Beam Control XXIV*. Ed. by Andrea M. Armani et al. SPIE, Mar. 2022, p. 12.

[81] W. Cao et al. "Lasing thresholds of cholesteric liquid crystals lasers". In: *Molecular Crystals and Liquid Crystals*. Vol. 429. 2005, pp. 101–110.

[82] V. A. Belyakov. "Low Threshold DFB Lasing in Chiral LC at Diffraction of Pumping Wave". In: *Molecular Crystals and Liquid Crystals* 453.1 (Sept. 2006), pp. 43–69.

[83] S M Morris et al. "The effects of reorientation on the emission properties of a photonic band edge liquid crystal laser". In: *Journal of Optics A: Pure and Applied Optics* 7.5 (May 2005), pp. 215–223.

[84] Yuhua Huang et al. "Incident angle and polarization effects on the dye-doped cholesteric liquid crystal laser". In: *Optics Communications* 261.1 (May 2006), pp. 91–96.

[85] Rachel Jakubiak et al. "Electrically switchable lasing from pyrromethene 597 embedded holographic-polymer dispersed liquid crystals". In: *Applied Physics Letters* 85.25 (Dec. 2004), pp. 6095–6097.

[86] Shing-Trong Wu and Andy Ying-Guey Fuh. "Lasing in Photonic Crystals based on Dye-Doped Holographic Polymer-Dispersed Liquid Crystal Reflection Gratings". In: *Japanese Journal of Applied Physics* 44.2R (Feb. 2005), p. 977.

[87] Y. J. Liu et al. "Low-threshold and narrow-linewidth lasing from dye-doped holographic polymer-dispersed liquid crystal transmission gratings". In: *Applied Physics Letters* 88.6 (Feb. 2006).

[88] Won-Kyu Lee et al. "CIS–ZnS quantum dots for self-aligned liquid crystal molecules with superior electro-optic properties". In: *Nanoscale* 5.1 (2013), pp. 193–199.

[89] Dharmendra Pratap Singh et al. "CuInS2/ZnS QD-ferroelectric liquid crystal mixtures for faster electro-optical devices and their energy storage aspects". In: *Journal of Applied Physics* 123.3 (Jan. 2018).

[90] Aradhana Roy et al. "InP/ZnS quantum-dot-dispersed nematic liquid crystal illustrating characteristic birefringence and enhanced electro-optical parameters". In: *Applied Physics A* 124.3 (Mar. 2018), p. 273.

[91] Tilak Joshi et al. "Tuning the photoluminescence of ferroelectric liquid crystal by controlling the size of dopant ZnO quantum dots". In: *Materials Letters* 114 (Jan. 2014), pp. 156–158.

[92] A. Kumar et al. "Enhancing the photoluminescence of ferroelectric liquid crystal by doping with ZnS quantum dots". In: *Applied Physics Letters* 100.13 (Mar. 2012).

[93] Yeasin Khan et al. "Waterproof perovskites: high fluorescence quantum yield and stability from a methylammonium lead bromide/formate mixture in water". In: *Journal of Materials Chemistry C* 8.17 (2020), pp. 5873–5881.

[94] Loredana Protesescu et al. "Nanocrystals of cesium lead halide perovskites (CsPbX3, X= Cl, Br, and I): novel optoelectronic materials showing bright emission with wide color gamut". In: *Nano letters* 15.6 (2015), pp. 3692–3696.

[95] Jorick Maes et al. "Light absorption coefficient of CsPbBr3 perovskite nanocrystals". In: *The journal of physical chemistry letters* 9.11 (2018), pp. 3093–3097.

[96] Minas M Stylianakis et al. "Inorganic and hybrid perovskite based laser devices: a review". In: *Materials* 12.6 (2019), p. 859.

[97] Qi Wei et al. "Recent progress in metal halide perovskite micro-and nanolasers". In: *Advanced Optical Materials* 7.17 (2019), p. 1900080.

[98] Haiyun Dong et al. "Materials chemistry and engineering in metal halide perovskite lasers". In: *Chemical Society Reviews* 49.3 (2020), pp. 951–982.

[99] Andrew P Schlaus et al. "How lasing happens in CsPbBr3 perovskite nanowires". In: *Nature communications* 10.1 (2019), p. 265.

[100] Daqin Chen and Xiao Chen. "Luminescent perovskite quantum dots: synthesis, microstructures, optical properties and applications". In: *Journal of Materials Chemistry C* 7.6 (2019), pp. 1413–1446.

[101] Yaxin Wang et al. "Recent advances in synthesis and application of perovskite quantum dot based composites for photonics, electronics and sensors". In: *Science and Technology of Advanced Materials* 21.1 (2020), pp. 278–302.

[102] Young-Chol Yang et al. "Photonic defect modes of cholesteric liquid crystals". In: *Physical Review E* 60.6 (Dec. 1999), pp. 6852–6854.

[103] J Schmidtke and W Stille. "Photonic defect modes in cholesteric liquid crystal films". In: *The European Physical Journal E* 12 (2003), pp. 553–564.

[104] M Becchi et al. "Defect modes in helical photonic crystals: an analytic approach". In: *Physical Review B—Condensed Matter and Materials Physics* 70.3 (2004), p. 033103.

[105] Victor I Kopp and Azriel Z Genack. "Twist defect in chiral photonic structures". In: *Physical Review Letters* 89.3 (2002), p. 033901.

[106] Fei Wang and Akhlesh Lakhtakia. "Optical crossover phenomenon due to a central 90-twist defect in a chiral sculptured thin film or chiral liquid crystal". In: *Proceedings of the Royal Society A: Mathematical, Physical and Engineering Sciences* 461.2061 (2005), pp. 2985–3004.

[107] Soon Moon Jeong et al. "Defect mode lasing from a double-layered dye-doped polymeric cholesteric liquid crystal films with a thin rubbed defect layer". In: *Applied physics letters* 90.26 (2007).

[108] A H Gevorgyan and K B Oganesyan. "Lasing in cholesteric liquid crystal cells with an isotropic defect layer inside". In: *Laser Physics Letters* 12.12 (2015), p. 125805.

[109] Shaohua Gao et al. "Coupling of Defect Modes in Cholesteric Liquid Crystals Separated by Isotropic Polymeric Layers". In: *Polymers* 10.7 (2018), p. 805.

[110] Myoung Hoon Song et al. "Defect-mode lasing with lowered threshold in a three-layered hetero-cholesteric liquid-crystal structure". In: *Advanced materials* 18.2 (2006), pp. 193–197.

[111] Yoichi Takanishi et al. "Defect-mode lasing from a three-layered helical cholesteric liquid crystal structure". In: *Japanese journal of applied physics* 46.6R (2007), p. 3510.

[112] Myoung Hoon Song et al. "Lasing from thick anisotropic layer sandwiched between polymeric cholesteric liquid crystal films". In: *Japanese journal of applied physics* 44.11R (2005), p. 8165.

[113] Na Young Ha et al. "Simultaneous RGB reflections from single-pitched cholesteric liquid crystal films with Fibonaccian defects". In: *Optics Express* 15.3 (2007), pp. 1024–1029.

[114] Na Young Ha et al. "Fabrication of a simultaneous red–green–blue reflector using single-pitched cholesteric liquid crystals". In: *Nature materials* 7.1 (2008), pp. 43–47.

[115] Julian S Evans et al. "Optical generation, templating, and polymerization of three-dimensional arrays of liquid-crystal defects decorated by plasmonic nanoparticles". In: *Physical Review E—Statistical, Nonlinear, and Soft Matter Physics* 87.3 (2013), p. 032503.

[116] Kuo Zhong et al. “Defect mode passband lasing in self-assembled photonic crystal”. In: *Acs Photonics* 3.12 (2016), pp. 2330–2337.

[117] M Li et al. “Recent advantages of colloidal photonic crystals and their applications for luminescence enhancement”. In: *Materials Today Nano* 6 (2019), p. 100039.

[118] Jui-Chieh Huang et al. “Electrically switchable organo–inorganic hybrid for a white-light laser source”. In: *Scientific Reports* 6.1 (June 2016), p. 28363.

[119] Kai L. Woon et al. “Stokes parameter studies of spontaneous emission from chiral nematic liquid crystals as a one-dimensional photonic stopband crystal: Experiment and theory”. In: *Physical Review E - Statistical, Nonlinear, and Soft Matter Physics* 71.4 (Apr. 2005).

[120] S. M. Morris et al. “The emission characteristics of liquid-crystal lasers”. In: *Journal of the Society for Information Display* 14.6 (2006).

[121] A. D. Ford et al. “Emission characteristics of a homologous series of bimesogenic liquid-crystal lasers”. In: *Physical Review E - Statistical, Nonlinear, and Soft Matter Physics* 76.5 (Nov. 2007).

[122] Th K. Mavrogordatos et al. “Density of photon states in dye-doped chiral nematic liquid crystal cells in the presence of losses and gain”. In: *Physical Review E - Statistical, Nonlinear, and Soft Matter Physics* 86.1 (July 2012).

[123] Fumito Araoka et al. “How doping a cholesteric liquid crystal with polymeric dye improves an order parameter and makes possible low threshold lasing”. In: *Journal of Applied Physics* 94.1 (July 2003), pp. 279–283.

[124] Ksenia Dolgaleva et al. “Enhanced laser performance of cholesteric liquid crystals doped with oligofluorene dye”. In: *Journal of the Optical Society of America B* 25.9 (Sept. 2008).

[125] H. J. Coles et al. “Red-green-blue 2 D tuneable liquid crystal laser devices”. In: *Liquid Crystals XIII*. Vol. 7414. SPIE, Aug. 2009, p. 741402.

[126] Masahiro Kasano et al. “Electrically tunable waveguide laser based on ferroelectric liquid crystal”. In: *Applied Physics Letters* 82.23 (June 2003), pp. 4026–4028.

[127] Scott J. Woltman and Gregory P. Crawford. “Tunable cholesteric liquid crystals lasers through in-plane switching”. In: *Emerging Liquid Crystal Technologies II*. Vol. 6487. SPIE, Feb. 2007, 64870B.

[128] Tsung Hsien Lin et al. “Electrically controllable laser based on cholesteric liquid crystal with negative dielectric anisotropy”. In: *Applied Physics Letters* 88.6 (Feb. 2006).

[129] Tatsunosuke Matsui, Masanori Ozaki, and Katsumi Yoshino. “Electro-tunable liquid crystal waveguide laser”. In: *Liquid Crystals VIII*. Vol. 5518. SPIE, Oct. 2004, p. 220.

[130] Mikhail I. Barnik et al. “Lasing from photonic structure: Cholesteric-voltage controlled nematic-cholesteric liquid crystal”. In: *Journal of Applied Physics* 103.12 (2008).

[131] H. Finkelmann et al. “Tunable Mirrorless Lasing in Cholesteric Liquid Crystalline Elastomers”. In: *Advanced Materials* 13.14 (July 2001).

[132] Yuhua Huang et al. “Tuning the photonic band gap in cholesteric liquid crystals by temperature-dependent dopant solubility”. In: *Optics Express* 14.3 (2006).

[133] Kazuhiro Funamoto, Masanori Ozaki, and Katsumi Yoshino. “Discontinuous Shift of Lasing Wavelength with Temperature in Cholesteric Liquid Crystal”. In: *Japanese Journal of Applied Physics, Part 2: Letters* 42.12 B (Dec. 2003).

[134] Andro Chanishvili et al. “Widely tunable ultraviolet-visible liquid crystal laser”. In: *Applied Physics Letters* 86.5 (Jan. 2005), pp. 1–3.

[135] Yuhua Huang et al. “Spatially tunable laser emission in dye-doped cholesteric polymer films”. In: *Applied Physics Letters* 89.11 (2006).

[136] Andro Chanishvili et al. “Phototunable lasing in dye-doped cholesteric liquid crystals”. In: *Applied Physics Letters* 83.26 (Dec. 2003), pp. 5353–5355.

[137] Seiichi Furumi et al. “Phototunable photonic bandgap in a chiral liquid crystal laser device”. In: *Applied Physics Letters* 84.14 (Apr. 2004), pp. 2491–2493.

[138] Zhi Gang Zheng et al. “Three-dimensional control of the helical axis of a chiral nematic liquid crystal by light”. In: *Nature* 531.7594 (2016), pp. 352–356.

[139] Eugene Hecht. *Optics*. Fifth edition. Boston : Pearson, 2017, pp. 366–391.

[140] Edward Collett. “Field guide to polarization”. In: Spie Bellingham, 2005.

[141] George Gabriel Stokes. “XXX. On the change of refrangibility of light”. In: *Philosophical Transactions of the Royal Society of London* 142 (Dec. 1852), pp. 463–562.

[142] Eugene Hecht. “Note on an Operational Definition of the Stokes Parameters”. In: *American Journal of Physics* 38.9 (Sept. 1970), pp. 1156–1158.

[143] Hans Mueller. “Memorandum on the polarization optics of the photoelastic shutter”. In: *Report of the OSRD project OEMsr-576* 2 (1943).

[144] Marcos A. de Araújo et al. “Measurement of Gaussian laser beam radius using the knife-edge technique: improvement on data analysis”. In: *Applied Optics* 48.2 (Jan. 2009).

[145] D. Wright et al. “Laser beam width, divergence and beam propagation factor — an international standardization approach”. In: *Optical and Quantum Electronics* 24.9 (Sept. 1992).

[146] Mark T. Sims. “Dyes as guests in ordered systems: current understanding and future directions”. In: *Liquid Crystals* 43.13-15 (Dec. 2016), pp. 2363–2374.

[147] Hamidreza Shirvani-Mahdavi, Ezeddin Mohajerani, and Shin-Tson Wu. “Circularly polarized high-efficiency cholesteric liquid crystal lasers with a tunable nematic phase retarder”. In: *Optics Express* 18.5 (Mar. 2010), p. 5021.

[148] Seong Yong Cho, Hiroyuki Yoshida, and Masanori Ozaki. “Emission Direction-Tunable Liquid Crystal Laser”. In: *Advanced Optical Materials* 8.16 (2020), pp. 1–6.

[149] Taimoor Ali et al. “On-Demand Polarization Controllable Liquid Crystal Laser”. In: *Advanced Materials Technologies* 8.3 (Feb. 2023).

[150] G. Zhang et al. “Non-mechanical optical beam-steering of a liquid crystal laser”. In: *Optics and Laser Technology* 157 (2023).

[151] Thomas Tanggaard Alkeskjold et al. “All-optical modulation in dye-doped nematic liquid crystal photonic bandgap fibers”. In: *Optics Express* 12.24 (2004).

[152] J. Etxebarria, J. Ortega, and C. L. Folcia. “Enhancement of the optical absorption in cholesteric liquid crystals due to photonic effects: an experimental study”. In: *Liquid Crystals* 45.1 (Jan. 2018), pp. 122–128.

[153] L. Penninck et al. “Light emission from dye-doped cholesteric liquid crystals at oblique angles: Simulation and experiment”. In: *Physical Review E - Statistical, Nonlinear, and Soft Matter Physics* 85.4 (Apr. 2012).

[154] Hun Ki Shin et al. “Fast polarization switching panel with high brightness and contrast ratio for three-dimensional display”. In: *Applied Physics Letters* 98.6 (Feb. 2011).

[155] Haiwei Chen et al. “Beam steering for virtual/augmented reality displays with a cycloidal diffractive waveplate”. In: *Optics Express* 24.7 (Apr. 2016), p. 7287.

[156] Duncan L. Hickman et al. “Polarimetric imaging: system architectures and trade-offs”. In: *Electro-Optical and Infrared Systems: Technology and Applications XV*. Ed. by Duncan L. Hickman, David A. Huckridge, and Helge Bürsing. SPIE, Oct. 2018, p. 10.

[157] Fei Cheng et al. “Polarization-switchable holograms based on efficient, broadband multifunctional metasurfaces in the visible regime”. In: *Optics Express* 26.23 (Nov. 2018), p. 30678.

[158] Ayman F. Abouraddy and Kimani C. Toussaint. “Three-Dimensional Polarization Control in Microscopy”. In: *Physical Review Letters* 96.15 (Apr. 2006), p. 153901.

[159] Keigo Iizuka. “3D microscope”. In: ed. by Jose-Angel Conchello et al. Feb. 2008, p. 686113.

[160] Gregory D. VanWiggeren and Rajarshi Roy. “Transmission of linearly polarized light through a single-mode fiber with random fluctuations of birefringence”. In: *Applied Optics* 38.18 (June 1999), p. 3888.

[161] Guanxiong Zhang et al. “Free-space Optical Communication Link with Liquid Crystal Beam-steering”. In: *IEEE Photonics Technology Letters* (2023), pp. 1–1.

[162] Chun Ta Wang and Tsung Hsien Lin. “Polarization-tunable chiral nematic liquid crystal lasing”. In: *Journal of Applied Physics* 107.12 (June 2010).

[163] D. S. Sabatke et al. “Optimization of retardance for a complete Stokes polarimeter”. In: *Optics Letters* 25.11 (June 2000), p. 802.

[164] Chao He, Jacopo Antonello, and Martin J. Booth. “Vectorial adaptive optics”. In: *eLight* 3.1 (Nov. 2023), p. 23.

[165] Yan Li et al. “Femtosecond laser micromachining and microfabrication in transparent materials”. In: ed. by ShuShen Deng, Akira Matsunawa, and Xiao Zhu. Nov. 2007, 68250K.

[166] Keir C. Neuman and Steven M. Block. “Optical trapping”. In: *Review of Scientific Instruments* 75.9 (Sept. 2004), pp. 2787–2809.

[167] Ton Koonen et al. “High-Capacity Optical Wireless Communication Using Two-Dimensional IR Beam Steering”. In: *Journal of Lightwave Technology* 36.19 (Oct. 2018), pp. 4486–4493.

[168] Philip J. Bos. “Wide-angle achromatic prism beam steering for infrared countermeasure applications”. In: *Optical Engineering* 42.4 (Apr. 2003), p. 1038.

[169] Bradley D. Duncan. “Wide-angle decentered lens beam steering for infrared countermeasures applications”. In: *Optical Engineering* 43.10 (Oct. 2004), p. 2312.

[170] Alan H. Lettington. “Design and development of a high-performance passive millimeter-wave imager for aeronautical applications”. In: *Optical Engineering* 44.9 (Sept. 2005), p. 093202.

[171] Jay Stockley and Steven Serati. “Advances in liquid crystal beam steering”. In: *Free-Space Laser Communications IV*. Vol. 5550. SPIE, Oct. 2004, p. 32.

[172] Rebecca Jane Bussjager et al. “Design of PLZT electro-optic beam-steering device”. In: *Photonic Component Engineering and Applications*. Ed. by Andrew R Pirich. Vol. 2749. SPIE, 1996, pp. 90–100.

[173] Vladimir V. Nikulin. “Modeling of an acousto-optic laser beam steering system intended for satellite communication”. In: *Optical Engineering* 40.10 (Oct. 2001), p. 2208.

[174] P.F. McManamon et al. “Optical phased array technology”. In: *Proceedings of the IEEE* 84.2 (Feb. 1996).

[175] Li Ge, Markus Duelli, and Robert W. Cohn. “Enumeration of illumination and scanning modes from real-time spatial light modulators”. In: *Optics Express* 7.12 (Dec. 2000).

[176] Jihwan Kim et al. “Demonstration of large-angle nonmechanical laser beam steering based on LC polymer polarization gratings”. In: *Acquisition, Tracking, Pointing, and Laser Systems Technologies XXV*. Ed. by William E Thompson and Paul F McManamon. Vol. 8052. SPIE, 2011, pp. 210–221.

[177] Jihwan Kim et al. “Wide-angle, nonmechanical beam steering with high throughput utilizing polarization gratings”. In: *Applied Optics* 50.17 (June 2011), p. 2636.

[178] Chulwoo Oh et al. “High-Throughput Continuous Beam Steering Using Rotating Polarization Gratings”. In: *IEEE Photonics Technology Letters* 22.4 (Feb. 2010), pp. 200–202.

[179] Jihwan Kim et al. “Wide-angle nonmechanical beam steering using thin liquid crystal polarization gratings”. In: *Advanced Wavefront Control: Methods, Devices, and Applications VI*. Ed. by John D Gonglewski, Richard A Carreras, and Troy A Rhoadarmer. Vol. 7093. SPIE, 2008, pp. 1–12.

[180] Ziqian He et al. “Liquid crystal beam steering devices: Principles, recent advances, and future developments”. In: *Crystals* 9.6 (June 2019).

[181] Ziqian He et al. “Recent advances in liquid-crystal polarization volume gratings”. In: *Liquid Crystals XXIII*. Ed. by Iam Choon Khoo. SPIE, Aug. 2019.

[182] Taimoor Ali et al. “A Thin-Film Flexible Defect-Mode Laser”. In: *Advanced Optical Materials* 8.8 (Apr. 2020).

[183] Gregory P. Crawford et al. “Liquid-crystal diffraction gratings using polarization holography alignment techniques”. In: *Journal of Applied Physics* 98.12 (Dec. 2005).

[184] Mario Ivanov and Tomoaki Eiju. “Compact spectral ellipsometer with polarization grating”. In: *Optoelectronics, Materials, and Devices for Communications*. Vol. 4580. SPIE, Oct. 2001, p. 664.

[185] Charles F. LaCasse et al. “Maximum bandwidth snapshot channeled imaging polarimeter with polarization gratings”. In: *Polarization: Measurement, Analysis, and Remote Sensing XII*. Vol. 9853. SPIE, May 2016, 98530U.

[186] Michael W. Kudenov et al. “Compact spatial heterodyne interferometer using polarization gratings”. In: *Polarization Science and Remote Sensing VI*. Vol. 8873. SPIE, Sept. 2013, 88730Q.

[187] G. Cincotti and G. Costa. “Polarization grating-based wavelength selective switches”. In: *2016 18th International Conference on Transparent Optical Networks (ICTON)*. IEEE, July 2016.

[188] Gabriella Cincotti. “Polarization Gratings: Design and Applications”. In: *IEEE Journal of Quantum Electronics* 39.12 (Dec. 2003), pp. 1645–1652.

[189] Comrun Yousefzadeh, Andre van Rynbach, and Philip J. Bos. “Tunable liquid crystal beam steering device based on Pancharatnam phase”. In: SPIE-Intl Soc Optical Eng, Feb. 2020, p. 27.

[190] Li Tan, Jacob Y. Ho, and Hoi Sing Kwok. “Extended Jones matrix method for oblique incidence study of polarization gratings”. In: *Applied Physics Letters* 101.5 (July 2012).

[191] Zishuo Wang et al. “Diffraction characteristics of a non-mechanical beam steering system with liquid crystal polarization gratings”. In: *Optics Express* 30.5 (Feb. 2022), p. 7319.

[192] Zhi-Wei Zhao et al. “High-efficiency large-angle reflective composite polarization grating”. In: *Liquid Crystals* 47.2 (Jan. 2020), pp. 191–198.

[193] Peter Gregorčič, Tomaž Požar, and Janez Možina. “Quadrature phase-shift error analysis using a homodyne laser interferometer”. In: *Optics Express* 17.18 (Aug. 2009).

[194] Michael Pircher, Christoph K. Hitzenberger, and Ursula Schmidt-Erfurth. "Polarization sensitive optical coherence tomography in the human eye". In: *Progress in Retinal and Eye Research* 30.6 (Nov. 2011).

[195] J. Schüttler, I. Babushkin, and W. Lange. "Labyrinthine patterns on an inhomogeneous background in a nonlinear optical system". In: *Physical Review A* 78.3 (Sept. 2008).

[196] Junji Kobashi et al. "Circularly-polarized, large-angle reflective deflectors based on periodically patterned cholesteric liquid crystals". In: *Optical Data Processing and Storage* 3.1 (Jan. 2017).

[197] Jihwan Kim et al. "Nonmechanical Laser Beam Steering Based on Polymer Polarization Gratings: Design Optimization and Demonstration". In: *Journal of Lightwave Technology* 33.10 (May 2015), pp. 2068–2077.

[198] Joseph W. Goodman. *Introduction to Fourier Optics*. Second edition. McGraw-Hill Book Co., 1996, pp. 63–75.

[199] Chang-Jae Yu et al. "Polarization Grating of Photoaligned Liquid Crystals with Oppositely Twisted Domain Structures". In: *Molecular Crystals and Liquid Crystals* 433.1 (June 2005), pp. 175–181.

[200] Tomoyuki Sasaki, Hiroshi Ono, and Nobuhiro Kawatsuki. "Functionalized polarization gratings in AZO-dye doped polymer films". In: *Molecular Crystals and Liquid Crystals* 472.1 (Aug. 2007), 131/[521]–136/[526].

[201] Yihan Jin et al. "Millisecond optical phase modulation using multipass configurations with liquid-crystal devices". In: *Physical Review Applied* 14.2 (Aug. 2020).

[202] Chi-Wai Chow et al. "Enabling Techniques for Optical Wireless Communication Systems". In: *Optical Fiber Communication Conference (OFC) 2020*. Washington, D.C.: Optica Publishing Group, 2020, M2F.1.

[203] Harald Haas et al. "What is LiFi?" In: *Journal of Lightwave Technology* 34.6 (Mar. 2016), pp. 1533–1544.

[204] Ahmad Helmi Azhar, Tuan-Anh Tran, and Dominic O'Brien. "A Gigabit/s Indoor Wireless Transmission Using MIMO-OFDM Visible-Light Communications". In: *IEEE Photonics Technology Letters* 25.2 (Jan. 2013), pp. 171–174.

[205] A. M. Khalid et al. "1-Gb/s Transmission Over a Phosphorescent White LED by Using Rate-Adaptive Discrete Multitone Modulation". In: *IEEE Photonics Journal* 4.5 (Oct. 2012), pp. 1465–1473.

[206] Ricardo X. G. Ferreira et al. "High Bandwidth GaN-Based Micro-LEDs for Multi-Gb/s Visible Light Communications". In: *IEEE Photonics Technology Letters* 28.19 (Oct. 2016), pp. 2023–2026.

[207] Hai-Han Lu et al. "A multiple-input-multiple-output visible light communication system based on VCSELs and spatial light modulators". In: *Optics Express* 22.3 (Feb. 2014), p. 3468.

[208] Ching-Hung Chang et al. "A 100-Gb/s Multiple-Input Multiple-Output Visible Laser Light Communication System". In: *Journal of Lightwave Technology* 32.24 (Dec. 2014), pp. 4723–4729.

[209] Chao Shen et al. "20-meter underwater wireless optical communication link with 15 Gbps data rate". In: *Optics Express* 24.22 (Oct. 2016), p. 25502.

[210] Xu-Hong Huang et al. "Bidirectional White-Lighting WDM VLC–UWOC Converged Systems". In: *Journal of Lightwave Technology* 39.13 (July 2021), pp. 4351–4359.

[211] Christos Danakis et al. "Using a CMOS camera sensor for visible light communication". In: *2012 IEEE Globecom Workshops*. IEEE, Dec. 2012, pp. 1244–1248.

[212] Chi-Wai Chow et al. "Display Light Panel and Rolling Shutter Image Sensor Based Optical Camera Communication (OCC) Using Frame-Averaging Background Removal and Neural Network". In: *Journal of Lightwave Technology* 39.13 (July 2021), pp. 4360–4366.

[213] Yu-Cheng Chuang et al. "Visible light communication and positioning using positioning cells and machine learning algorithms". In: *Optics Express* 27.11 (May 2019), p. 16377.

[214] Chin-Wei Hsu et al. "Real-time Demonstration of 5G MMW Beamforming and Tracking Using Integrated Visible Light Positioning System". In: *Optical Fiber Communication Conference (OFC) 2021*. Washington, D.C.: Optica Publishing Group, 2021, Tu5E.6.

[215] Nan Chi et al. "Visible Light Communication in 6G: Advances, Challenges, and Prospects". In: *IEEE Vehicular Technology Magazine* 15.4 (Dec. 2020), pp. 93–102.

[216] Chin-Wei Hsu et al. "High Speed Imaging 3 × 3 MIMO Phosphor White-Light LED Based Visible Light Communication System". In: *IEEE Photonics Journal* 8.6 (Dec. 2016), pp. 1–6.

[217] G. Cossu et al. "34 Gbit/s visible optical wireless transmission based on RGB LED". In: *Optics Express* 20.26 (Dec. 2012), B501.

[218] Kou Yoshida et al. "245 MHz bandwidth organic light-emitting diodes used in a gigabit optical wireless data link". In: *Nature Communications* 11.1 (Mar. 2020), p. 1171.

[219] Fangchen Hu et al. "High-speed visible light communication systems based on Si-substrate LEDs with multiple superlattice interlayers". In: *PhotoniX* 2.1 (Dec. 2021), p. 16.

[220] Xiping Wu et al. *Hybrid LiFi and WiFi Networks: A Survey*. Apr. 2021.

[221] Wahyu Hendra Gunawan et al. "Optical Beam Steerable Visible Light Communication (VLC) System Supporting Multiple Users Using RGB and Orthogonal Frequency Division Multiplexed (OFDM) Non-Orthogonal Multiple Access (NOMA)". In: *Sensors* 22.22 (Nov. 2022), p. 8707.

[222] Ravinder Singh et al. "Design and Characterisation of Terabit/s Capable Compact Localisation and Beam-Steering Terminals for Fiber-Wireless-Fiber Links". In: *Journal of Lightwave Technology* 38.24 (Dec. 2020), pp. 6817–6826.

[223] Caleb Knoernschild et al. "MEMS-based optical beam steering system for quantum information processing in two-dimensional atomic systems". In: *Optics Letters* 33.3 (Feb. 2008), p. 273.

[224] Daniel A. Goldman et al. "MOEMS-based Lens-Assisted Beam Steering for Free-Space Optical Communications". In: *Journal of Lightwave Technology* (2023), pp. 1–16.

[225] Vuong Mai and Hoon Kim. "Non-Mechanical Beam Steering and Adaptive Beam Control Using Variable Focus Lenses for Free-Space Optical Communications". In: *Journal of Lightwave Technology* 39.24 (Dec. 2021), pp. 7600–7608.

[226] Chin Wan Oh et al. "Free-space transmission with passive 2D beam steering for multi-gigabit-per-second per-beam indoor optical wireless networks". In: *Optics Express* 24.17 (Aug. 2016), p. 19211.

[227] Chi-Wai Chow et al. "Actively Controllable Beam Steering Optical Wireless Communication (OWC) Using Integrated Optical Phased Array (OPA)". In: *Journal of Lightwave Technology* 41.4 (Feb. 2023), pp. 1122–1128.

[228] Lican Wu et al. "12 Gbit/s indoor optical wireless communication system with ultrafast beam-steering using tunable VCSEL". In: *Optics Express* 30.9 (Apr. 2022), p. 15049.

[229] S.H. Khoo. "Eyesafe optical link using a holographic diffuser". In: *IEE Colloquium Optical Wireless Communications*. IEE, 1999, pp. 3–3.

[230] J. Camacho, M. Parrilla, and C. Fritsch. "Phase Coherence Imaging". In: *IEEE Transactions on Ultrasonics, Ferroelectrics and Frequency Control* 56.5 (May 2009), pp. 958–974.

[231] Min Gu. *Advanced optical imaging theory*. Vol. 75. Springer, 2013.

[232] Aris L. Moustakas et al. "Communication Through a Diffusive Medium: Coherence and Capacity". In: *Science* 287.5451 (Jan. 2000), pp. 287–290.

[233] Yong Geng et al. "Coherent optical communications using coherence-cloned Kerr soliton microcombs". In: *Nature Communications* 13.1 (Feb. 2022), p. 1070.

[234] D. Leibfried et al. "Quantum dynamics of single trapped ions". In: *Reviews of Modern Physics* 75.1 (Mar. 2003), pp. 281–324.

[235] Jun Ye, H. J. Kimble, and Hidetoshi Katori. "Quantum State Engineering and Precision Metrology Using State-Insensitive Light Traps". In: *Science* 320.5884 (June 2008), pp. 1734–1738.

[236] Claas Falldorf. "Exploring the coherence function for optical metrology and beyond". In: *Optics and Photonics for Advanced Dimensional Metrology II*. Ed. by Peter J. de Groot, Richard K. Leach, and Pascal Picart. SPIE, May 2022, p. 11.

[237] Dinesh N. Naik et al. "Real-time coherence holography". In: *Optics Express* 18.13 (June 2010), p. 13782.

[238] Govind P Agrawal. *Fiber-optic communication systems*. John Wiley & Sons, 2012.

[239] Chansuk Park et al. "Low-coherence optical diffraction tomography using a ferroelectric liquid crystal spatial light modulator". In: *Optics Express* 28.26 (Dec. 2020), p. 39649.

[240] Lluís Martínez-León, Giancarlo Pedrini, and Wolfgang Osten. "Applications of short-coherence digital holography in microscopy". In: *Applied Optics* 44.19 (July 2005), p. 3977.

[241] Wolfgang Drexler and James G Fujimoto. *Optical coherence tomography: technology and applications*. Springer Science & Business Media, 2008.

[242] Yihan Jin et al. "Zwitterion-doped liquid crystal speckle reducers for immersive displays and vectorial imaging". In: *Light: Science & Applications* 12.1 (Sept. 2023), p. 242.

[243] Daniel Younis et al. "Evolving Deformable Mirror Control to Generate Partially Coherent Light Fields". In: *Proceedings of the Companion Conference on Genetic and Evolutionary Computation*. New York, NY, USA: ACM, July 2023, pp. 2429–2437.

[244] Gerhard K Ackermann and Jürgen Eichler. *Holography: a practical approach*. John Wiley & Sons, 2007.

[245] N. P. Barnes and I. A. Crabbe. "Coherence length of a Q-switched Nd:YAG laser". In: *Journal of Applied Physics* 46.9 (Sept. 1975), pp. 4093–4095.

[246] I.Yu Anikeev and J Munch. "Variation in the coherence length of a phase conjugating oscillator". In: *Optics Communications* 178.4-6 (May 2000), pp. 449–456.

[247] L. Cohen. "The generalization of the Wiener-Khinchin theorem". In: *Proceedings of the 1998 IEEE International Conference on Acoustics, Speech and Signal Processing, ICASSP '98 (Cat. No.98CH36181)*. IEEE, May 1998, pp. 1577–1580.

[248] S. Yokoyama et al. "Laser Emission from a Polymer-Stabilized Liquid-Crystalline Blue Phase". In: *Advanced Materials* 18.1 (Jan. 2006), pp. 48–51.

[249] Kibeom Kim et al. "A well-aligned simple cubic blue phase for a liquid crystal laser". In: *Journal of Materials Chemistry C* 3.21 (2015), pp. 5383–5388.

[250] Jie Liu et al. "Single-, Dual-, Triple, and Quadruple-Wavelength Surface-Emitting Lasing in Blue-Phase Liquid Crystal". In: *Advanced Materials* 34.9 (Mar. 2022).

[251] Hyeon-Joon Choi et al. "Development of a liquid crystal laser using a simple cubic liquid crystalline blue phase platform". In: *RSC Advances* 9.56 (2019), pp. 32922–32927.

[252] Hirotsugu Kikuchi et al. “Polymer-stabilized liquid crystal blue phases”. In: *Nature Materials* 1.1 (Sept. 2002), pp. 64–68.

[253] Jin Yan and Shin-Tson Wu. “Polymer-stabilized blue phase liquid crystals: a tutorial [Invited]”. In: *Optical Materials Express* 1.8 (Dec. 2011), p. 1527.